FORSCHUNGSZENTRUM ROSSENDORF FZR

WISSENSCHAFTLICH-TECHNISCHE BERICHTE
FZR-277
November 1999
ISSN 1437-322X

Matthias Strobel

Modeling and Computer Simulation of Ion Beam Synthesis of Nanostructures

Herausgeber:
FORSCHUNGSZENTRUM ROSSENDORF
Postfach 51 01 19
D-01314 Dresden
Telefon +49 351 26 00
Telefax +49 351 2 69 04 61
http://www.fz-rossendorf.de/

Als Manuskript gedruckt

FORSCHUNGSZENTRUM ROSSENDORF

WISSENSCHAFTLICH-TECHNISCHE BERICHTE

FZR-277

November 1999

Matthias Strobel

Modeling and Computer Simulation of Ion Beam Synthesis of Nanostructures

Dissertation

FORSCHUNGSZENTRUM ROSSENDORF
Institut für Ionenstrahlphysik und Materialforschung

Modeling and Computer Simulation of Ion Beam Synthesis of Nanostructures

von der
Fakultät Mathematik und Naturwissenschaften
der Technischen Universität Dresden
genehmigte

Dissertation

zur Erlangung des akademischen Grades
Doctor Rerum Naturalium
(Dr. rer. nat.)

vorgelegt von

Dipl.-Phys. MATTHIAS STROBEL
geboren am 22. Februar 1969 in Würzburg

FZR

Tag der Einreichung: 30. Juni 1999
Tag der Verteidigung: 13. Oktober 1999

Vorsitzender der Prüfungskommision: PROF. DR. GERHARD SOFF

Gutachter:

PROF. DR. WOLFHARD MÖLLER	Technische Universität Dresden
PROF. HARRY BERNAS, PHD	CNRS–CSNSM Orsay, Frankreich
PROF. DR. SIGISMUND KOBE	Technische Universität Dresden

Physic ist wahrlich das eigentliche Studium des Menschen

Georg Christoph Lichtenberg
(Deutscher Physiker und Philosoph, 1742 – 1799)

Contents

Abbreviations

An author of a (scientific) publication faces the conflict of using acronyms versus writing technical or often repeated expressions always in full length. Some claim that acronyms facilitate reading while others complain about the problem memorizing them. By carefully balancing the convenience of using abbreviations versus the readability of this thesis, I finally decided to introduce the following ones which are partly standard in the physical literature:

BC	boundary condition
BCA	binary collision approximation
bcc	body-centered cubic
CA	cellular automaton
CBII	conventional beamline ion implantation
CM	collisional mixing
CPU	central processor unit
dpa	displacements per atom
fcc	face-centered cubic
FIB	focused ion beam
GT	GIBBS-THOMSON
IA	impurity atom
IBS	ion beam synthesis
K3DLMC	kinetic three-dimensional lattice Monte-Carlo
KIM	kinetic ISING model
lhs	left hand side
LSW	LIFSHITZ-SLYOZOV-WAGNER
MC	Monte-Carlo
MCS	Monte-Carlo step
MD	Molecular Dynamics
NC	nanocluster
OR	OSTWALD ripening
PRD	particle radius distribution
RBS	RUTHERFORD backscattering
RDE	reaction-diffusion equation
rhs	right hand side

sc	simple-cubic
SRIM	Stopping and Range of Ions in Matter
TEM	transmission electron microscopy
TRIM	TRansport of Ions in Matter
VG	VOORHEES-GLICKSMAN
XTEM	cross-section TEM

Chapter 1

Introduction

Ever since the invention of particle accelerators energetic ions have been used to explore the physical laws of ion-solid interactions [1]. Besides these fundamental studies the potential of ions to modify selectively the properties of substrates has been recognized and thus found a wide area of technological applications. In modern microelectronics, for instance, current integrated circuit fabrication is based on the precise control of doping of Si wafers by implantation [2]. A further example is the hardening of steels with energetic nitrogen ions, which proceeds via the formation of nitrides close to the surface [3].

Depending mostly on the implanted fluence F_0, ion beam modification of materials can be roughly grouped into three major ranges:

- For fluences $F_0 \lesssim 10^{14}\,\mathrm{cm}^{-2}$ the implanted ions are assumed to remain isolated within the substrate. Implanted into crystals these impurities may reside on regular lattice sites and thus change the electrical properties of the host material (doping range);
- For fluences in the range $10^{15}\ \mathrm{cm}^{-2} \lesssim F_0 \lesssim 10^{16}\ \mathrm{cm}^{-2}$, in the course of implantation the deposited impurities start to exceed the solubility threshold. This causes the formation of isolated domains of a new phase [in general called nanoclusters (NCs), precipitates, quantum dots, or, if in a crystalline state, nanocrystals], which besides the mechanical may also change the optical properties of the substrate;
- For fluences $F_0 \gtrsim 10^{17}\ \mathrm{cm}^{-2}$ the second phase domains start to coalesce, which might result in the formation of a continuous buried layer of a new composition in a predefined depth of the substrate.

Ion beam synthesis (IBS) of nanostructures refers to items two and three of the above listing and consists usually of two independent steps. First, the implantation of a certain fluence F_0 is performed in a rather well defined parameter range, i.e. ion energy E, ion flux j, and substrate temperature T_{imp}. Very often this step is followed by a thermal heat treatment because (i) radiation damage is annealed out and (ii) the thermally activated redistribution of the impurities can be tailored to a large extent.

As evidenced by a vast literature, a huge variety of different NC/substrate systems has been achieved by IBS. For instance, the formation of Au [4, 5], Ag [6], Cu [7] or

Ni [8] precipitates in silica glasses or other insulators has been reported (for a review of metallic NC formation by IBS see, e.g. MAZZOLDI *et al.* [9]). The synthesis of elemental semiconducting NCs in neutral (chemically inert) matrices has been observed [10], as well as compound nanocrystal formation in single-type implantations due to chemical reactions between impurity and substrate atoms, e.g. silicide formation for metal implantation into Si [11]. Additionally, in a neutral matrix compound NCs could be detected by co- or sequential implantation of various atom types, e.g. II-VI, III-V or IV-IV semiconductor NCs in SiO_2 [12], Al_2O_3 [13] or Si [14] as well as metallic compound NCs in SiO_2 [15]. Further examples and applications of ion beams in materials science can be found in Proceedings of annual or biannual conferences in ion beam physics (for recent examples, see Refs. [16, 17]).

This work concentrates on the synthesis of NCs by ion implantation, because a precise control of the formation of these essentially zero-dimensional structures helps to use their unique physical properties in technological applications. Consisting of approximately 10^1 to 10^5 single atoms, the properties of NCs are governed by a combination of effects known from atomic and solid state physics. Hence, for their description well established concepts from both of these branches of physics are used.

Besides their attraction for conducting fundamental research, e.g. on quantum confinement [18, 19] or on hysteresis effects in structural phase transitions [20], the following examples should enlighten promising applications as well as the large technological potential of NCs:

- The non-linear optical properties of metallic NCs embedded in insulators make them attractive for all-optical switching devices [21, 7];
- For opto- and electro-luminescence from semiconducting NCs in SiO_2 the understanding and controlling of the microstructure of the precipitates seems to be vital for a tailoring of efficient devices [22, 23];
- Within the challenges of miniaturization in microelectronics is the promising use of nanocrystals in non-volatile memories [24] and even as single-electron transistors [25].

Additional to conventional IBS, the formation of NCs can be achieved by ion beam-induced disintegration of buried (multi-) layer structures due to collisional mixing effects [26, 27]. Furthermore, among others, the following preparation methods have been successfully applied to form NCs: (i) Colloidal chemistry [28]; (ii) Sol-gel processes [29]; (iii) In thin film deposition processes specific (system- and parameter-dependent) growth modes favor three-dimensional island formation (STRANSKY-KRASTANOV regime) [30, 31].

All NC synthesis methods have their specific advantages and disadvantages and, therefore, their special fields of application. For instance, the synthesis of NCs by colloidal chemistry allows by subsequent dilution steps the study of fundamental properties of single NCs [32]. Furthermore, with this method the formation of core/shell nanocrystals has been achieved [33]. It is not within the scope of this work to discuss the details of the above mentioned synthesis methods. However, a few remarks should be made about the technological importance of IBS of NCs:

+ The method is fully compatible with current microelectronics device fabrication, which allows for a convenient implementation of NC-based storage devices;

+ Ion implantation can transform a system to a state far from equilibrium, e.g. very high supersaturations can be obtained (these states in the phase diagram are usually not accessible by other processes);

+ Specific NC distributions characteristic for high implantation fluxes or high temperatures can be frozen in by rapid cooling of the system;

+ The principles of NC formation by precipitation from a depth- and time-dependent supersaturated solid solution is widely independent of the ion/substrate combination;

+ Specific isotopes of the impurity species can by selectively implanted by the use of mass filters;

+ A proper choice of implantation parameters allows to a large extent to control the density, size, and depth distributions (which are, however, in general not independent of each other) of the synthesized NCs within the host material.

These advantages are partly counterbalanced by certain disadvantages, among which the following should be mentioned:

– NC ensembles formed by IBS show a characteristic size distribution, whereas there is a need of monodisperse NCs for specific applications, which are based on size-dependent (quantum) effects;

– Even by multiple implantations with cascading energies, (nearly) homogeneous spatial distributions of NCs are restricted to the first micrometers of the substrate;

– Beam line ion implantation is a technologically extensive process, and large scale implantation of high fluences is a time consuming, and thus expensive, step.

The formation of nanostructures by ion implantation is governed by various physical processes on multiple time and length scales, which range from basic ion-solid interactions to late stage phase separation phenomena. For a comprehensive understanding of IBS one needs a consistent description of the main stages, i.e. accumulation and supersaturation of impurities, nucleation of precipitates, their subsequent growth, and, if a post-implantation annealing is applied, OSTWALD ripening (OR). Although the (homogeneous) nucleation stage of first-order phase transitions is well understood and consistent (analytical) descriptions exist, which cover the evolution of a metastable state from nucleation of second-phase particles via their subsequent growth to coarsening (see e.g. [34]-[36]), the space- and time-dependent supersaturation inherent in high-dose ion implantation imposes certain restrictions on their straightforward applicability to this process.

Technological applications of IBS are based on an understanding and control of mesoscopic properties of the implanted samples, e.g. NC size and depth distributions (NC

engineering) or characteristics of buried layers, rather than on a complete understanding and control on an atomic scale (defect engineering). This is reflected by the respective modeling approaches. While in the latter case binary collision approximation (BCA) and Molecular Dynamics (MD) simulations are the method of choice to obtain detailed atomic descriptions of ion beam induced point defect generation, migration and stability of defect clusters, in IBS the redistribution of implanted impurities is of concern on quite different time and length scales. Here, descriptions are needed, which cover the redistribution of the impurities across the implantation profile during the complete process. As will be shown in this work, appropriate modeling approaches are Monte-Carlo (MC) methods for the first to intermediate stages governed by local kinetic processes and a thermodynamic description for the late stage of NC evolution.

The motivation of this work is based on the higher-than-ever need for realistic modeling and accurate simulations of microstructural evolution in general and, due to their technological importance, of implantation phenomena in particular. For instance, with shrinking device dimensions in microelectronics, the design and conductance of crucial experiments in order to identify unambiguously the fundamental physical processes in charge of device performance becomes more and more complex. Therefore, any insight and predictions gained from theory or corresponding computer experiments becomes more and more important.

Based on pre-existing computational models used for many years in statistical physics as well as successfully applied in various areas of materials science, the task of this work was to develop and refine methods with respect to specific problems of NC formation and evolution by IBS. On an atomic scale effective particle models used in kinetic Monte-Carlo simulations [37] have proven to yield accurate descriptions of critical phenomena and of microstructural evolution in phase transitions [38]. Thus, in order to obtain size- and depth-distributions of ion beam synthesized NC ensembles, a kinetic three-dimensional lattice Monte-Carlo (K3DLMC) model has been developed. Due to its atomic nature, it is ideally suited to deal with systems being far from thermodynamic equilibrium as typical for ion implantation.

On the other hand, (equilibrium) thermodynamic concepts are the method of choice for quasi-equilibrium processes like OR of NCs, which is usually observed during subsequent annealing of implanted samples. Therefore, for the study of coarsening phenomena, a model is used, which is based on the numerical integration of the corresponding reaction-diffusion equations [39, 40]. By combining both models, the IBS of NCs can be consistently described form the very beginning of ion implantation to the late stages of annealing.

This work is organized as follows: In Chapter 2 the basic concepts of IBS are introduced and the physics of nucleation, growth, and OR of NCs discussed. Then modeling approaches to phase transitions in general and to ion beam induced phenomena in particular are shortly reviewed. The next two Chapters introduce the simulation methods used in this work in order to describe the evolution of ion-beam synthesized ensembles of precipitates: The details and intrinsic properties of the MC model are discussed in Chapter 3 followed by the description of the rate-equation approach to OR in Chapter 4, where also the results of reaction-controlled OR are presented. The next Chapter is devoted to

the study of NC formation during ion implantation in the cases of constant and varying implantation conditions and discusses corresponding Au^+ implantation experiments into SiO_2. Furthermore, modifications of the NC evolution due to ballistic effects typical for irradiation are studied on the basis of an isotropic collisional mixing model. In particular, the influence of the mixing parameters on the capillary length will be presented. Chapter 6 contains examples of simulation results obtained by combining both simulation methods. Here, a detailed study of the similarities and differences of both descriptions with respect to OR are presented. Furthermore, self-organization of ion beam synthesized NCs and specific aspects of focused ion implantation are addressed. Special applications of the MC method are discussed in Chapter 7, e.g. the redistribution of implanted impurities in the presence of an oxidizing annealing atmosphere or the extension of the model to two types of impurities in order to study the synthesis of compound NCs. Finally, a summary is given, further examples of promising applications of the Monte-Carlo method are presented, and future approaches will be envisioned.

It is naturally a difficult and challenging task to structure a thesis, in which (i) two conceptually different simulation methods are used, (ii) a good deal of theory concerning fundamental aspects of the formation and evolution of NCs is involved and should be presented, (iii) basic results of both simulation methods have to be checked with theoretical predictions and compared for similarities and differences in their common range of applicability, and (iv) studies of the physics of real systems should be performed and comparisons to experiments should be made. Not to mention the problem of introducing the basic physical concepts beginning, for instance, with the smallest scale (here single atoms) and going bottom-up to continuum descriptions as the characteristic length scales increase or to follow more the historical path and proceed vice versa. Rather than setting up Chapters dealing exclusively with one of the four points listed above, I found it more instructive to proceed on the basis of a "building-up" strategy. By this I mean, that physical processes, concepts, or methods will be discussed upon their first encounter appropriately within the actual context and extended later on if necessary. For instance, nucleation phenomena, theoretically introduced in Chapter 2, will play a major role in Chapters 5-7. A second example is the description of the K3DLMC method, which is introduced in Chapter 3 for one atomic species on the basis of thermally activated processes, and will appropriately be extended in Chapters 5 and 7 in the context of the ion implantation related physics to be considered there. May the rather extensive use of cross-references help those, who would have favored a different ordering of the subjects!

Chapter 2

Ion beam synthesis of nanostructures

Conventional IBS of nanostructures consists of the ion implantation step at low to moderate temperatures T_{imp} which is usually followed by subsequent annealing. In this work the implanted substrate is considered as a solid host of a two-phase system, namely dissolved impurity atoms (IAs, also in the following called monomers) and NCs, which either consist solely of precipitated IAs or of a chemical compound of impurities with matrix atoms (see Fig. 2.1). The complex physical processes occurring during IBS can be roughly grouped into four to five major stages [41] (see Fig. 2.2):

Accumulation/Saturation: After the energetic ions have been slowed down to the average thermal energy of the substrate by nuclear and electronic interactions, they are incorporated into the host material. In a crystalline material, for instance, the IAs can be found either on substitutional or interstitial lattice sites. Depending on temperature the impurities may diffuse through the surrounding matrix.

Supersaturation/Nucleation: After a critical concentration has been exceeded the formation of precipitates is initiated either by thermal fluctuations (homogeneous) or by heterogeneities (e.g. defects) of the substrate (inhomogeneous nucleation).

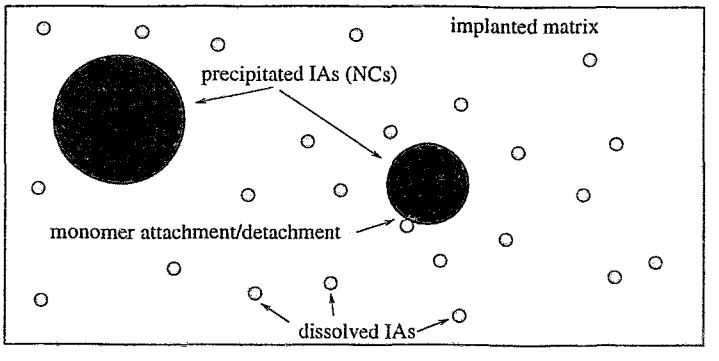

Figure 2.1: Schematic definition of impurity-substrate system and occurring impurity phases (dissolved monomers or precipitates).

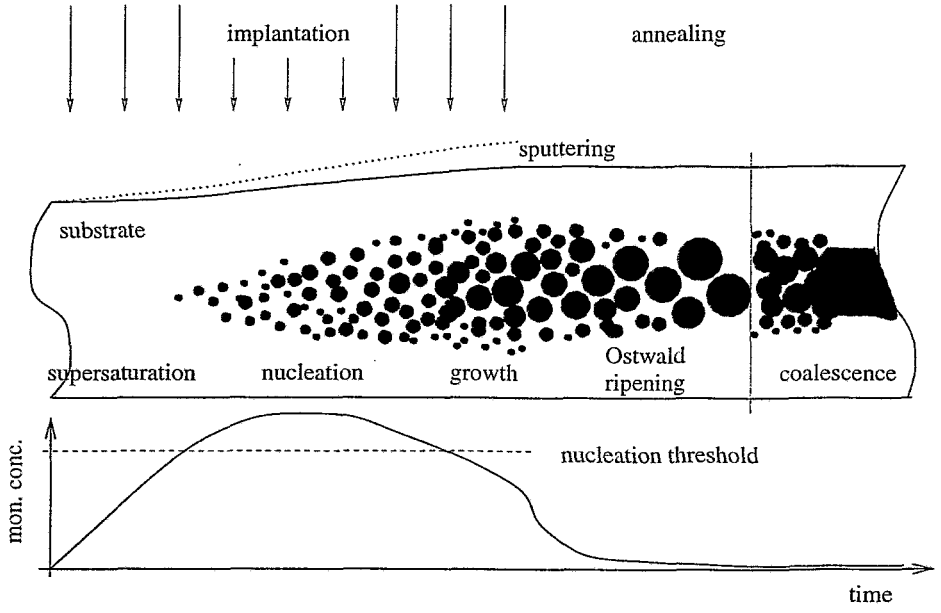

Figure 2.2: Scheme of major physical stages encountered in IBS of precipitates or buried layers for a system, where swelling due to second-phase formation exceeds sputtering. Note, that coalescence can also occur during implantation. In the bottom the corresponding evolution of the monomer concentration is shown.

Growth: As long as the local monomer concentration around the nucleated NCs is above their equilibrium monomer concentration, all NCs grow at the expense of the surrounding reservoir of dissolved IAs.

Ostwald ripening: After implantation, during annealing the monomer concentration decreases further, and in a competitive coarsening process large NCs grow at the expense of small ones which may finally dissolve.[1]

Coalescence: Neighboring NCs touch each other and merge to one (in solid-solid systems this stage is usually only met in very high-dose implantations aimed at the formation of buried continuous layers).

This scheme is, of course, to some degree artificial, because sharp boundaries between successive stages can in general not be defined (see, e.g. the review of WAGNER and KAMPMANN [34] on nucleation and phase transition phenomena). For instance, in very high-dose implantations nucleation may be replaced by spinodal decomposition. Moreover, coalescence may set in already during implantation replacing OR as driving mechanism of impurity redistribution. Furthermore, the onset of individual processes depends in general on the ion-substrate system as well as the implantation parameters.

[1] In principle, OR, i.e. the surface tension-driven diffusional mass transport form small to large NCs, is also present during implantation, but at this stage of IBS it can be regarded as a process of second order.

2.1 Ion implantation methods

A primarily used method for ion implantation is conventional beamline ion implantation (CBII). Here, ions are extracted from an ion source by an applied potential and focused into a beam which enters a mass analyzer, where one specific isotope is selected. The mono-energetic beam is then refocused by electromagnetic lenses and can be accelerated for a second time to reach a specific energy. Accordingly, for low energy purposes, e.g. implantation into ultrathin gate oxides, the last step can also be used to decelerate the ions. In the process chamber the beam is then scanned across the target (line-of-sight process), which usually provides laterally homogeneous implants (heterogeneities $\lesssim 1$ %). With conventional implanters NCs have been synthesized using ion energies from about 1 keV [42] to several MeV [43].

A special version of CBII is the explicit use of the focused ion beam (FIB) for inhomogeneous patterning, e.g. the implantation of certain areas in maskless processes. Depending on the properties of the focus, the synthesis of quantum wires and quantum dots can be achieved. In this context an interesting application is the synthesis of periodic arrays of nanocrystals (see Section 6.3), where first attempts have been made [44].

In CBII high-purity mono-energetic implants are achieved on the expense of long implantation times. An interesting alternative method is plasma immersion ion implantation suited for high-flux and large (also non-planar) area implantations which do not have to meet such stringent requirements (see e.g. [45]). In this technique a plasma containing the implantation species is generated in the process chamber. Applying a negative high voltage pulse to the target, positive ions are accelerated out of the plasma and impinge onto the target. Since the plasma boundary follows the contour of the (smooth) substrate surface, this non-line-of-sight method can be used for specimens with rather complicated topologies.

2.2 Principles of ion-solid interaction

Since materials modifications by energetic ion beams are based on irradiation-induced microstructural changes and/or the chemical nature of the deposited atoms much effort has been devoted to understand fundamental ion-solid interactions [1]. Besides a particular interest in the basic mechanisms of damage creation as well as damage accumulation, a precise knowledge of the final distribution of implanted impurities is mandatory for IBS of nanostructures.

Energetic ions impinging onto a substrate successively lose their kinetic energy by complex interactions with the bulk atoms. On its stochastic track a penetrating ion is slowed down by elastic (nuclear collisions) and inelastic (electronic excitations, ionization, ...) interactions (neglecting here nuclear reactions). Therefore, the energy loss per unit length (stopping power), which itself depends on energy, can be written as

$$\frac{\partial E}{\partial x} = \left(\frac{\partial E}{\partial x}\right)_{\text{nuc}} + \left(\frac{\partial E}{\partial x}\right)_{\text{el}} = -\rho\left[S_{\text{nuc}}(E) + S_{\text{el}}(E)\right] = -\rho S(E), \tag{2.1}$$

where ρ denotes the number density of atoms in the sample. For a given ion species both the nuclear S_{nuc} and electronic S_{el} stopping cross-sections depend on the substrate and are usually assumed not to be correlated. Knowing precisely $S_{\mathrm{nuc}}(E)$ and $S_{\mathrm{el}}(E)$ would allow to predict the dependence of defect production in the substrate on the implantation parameters.

Nuclear stopping power

Within a ballistic model the nuclear energy loss is described by a sequence of independent binary collisions (binary collision approximation (BCA) [1]), by which energy is transferred to substrate atoms. The probability of such a collision is determined by the scattering cross-section $\mathrm{d}\sigma(E, V)$, where E is the energy of the projectile prior to the collision and V the interatomic potential. The nuclear stopping cross-section is then defined as

$$S_{\mathrm{nuc}}(E) = \int_0^{T_{\mathrm{max}}} T \mathrm{d}\sigma. \tag{2.2}$$

The energy T transferred by a collision is given by (in the following, subscripts 1 and 2 refer to the incident and resting particle, respectively)

$$T = \frac{4M_1M_2}{(M_1+M_2)^2} E \sin\left(\frac{\theta}{2}\right), \qquad T_{\mathrm{max}} = T(\theta = \pi), \tag{2.3}$$

where E is the incident energy and θ the scattering angle in the center-of-mass frame. Due to this kinematic, in head-on collisions ($\theta = \pi$) of two atoms of equal mass the complete kinetic energy can be transferred to a substrate atom. After the kinetic energy of the ion has fallen below a few tens of eV, which is a rough measure for the energy needed to displace a substrate atom, its excess energy with respect to the surrounding matrix is transferred into phonons, which gives rise to an intense local heating.

Any attempts to understand the basic physical processes during ion implantation are based on a reliable description of the interaction potential. Even if the complex ion-solid interactions are decomposed into independent binary collisions, still an interatomic potential has to be found for a $(N_1 + N_2 + 2)$ body problem, since the two nuclei and the corresponding electrons interact via COULOMB forces.

Assuming that the interatomic potential is only a function of the distance $R = |\vec{r}_1 - \vec{r}_2|$ of the interacting particles, there has been much effort to generalize $V(R)$ to an universal form, which is not depending on specific electronic configurations [1]. For this purpose the effective interaction is described with the help of a screening length $a(Z_1, Z_2)$, which includes the essential parts of the Z-dependences. Usually one assumes

$$V(R) = \frac{Z_1 Z_2 e^2}{4\pi\epsilon_0 R} \Phi\left(\frac{R}{a}\right) \tag{2.4}$$

with an appropriately chosen screening function Φ. With respect to experimental data the best choice is the universal potential based on the universal screening length $a_{\mathrm{u}} =$

$0.8854a_0/(Z_1^{0.23}+Z_2^{0.23})$, where a_0 is the BOHR radius [46]. This potential has been the basis for binary collision codes like TRIM (SRIM) [47], which are frequently used to compute implantation profiles.

Electronic stopping power

For high energies (MeV-GeV regime) the electronic stopping cross-section $S_{\mathrm{el}}(E)$ exceeds $S_{\mathrm{nuc}}(E)$ and is reasonably described by the relativistic BETHE-BLOCH formulation [1]. For low energies, $S_{\mathrm{el}}(E)$ is roughly proportional to the ion velocity in the regime $v \leq Z^{2/3}e^2/(4\pi\epsilon_0\hbar)$. The intermediate regime is usually bridged by interpolation formulas.

Whereas an accurate knowledge of the nuclear and electronic stopping powers are mandatory for a detailed understanding of ion-solid interactions, in IBS of nanostructures they are basically only considered in order to derive depth profiles of implanted IAs.

Implantation profiles

If the stopping powers are known, the penetration length l of an ion can be calculated by integrating the energy loss, i.e. $l = \int_E^0 [(\mathrm{d}E)/(\mathrm{d}x)]^{-1}\mathrm{d}E$. However, one is usually more interested in the average lateral and vertical distributions of the implanted species. In CBII of large plane areas, the lateral straggling is smeared out and the resulting depth profile (the number of IAs deposited in the interval between z and $z + \mathrm{d}z$) is reasonably approximated by a Gaussian distribution

$$N(z) = \frac{F_0}{\sqrt{2\pi}\Delta R_{\mathrm{p}}} \exp\left\{-\frac{(z-R_{\mathrm{p}})^2}{2(\Delta R_{\mathrm{p}})^2}\right\}. \tag{2.5}$$

Here, F_0 denotes the implanted fluence, R_{p} the projected range and ΔR_{p} is the width of the profile due to straggling. The radial straggling ΔR_{r} becomes important in FIB experiments [48] if the beam size is of the order of ΔR_{r} or smaller. Furthermore, radial straggling has to be considered if a FIB is used for lateral patterning (see e.g. [49]) and for implantation in non-planar substrates [50], where it gives rise to lateral concentration variations.

Irradiation damage

The nuclear stopping of energetic ions creates collision cascades, in which a fraction of target atoms are set in motion. If the energy transferred to a target atom exceeds a critical value, i.e. the displacement threshold energy E_{d}, it will not return to its original site prior to the collision. In this case, a stable FRENKEL (i.e. vacancy-interstitial) pair is created. Depending on its energy the recoiling atom, in turn, can then displace further substrate atoms adding to the irradiation damage.

The number of stable FRENKEL pairs $\nu(E)$ produced by an energetic ion of energy E has been first approximated by KINCHIN and PEASE [51]: $\nu(E) = E/(2E_{\mathrm{d}})$. This

expression was later modified by SIGMUND [52] to

$$\nu(E) = \frac{\xi(E, E_\mathrm{d}) E_\mathrm{n}}{2E_\mathrm{d}}, \tag{2.6}$$

where E_n denotes the fraction of the ion's energy lost in nuclear collisions. The numerical factor $\xi(E, E_\mathrm{d})$ varies with energy and reads $\xi = 0.8$ for $E \geq 2.5E_\mathrm{d}$ (see also [53]).

For low substrate temperatures the defects are essentially immobile. Thus in the course of implantation the damage accumulates, which in the case of crystalline targets can cause their amorphization. At elevated temperatures point defects become mobile and start to recombine, thus, depending on the ratio of irradiation to recombination, a certain damage state will not be exceeded.

2.3 Formation of second-phase precipitates

The formation of nanocrystals from a supersaturated solid solution of IAs can be described within the framework of a first-order phase transition. For this purpose for simplicity the IAs are regarded as effective particles interacting with each other within a neutral matrix. The resulting evolution of the system can be understood with respect to the corresponding phase diagram.

2.3.1 Impurity-substrate phase diagram

The phase diagram of Fig. 2.3a qualitatively describes the impurity-substrate system. At a given temperature T for low impurity concentrations c the physically stable state consists of dissolved monomers. If the concentration exceeds the corresponding value $c^{(1)}_\mathrm{coex}(T)$,[2] the system is in a metastable state and tends to decay via nucleation and growth to impurity NCs embedded in the substrate. In cases, where the systems is quenched into the spinodal region of the phase diagram [here, the (classical) spinodal is defined as the curve, where the second derivative of the GIBBS free energy G with respect to the concentration of impurities vanishes [55], i.e. $\partial^2 G/\partial c^2 = 0$], the phase transition proceeds via spinodal decomposition (for reviews see, for instance, LANGER [56] and BINDER [57]). In thermal equilibrium, the one-phase region is homogeneous, whereas the two-phase region is inhomogeneous. In the last case, according to the *lever rule* (see e.g. [54]), for a given point (c, T) in phase space a fraction $[c - c^{(1)}_\mathrm{coex}(T)]/[c^{(2)}_\mathrm{coex}(T) - c^{(1)}_\mathrm{coex}(T)]$ is in precipitated domains of concentration $c^{(2)}_\mathrm{coex}(T)$. The remaining fraction $[c^{(2)}_\mathrm{coex}(T) - c]/[c^{(2)}_\mathrm{coex}(T) - c^{(1)}_\mathrm{coex}(T)]$ has composition $c^{(1)}_\mathrm{coex}(T)$.

In Fig. 2.3b various process paths occurring in IBS of nanostructures are shown. In the general case (path 1), as implantation proceeds the (depth-dependent) concentration of impurity monomers increases, and the system gradually transforms from a stable to a metastable state and starts to decay via nucleation and growth of second-phase precipitates. However, several different scenarios are possible: (i) if the implantation temperature

[2] Superscript (1) denotes here the phase of dissolved impurities, whereas superscript (2) denotes the clustered phase.

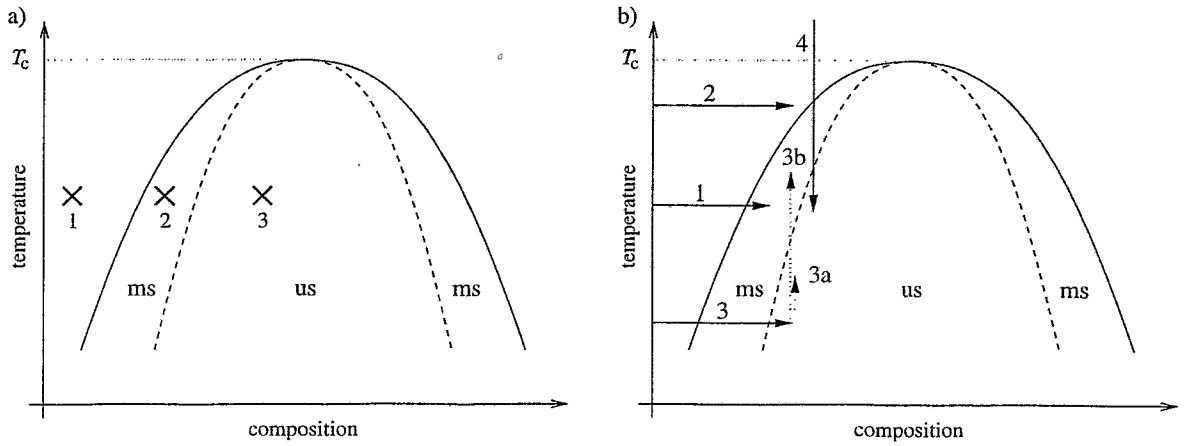

Figure 2.3: Schematic drawing of the phase diagram (see e.g. [54]). For temperatures larger than T_c no phase transition from disorder to an ordered state is observed. The solid line denotes the two branches of the coexistence curve and the dashed line is the spinodal. The metastable (ms) part is located between the coexistence curve and the spinodal, whereas the unstable (us) part is confined by the spinodal. In a) the points 1-3 refer to stable, metastable and unstable states of the system. In b) arrows 1-3 denote process paths during ion implantation, whereas arrow 4 indicates a quench from infinite temperature.

is too high and/or the ion fluence too low[3] (path 2), no NCs will form; (ii) if the implantation temperature is very low and the fluence high enough (path 3), the system could be transformed into the unstable part of the phase-diagram. Depending on the temperature of a subsequent annealing step, the resulting phase transition would then occur either via spinodal decomposition or via nucleation and growth.

The chemical potential per IA $\mu = k_B T \ln c + \varphi$ serves as an useful quantity to describe the state of the system, where the thermodynamic potential φ does not depend on the monomer concentration c [54]. The location of the phase transition (coexistence curve) is characterized by the critical chemical potential $\mu_c = \mu(c^{(1)}_{coex}(T))$. Homogeneous nucleation caused by thermal fluctuations starts, if the supersaturation expressed by $\delta\mu := (\mu - \mu_c) > 0$ is maintained on the order of the time scale of the inverse nucleation rate $[I(\delta\mu)]^{-1}$.

2.3.2 Homogeneous nucleation

The basics of the nucleation behavior of nanocrystals formed by IBS can be understood in terms of the classical kinetic nucleation theory developed by VOLMER and WEBER for equilibrium [58] and BECKER and DÖRING for steady-state conditions [59]. Applied to supersaturated gases of undercooled liquids and glasses this theory can successfully describe several features of observed nucleation phenomena.

[3] A typical example is doping of Si via low-fluence implantation in electronic device technology.

In general, the nucleation rate can be written as

$$I = A \exp\{-W\beta\}, \quad \beta = 1/(k_B T), \tag{2.7}$$

where W is the thermodynamical nucleation barrier and A a dynamical factor which describes the rate of nucleation. The following overview relating $W_{\min}$ and A to physical quantities encountered in IBS is based mainly on reviews of various experimental and theoretical aspects of homogeneous (with a few excursions to inhomogeneous) nucleation phenomena given by LANGER [56], KELTON [60], GUNTON *et al.* [61], BINDER [62], WU [63], and recently SPINELLA *et al.* [64].

For simplicity only spherical isotropic NCs with sharp interfaces are considered and any influence of strain fields is neglected. Assuming a finite mobility (either during implantation or during a subsequent heat treatment) diffusing IAs can interact and thus form tiny agglomerations, e.g. dimers, trimers, ... According to thermodynamic principles the equilibrium size distribution U per unit volume for clusters consisting of i IAs formed by thermal fluctuations is given by

$$U_{\text{eq}}(i > 1) = U(1) \exp\{-W_{\min}(i)\beta\}, \quad U(1) = c. \tag{2.8}$$

Here, $W_{\min}(i)$ denotes the minimum reversible energy needed in order to form a cluster of size i and c is the impurity monomer concentration.

The transition from a solid solution to precipitates involves the formation of an energetically unfavorable phase boundary, thus the corresponding change of the GIBBS free energy per IA ΔG can be written as [56]

$$\Delta G(i) = -(\delta\mu)i + \gamma i^{2/3}. \tag{2.9}$$

In the last equation the first term denotes the bulk and the second the interface contribution which is proportional to the surface tension σ [i.e. $\gamma = (36\pi V_a^2)^{1/3}\sigma$, where V_a is the atomic volume]. In the standard framework of classical nucleation theory, the surface contribution is assumed to be independent of size, i.e. $\sigma \neq \sigma(i)$ (for a discussion of modifications due to a size-dependent surface tension see [65]). The underlying capillarity approximation of Eq. (2.9) is, of course, only applicable for reasonably large clusters which possess clearly distinct bulk and surface energy states.

Fig. 2.4 shows typical examples of the dependence of ΔG on the cluster size. It is obvious that as long as $\delta\mu < 0$, all clusters are unstable. However, for $\delta\mu > 0$ there exists a critical size i^* associated with a maximum of ΔG

$$W_{\min} = \Delta G(i^*) = \frac{4\gamma^3}{27(\delta\mu)^2} \quad \text{for} \quad i^* = \left(\frac{2\gamma}{3\delta\mu}\right)^3, \tag{2.10}$$

which denotes the nucleation barrier (see Fig. 2.4). According to classical nucleation theory the higher the supersaturation $\delta\mu$ the lower is the corresponding critical cluster size.[4] In general clusters with $i > i^*$ can lower their free energy per atom by attachment of further monomers, whereas ones with $i < i^*$ prefer detachment of monomers.

[4]Note, that close to the spinodal $W_{\min} \approx k_B T$, and spinodal composition itself is characterized by the absence of any nucleation barrier [57].

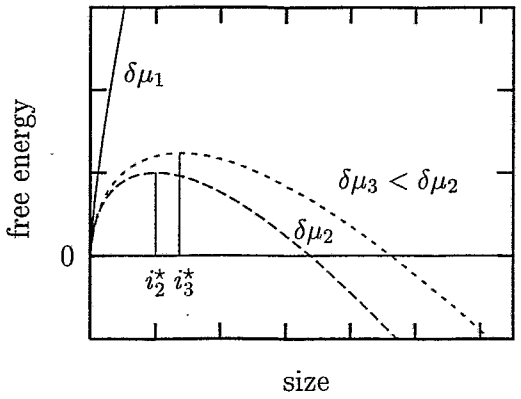

Figure 2.4: For three different cases ($\delta\mu_1 < 0$, $0 < \delta\mu_3 < \delta\mu_2$) the dependence of the GIBBS free energy G on the size i of a precipitate is plotted according to Eq. (2.9). In the absence of supersaturation, i.e. $\delta < 0$, precipitates of any size are unstable. For metastable systems, i.e. $\delta\mu > 0$, the nucleation barrier depends on the degree of supersaturation (here $i^*_{2,3}$ denotes the corresponding cluster size).

In order to obtain the rate of nucleation I concepts from non-equilibrium statistical mechanics have to be applied. For this purpose it is assumed that NCs grow or shrink only by bimolecular steps, i.e. evaporation or condensation of one monomer at a time. This implies, that coalescence of NCs can be neglected which is a reasonable assumption for nucleation in a condensed matter system, because the cluster diffusivity rapidly decreases as a function of size. The derivation of the nucleation rate is usually done in the steady-state regime, where one assumes, that supercritical NCs of size $i > i^*$ are removed and the i monomers are brought back into solution such as to keep $\delta\mu$ constant. Within this approach, which ignores depletion effects, the steady-state nucleation rate is independent of time and cluster size, i.e. $I_s \neq I(i,t)$

Let $I(i)$ be defined as the rate at which NCs of size $(i-1)$ are transformed to size i, then the NC distribution U in size space is given by

$$\frac{\partial U(i,t)}{\partial t} = I(i) - I(i+1). \tag{2.11}$$

The nucleation rate can be expressed as

$$I(i) = k_+(i-1)U(i-1,t) - k_-(i)U(i,t), \tag{2.12}$$

where the coefficients $k_+(i)$ and $k_-(i)$ denote the rate of attachment and detachment, respectively, of one monomer with respect to a NC of size i. The difference between the VOLMER-WEBER [58] and BECKER-DÖRING [59] approaches is the use of the equilibrium U_e or steady-state U_s size distributions, respectively.

By applying the principle of detailed balance (which is strictly valid only for equilibrium conditions) the kinetic coefficients can be related

$$\frac{k_+(i-1)}{k_-(i)} = \frac{U_{\rm eq}(i)}{U_{\rm eq}(i-1)} = \exp\left\{-[\Delta G(i) - \Delta G(i-1)]\beta\right\}. \tag{2.13}$$

From this it can be shown, that the dynamics of the system can be expressed in terms of a FOKKER-PLANCK equation

$$\frac{\partial U(i,t)}{\partial t} = \frac{\partial}{\partial i}\left\{k_+(i)\left[\beta\frac{\partial \Delta G(i)}{\partial i}U(i,t) + \frac{\partial U(i,t)}{\partial i}\right]\right\}. \tag{2.14}$$

Eq. (2.14) can be interpreted as the diffusion equation for NCs in one-dimensional NC size space [62] with a size-dependent "diffusion coefficient" $[k_+(i)]$ and a term accounting for a "drift" $[k_+(i)\beta(\partial\Delta G(i))/(\partial i)]$. The details of the kinetics of this stochastic process in size space are determined by $k_+(i)$.

On the basis of physically reasonable approximations of Eq. (2.14), e.g. saddle-point integration [56], the steady-state nucleation rate is given by

$$I_{\rm s} = U(1)k_+(i^*)Z\exp\left\{-\Delta G(i^*)\beta\right\}, \tag{2.15}$$

where the ZELDOVICH factor Z [66] accounts for the fact, that not all precipitates which reach size i^* actually continue to grow. For a complete description of homogeneous nucleation it remains to determine the kinetic coefficient $k_+(i^*)$ for special systems.

Nucleation in condensed systems

For nucleation within a condensed system the forward and backward rate constants can be calculated assuming that the system passes through an activated complex [67]

$$k_+(i) = 4i^{2/3}\nu\exp\{-\Delta g(i)\beta/2\} \tag{2.16}$$

$$k_-(i) = 4(i-1)^{2/3}\nu\exp\{\Delta g(i)\beta/2\}. \tag{2.17}$$

Here, $\Delta g(i) = \Delta G(i+1) - \Delta G(i)$ and ν is the atomic jump frequency at the nanocrystal interface. If ν is assumed to be equal to the jump frequency of bulk diffusion, then the relation $\nu = 6D/\lambda^2$, where λ is the atomic jump distance, can be used to rewrite the steady-state nucleation rate [60]

$$I_{\rm s} = U(1)\frac{24Di^{*2/3}}{\lambda^2}Z\exp\left\{-\Delta G(i^*)\beta\right\}. \tag{2.18}$$

Thus $I_{\rm s}$ is explicitly proportional to the monomer concentration $c = U(1)$, but nonlinearities arise due to the additional dependence of the critical NC size i^* [Eq. (2.10)] on the supersaturation (and thus on c). Furthermore, the steady-state nucleation rate is characterized by the total thermodynamic energy barrier given by the sum $E_{\rm A} + \Delta G(i^*)$, where $E_{\rm A}$ is the activation energy for diffusion. Thus it is obvious form Eq. (2.18), that although

a system can be in a highly supersaturated state, there might be no nucleation, if thermal fluctuations are too weak to make atoms mobile.

In cases, where there is a lattice mismatch between the precipitated phase and the surrounding matrix or where elemental nanocrystals are formed, nucleation depends on the associated elastic potential. This can be described by adding a volume-dependent term to the change in ΔG [Eq. (2.9)]. Furthermore, the NC growth rate is modified in a sense that monomer diffusion in the strained vicinity of a NC is influenced.

2.3.3 Nucleation in IBS

Before discussing the applicability of classical homogeneous nucleation theory to NC formation in IBS, some additional aspects of nucleation should be mentioned briefly.

Inhomogeneous nucleation

While homogeneous nucleation is completely due to thermal fluctuations of the metastable system heterogeneities within the system can catalyze the phase transition. For nucleation within a condensed system, such catalytic sites can be grain boundaries, impurities, or defect complexes like dislocations or vacancy clusters [68]. In such an environment, the effective nucleation rate can differ substantially form the homogeneous one [Eq. (2.18)] and can be written as

$$I_\mathrm{i} = A_\mathrm{i} \exp\{-W_\mathrm{i}\beta\}\,. \tag{2.19}$$

Usually, the relation $W_\mathrm{i} < W$ can be assumed which is due to an effectively lower interface energy contribution to the nucleation barrier. Since the dependence of I_i on W_i is exponentially, a reduction of the energy barrier can greatly enhance the nucleation rate.

Time-dependent nucleation

Classical nucleation theory is often applied to systems which are rapidly quenched from the stable to the metastable state, e.g. the expansion of a cloud chamber. It is obvious that nucleation does not start instantaneously, rather, after a time lag (an incubation period), a transient nucleation rate is observed, which asymptotically tends to the steady-state value provided that depletion effects can be neglected.

According to various analytical treatments within the classical nucleation theory, i.e. for $\delta\mu = \mathrm{const} > 0$, the transient regime can be approximated by

$$I(i^*,t) = I_\mathrm{s}\left(1 - \exp\{-t/\tau_\mathrm{t}\}\right), \quad \tau_\mathrm{t} = \alpha/(k_+(i^*)Z^2), \tag{2.20}$$

where Z denotes the ZELDOVICH factor and the numerical constant α depends on the particular derivation (see [69, 60] and further references therein). The transient time τ_t decreases with increasing temperature as well as with increasing supersaturation.

In general, also depletion effects have to be taken into account during the nucleation stage, which, in turn, influence the nucleation rate. This can be done by considering the

normalized volume $v(t)$, which is available for the formation of supercritical clusters [70]. However, while for solid-to-solid phase transitions $v(t)$ is simply given by $1 - v_0(t)$, where $v_0 = \phi$ is the volume fraction of the (nucleated) new phase, in IBS nucleation is restricted to the volume fraction characterized by $\delta\mu > 0$. Depending on the size of the depletion zone (i.e. the volume for which $\delta\mu < 0$ holds) around each NC, which is no longer available for nucleation, v_0 can considerably exceed ϕ. During implantation, v_0 is a function of the ratio of the deposition to the diffusion rate.

Discussion of nucleation in IBS

In high-dose ion implantation nucleation of NCs can be encountered at two quite different stages of the process. The phase transition occurs either during implantation and/or during a post-implantation heat treatment. For a given ion-substrate system the primary nucleation stage can roughly be classified with respect to the diffusion length $L_{\mathrm{Diff}} = \sqrt{2Dt}$ of impurity monomers during implantation, where the implantation time t for a nominal fluence F_0 and an ion flux j is given by $t = F_0/j$. Furthermore, the local accumulation of impurities is a function of the ratio j/D. The comparison of L_{Diff} with $\tilde{R}$, which is the radius of a hypothetical sphere defined by $4/3\pi\tilde{R}^3\bar{c}(F_0) \lesssim i^\star$ ($\bar{c}(F)$ denotes the averaged local concentration after a fluence F has been implanted), and ΔR_{p} allows the following phenomenological categorization:

(i) $L_{\mathrm{Diff}} < \tilde{R}$**:** This condition states that thermal fluctuations do not initiate precipitation. For instance, this situation is assumed to be encountered for Ge implantation into SiO_2 at or below room temperature [71].[5]

(ii) $L_{\mathrm{Diff}} \approx \Delta R_{\mathrm{p}} > \tilde{R}$**:** Nucleation starts during implantation, when the monomer concentration exceeds the nucleation threshold ($\delta\mu > 0$). Due to the implantation profile the first stable precipitates appear close to R_{p}. Since the concentration increase is proportional to the implantation profile, a larger supersaturation is reached in the center of the profile than in the tails. Accordingly, the critical NC size is supposed to increase from the center to the tails. In the course of implantation, the nucleation region spreads outside, whereas behind the nucleation front the growth stage sets in. In this case NCs are formed essentially across the whole deposition range with a density roughly proportional to the impurity profile.

(iii) $L_{\mathrm{Diff}} \gg \Delta R_{\mathrm{p}} > \tilde{R}$**:** NCs formation starts close to R_{p}, where the highest concentration of IAs is achieved. Due to the high mobility of the impurities, during the ongoing implantation those deposited in the tails of the distribution either diffuse away from the implantation region or diffuse into the center, where the already formed NCs act as sinks. The resulting monomer fluxes prevent a spreading of the nucleation region across the profile, because in the tails the critical monomer concentration will not be exceeded. Therefore, the nucleation region is restricted close to R_{p}.

[5] If tiny NCs have been formed during implantation they are below the TEM detection limit.

Implantation modes (ii) and (iii) are usually met for metal implantation into insulators.

However, classical nucleation theory as described above is based on several assumptions which can not be expected to be met in IBS of nanocrystals:

- Due to the depth-dependence of the implantation profile [Eq. (2.5)], there are spatial inhomogeneities in the layer of phase transition, i.e. $\delta\mu = \delta\mu(\vec{r})$. In contrast to a homogeneous supersaturation background the modification of the nucleation behavior in presence of concentration gradients is not clear.

- Since a certain fluence is implanted, depletion effects have to be considered, at least at the end of the nucleation stage, i.e. $\delta\mu(\vec{r}) = \delta\mu(\vec{r}, t)$. In case (iii) additionally the evolution of the supersaturation in the course of implantation influences the phase transition. Thus it is not clear, if the steady-state nucleation rate I_s is reached at all.

- Furthermore, in the case of precipitation during implantation collisional mixing modifies the nucleation rate by enhancing the rate of dissolution of a NC which can be written as [64]

$$I_{\mathrm{CM}}(i) = k_+(i-1)U(i-1,t) - [k_-(i) + k_{\mathrm{CM}}(i)]U(i,t). \tag{2.21}$$

  As a consequence, for a given implantation temperature the critical NC size shifts to a higher value, i.e. $i^*_{\mathrm{CM}} > i^*$. However, assuming a fixed ion flux, i^*_{CM} decreases to i^* for increasing temperature [64]. Note, that this is in line with the model of MARTIN [72], according to which the effect of an ion flux can be cast to some extent into an effective higher temperature $T_{\mathrm{eff}} = T + \Delta T_{\mathrm{CM}}$.

- Classical nucleation theory assumes isotropic spherical precipitates, whereas NCs may be crystalline having an anisotropic faceted shape. Thus, not all surface positions are equivalent with respect to attachment and detachment of monomers, which, in turn, modifies the kinetic growth parameters k_+ and k_- [69].

- The distribution of damage in the substrate caused by ion implantation is depth-dependent. Thus, if heterogeneous nucleation has a major influence, the final NC distribution should be correlated to the damage profile.

It is obvious from this listing that for IBS the effective supersaturation $\delta\mu(\vec{r}, t)$ is difficult to compute, and hence the number of nucleated NCs, given by

$$N_{\mathrm{NC}} = \iint I(\vec{r}, t)\mathrm{d}^3 r\mathrm{d}t, \tag{2.22}$$

can hardly be predicted analytically.

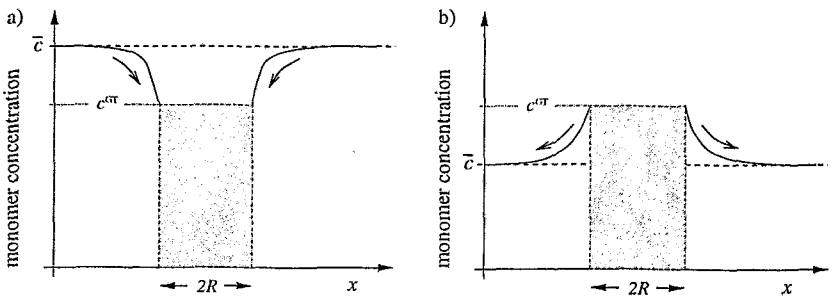

Figure 2.5: Schematic drawing of the monomer concentration field of a single NC of radius R in one dimension. The NC grows (a), if the surrounding average concentration $\bar{c}$ is larger than its own equilibrium concentration. In the opposite case (b), it shrinks.

2.4 Growth, coarsening, and coalescence of nanoclusters

A single isolated second-phase precipitate interacts with the initial phase by monomer exchange via the common phase boundary. In general this interface is curved and the explicit monomer attachment and detachment rates depend on this curvature. Accordingly, the equilibrium concentration in a volume ΔV above a surface segment ΔA is also a function of the local curvature (for simplicity the following discussion is restricted to the diffusion controlled case; a more general discussion will be presented in Chapter 4). For a spherical isotropic NC of radius R this relation is given in a thermodynamic description by the GIBBS-THOMSON (GT) relation [73]

$$c^{\mathrm{GT}}(R) = c_\infty \exp\left\{\frac{R_\mathrm{c}}{R}\right\}, \quad R_\mathrm{c} = 2\sigma V_\mathrm{a}\beta. \tag{2.23}$$

Here, c_∞ denotes the impurity equilibrium concentration at a flat ($R \to \infty$) phase boundary (i.e. the solidus), and the capillary length R_c is given by the material parameters surface tension σ and the atomic volume V_a. If the average surrounding concentration $\bar{c}$ is larger than c^{GT}, this NC acts as a sink for monomers and will grow (see Fig. 2.5a). In the opposite case, i.e. $\bar{c} < c^{\mathrm{GT}}$, it behaves like a monomer source and will shrink (see Fig. 2.5b).

Although the evolution of diffusionally interacting NCs is a complex many-body process, a good basic understanding can be achieved by studying the behavior of a single precipitate in a mean-field approach. Restricting this description furthermore to the adiabatic limit, which implies that the growth rate of a NC is slow compared to the resulting adjustment of the concentration profile of IAs, the stationary diffusion equation has to be solved. In the presence of a constant position-independent volume source term $G \neq G(\vec{r}, t)$ of monomers, which approximates the effect of impurity deposition due to the ion beam, one obtains for

a spherical isotropic precipitate of radius R at site $\vec{r}_0$

$$\frac{1}{r^2}\frac{\partial}{\partial r}\left(r^2\frac{\partial}{\partial r}\right)c(r) = -\tilde{G} = -\frac{G}{D}. \tag{2.24}$$

For the different stages encountered during IBS a solution of the last equation has to be sought with respect to the boundary conditions (BCs)

$$c(\vec{r})|_{|\vec{r}-\vec{r}_0|=R} = \hat{c} \tag{2.25}$$

and either one of the two following

$$\lim_{|\vec{r}|\to\infty} c(\vec{r}) = c_\mathrm{u} \tag{2.26}$$

$$\left.\frac{\partial c(r)}{\partial r}\right|_{|\vec{r}-\vec{r}_0|=s>R} = 0. \tag{2.27}$$

Usually, one assumes (i) that the monomer concentration at the curved phase boundary is given by the GT relation [Eq. (2.23)], i.e. $\hat{c} = c^\mathrm{GT}$, and (ii) that the monomer concentration at infinite distance can be identified with the average concentration, i.e. $c_\mathrm{u} = \bar{c}$.

Growth stage

The NC growth stage is encountered during implantation when nucleation has ceased, i.e. after the monomer concentration has fallen below the effective nucleation threshold. Due to the continuous impurity deposition, the monomer concentration may stay above the equilibrium values of all supercritical NCs, i.e. $\bar{c} > c^\mathrm{GT}(R_\mathrm{min})$ of the smallest stable precipitate. In this case OR due to the inevitable size dispersion is only a second order process since the concentration field effectively screens competitive coarsening (see Fig. 2.6a).

The growth law of a single NC is then related to the available volume for which it acts exclusively as a sink for diffusing monomers. If n denotes the NC density after the nucleation stage, then this monomer reservoir is of the order $s^3 \approx n^{-1}$. To proceed further it is assumed, that there is no monomer flux [see BC Eq. (2.27)] between adjacent cells containing one precipitate ("muffin tin" configuration). Neglecting collisional mixing [i.e. ballistic effects of ion irradiation which would add an additional source term on the rhs of Eq. (2.24)], the concentration field is given by

$$c(r) = \hat{c} + \frac{\tilde{G}}{6R}\left(R^3 + 2s^3\right) - \frac{\tilde{G}r^2}{6} - \frac{\tilde{G}s^3}{3r} \quad \text{for} \quad R \le r \le s. \tag{2.28}$$

By evaluating the monomer flux through the NC surface the growth law reads

$$\frac{\mathrm{d}R}{\mathrm{d}t} = \frac{V_\mathrm{a}G}{3R^2}\left(s^3 - R^3\right). \tag{2.29}$$

The last equation simply states, that the rate of growth is proportional to the available volume of monomer deposition. In the case $s^3 \gg R^3$, one obtains a constant volume growth rate $\mathrm{d}V_\mathrm{NC}/\mathrm{d}t$. It should be noted, that Eq. (2.29) is not explicitly temperature dependent. Rather, the temperature enters indirectly via the value of s, because the density of NCs is determined in the (temperature-dependent) nucleation stage.

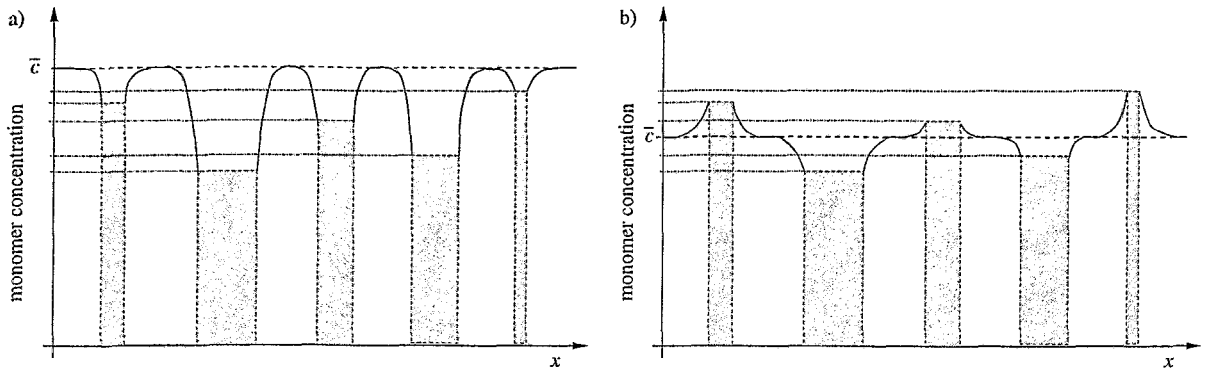

Figure 2.6: Scheme of the monomer concentration in an one-dimensional ensemble of NCs. In (a) all NCs grow, because the average concentration $\bar{c}$ fed by continuous monomer deposition is larger than the corresponding equilibrium concentrations. In (b) the situation for OR is shown. Here, the NC equilibrium concentrations are such, that the two largest grow while the three smaller NCs shrink.

Coarsening stage

After implantation, the monomer concentration rapidly decreases and its local value is determined by the surrounding NCs rather than by feeding through the ion beam. Now, c^{GT} of the smallest NCs will be above the average concentration, which, in turn, initiates their dissolution (see Fig. 2.6b). This process of diffusional material redistribution from small to large NCs is known as OR. The driving force is the minimization of the surface energy of the whole ensemble of second-phase particles.

With respect to the BCs Eqs. (2.25) and (2.26) the solution of Eq. (2.24) in the case $G = 0$ is given by

$$c(r) = c_{\mathrm{u}} - \frac{R[c_{\mathrm{u}} - \hat{c}(R)]}{r} \quad \text{for} \quad r \geq R. \tag{2.30}$$

After substituting the average local concentration $\bar{c}$ for c_{u} and assuming $\hat{c} = c^{\mathrm{GT}}$, the corresponding growth law reads

$$\frac{\mathrm{d}R}{\mathrm{d}t} = -\frac{DV_{\mathrm{a}}}{R}\left[c^{\mathrm{GT}}(R) - \bar{c}\right], \tag{2.31}$$

which is obtained by integrating the monomer flux through the NC surface.

A more detailed discussion of OR, including the influence of diffusion and reaction control, will be given in Chapter 4. There it will be discussed that this NC description is a good approximation for highly dilute systems, i.e. for vanishing volume fraction ϕ of the second phase. However, typical systems in IBS have volume fractions of the impurity phase of several percent. In this case, NCs are not embedded independently in an uniform background sea of dissolved monomers. Rather, NCs interact via monomer diffusion and the local monomer concentration is now a function of the NC size and space distributions.

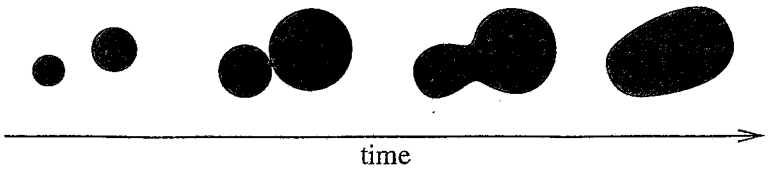

Figure 2.7: Schematic drawing of coalescence of two growing NCs in the course of implantation.

As a consequence, in a local mean-field approach Eq. (2.31) is modified by a term taking into account the diffusional NC interactions.

Coalescence stage

In systems with very high precipitate densities and/or continuous monomer supply during implantation, neighboring NCs may touch each other and start to merge (see Fig. 2.7). For these coalescence events the touching zone is characterized by surfaces with negative curvature which have a lower equilibrium concentration than the solidus. Therefore, IAs will preferentially migrate in this area either by surface or bulk diffusion and a rod-like precipitate will evolve in a transient stage. The formation of a continuous buried layer by IBS proceeds on the basis of coalescence of smaller precipitates.

2.5 Modeling and simulation approaches

Progress in Materials Science is driven by a thorough qualitative as well as accurate quantitative understanding of basic physical and chemical processes. Supported by the tremendous increase of computing power, modeling and simulation of system properties starts to compete with conventional experiments in gaining knowledge of complex systems. This has created the new discipline of Computational Materials Science with the ultimate goal to give precise predictions of the physics and chemistry of materials.

In the area of ion beam modification of materials (simulation) models describing the implanted impurity redistribution as well as defect generation are of general interest. Using the BCA of ion-solid interactions, TRIM (SRIM) [47], for instance, is widely used to calculate implantation profiles as well as to obtain defect-related data, e.g. vacancy or interstitial distributions. Special developments of BCA codes include the treatment of channeling effects in crystals (CRYSTAL-TRIM [74]) and the consideration of dynamical changes of the substrate composition in the course of implantation (TRIDYN [75, 76]). However, these approaches do not include (i) the phase transition to precipitates usually observed in high-dose implantations and (ii) defect evolution. Thus a consistent model describing all processes of IBS starting from a BCA description of ion-solid interaction to late-stage annealing phenomena is not yet available.

The traditional way of modeling phase transitions *given* a particular supersaturation is based on two complementary descriptions due to the experimental observation methods:

- Information about phase separation can be obtained by (small angle) X-ray and neutron scattering (see, e.g. [34]), where one measures the structure factor $S(\vec{k},t)$ of the system (with respect to the scattering wave vector $\vec{k}$). The structure factor is defined as the FOURIER transform of the two-particle (or local concentration) correlation function $G(\vec{r},t) = \langle c(\vec{x}+\vec{r},t)c(\vec{x},t)\rangle$ and reads

$$S(\vec{k},t) = \sum_{\vec{r}} \exp\{i\vec{k}\vec{r}\}G(\vec{r},t). \tag{2.32}$$

The evolution of the system can be studied by seeking a solution to the highly nonlinear equation of motion for the structure factor [56, 77]

$$\begin{aligned}\frac{\partial S(\vec{k},t)}{\partial t} &= -2Mk^2\left[\left(Kk^2 + \left.\frac{\partial^2 f}{\partial c^2}\right|_{c_0}\right)S(\vec{k},t)\right. \\ &\quad \left. + \sum_{n=3}^{\infty}\frac{1}{(n-1)!}\left.\frac{\partial^n f}{\partial c^n}\right|_{c_0} S_n(\vec{k},t)\right] + 2Mk^2\beta^{-1},\end{aligned} \tag{2.33}$$

where M denotes the mobility of single particles and K is proportional to their squared mean interaction range. The coarse-grained free energy f of the system is expanded around the (macroscopically) averaged concentration c_0 of the minority component and $S_n(\vec{k},t)$ are FOURIER transforms of higher-order pair-correlation functions. This description is especially suited to study spinodal decomposition.

- A more direct method is to determine the distribution function of NCs $f(s,t)$ via TEM, where s is a measure of the NC size (either the radius R or the number of particles i). In principle the evolution of the phase separation is completely defined by the general kinetic equation of the time evolution of $f(i,t)$ [78]

$$\begin{aligned}\frac{\partial f(i,t)}{\partial t} &= \sum_{i'=1}^{\infty} k_-(i+i',i')f(i+i',t) + \frac{1}{2}\sum_{i'=1}^{i-1} k_+(i-i',i')f(i',t)f(i-i',t) \\ &\quad - \frac{1}{2}\sum_{i'=1}^{i-1} k_-(i,i')f(i,t) - \sum_{i'=1}^{\infty} k_+(i,i')f(i,t)f(i',t).\end{aligned} \tag{2.34}$$

Taking additionally into account the splitting of NCs into smaller fragments (first term on rhs) as well as coagulation of NCs of sizes i and i' (third term), the last equation is a generalization of Eq. (2.11), where only monomer evaporation and condensation have been considered. The fundamental problem is to determine the rate coefficients $k_\pm(i,i')$.

Various aspects of IBS of precipitates and the corresponding redistribution of implanted IAs have been modeled on a wide range of time and length scales. Whereas Molecular Dynamics (MD) studies deal with detailed atomic interactions on time scales of picoseconds

and Monte-Carlo (MC) methods stochastically describe the dynamics of large numbers of particles, several mesoscopic and continuum (thermodynamic) approaches allow to model phase transitions starting from nucleation or spinodal composition to late-stage coarsening phenomena of large ensembles of NCs.

2.5.1 Atomic description

On an atomic scale two simulation methods are commonly used, which are based on quite different footings. Since MD studies are only of marginal and supporting use with respect to IBS of nanostructures, the emphasis in this work will be on MC methods.

Molecular Dynamics approach

In MD simulations (see e.g. [79]) the evolution of a set of interacting atoms is followed by solving the corresponding Newtonian equations of motion. At a given instant the positions $\{\vec{r}_i(t)\}$ and momenta $\{\vec{p}_i(t)\}$ are known. Then, according to the chosen interaction potential, the forces acting on each atom are computed. This specifies the evolution of the system within a time interval Δt, after which the algorithm is repeated.

The most important part of MD simulations is the choice of the interaction potential. Depending on the size of the model system and the accuracy needed, interaction potentials range from first principles quantum mechanical based to semi-empirical and empirical potentials.

Since typical time scales of atomic motions within a condensed matter system are on the order of picoseconds this computationally intensive method is only applicable for phenomena at best on the order of a few nanoseconds. Thus, at present MD is restricted to the study of fundamental ion-solid interaction processes, for instance the physics of damage creation (see e.g. [53]).

However, MD simulations have proven to be very valuable in computing structural and electronic properties of materials. For instance, energy barriers for diffusion can be computed and equilibrium properties of small to medium nanoclusters like configuration-dependent binding energies and geometries can be obtained. MD results are often used as input parameters for other simulation approaches like MC methods.

Monte-Carlo approach

The MC method has been proven to be an efficient means to describe complex systems with very large degrees of freedom, as they are characteristic for problems in condensed matter physics [37, 80]. Since for such systems the exact computation of physical observables is impractical, one relies on statistical methods like MC simulations in order to get numerical approximations. Based on specific physical models, MC simulations allow for direct comparisons to experiments as well as they can bridge the gap between experiment and theory by exploring the consequences of particular theoretical assumptions and approximations.

In a statistical model the state of a system is described by a corresponding configuration $\mathcal{X}$ in phase space. Let $S = \{\mathcal{X}\}$ denote the set of all possible configurations and $P(\mathcal{X}, t)$ their time-dependent probability distribution, where $d = \dim(\mathcal{X})$ denotes the microscopic degrees of freedom. If a system is described by a model Hamiltonian $\mathcal{H}$ then the thermodynamic equilibrium value of an observable O at time t_0 is given by

$$\langle O \rangle (t_0) = \int_S O(\mathcal{X}, t_0) P(\mathcal{X}, t_0) \mathrm{d}\mathcal{X}, \quad P(\mathcal{X}, t) = \frac{1}{Z} \exp\{-\mathcal{H}(\mathcal{X}, t)\beta\}, \tag{2.35}$$

where Z denotes the partition function.

The underlying idea of MC simulations is to compute average values of observables based on stochastically chosen phase space configurations. For this purpose one can randomly choose N configurations, weigh them according to their thermodynamic probability, i.e. their BOLTZMANN weight, and calculate their average. The problem of this "simple sampling" method is the high-dimensionality of the phase space which makes it difficult to pick out the important configurations. This problem can be circumvented by the method of "importance sampling", where only statistically significant states enter the calculation of expectation values $\langle O \rangle$. This is achieved by constructing a Markovian chain of configurations $\mathcal{X}_k, k = 1, ..., M$, which tends to converge to the thermodynamic probability distribution P_{eq} in the limit $k \to \infty$. Starting with the Master equation describing the evolution of the system,

$$\frac{\partial P(\mathcal{X}, t)}{\partial t} = \sum_{\mathcal{X}'} W(\mathcal{X} \to \mathcal{X}') P(\mathcal{X}, t) + \sum_{\mathcal{X}'} W(\mathcal{X}' \to \mathcal{X}) P(\mathcal{X}', t), \tag{2.36}$$

where the transition probabilities W connect two states, the principle of detailed balance

$$P_{\mathrm{eq}}(\mathcal{X}_k) W(\mathcal{X}_k \to \mathcal{X}_{k+1}) = P_{\mathrm{eq}}(\mathcal{X}_{k+1}) W(\mathcal{X}_{k+1} \to \mathcal{X}_k) \tag{2.37}$$

is used to generate the configurations $\mathcal{X}_k$. While the application of Eq. (2.37) is sufficient to guarantee convergence of the Markovian chain [37] the explicit form of the transition probability W is not fixed. Whereas any choice satisfying

$$\frac{W(\mathcal{X}_k \to \mathcal{X}_{k+1})}{W(\mathcal{X}_{k+1} \to \mathcal{X}_k)} = \exp\{-\Delta\mathcal{H}\beta\}, \quad \Delta\mathcal{H} = \mathcal{H}(\mathcal{X}_{k+1}) - \mathcal{H}(\mathcal{X}_k) \tag{2.38}$$

is permissive, the METROPOLIS method [81], where

$$W(\mathcal{X}_k \to \mathcal{X}_{k+1}) = \begin{cases} \tau_0^{-1} \exp\{-\Delta\mathcal{H}\beta\} & , \quad \Delta\mathcal{H} > 0 \\ \tau_0^{-1} & , \quad \text{otherwise,} \end{cases} \tag{2.39}$$

has gained considerable attention. The constant τ_0 in Eq. (2.39) is an arbitrary constant, which is interpreted as a time scale in dynamic MC simulations (see Section 3.5.2). Usually the METROPOLIS algorithm corresponds to the local change of one degree of freedom, but also cluster algorithms changing many degrees of freedom at one instant are frequently used [82, 83]. The acceptance of transitions to states with higher energy can be understood by noting, that the *free energy* rather than the internal energy is subjected to minimization.

Standard MC is used to calculate thermodynamical equilibrium values, thus the transition probabilities have not to be related to the explicit dynamics of the system. In contrast, in kinetic Monte-Carlo simulations the emphasis is on relaxation or non-equilibrium processes. Thus the Markovian chain to be generated has to represent a possible evolution of the system, i.e. configuration changes have to correspond to actual physical processes. Since each event in real systems, e.g. a thermally activated single diffusion step of a particle, happens with some probability per unit time, this provides a means to couple physical time scales to the time scale τ_0 of kinetic MC events.[6]

Besides the dynamical part MC simulations are characterized by the geometry. In general MC simulations are used for continuum as well as for discrete models. If the particles are defined on lattice positions then the system is usually called a lattice model.

MC methods have been extensively applied to study the properties of magnetic systems. A frequently used model Hamiltonian for uniaxial ferromagnets is based on the ISING [84] model, where interactions are restricted to nearest-neighbor spins

$$\mathcal{H} = -J \sum_{\langle i,j \rangle_{\mathrm{nn}}} S_i S_j - H \sum_{i}^{N} S_i \,, \quad S_i = \pm 1. \tag{2.40}$$

Here S_i corresponds to the spin of lattice site i (pointing either up or down), J is the exchange energy ($J > 0$ for ferromagnetic and $J < 0$ for antiferromagnetic systems, respectively), H denotes an external magnetic field, and the summation is to be taken once over all nearest-neighbor pairs and N lattice sites, respectively.

By the transformation $C_i = (1 - S_i)/2$ this system is isomorph to a lattice gas model [85, 80] (binary alloy), where each site is either occupied or empty (either occupied by an A or B atom). Thus, the average magnetization per lattice site given by $\langle M \rangle = N^{-1} \sum_i S_i$ is now equivalent to the concentration $c = N^{-1} \sum_i C_i$. Furthermore, the chemical potential μ, measured from its temperature-dependent critical value μ_c, replaces the magnetic field as driving force of phase transitions. The correspondence between ISING ferromagnet and lattice gas can be summarized as

$$\langle M \rangle \longleftrightarrow (1 - 2c), \quad \text{and} \quad 2H \longleftrightarrow (\mu - \mu_c). \tag{2.41}$$

In magnetic systems, the number of, say, up-spins is not fixed, thus the state of the systems is described by the non-conserved order parameter magnetization M. Accordingly, in MC studies the evolution of such systems is modeled by single spin-flip attempts (known as kinetic GLAUBER model [86]; usually referred to as model A). In lattice gas models, the density of particles is usually fixed and described by the conserved order parameter c. Therefore, a MC simulation consists of moving a particle to an empty neighboring site, which is equivalent to the spin-exchange formalism of KAWASAKI [87] (usually referred to as model B).

[6] This coupling is justified, if at any time instant only one event takes place, and all events are POISSON processes [83].

Monte-Carlo studies of phase transformations

Parallel to the increase of available computing power, MC studies of phase transition phenomena were first performed to check analytical models, only to take later on the lead in certain areas of statistical physics, where now analytical theories are to be checked with respect to simulation results. Due to the simplicity of the ISING model it has frequently been used to describe effective interactions in many-body systems. For instance, phase diagrams of alloys have been simulated [88], and meanwhile MC calculations of critical temperatures T_c (see Fig. 2.3) of ISING models [89] can be considered to be more accurate than analytical approximations [90].

Concentrating in this work on systems with conserved order parameter, the first comprehensive MC studies on phase transitions of binary alloys in three dimensions were performed in the seventies [91, 92]. Dealing with concentrations of the minority phase[7] up to $c = 0.5$, these simulations were primarily intended to study concepts of spinodal decomposition. One important result has been the observation of dynamical scaling of the structure function $S(\vec{k}, t)$ [93]-[95], which can be expressed as [62, 96, 97]

$$S(k,t) \propto [k_m(t)]^{-d} F(k/k_m(t)) \tag{2.42}$$

in d dimensions. Here, $k_m(t)$ is the position of the maximum of S and the scaling function $F(x)$ becomes asymptotically independent of time. Note, that studies of the evolution of $S(\vec{k}, t)$ are not restricted with respect to the volume fraction ϕ of the minority phase, whereas a characterization in terms of the size distribution function $f(s,t)$ becomes meaningless as the percolation threshold c_p is approached ($c_p \approx 0.31$ for the sc lattice).

The BECKER-DÖRING theory of nucleation [59] has been the focus of simulation studies [98, 99] for systems of low concentrations quenched into the metastable part of the phase diagram close to the coexistence curve. Additionally, simulations of growth and coarsening of NCs have been performed [100]. However, in three dimensions these simulations barely exceeded a few 10^4 jump attempts per IA, thus doubt arises, if the late stage of phase separation has been approached.

2.5.2 Mesoscopic and continuum descriptions

Besides the direct atomic approach there exist several field-theoretic descriptions of phase separation (for reviews, see GUNTON *et al.* [61] and LANGER [56]). The CAHN-HILLIARD-COOK [55, 101] formulation is widely used to study phase transitions, especially those proceeding via spinodal decomposition. The evolution of the system is expressed in terms of a conserved concentration field $\psi(\vec{r}, t)$ and a time-dependent (coarse-grained) free energy functional $F[\psi(\vec{r}, t)]$

$$\frac{\partial \psi(\vec{r}, t)}{\partial t} = M \vec{\nabla}^2 \frac{\delta F}{\delta \psi} + \eta(\vec{r}, t). \tag{2.43}$$

[7] Note, that the ISING Hamiltonian Eq. (2.40) shows particle-hole symmetry.

Here, M denotes the mobility of monomer components and η is a thermal noise term taking into account thermal fluctuations (LANGEVIN approach [56]). The free energy functional is usually assumed to have the GINSBURG-LANDAU form $F = \int \mathrm{d}^3 r(K|\vec{\nabla}\psi| - a\psi^2 + b\psi^4)$. Combining both equations leads to a nonlinear partial differential equation, for which analytical approximations successfully describe early stages of phase separation. The late stages of the evolution can be studied by numerical integration of the governing equation [102] and has been applied to spinodal composition in binary mixtures [103]. This method does not pose any restriction on the volume fraction ϕ of the domains of the second phase. More advanced field-theoretic approaches try to solve the equation of motion [Eq. (2.33)] of the structure factor S via analytical approximations and/or numerical integrations [56, 57].

Another widely used approach describing the decay of a metastable state after the nucleation stage is based on thermodynamic considerations. In the multiply connected space between the second-phase domains a solution for the monomer concentration field c subject to suitable BCs is sought. The classical theory of the late stage of phase separation has been formulated in a global mean-field manner for vanishing ϕ by LIFSHITZ and SLYOZOV [104] and WAGNER [105] (LSW theory). They succeeded to derive a stationary particle radius distribution $f(s,t) = f(s)$ and a power growth law for the characteristic system size, i.e. $s \propto t^m$ (see Chapter 4).

In general, in a more realistic local mean-field approach for finite ϕ, the evolution of second-phase domains is given by the multi-droplet diffusion equation

$$\frac{\partial c(\vec{r},t)}{\partial t} = D\vec{\nabla}^2 c(\vec{r},t) + \sum_i Q_i \delta(\vec{r} - \vec{r}_i) + G(\vec{r},t). \tag{2.44}$$

Here, for a system with monomer diffusion coefficient D the effect of an external source term G as well as modifications due to the clusters are considered, which are assumed to be point-like objects characterized by a source strength Q. Recent approaches additionally allow to include nucleation [106, 35, 36].

Other descriptions of the evolution of second phase precipitates are based on a numerical integration of the basic kinetic equations [107]-[109]. Starting with the balance equation for the cluster distribution function [Eq. (2.11)] and determining the kinetic coefficients $k_\pm$ for monomer condensation and evaporation in the limits of diffusion or interface reaction control, the evolution of NCs can be followed from the early nucleation to the late-stage coarsening regime. This method [110] allows also to show the connection between the kinetic approach of BECKER and DÖRING [59] the thermodynamic approach of LIFSHITZ and SLYOZOV [104] and WAGNER [105].

Furthermore, systems of coarsening second-phase precipitates have been described in statistical approaches by appropriate multi-particle distribution functions [111, 112]. Here, the evolution of individual domains is determined self-consistently by averaging the multi-particle distribution functions over the positions and sizes of the precipitates. The resulting description in terms of a hierarchy of equations of many-particle distribution functions is usually truncated at the lowest level. A mean-field approach based on a single-particle distribution function can be used to model self-organization in finite systems [113].

Chapter 3

Kinetic 3D lattice Monte-Carlo method

This Chapter introduces the main simulation tool used in this work in order to study the evolution of nanostructures. Besides presenting some principles and technical details of the MC method, the focus will be on the characteristics of the model with respect to thermally activated processes, i.e. the solubility properties and the validity of the GT relation [Eq. (2.23)]. The incorporation of ballistic effects typical for ion irradiation will only be briefly sketched; a more detailed description of collisional mixing effects will be given in Section 5.3.1.

3.1 Basic description

The IBS of nanostructures involves stages like the nucleation of precipitates out of a time- and space-dependent supersaturated solid solution of IAs which can hardly be modeled with statistical equilibrium concepts. A more appropriate method is an atomic description and, therefore, a kinetic 3D lattice Monte-Carlo (K3DLMC) method in the tradition of lattice gas models has been developed [114], which allows to study the evolution of the implanted IAs. In this model the positions of the impurities are defined on a 3D periodic lattice and for their kinetics effective nearest-neighbor interactions between impurities are taken into account. This simplified effective-particle approach assumes, that the impurity atoms are embedded in a position-independent potential of the substrate, which includes all the complex interactions between impurity and matrix atoms.

For a particular simulation the crystallographic structure of the nanocrystals under investigation determines the type of lattice within the K3DLMC method. For this purpose three lattice types have been implemented in the computer code: (i) the simple cubic (sc), (ii) the body-centered cubic (bcc), and (iii) the face-centered cubic (fcc) lattices. However, for most of the results presented in this work a fcc lattice description has been used for several reasons:

- a variety of metals can be found in this crystal structure, e.g. Au or Ag precipitates

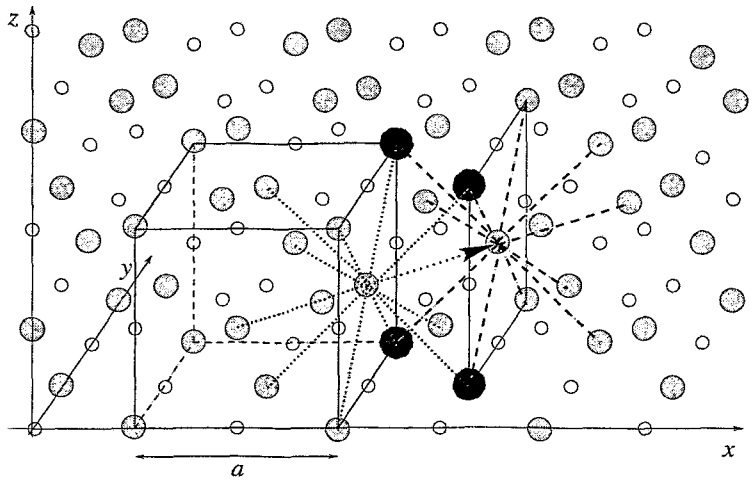

Figure 3.1: Construction of the main fcc lattice (grey circles) out of the underlying sc lattice. The remaining non-occupied sc sites (small circles) build up an additional fcc lattice. The configuration for an arbitrary jump in [110] direction is indicated together with the four nearest-neighbor positions (black circles) common to the initial and final site of the jump.

formed by IBS in SiO_2;

- the Co subsystem in $CoSi_2$ forms a fcc lattice [11];
- the fcc structure is one of the most isotropic lattices and thus suited to describe precipitation in amorphous matrices;
- since Si is composed of two fcc sublattices, the simple fcc description is compatible with directional precipitation effects in this technologically most relevant material.

These advantages outweigh the technically (numerically) more expensive treatment compared to simpler lattices like the sc or bcc structures. Since some metals show a bcc geometry of their unit cell, this lattice type is appropriate for corresponding material systems, whereas no elemental NCs crystallize in the sc lattice.

The crystallographic structure of a compound of stoichiometry X_iY_j for a system of impurities of types X and Y determines the choice of the appropriate lattice for K3DLMC studies. By IBS mostly compound NCs of equal stoichiometry, i.e. of XY composition, have been studied. In this case a fcc lattice is not suited due to its intrinsic phase diagram, which includes X_3Y, XY, and XY_3 phases, respectively [115]. This becomes clear, because any two nearest-neighbor sites have four other nearest-neighbor sites in common (see Fig. 3.1). For a nearest-neighbor pair XY this implies, that it is energetically more favorable for atom X (Y) to have these four sites occupied by Y (X) atoms. The corresponding degeneracy of the ground state gives rise to a frustrated system. Therefore, this geometry

does not lead automatically to a periodic arrangement of both components, if their fluctuating local concentrations determine the nanocrystal formation and composition. For the study of the IBS of compound NCs (see Chapter 7.2) corresponding K3DLMC simulations are thus performed using either the sc or bcc lattices, which correspond to the NaCl or CsCl structures, respectively.

In this K3DLMC method effective atomic interactions among IAs are incorporated on the basis of a probabilistic stochastic Cellular Automaton (CA) approach [116, 117]. Although the description in terms of a CA supports the consideration of configuration-dependent interactions among IAs, the results presented in this work are based on the ISING model [84, 118, 90] as the most simple implementation of a CA. In the ISING model, the potential energy of an IA is just proportional to the number $n \leq \xi_l$ of nearest-neighbor bonds, where ξ_l denotes the coordination number, i.e. maximum number of nearest-neighbor bonds. Depending on the lattice type l, the coordination numbers are $\xi_l = 6, 8$ and 12 for the sc, bcc, and fcc lattices, respectively.

As the fcc lattice has been most widely used for simulations the corresponding geometry of a jump configuration is shown in Fig. 3.1 in order to discuss the method. In the course of the simulation for every jump attempt an IA is chosen stochastically and one out of its ξ_l (here $\xi_{\text{fcc}} = 12$) jump directions is determined randomly (if the corresponding lattice site is occupied a new IA is chosen). Next, for both the initial $\vec{r}_i$ and final $\vec{r}_f$ sites the number of occupied nearest-neighbor sites is counted. Based on this local configuration the jump probability is determined,[1] and, accordingly, the jump will be either performed or rejected.

Since each lattice site is completely defined by its occupation state, only a single bit is needed to represent each position. Thus the K3DLMC method can be implemented very efficiently on the basis of bit manipulations [114, 119] in order to perform jump attempts of IAs, the core procedure of the code. Furthermore, using a double book-keeping strategy in bit and coordinate space to keep track of the positions of the impurities (for details see Appendix A), this code (not parallelized) allows the simulation of reasonably sized systems on current top-level workstations. In particular, depending on the emphasis of the simulation – either large simulation volumina for dilute systems or dense nanostructure distributions – lattice sites of the order of 10^9 and/or up to several 10^5 IAs can be modeled for 10^5–10^7 Monte-Carlo steps (MCSs) on a CPU time scale of several days.

Technically, the basic fcc lattice is constructed from an underlying simple cubic one (see Fig. 3.1). This approach has the advantage of having an additional fcc lattice shifted by $(\frac{1}{2}a, 0, 0)$ with respect to the first one. Due to the fact, that a bit representation gives only information about the occupation state but not about the type of occupying species, simulation involving different types of atoms need a further criterion for distinguishing atom types. Thus the second fcc lattice can be used to model special problems of IBS, e.g. the effect of an in-diffusing reactive component of the annealing atmosphere on the redistribution of the implanted impurities (see Chapter 7.1). Since the diamond lattice is also composed of two fcc lattices shifted by $(\frac{1}{4}a, \frac{1}{4}a, \frac{1}{4}a)$, the division of a sc lattice into

[1] For all possible local configurations of IAs the jump probabilities are computed once (at the beginning of the simulation and after each temperature change) and then tabulated.

two independent sublattices used in this approach would provide an effective way for the implementation of the diamond lattice. The loss of coincidence of geometrical relation and internal representation by this conformal mapping is of no relevance, because in the K3DLMC method the lattice type is cast into the properly constructed jump configuration.

The chosen geometric implementation of the lattice is especially suited to study systems with (100) boundaries. However, by topological distortions also (110) boundaries can be mapped directly into the cubic simulation cell of this approach [120].

3.2 Energetics and jump probabilities

If $J_l > 0$ denotes the energy (bond strength) of a nearest-neighbor bond with respect to lattice type l, then the total potential energy of the impurities within the ISING model is given by the Hamiltonian

$$\mathcal{H} = -J_l \sum_{\langle ij \rangle_{\mathrm{nn}}} C_i C_j. \tag{3.1}$$

Here, C_i denotes the occupation state of site i ($C_i = 1$ for an occupied and $C_i = 0$ for an empty lattice site, respectively) and the sum is to be taken once over all nearest-neighbor pairs. Obviously, by establishing a nearest-neighbor bond the energy gain of the system is J_l. Since any bond is shared by two atoms the potential energy of one IA is $E = \frac{1}{2} n J_l$, where n is the number of occupied nearest-neighbor sites. Thus the binding energy of a bulk IA (sublimation energy) is

$$E_{\mathrm{b}} = \frac{1}{2} \xi_l J_l. \tag{3.2}$$

In the schematic drawing of Fig. 3.2a the energetics of an IA in the averaged potential within the ISING model is shown. The activation energy E_{A} denotes the diffusion barrier governing a single nearest-neighbor jump of an IA. In this model both the matrix diffusion of a free monomer and the surface diffusion of an adatom on a precipitate surface are subjected to the same activation energy E_{A}. The cluster properties are defined by the bond strength J_l between two nearest-neighbor IAs. If necessary an additional energy barrier E_{R} at the precipitate-matrix interface (which is beyond the ISING model, but within the CA approach) can easily be incorporated for a more accurate treatment of monomer attachment and/or detachment rates, i.e. the interface reaction kinetics.

Thus the transition probability W_{if} for one atom to jump from the initial site i to an empty final site f [see also Eq. (2.39)] is given by

$$W_{if} = \begin{cases} \tau_0^{-1} \exp\{-E_{\mathrm{A}}\beta\} & , \quad n_f \geq n_i \\ \tau_0^{-1} \exp\{-[E_{\mathrm{A}} + (n_i - n_f) J_l]\,\beta\} & , \quad n_f < n_i, \end{cases} \tag{3.3}$$

where $\Gamma_0 = \tau_0^{-1}$ denotes the frequency of jump attempts, and $n_{(i,f)}$ represents the number of nearest-neighbor bonds at the two sites.

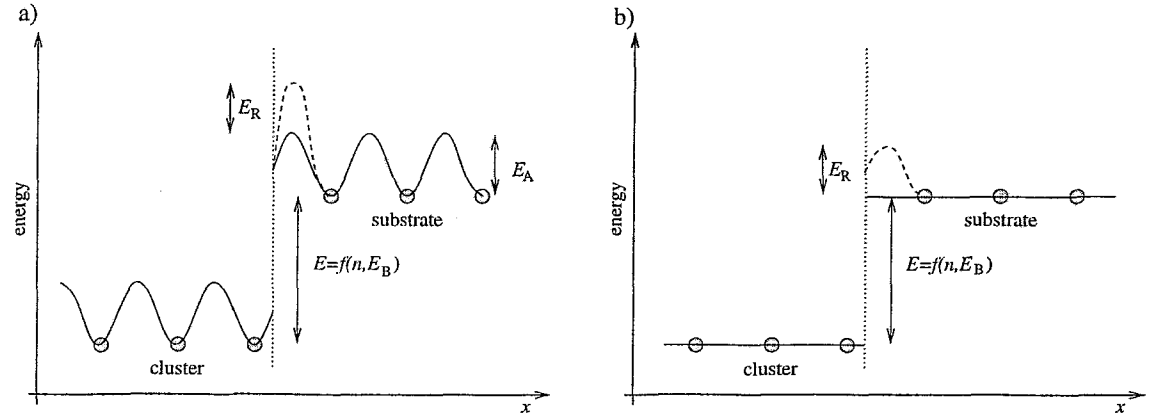

Figure 3.2: Energetics of the simulation model. In a) the physical model is schematically shown, where the activation energy E_A governs diffusion and the energy gain E for monomer attachment is a function of the nearest-neighbor bond strength E_B. Additionally, an interface energy barrier E_R is shown. In b) the renormalized model $E_A \to 0$ is shown.

In order to reduce simulation time it is convenient to allow every diffusion attempt, i.e. $\tilde{W}_{if} = W_{if}/(\tau_0^{-1} \exp\{-E_A\beta\})$, which renormalizes just the time scale of the model (see Fig. 3.2b). Defining $\epsilon_l = J_l\beta$ this leads to the dimensionless transition probability

$$\tilde{W}_{if} = \begin{cases} 1 & , \quad n_f \geq n_i \\ \exp\{-(n_i - n_f)\epsilon_l\} & , \quad n_f < n_i, \end{cases} \tag{3.4}$$

and the quantity $\tau = \tau_0 \exp\{E_A\beta\}$ gives a measure for the time scale during a single MCS (see Section 3.5.2). In cases where $n_i > n_f$, (i.e. transitions, which are energetically not favored), the jumps are nevertheless allowed if a random number chosen from the interval $[0, 1]$ is less than $\tilde{W}_{if}$.

In this work a MCS is defined by a sequence of N jump attempts of statistically independently chosen IAs out of the full set of N IAs. If for a single jump attempt the randomly determined nearest-neighbor site $\vec{r}_f$ is already occupied, another randomly chosen IA is checked for a possible jump.

For all the simulation results presented in this work the METROPOLIS algorithm [81] guaranteeing local relaxation dynamics has been used. Neither GLAUBER dynamics [86] nor cluster updating methods have been applied. Within the ISING model the extension to two different interacting types of IAs is straightforward and will be dealt with in Section 7.2.1.

3.3 Intrinsic properties of the model

According to the phase diagram (see Fig. 2.3) above a critical temperature T_c no phase transition from the disordered to the ordered state is expected. For the nearest-neighbor

ISING model used in the K3DLMC simulations, the critical point depends on the lattice type. Table 3.1 summarizes the critical properties, which have been obtained either by high-temperature expansions in the case of the bcc and fcc lattices [121] or by extensive MC simulations in the case of the sc lattice [89] (see e.g. KOBE [90] for a survey of critical temperatures and exponents), respectively, since analytic solutions in three dimensions are not known.

Based on high-temperature series expansions, the spontaneous magnetization ($H \to 0$) near below the critical point is known quite accurately [122]

$$\langle M \rangle = K_l(1 - T/T_c)^{\kappa}, \quad \kappa \cong 5/16. \tag{3.5}$$

The amplitudes K_l depend on the lattice type ($K_{fcc} \approx 1.49$, $K_{bcc} \approx 1.51$, $K_{sc} \approx 1.57$ [123]), whereas the exponent κ is believed to be universal in three dimensions. Since the critical chemical potential μ_c corresponds to the spontaneous magnetization (see Section 2.5.1), with the help of Eqs. (2.41) and (3.5) the phase diagram of the lattice gas close to T_c can be determined (see Section 3.5.3).

From Eq. (3.3) follows that the K3DLMC model exhibits some general intrinsic properties, which depend only on the value of the dimensionless simulation parameter ϵ_l and the value of the activation energy for diffusion E_A, if the number N of IAs is kept constant. In particular, in the renormalized model, NC systems with differing binding energies will evolve similar provided that besides $J_l^{(2)} = \alpha J_l^{(1)}$ also the relation $T^{(2)} = \alpha T^{(1)}$ holds. The physical time scales, of course, will be usually different.

For temperatures considerably below T_c the shape of a (quasi-equilibrated) NC depends on the choice of the simulation lattice. In the case of a sc lattice, the surface of a reasonably large NC consists mainly of (100) surfaces (Fig. 3.3a), whereas for a bcc nanocrystal the (110) surfaces are energetically favored (Fig. 3.3b). In the case of a fcc lattice the corresponding NCs tend to have a faceted octahedral-like shape with dominating (111) surfaces (see Fig. 3.3c). With increasing temperature the pronounced faceting starts to be smeared out [124] and the interface morphology gradually changes from a sharp to a diffuse phase boundary.

The characteristic NC shapes can be understood in terms of the surface energies of the principal crystal surfaces. Within the nearest-neighbor ISING model, the internal energy part of the surface tension $\sigma_I(hkl)$ is proportional to the number of bonds $n(hkl)$ which

Table 3.1: Critical points of the three-dimensional ISING model expressed per nearest-neighbor bond [$\beta_c = (k_B T_c)^{-1}$].

l	sc	bcc	fcc
$J_l\beta_c$	0.2217	0.1574	0.1021

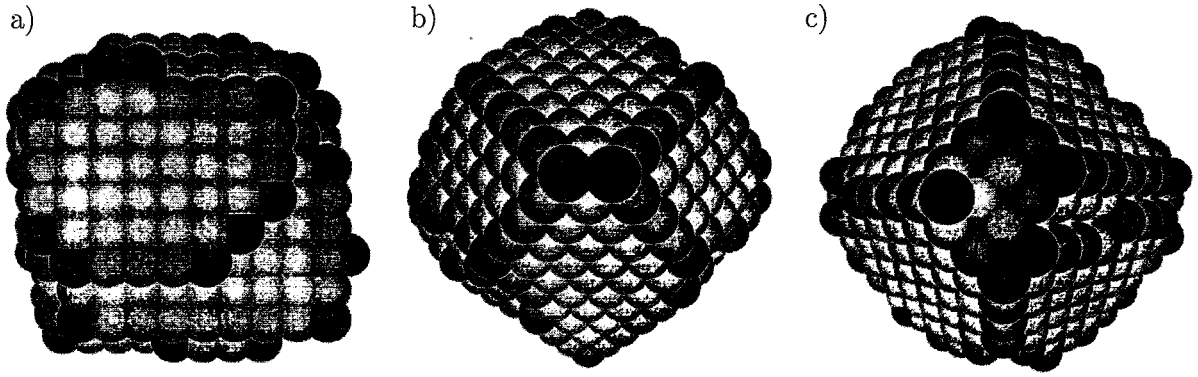

Figure 3.3: Quasi-equilibrated shape of a NC at $T \approx 0.05\,T_c$ consisting of roughly 1000 atoms condensed into the (a) sc, (b) bcc, and (c) fcc structures (the darker the blue (grey) scale, the higher the energy state). In each case, the line-ofsight is the [100] direction.

have to be broken in order to bring a bulk atom to the (hkl) surface layer. Thus

$$\sigma_{\rm I}(hkl) = \frac{J_l n(hkl)}{2S(hkl)}, \tag{3.6}$$

where S denotes the surface area per atom, and the factor $1/2$ accounts for the fact, that per nearest-neighbor bond only the energy $J_l/2$ is associated with each atom (by cutting through a crystal, two new surfaces are created).

Table 3.2 lists the surface energies for the three principal surfaces of each of the three lattices. For instance, since for a fcc structure the (111) planes are energetically most favored, the surface of a single NC consists to a large fraction of the eight geometrically different (111) planes. Resulting sharp edges are usually smoothed to (100) planes. This specific shape is predicted by constructing a fcc nanocrystal according to the WULFF plot

Table 3.2: Characterization of the low-indexed surfaces of the sc, bcc and fcc lattices in terms of the number of broken bonds n per surface area S of an atom belonging to a (hkl) surface [125, 126].

l	sc			bcc			fcc		
hkl	$n(hkl)$	$S(hkl)$	$\frac{\sigma_{\rm I}(hkl)}{\sigma_{\rm I}(100)}$	$n(hkl)$	$S(hkl)$	$\frac{\sigma_{\rm I}(hkl)}{\sigma_{\rm I}(110)}$	$n(hkl)$	$S(hkl)$	$\frac{\sigma_{\rm I}(hkl)}{\sigma_{\rm I}(111)}$
100	1	a^2	1	4	a^2	$\sqrt{2}$	4	$1/2\,a^2$	$2/\sqrt{3}$
110	2	$\sqrt{2}\,a^2$	$\sqrt{2}$	2	$\sqrt{2}a^2$	1	6	$\sqrt{2}/2\,a^2$	$\sqrt{6}/2$
111	3	$\sqrt{3}\,a^2$	$\sqrt{3}$	6	$\sqrt{3}a^2$	$\sqrt{6}$	3	$\sqrt{3}/4\,a^2$	1

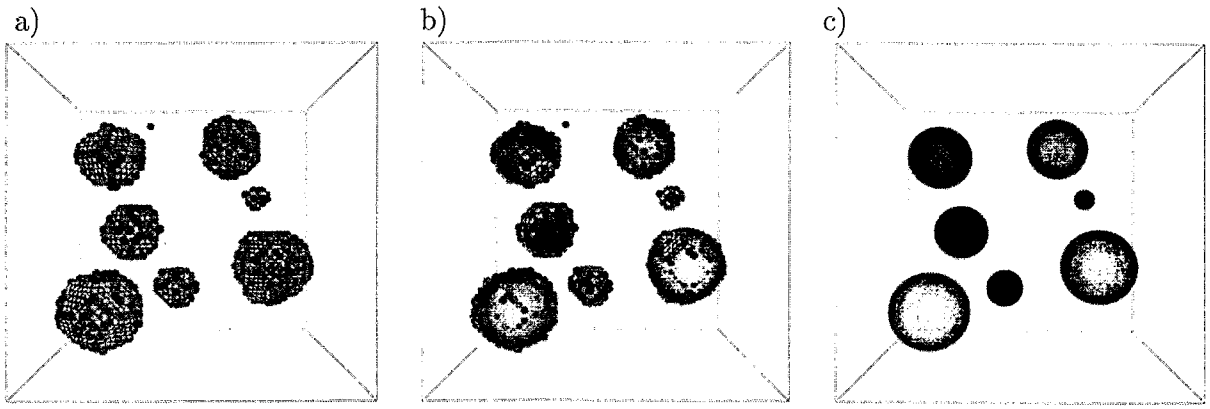

Figure 3.4: Scheme of the transition from atomic-scale to spherical cluster representation. In a) an ensemble of fcc NCs is shown. In b) each NC is superimposed by a sphere, whose radius is given by Eq. (3.7). In c) only the spheres representing the NCs are drawn.

(see e.g. [127]). Recently, HUANG *et al.* explicitly compared the shape of fcc NCs obtained by a similar lattice MC method with the corresponding WULFF construction and found very good agreement [128].

3.4 Analysis of simulation data

For the extraction of simulation data (mainly the size and space distribution of the NCs) after a certain number of MCSs the whole simulation volume is scanned for the lattice positions of the IAs. For instance, if a l-lattice site is occupied a recursive procedure checks all ξ_l nearest-neighbor positions for further IAs. After the scan the numbers of monomers, dimers, trimers, ..., or any agglomeration of interconnected IAs are known.

In this work the size of a cluster is given by the number i of atoms it consists of. This standard ISING droplet model is justified at low temperatures and concentrations close to the coexistence curve, but fails close to T_c (diverging correlations) or beyond the percolation threshold. Furthermore, the position of each NC is calculated, which is defined as the center of mass of its IAs (with appropriate translations at periodic boundaries of the simulation box). Since the system is completely defined by the coordinates of the IAs, more advanced data analysis, e.g. pattern recognition, can be done.

Since TEM micrographs are the main method for the analysis of NC distributions formed by IBS, a characterization in terms of the number of IAs is not adequate. Hence, in this model the size of one (equilibrated) NC is approximated by the radius of the smallest possible sphere which allows to accommodate the number of its atoms on regular lattice sites (see Fig. 3.4). This relation is given by

$$\frac{4\pi}{3}R^3 = iV_a = i\frac{a_l^3}{p_l}, \quad i \gg 1, \tag{3.7}$$

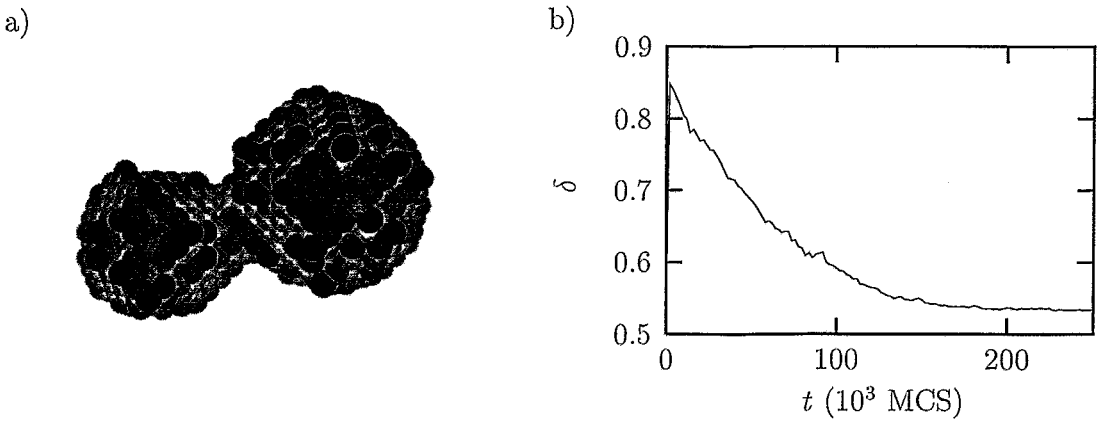

Figure 3.5: K3DLMC simulation of coalescence of two NCs consisting of $N_1 \approx 460$ and $N_2 \approx 1050$ IAs at $\epsilon_{\text{fcc}} = 2$. Snapshot a) shows both NCs shortly after merging. In b) the evolution of δ as defined in Eq. (3.8) is plotted.

where p_l denotes the number of atoms per unit cell ($p_{\text{sc}} = 1$, $p_{\text{bcc}} = 2$, and $p_{\text{fcc}} = 4$, respectively). However, the problem arises to define a lower limit i_1 of NC size, because a monomer can hardly be considered as a NC. Unless otherwise stated, in this work the (arbitrary) choice $i_1 = 6$ has been used.

It should be noted that this procedure of a spherical cluster approximation does a very poor job in the case of two coalescing precipitates. In this case the analysis of the radial inhomogeneity of a NC helps to some extent to reveal its shape. For this purpose the normalized mean square distance δ from the center of mass of the NC has been introduced, which is defined as (analogous to the moment of inertia)

$$\delta = \frac{1}{MR^2} \int_{V_{\text{NC}}} r^2 \mathrm{d}m. \tag{3.8}$$

Here R denotes the radius of the NC [as determined by Eq. (3.7)], M its mass, and the integration is to be carried out over the whole volume V_{NC} of the NC.[2] The evolution of δ for two coalescing NCs can be seen in Fig. 3.5. For comparison it should be noted that for an equilibrated octahedral-like NC $\delta_{\text{NC}} \approx 0.54$, which is only approximately 10 % off the value of a homogeneous sphere ($\delta_{\text{sphere}} = 0.6$). Recording δ for each NC during the K3DLMC simulation provides a means to check, for instance, the ion fluence threshold of NC coalescence during ion implantation, or the relative contribution of coagulation to NC coarsening (see Section 6.1), because in the case of two touching precipitates δ considerably exceeds the value of a homogeneous sphere.

[2]In this discrete lattice model for the evaluation of δ the integral is replaced by the sum over all interconnected IAs.

3.5 Gauging of simulation parameters

The K3DLMC method allows to give predictions of the nucleation and growth behavior of NCs of specific ion-solid systems if the parameters of the simulation are chosen according to the applied implantation parameters and the material properties of the NC/substrate system. The free simulation parameters of the model, i.e. the lattice constant a_l, the activation energy for diffusion E_A and the energy J_l of a nearest-neighbor bond between IAs, can be deduced from the implantation parameters and the material constants.

3.5.1 Length scale

The basic length scale of this K3DLMC model is the lattice constant a_l of the lattice, on which the IAs diffuse and may condense to precipitates or form other kinds of nanostructures. For corresponding K3DLMC simulations the value of a_l is accessible by X-ray diffraction measurements at samples containing reasonably large NCs or simply by taking tabulated bulk values.

The sizes of the simulation box are hence expressed in terms of the lattice constant a_l, i.e. $L_i = 2^{n_i} a_l$, $i = x, y, z$. The discretization of the box volume in powers of 2 has advantages concerning the implementation of periodic BCs. Since each lattice point is stored as a bit, the determination of the coordinates of the final site of a nearest-neighbor jump can be performed merely by bit manipulations, even if the jump of an IA takes place across the boundaries of the simulation volume.

Besides the implantation temperature, the main parameters of IBS of nanostructures are the projected range R_p of the impurity profile (related to the ion energy E) and the ion flux j and ion fluence F. Since all three quantities are related to a length scale they are derived in the K3DLMC model with respect to the lattice constant a_l of the specific NCs under investigation.

3.5.2 Diffusion coefficient, time scale, and ion flux

Time dependent quantities like the diffusion coefficient D_sim or the ion flux j are transformed to corresponding K3DLMC quantities via the intrinsic lattice diffusion coefficient.

Diffusion coefficient

The diffusion coefficient D_sim of the K3DLMC method as well as the time scale τ of a MCS [see Eq. (3.3)] are coupled to the experimentally measured diffusion coefficient $D_\mathrm{exp} = D_0 \exp\{-E_\mathrm{A}^\mathrm{exp}\beta\}$, where $E_\mathrm{A}^\mathrm{exp}$ denotes the activation energy for diffusion. Both D_sim and τ are derived within the framework of the random walk theory of diffusion (see, e.g. [129]), which assumes independence of successive diffusion steps. The diffusion coefficient for particles on a lattice, which are only allowed to migrate to nearest-neighbor positions,

is given by [129]

$$D_{\text{latt}} = \frac{1}{\xi_l}\Gamma a_l^2, \tag{3.9}$$

where $\Gamma = \tau^{-1}$ is the effective jump frequency, a_l is the lattice constant, and $\xi_l = \{6, 8, 12\}$ denotes the corresponding coordination number of the three lattices used for the simulations. Note, that the jump frequency is the product of the frequency of jump attempts Γ_0 times a temperature-dependent probability, i.e. $\Gamma = \Gamma_0 \exp\{-E_A\beta\}$.

Since it is convenient in kinetic MC simulations to normalize the event with the highest probability to unity, which in the current model corresponds to allow every diffusion attempt, the normalized K3DLMC diffusion coefficient is given by

$$D_{\text{sim}} = \frac{D_{\text{latt}}}{\Gamma} = \frac{a_l^2}{\xi_l}. \tag{3.10}$$

By the last equation a jump frequency of one is implied, i.e. $\Gamma \equiv 1/(\text{jump attempt})$, and accordingly D_{sim} is expressed in units of a_l^2 per MCS. With the help of the EINSTEIN relation [129] the diffusion lengths are related by

$$\sqrt{2D_{\text{exp}}t} = x = \sqrt{2D_{\text{latt}}\tau k} = \sqrt{2D_{\text{sim}}k}, \tag{3.11}$$

where k denotes the number of MCSs. Eq. (3.11) is valid in the asymptotic limit, i.e. for very large numbers of MCSs.

Time scale

With the help of Eq. (3.11) the time constant τ, or, equivalently, the jump frequency Γ, can be obtained

$$\tau = \frac{\frac{1}{\xi_l}a_l^2}{D_0 \exp\{-E_A^{\text{exp}}\beta\}}. \tag{3.12}$$

Thus, due to the temperature-dependent diffusion coefficient, one MCS can correspond to time intervals, which may differ by orders of magnitude. The total number of MCSs times the duration of a single MCS determines the physical time scale which can be modeled by the K3DLMC method, i.e. $t = \tau k$.

It should be noted that the common choice [37] for the (normalized) transition probability $\tilde{W} = [1+\tanh(\Delta\mathcal{H}\beta/2)]/2$ rescales the diffusion coefficient, and hence the time scale, by a factor two, because now not every diffusion step is performed $[\tilde{W}(\Delta H = 0) = 1/2]$.

Ion flux

The ion flux j is defined as the number of ions crossing an unit area element per second. In MC terms this corresponds to the number of ions crossing the area a_l^2 of an unit cell per MCS τ. Since the duration of a MCS is temperature-dependent [Eq. (3.12)] the corresponding dimensionless K3DLMC current is given by

$$j_{\text{MC}} = j a_l^2 \tau = j\frac{a_l^4}{\xi_l D_{\text{exp}}}. \tag{3.13}$$

3.5.3 Nearest-neighbor bond strength, solubility, capillary length, and surface tension

Within the framework of the lattice gas model the value of the nearest-neighbor bond strength J_l can be gauged by the solubility of the IAs in the substrate and/or by the surface tension. If the solubility (solidus) is known, the bond strength J_l can be derived via the intrinsic dissolution properties at a flat interface of the bulk phase, whereas the GT relation [Eq. (2.23)] is used to connect J_l to the surface tension. In the following it is assumed that the solubility can be described by an ARRHENIUS law $c_\infty = c_\infty^0 \exp\{-E_S\beta\}$, where E_S is the activation energy for the dissolution of one monomer.

Flat interface solubility

The underlying idea is to determine the concentration c of dissolved IAs which are in equilibrium with a flat interface of the bulk phase of this material. If c is known for different values of ϵ_l, an ARRHENIUS plot allows to relate the parameters c_∞^0 and E_S to simulation parameters.

The initial setup for this simulation approach consists of a layer of atoms, which acts as the condensed phase [130]. If the layer extends from z_1 to z_2, its "bulk" behavior is achieved by keeping the atoms at $z = z_2$ fixed at their positions (see Fig. 3.6a). Additionally, simulations have been performed for the sc and bcc lattices, where in the initial configuration a quarter of a monolayer was randomly deposited on top ($z = z_1 - 1$) of the bulk layer. Applying periodic BCs in the x and y directions and preventing diffusion through the boundary at $z = 0$, the minimization of the corresponding thermodynamic potential drives the evolution of the system. This particular setup represents a canonical ensemble (fixed simulation volume, number of atoms and temperature), thus the free energy $F = U - TS$ will be minimized. However, the evolution of both subsystems ("gas" of dissolved monomers and bulk) is determined by achieving the same chemical potential, thus the concentration of monomers is related to the phase equilibrium.

For the three lattice types in a series of simulations for different values of ϵ_l the averaged number of dissolved IAs[3] is determined after the configuration has reached equilibrium. For this purpose, the evolution of the system was followed for 4×10^6 MCSs. This period was divided into 500 equi-distant time intervals, where at the end of each of the last 400 intervals the number of dissolved IAs was determined. The corresponding averaged concentrations normalized with respect to the available volume within the unit cell of the sc, bcc, and fcc lattices are given in Fig. 3.6b-d, respectively.

The relation between concentration and scaled temperature has been established with the help of the ARRHENIUS form

$$c_\infty^{(l)}(\epsilon_l) = A_l \exp\{-B_l \epsilon_l\}. \tag{3.14}$$

The fitted values of the pairs of constants A_l and B_l are listed in Table 3.3. For each

[3] In this context, all IAs are counted, which are not connected to the bulk layer. This includes very tiny clusters like dimers, trimers, ...

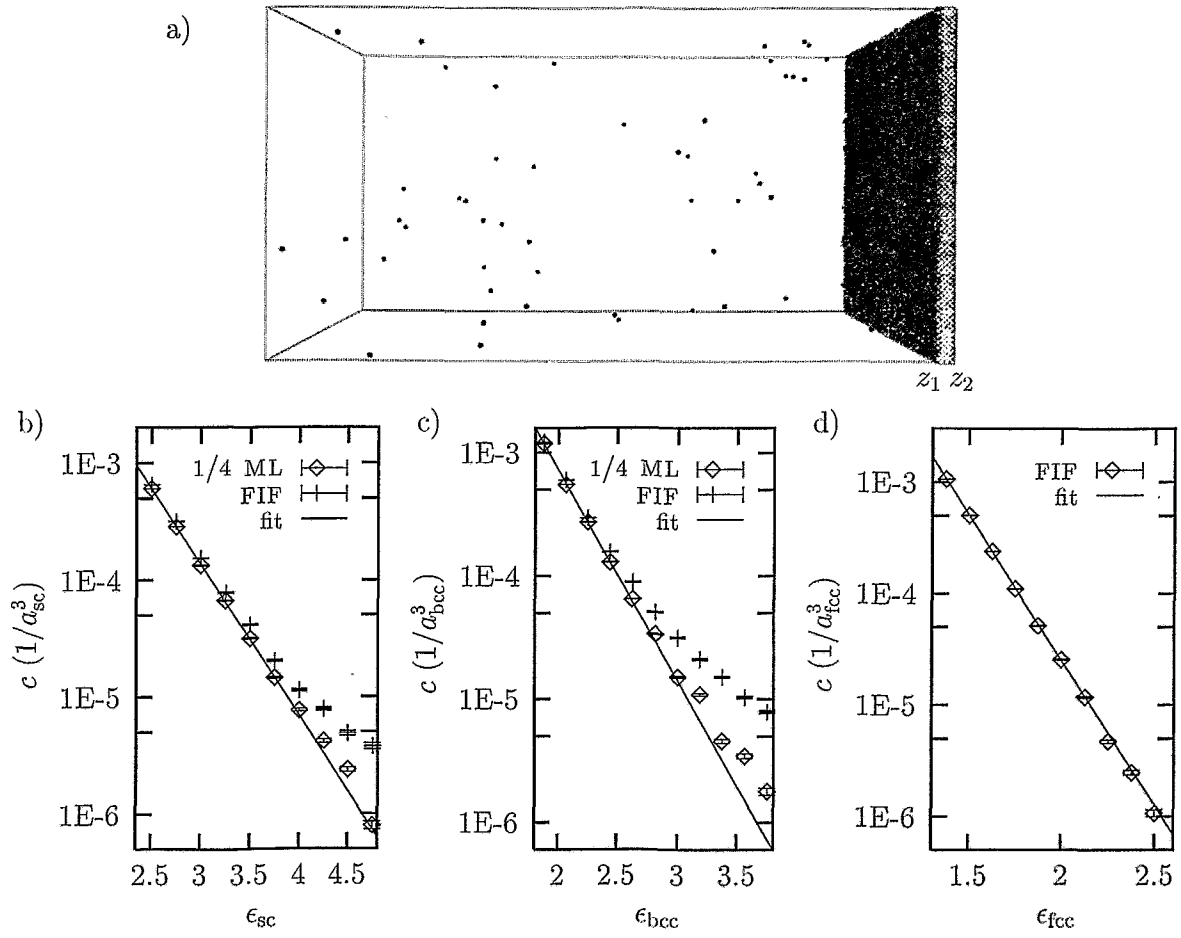

Figure 3.6: Intrinsic solubility properties of the K3DLMC model for the three lattice types. The snapshot of a) obtained after 2×10^6 MCSs for $\epsilon_{fcc} = 1.75$ indicates the simulation setup in (100) geometry. The ARRHENIUS plots in b)-d) show the temperature dependence of the solubility of monomers for the sc, bcc and fcc lattices, respectively (labels 'FIF' and '1/4 ML' refer to initial conditions of the interface either perfectly flat or decorated randomly with a quarter of a monolayer). In the case of the sc and bcc lattices, only high temperature fits have been performed, where the four lowest simulation points have been omitted.

lattice type, the fitted slope B_l is $\xi_l/2$. Therefore, the total binding (i.e. sublimation) energy [Eq. (3.2)] of a monomer $E_b = B_l J_l$ is equivalent to the activation energy E_S for its dissolution. This allows to gauge the nearest-neighbor bond strength and thus to introduce an absolute temperature into the K3DLMC model. Furthermore, in the limit $T \to \infty$, the bulk density is reached, because the parameter A_l for each lattice type is equal to the corresponding number of atoms per unit cell. Since Eq. (3.2) has been verified (at least in the "high-temperature" parts of the simulated ϵ_l regimes) for all three lattice types, equilibrium conditions *independent* of the (100) phase boundaries have been achieved.

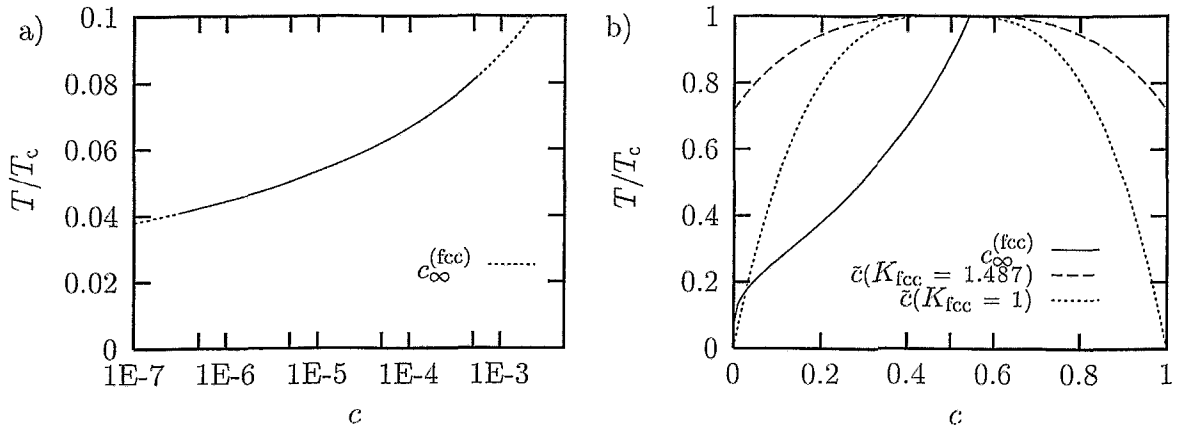

Figure 3.7: Phase diagram of the fcc ISING model. Using $B_{fcc} = 6$ and T_c as given by Table 3.1 in a) the solubility according to Eq. (3.14) is plotted. Combining Eqs. (2.41) and (3.5) in b) the high-temperature approximation $\tilde{c} = [1 - K_{fcc}(1 - T/T_c)^{5/16}]/2$ is plotted as well.

Physically, the extrapolation towards $T \to \infty$ is only defined for temperatures below the critical temperature T_c, because any condensed substance vaporizes above this point. The nature of the coexistence of phases is defined by the thermodynamic properties of the interface. Since it is known, that at a certain temperature $T_R \approx T_c/2$ there is a roughening phase transition from a smooth to a rough interface (with diverging interface correlation length) (see e.g. [131, 132] and references therein), the above analysis is furthermore restricted to the regime $T < T_R$.

According to the critical temperature of the fcc KIM in Fig. 3.6d the $c(T)$ phase diagram has been computed in the (normalized) temperature range $0.0408\,T_c < T < 0.0817\,T_c$ far below any critical phase transition (see Fig. 3.7a). While in this temperature regime physically reasonable solubility properties are observed, the limited validity of Eq. (3.14) becomes obvious in Fig. 3.7b, where this relation has been extrapolated into the high-temperature part of the phase diagram. Obviously, at $T = T_c$ the particle-hole symmetry of the ISING lattice gas Hamiltonian is violated, i.e. $c(T = T_c) \neq 0.5$.

It should be noted, that measured values of solubilities (c_∞^0, E_S) are usually restricted to certain temperature regimes. Therefore, values of c_∞^0 exceeding the bulk density by

Table 3.3: Values of the solubility constants of Eq. (3.14) for the three lattice types according to the fits of Figs. 3.6.

l	sc	bcc	fcc
A_l (a_l^{-3})	1.04 ± 0.03	1.90 ± 0.11	4.02 ± 0.07
B_l	2.98 ± 0.01	3.94 ± 0.03	5.993 ± 0.013

orders of magnitude (e.g. the solubility of Co in crystalline Si has been determined to $c_\infty = 10^{26} \exp\{-(2.83\,\mathrm{eV})\beta\}$ $1/\mathrm{cm}^3$ [133]) are not contradictory, but prevent an exact gauging of K3DLMC parameters.

Within the regime of the simulation parameters, in the low temperature range differences arise with respect to the initial condition (see Fig. 3.6). For instance, starting with a perfect (100) surface in the case of the sc lattice leads to solubility properties in the low temperature range, which are not in accordance with an ARRHENIUS-like behavior. Very likely, the system has not yet reached equilibrium, which is due to the special interface kinetics. A detachment event from a perfect (100) surface is only permitted by breaking five out of the six nearest-neighbor bonds, whereas an (diffusing) adatom has just one effective bond. Thus a large time lag is expected before an equilibrium of the chemical potential has been reached.

In the case of the fcc lattice two points should be noted: (i) at most seven out of twelve bonds can be broken in any nearest-neighbor jump, and (ii) due to the relatively high isotropy interface mass transfer is supposed to happen via cascade processes involving the break of only a few bonds, which gives a smooth kinetics. Thus even for low temperatures equilibrium conditions should be reached quickly.

It would be interesting to compare the solubility with computed values of the chemical potential μ for the lattice gas [134]. However, this was beyond the scope of this work.

Gibbs-Thomson relation

A connection between atomic and thermodynamic quantities is established by the GT relation Eq. (2.23), which defines the equilibrium concentration around a (spherical) NC of size $2R$ with respect to the materials-dependent capillary length R_c.

In order to exploit Eq. (2.23) it has first to be shown that the K3DLMC method reproduces the GT relation. This has been done by a series of simulations, where a NC of a specific size ("radius" R) is put in a simulation box of volume $V = 2^{n_x+n_y+n_z}a^3$ with $V^{1/3} \gg R$ (Fig. 3.8a shows the simulation setup). Like in the case of the flat interface simulation, this highly artificial initial configuration will evolve at finite temperatures to a state with phase equilibrium between dissolved monomers and the *curved* bulk phase boundary (see also [135]). For the analysis, averaged over a period of 2.5×10^6 MCSs (for the three highest values of ϵ_fcc in Fig. 3.8b the averaging was over 7.5×10^6 MCSs) the number of dissolved monomers is determined, which are in equilibrium with this precipitate [136, 137]. For the following analysis the radius of the NC is derived according to Eq. (3.7).

In the case of a fcc lattice Fig. 3.8b shows the averaged simulated equilibrium monomer concentrations for several fixed MC parameters ϵ_fcc for various cluster sizes. For each value of ϵ the simulation results are approximated reasonably well by the GT relation. Thus two properties of the model can be deduced:

- The K3DLMC method excellently reproduces the GT relation even for very small NCs;

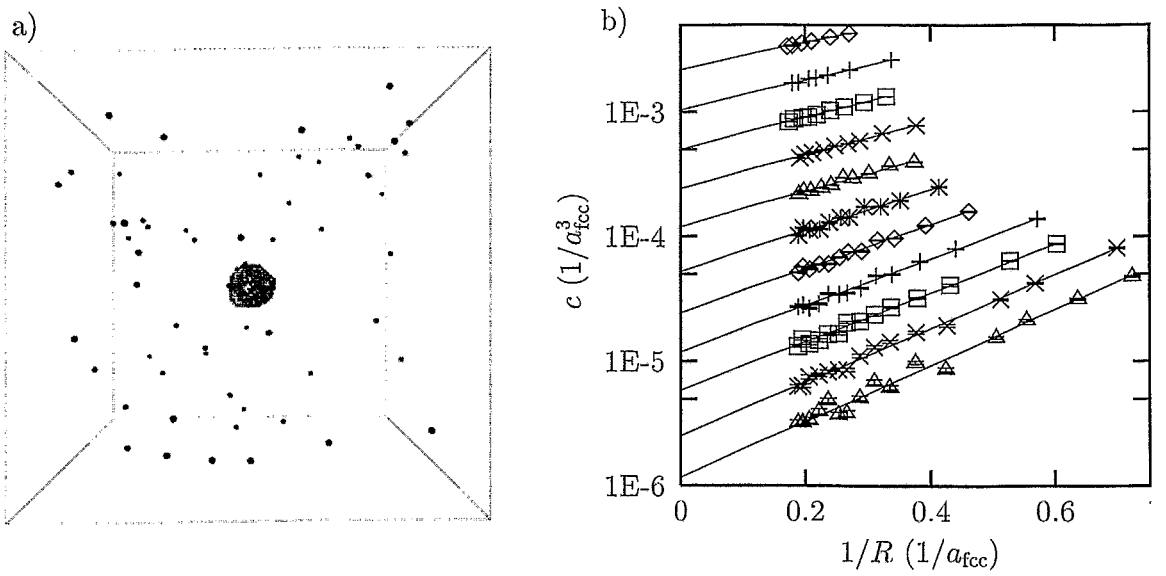

Figure 3.8: Check of the validity of the GIBBS-THOMSON relation within the K3DLMC method. In a) the simulation setup is shown. For the fcc lattice in b) the normalized monomer concentration is plotted versus the inverse NC radius. From top to bottom, the simulations have been performed for $\epsilon_{\rm fcc} = 1.25$ to $\epsilon_{\rm fcc} = 2.5$ in steps of $\Delta\epsilon_{\rm fcc} = 0.125$.

- By extrapolating for a given ϵ the GT relation to a flat interface (i.e. $R \to \infty$) the intersection of a fit with the y-axis determines the solidus concentration.

Furthermore, by plotting the values of the solidus versus the simulation parameter ϵ (Fig. 3.9a) the solubility can be derived. Applying Eq. (3.14) to the simulation results one obtains $A_{\rm fcc}^{\rm GT} = (3.64 \pm 0.08)\, a_{\rm fcc}^{-3}$ and $B_{\rm fcc}^{\rm GT} = (5.93 \pm 0.02)$, which is in good agreement with the results of the flat interface analysis (Table 3.3). While one could argue, that the flat interface simulations are influenced by the specific choice of (100) phase boundaries, the agreement of both simulation results is evidence that the interface orientation of the phase boundary does not effect intrinsic properties of the K3DLMC model.

It should be noted, that the GT relation is supposed to be valid also for concave interfaces. For instance, the monomer concentration in a spherical cavity of radius R within the bulk phase should be given by Eq. (2.23) after performing the transformation $R \to -R$ (see Fig. 3.10). In the particle picture, a positive (negative) curvature corresponds to a convex (concave) phase boundary. In the vacancy picture, the effective surface curvatures are reversed, i.e. convex $\leftrightarrow$ concave. Furthermore, due to the symmetry of the ISING Hamiltonian Eq. (3.1) with respect to a particle-vacancy interchange [i.e. $C_i \to (1 - C_i)$],[4] the surface tension transforms appropriately. This particle-vacancy symmetry is reflected in the GT relation of Fig. 3.10. As an implication, the product of the averaged monomer

[4]Neglecting a constant term $J(L_x L_y L_z - 2N_{\rm V})$, which fixes just the total energy of a lattice containing $N_{\rm V}$ unoccupied sites.

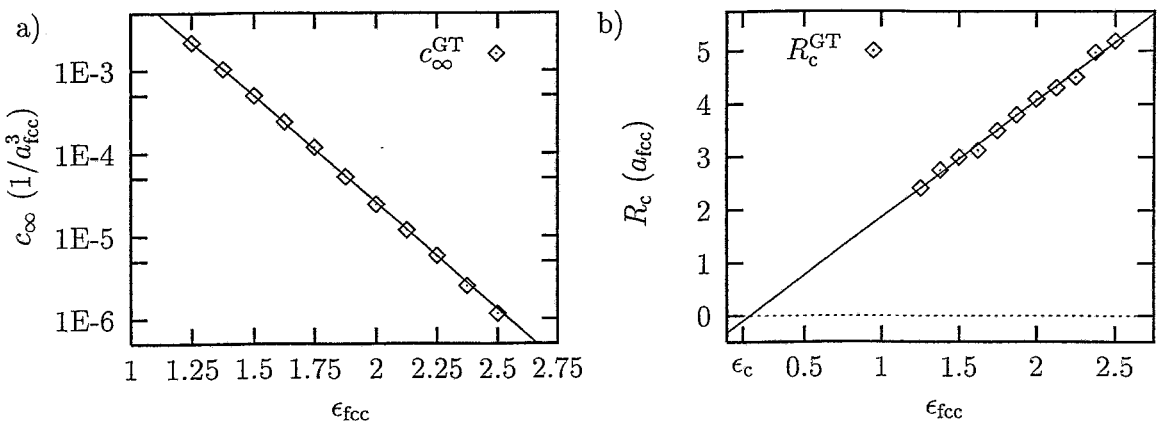

Figure 3.9: In a) the solubility properties are derived using results of the solidus obtained by the GT simulations. In b) the fitted capillary lengths are plotted versus ϵ_{fcc}, where ϵ_c denotes the critical point (see Table 3.1).

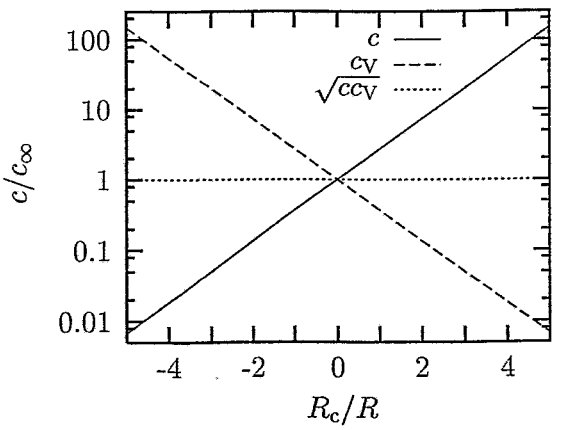

Figure 3.10: Generalized GT relation of the ISING model relating the equilibrium monomer and vacancy concentrations c and c_V to convex and concave phase boundaries, respectively.

and vacancy concentrations outside and within a NC is constant, i.e. $cc_V = c_\infty^2$.

However, up to now the kinetics of phase transitions has been predominantly studied on the basis of the linearization of the GT relation. For instance, cluster growth in the sc KIM has been discussed by PENROSE *et al.* [61, 100] in terms of the monomer concentration c. Without referring directly to the GT relation they use as expression for the equilibrium monomer concentration c_i of a NC consisting of i particles

$$c_i = c_\infty \left[1 + \frac{\alpha}{(i-2)^{1/3}}\right], \quad i > 2, \tag{3.15}$$

where α is related to the surface tension.

Capillary length and surface tension

A further analysis of the GT data allows an explicit determination of the effective surface tension σ, which according to the standard terminology denotes the interface free energy per unit area. Plotting the capillary lengths R_c^{GT} versus the scaled bond strength ϵ_{fcc} (see Fig. 3.8b) a linear dependence is observed

$$R_c(\epsilon_{fcc}) = R_{c0}^{(fcc)} + \zeta_{fcc} a_{fcc} \epsilon_{fcc}. \tag{3.16}$$

According to the least-square fit the constants are given by $R_{c0}^{(fcc)} = (-0.32 \pm 0.09)\, a_{fcc}$ and $\zeta_{fcc} = (2.19 \pm 0.05)$. The offset is based on the fact, that at $T = T_c$ the surface tension (and thus the capillary length) vanishes (see e.g. [138, 139]).[5]

With the help of the relation $R_c = 2\sigma V_a \beta = (2\sigma V_a / J_l)\epsilon_l$ [see Eq. (2.23)] for the capillary length, the surface tension is coupled to the nearest-neighbor bond strength J_{fcc} according to

$$\sigma = \frac{J_{fcc}}{2V_a \epsilon_{fcc}} (R_{c0}^{(fcc)} + \zeta_{fcc} a_{fcc} \epsilon_{fcc}) = \frac{2J_{fcc}}{a_{fcc}^2} \left(\frac{R_{c0}^{(fcc)}}{a_{fcc} \epsilon_{fcc}} + \zeta_{fcc} \right), \tag{3.17}$$

where $4V_a = a_{fcc}^3$ has been used. The last equation establishes a spherically averaged effective surface tension of a NC, while usually macroscopically measured surface tensions are defined with respect to a specified interface orientation. Moreover, the temperature dependence of σ (at least in the simulated temperature regime; see also Footnote 5) is given by Eq. (3.17), indicating a limiting value $\sigma \to \sigma_{T_0} = 2\zeta_{fcc} J_{fcc} / a_{fcc}^2$ for vanishing temperature. In comparison with the surface energies of the principal surfaces (see Table 3.2), σ_{T_0} is slightly above the zero-temperature value of $\sigma_I(110)$. Relations similar to Eq. (3.17) also hold for the sc and bcc lattices, but will not be presented in this work.

It should be noted, that the surface tension can not simply be obtained by counting the average number $\overline{N_J}$ of broken bonds of the cluster surface atoms and dividing this value by the mean (spherical) surface area $\overline{A}$. Having in mind, that the surface tension is composed of an internal σ_I and entropic σ_E part (i.e. $\sigma = \sigma_I + \sigma_E$), this approach would just specify σ_I. The entropic part $\sigma_E = -\beta^{-1}/\overline{A} \ln S(\overline{N_J})$ accounting for the number of different states $S(\overline{N_J})$ in phase space is not accessible by this method.

An alternative method to obtain the surface tension is the use of Eq. (2.9), i.e. by plotting $\ln(I) - (\delta\mu)i$ versus $i^{2/3}$, if the discrete size of the critical cluster and the (constant) supersaturation $\delta\mu$ are known [140, 141] (note that these authors used the spin-flip kinetic GLAUBER model, where a given magnetic field translates to a corresponding supersaturation via $2H \leftrightarrow \delta\mu$).

Although Eq. (2.9), the basic assumption of classical nucleation theory, is usually referred to as capillarity approximation, the capillary length R_c is not related to the critical radius of nucleation. This becomes obvious in Fig. 3.11, where both quantities are plotted.

[5] This condition is reasonably satisfied by the *linear* extrapolation of the simulation results. However, close to the critical point the surface tension is known to vanish like $\sigma \propto (1 - T/T_c)^{2\nu}$ with a critical exponent $\nu \approx 0.6$ [139].

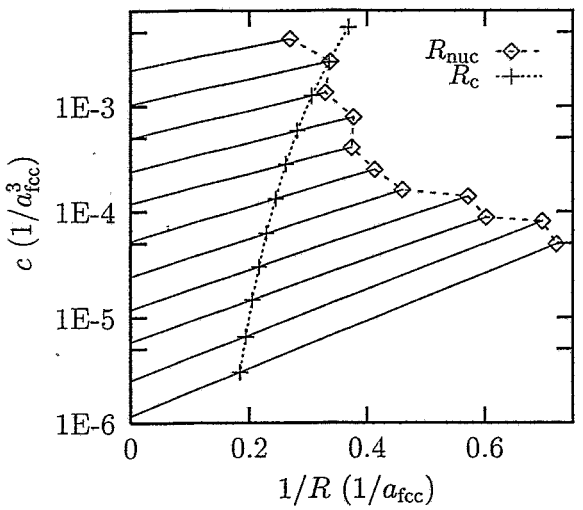

Figure 3.11: Replot of Fig. 3.8b, where the final points in the limit $R \to 0$ of the GT curves give a good approximation of the temperature dependence of the critical NC size. For comparison the temperature-dependent capillary length has been added.

For this comparison it has been used, that in general the final point of the GT curve in the limit $R \to 0$ denotes the critical cluster size i^* for nucleation (Section 2.3.2). Although this simulation series was not aimed at determining $i^*(\epsilon_l)$ exactly, the dependence of the critical size on simulation parameters can roughly be guessed in Fig. 3.11 (upper right part of the plot; a smooth dependence on temperature is expected).

Eqs. (3.14) and (3.17) reflect intrinsic properties of the nearest-neighbor KIM. Combining both relates the surface tension directly to the solubility. Thus care should be taken if for a specific system discrepancies arise in gauging of J_l according to reliably measured values of the solubility *and* the (effective) surface tension. This could be a hint, that the nearest-neighbor KIM might fail to give a reasonable description of the system and other approaches like the use of more sophisticated many-body potentials (e.g. embedded atom model) are more appropriate.

3.6 A simple approach to collisional mixing

Ion implantation is inevitably accompanied by a specific intensity of collisional mixing (CM), because decelerating ions displace host atoms or previously implanted impurities. In this process both primary knock-ons (recoil mixing) and interactions with the collision cascade (cascade mixing) determine the displacement probability and contribute to the mean displacement length [142, 143].

Therefore, in order to model NC formation during ion implantation or irradiation, the basic effects of CM, i.e. the displacements of atoms, should be incorporated into the K3DLMC method. From the statistical point of view, CM can be considered as an exter-

nal force, which in addition to thermal forces introduces a further dynamical component. Hence, thermally activated processes, e.g. monomer diffusion or evaporation steps, characterized by a finite temperature $\beta > 0$ compete with ballistic processes, e.g. atomic displacements, independent of temperature ($\beta = 0$). For binary systems, irradiation-induced (dis-) ordering phenomena have been studied for many years [144], and are usually referred to as driven alloys (for a recent review, see MARTIN and BELLON [145]).

The incorporation of CM into the K3DLMC model uses some simplifying assumptions:

- a displacement probability Ω (displacements per IA per implanted impurity) related to the nuclear energy deposition of the ion and a system-specific displacement length λ are assumed;
- the displacement distribution is chosen to be isotropic (which is a rather good approximation of cascade mixing but does not treat correctly the anisotropic nature of recoil mixing [146]) and exponentially decaying, i.e. $f(r) \propto \exp\{-r/\lambda\}$;
- due to the lattice nature of the model, only discrete displacements to (regular) lattice sites are considered;
- the displacements of IAs are not correlated in time and space. In particular no cylindrical region around a hypothetical ion or energetic recoil track is assumed, within which the displacements take place (thermal spike model);
- if for a statistically chosen IA the final site for a displacement attempt is occupied, no displacement is performed (e.g. for a displacement of a "bulk" IA within a NC). Furthermore, no replacement cascades are considered.

The displacement parameters for specific systems can be estimated by corresponding TRIM (SRIM) simulations [47]. Note, that this approach does not account for the displacement of substrate atoms into a NC and, as a consequence, their evolution within an (compound) impurity NC.

Because this Chapter is devoted to the intrinsic properties of the K3DLMC model, which are based on thermally activated processes, a more detailed discussion of the modifications due to ballistic effects will be postponed to Section 5.3.1.

3.7 Simulation of ion implantation and annealing

In the most general case the evolution of IAs during implantation has to be simulated by taking into account deposition, CM, and diffusion steps:

Deposition: For each single implantation step the new IA is set in the simulation box at a position, which x and y coordinates have been chosen randomly and the z coordinate according to a specified depth distribution, usually a Gaussian. Reasonable choices of the corresponding parameters R_p and ΔR_p can be obtained by TRIM (SRIM) calculations [47].

Collisional mixing: According to the number of impurity displacements per atom (dpa) statistically chosen impurities are checked for a displacement;

Diffusion: The implantation parameters then determine the ratio of implantation to diffusion steps. For instance, for a fixed implantation current, the higher the implantation temperature the more diffusion steps occur between two single implantation events.

For simulations in cases, where no NCs can be observed in as-implanted samples, steps two and three of the above scheme are simply skipped. In this case a subsequent simulation of annealing starts with the as-implanted profile (this corresponds to a quenched system; see process path 4 in Fig. 2.3). However, a detailed modeling of NC formation according to the above scheme, i.e. taking into account CM, has not yet been accomplished. So far, only general aspects of CM have been studied (see Section 5.3.2).

For all simulations periodic BCs have been applied in the x and y directions, i.e. perpendicular to the ion beam. In the z direction either periodic, reflecting, or absorbing BCs have been used depending on the particular materials system under investigation. In the case of a reflecting interface, for instance at $z = 0$ (the surface), a chosen jump direction across the surface terminates the jump attempt for this atom. A successful jump attempt across an absorbing interface (the virtual lattice sites in the layer directly adjacent to this interface are defined to be empty) causes the removal of this IA.

For the simulation of annealing, simply no new IAs are deposited and usually the temperature is increased, i.e. ϵ_l is decreased. All temperature changes are performed instantaneously (this approximation is justified, since usually the annealing time is much longer than the time the system needs to achieve the new temperature, but may cause problems with respect to the number of nucleated NCs).

3.8 Applicability of the K3DLMC method and discussion

To conclude this Chapter, some aspects of the K3DLMC model should be discussed before presenting applications of this method in Chapters 5-7.

By IBS two distinct classes of NCs can be formed. One distinguishes between mixed compound NCs consisting of impurity and substrate atoms, e.g. $CoSi_2$ nanocrystals observed after Co implantation into c-Si, and pure precipitates solely built up by IAs, e.g. Au NCs embedded in SiO_2 (impurity compound NCs consisting of two or more implanted atom species also belong to the second class). The approach to assume an averaged position- and configuration-independent potential, which describes an IA within the host matrix, has to be discussed with respect to the two NC classes.

For nanocrystals belonging to the first group, this simplified attempt to model the energetics is justified, if for the precipitation and further growth of these compound NCs only local rearrangements of the bulk atoms occur, which preserve the density of host atoms. For instance, in the phase transition from dissolved Co in c-Si to $CoSi_2$ precipitates

the number of Si atoms per unit cell remains the same (8 Si atoms in a diamond-like cell as well as 8 Si atoms in the CaF_2-like $CoSi_2$ cell, which both have nearly the same lattice constant a), but they reside on different positions. This implies, that the number of host atoms, with which an IA interacts, is constant, and thus this absolute contribution to its energy state can be to first order neglected.

For NCs of the second class, the attachment of an additional monomer is also achieved only by local (on a length scale of the order of an unit cell) rearrangements of (host) atoms, but now the density of the substrate atoms is not preserved, since they are pushed out of the volume, where the precipitate grows. As a consequence, the IAs within this NC do not directly interact with the atoms of the substrate. In this case, the use of an averaged, position-independent potential is not a priori justified and deserves for thorough studies a further discussion.

Associated with the work to be spent to move the host atoms (radially) away from the NCs of the second type, the resulting densification in the shell surrounding the precipitate is likely accompanied by the development of a strain field. This influences the monomer diffusion [129] in the vicinity of the NCs, and could result in a size-dependent growth law with a possible upper limit for the NC size. The experimental observation of strong strain fields around NCs would clearly restrict the use of the above described K3DLMC method (for a MC modeling of domain growth in the presence of strain see e.g. FRATZL and PENROSE [147, 148]). However, the effect of strain fields can be neglected in systems, where the lattice mismatch between nanocrystals of the first type and the (crystalline) matrix is negligible. Furthermore, if the substrate is viscous enough at implantation and annealing temperatures, strain is also not supposed to influence the impurity redistribution considerably.

As indicated in Fig. 3.2, a more precise treatment of precipitate-matrix interface reactions can be achieved by the introduction of an additional energy barrier E_R, which influences the attachment and/or detachment of monomers. It is known from OR, that for an ensemble of precipitates the evolution depends on the relative strength of diffusion and interface reactions [105, 149]. The value of E_R controls the degree of diffusion to reaction controlled coarsening with large values delaying absorption/desorption events, which then causes a more and more homogeneous monomer concentration in the substrate. An energy barrier effective only for attachment attempts might be a possible way for a simple modeling of the effect of a strain field around a NC. On the other hand it had been shown, that the evolution of Au NCs in SiO_2 depends on the annealing atmosphere. WHITE *et al.* [150] found, that coarsening in an Ar + H_2 atmosphere proceeds much slower than in an oxidizing atmosphere. It is reasonable to assume, that hydrogen diffusing into the sample passivates the Au/SiO_2 interface, which reduces the driving force for OR. This could be simulated by assuming an additionally energy barrier effective only for detachment.

For all simulations homogeneous and constant conditions throughout the simulation volume have been assumed. No attempt has been made to include damage effects caused by ion implantation, thus possibly preferred heterogeneous nucleation of NCs in areas of large damage is neglected, which could influence the NC distribution. Furthermore, the effect of radiation enhanced diffusion is not explicitly taken into account as well as a possible

trapping of single IAs at lattice defects, which by an artificially increased solubility delays the formation of NCs. For the description of diffusion, no other diffusion channels than nearest-neighbor jumps are considered, irrespective, if the modeled impurity redistribution takes place in a crystalline or amorphous substrate. Due to the lattice description the detailed atomic diffusion mechanisms (e.g. interstitial diffusion, direct exchange, vacancy-mediated diffusion, etc [129]) are not taken into account. The K3DLMC method rather resembles interstitial diffusion of impurities in crystals. For modeling of binary alloys the use of the direct X-Y exchange mechanism is questionable because atomic movements are most likely caused by vacancy diffusion (recent simulation attempts of phase separation compared vacancy dynamics with the conventional KAWASAKI model [151]). It is assumed, that diffusion of impurities can be described either by coupling to experimentally observed diffusion coefficients or by using the activation energy E_A of the most effective diffusion channel as obtained by MD simulations.

The use of the ISING model to describe nearest-neighbor interactions among IAs is a good basis for an efficient description of the evolution of NCs. Despite its simplicity it correctly reproduces the GT relation [Eq. (2.23)], and thus allows a coupling to a thermodynamic treatment of the late stage of the phase transition. However, more sophisticated interaction potentials may be needed in order to model specific problems, e.g. an embedded atom-like potential for the understanding of stress-induced sub-100 nm patterning of $CoSi_2$ layers, where a modified version of this K3DLMC method has been successfully applied [120].

One inherent property of this K3DLMC method is the fixed bonding length between two IAs, irrespective, if it is a dimer or one out of ξ_l bulk bondings. However, agglomerations of a few impurities are presumably not positioned on regular lattice sites, rather they are supposed to be in an amorphous order. Hence, this model is not suited to study the properties of very small embryo-like NCs as well as of precipitates, which condense in the amorphous state.

Within an ensemble of NCs, the diffusional screening length [111]

$$\lambda_\mathrm{D}(t) = \frac{1}{\sqrt{4\pi n(t)\bar{R}(t)}}, \tag{3.18}$$

where $n(t)$ denotes the density of NCs, is an important quantity, because it sets the length scale of NC interactions. Since a monomer detaching from a NCs is very likely to migrate to a nearby precipitate on his random walk, λ_D denotes the distance beyond which the diffusional interaction is screened by the remaining ensemble a NC is embedded in. Thus the K3DLMC simulations have to be checked, that self-interactions of NCs are avoided in cases, where periodic BCs are applied.

Due to the lattice description all ordered phases have the same orientation. This provides a good description for a phase transition in a single crystal, but fails to model the random orientation of NCs in amorphous substrates like SiO_2. Furthermore, since in this K3DLMC model all ordered domains are in phase (all IAs are located on the same lattice) no grain boundary effects can be studied. By appropriately extending the model, e.g. by

using the q-state POTTS model [152, 153] or assigning a further parameter to each lattice point [128] grain boundary studies have been performed.

Furthermore, systems with different coexisting NC types can not be modeled in detail, for instance IBS of $CoSi_2$ precipitates in Si, where A- and B-type clusters are formed (the platelet-shape of B-type $CoSi_2$ NCs is not caused by intrinsic lattice properties rather by a rotated (111) surface with respect to the Si lattice). Phase transformations characterized by different crystallographic structures of the ordered domains (e.g. $FeSi_2$ phase diagram) are also not directly accessible by the current K3DLMC model.

Chapter 4

General description of diffusion and reaction controlled Ostwald ripening

4.1 Characterization of OR and recent developments

The last stage of IBS consists usually of a thermal heat treatment of the implanted sample because of two major reason: (i) the radiation damage within the substrate can be (at least partially) annealed out; (ii) the mean NC size can be increased and, therefore, be adjusted to a predefined value. In case (ii) the physical process governing the evolution of an ensemble of precipitates is known as OSTWALD ripening (OR) [154]. More precisely, OR controls the late stage of a phase transition of a closed two-phase mixture (either dissolved monomers or second-phase precipitates) within a chemically neutral matrix (see Fig. 2.1). Since a considerable amount of energy is associated with the phase boundary, i.e. the precipitate/matrix interface, the system is not in its lowest energy state. Therefore, the minimization of the surface contribution to the total energy is the driving force governing the dynamics of the material redistribution. Accordingly, small NCs (characterized by a high surface-to-volume ratio) will dissolve and the corresponding material mass transfer to larger precipitates is mediated by diffusion. A measure of the instability of the system is the degree of supersaturation of monomers, which is defined as the difference between the average concentration due to the presence of NCs and the equilibrium solubility.

From the theoretical point of view OR can take place in between two limiting kinetic regimes: (i) diffusion controlled ripening or (ii) reaction controlled ripening. For specific systems the coarsening characteristics is determined by the ratio of the monomer diffusion coefficient D and the interface reaction rate k, which is given by the transfer velocity of impurities across the phase boundary [105]. The latter quantity takes into account the concept of a reaction barrier by fixing the reaction rate of dissolved impurities at the precipitate/matrix interface. The ratio D/k relates the time scales of diffusion jumps to monomer attachment/detachment rates. In ripening mode (i) the limiting process is the diffusion of monomers between precipitates assuming that monomer attachment/detachment events take place on a much shorter time scale. Therefore, rather large concentration gradients

should be established between well-defined equilibrium monomer concentrations of shrinking and growing NCs. In reaction controlled ripening, diffusion is fast compared to mass transfer across the interface, which results in much less pronounced concentration gradients between NCs.

A comprehensive theory of OR in 3D was first developed by LIFSHITZ and SLYOZOV [104] and independently by WAGNER [105] (LSW theory) for the limit of vanishing volume fraction $\phi \to 0$ of the impurity phase. In the regimes of pure diffusion or reaction controlled coarsening, they derived the time dependence of OR in the asymptotic limit, i.e. the growth law for the mean NC radius $\bar{R} \propto (t/\tau)^m$, where τ is a characteristic time constant and m is determined by the mode of ripening. Furthermore, they showed, that the particle radius distributions (PRDs) have a time-independent stationary shape, if the NC sizes are scaled by $\bar{R}$. Although being qualitatively very successful in describing coarsening phenomena, a serious shortcoming of the LSW-theory is the inherent global mean-field approach. Since each precipitate is treated as an isolated particle, diffusional interactions between individual precipitates are not taken into account.

In order to extent the limited validity of the LSW theory, much effort was devoted to study the effect of finite volume fractions and, as a consequence, spatial correlations on particle coarsening. Using different approaches, among others BRAILSFORD *et al.* [155], TSUMURAYA *et al.* [156], MARQUSEE *et al.* [157], and MARDAR [158] derived a dependence of OR on ϕ. While there is agreement that a finite volume fraction does not change the time exponent m but increases the rate of coarsening $[\tau(\phi) < \tau(\phi = 0)]$ and gives rise to a broader PRD than compared to the LSW theory, the precise dependence on ϕ (usually expressed as an expansion in $\sqrt{\phi}$) seems still to be controversial (see, e.g. [159, 160] and further references therein). Very recently, ALKEMPER *et al.* [161] have shown for a solid-liquid system (with $\phi \approx 10\%$) satisfying all assumptions of the LSW theory the importance of transient effects [162] during phase separation. While most theories assume steady-state coarsening, they have pointed out that such conditions are usually not met in experiments and, therefore, give a reasonable explanation of the observed discrepancies.

Computer simulations based on mean-field descriptions have been performed mainly in the diffusion controlled limit. Pioneering work was done by VOORHEES and GLICKSMAN (VG) [39, 40], who treated the interacting precipitates as fixed point-like sources characterized by a (fictitious) radius. By defining a dimensionless supersaturation $\Theta(\vec{r}, t) = [c(\vec{r}, t) - c_\infty]/c_\infty$ they solved the modified time-independent multi-droplet diffusion equation

$$\vec{\nabla}^2 \Theta(\vec{r}) = -4\pi \sum_i Q_i \delta(\vec{r} - \vec{r}_i) \tag{4.1}$$

with respect to BCs given by the linearized GT equation [Eq. (2.23)]. In their approach the individual source strengths Q_i (corresponding to a monopole approximation of a full treatment of NC interactions) determine the evolution of NCs ($\mathrm{d}R_i/\mathrm{d}t \propto Q_i$) within the restriction of material conservation, i.e. $\sum_i Q_i = 0$. While the VG method is computationally very extensive due to the included mutual interaction of *all* precipitates, different simulation approaches by BEENAKKER [163] and ENOMOTO *et al.* [164] explicitly used diffusional screening properties present in an ensemble of NCs. By restricting the range

of NC interactions they were able to model larger and thus statistically more significant systems. With the rapid increase of computer power, it has later been possible to include higher-order (dipole, ...) terms of NC interactions which account for migration and spherical shape deviations of precipitates [165, 166].

Whereas most of the theoretical and simulation studies considered fundamental properties of (at least on a large scale) homogeneous coarsening systems, special attention was paid also to the mechanisms of pattern formation [167, 168]. In a theoretical study VENZL found first indications of self-organization of precipitates by OR [169, 170]. Later on REISS *et al.* [171, 172] developed a model based on VG, which allowed to study properties of spatially inhomogeneous systems. A typical example are precipitates formed by ion implantation which evolve in a thin film with explicit boundaries (e.g. the surface of the sample) and show a depth-dependent size distribution. In particular, they could explain the self-structuring of NCs by OR into bands parallel to the surface as has been observed in IBS. A more general study of OR has shown that self-organization of spatial patterns is an inherent property of an inhomogeneous ensemble of clusters [113].

Other widely studied areas of OR are theoretical descriptions of 2D systems (see, e.g. [173, 174] and references therein), with special attention to the evolution of dislocation loops [175, 176] and the coarsening behavior of clusters on surfaces [30]. Since in a lot of cases the evolution of NCs in solids is influenced by elastic forces (e.g. lattice mismatch between nanocrystals and crystalline substrate), the description of OR in the presence of strain fields is also a vividly studied part of materials science (see, e.g. [177, 178] and references therein).

After WAGNER'S treatment of reaction controlled OR, in mean-field approaches the influence of interface kinetics on particle coarsening appears to have been studied only occasionally. Based on the growth behavior of an alloy, which was not conform with the diffusion controlled regime of OR [179], WHITE derived a description for competing influences of diffusion and reaction control [180]. On an atomic level LAVINE *et al.* set up a MC model, where they explicitly included an escape probability of monomers from NCs in order to simulate different regimes of coarsening [181].

In this Chapter the model of REISS [171, 41, 172, 182] has been extended from the diffusion controlled limit to the whole range of the quantities D and k. In addition to demonstrating that this local mean-field approach reproduces the basic results of the LSW theory in the two limiting cases, this general description is applied to study intermediate coarsening processes. Furthermore, this approach allows to model open systems, e.g. growth of NCs during implantation, as well as the correct treatment of external sinks, e.g. absorbing interfaces.

In what follows, at first the basic physical concepts are introduced by considering a single isolated NC, and results of the LSW theory are presented. Then a general expression for the source strengths of interacting NCs is derived and, finally, typical results will be discussed.

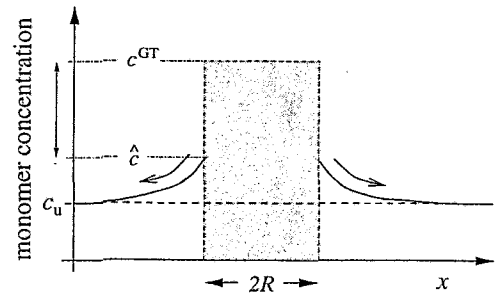

Figure 4.1: Schematic drawing of the monomer concentration field around a single NC of radius R due to diffusion and interface reaction influences. In the general case, $\hat{c}$ adjusts between the diffusion controlled (c^{GT}) and reaction controlled (c_u) values.

4.2 Fundamentals of the model

4.2.1 Evolution of a single nanocluster

In an extension of the discussions of Section 2.4 first the evolution of a single NC is described in the general case of diffusion and reaction controlled OR. Considering the adiabatic limit (i.e. neglecting the time derivative of the concentration field, which is justified if the growth rate of a NC is slow compared to the resulting changes of the impurity concentration) the stationary homogeneous diffusion equation $\vec{\nabla}^2 c(\vec{r}) = 0$ (LAPLACE equation) has to be solved.

With respect to BCs Eqs. (2.25) and (2.26) the solution of Eq. (2.24) in the case $G = 0$ is repeated here for convenience

$$c(r \geq R) = c_u - \frac{R[c_u - \hat{c}(R)]}{r}. \tag{4.2}$$

Material conservation requires, that the reaction flux "through" the precipitate/matrix interface, i.e. the net attachment and detachment rate for growing or shrinking NCs, is equal to the diffusion current $\vec{j}_{diff} = -D\vec{\nabla}c(\vec{r})$ evaluated at this interface. Assuming a linear ansatz [105]

$$\vec{j}_{reac} = k\left[c^{GT}(R) - \hat{c}\right]\vec{e}^{(r)}, \tag{4.3}$$

where k is a radius-independent reaction rate describing both monomer attachment and detachment, $c^{GT}(R)$ the radius-dependent equilibrium solubility [Eq. (2.23)], and $\vec{e}^{(r)}$ the radial unit vector pointing outward, the monomer concentration at the interface (see Fig. 4.1) can be evaluated as

$$\hat{c}(R) = \frac{kRc^{GT}(R) + Dc_u}{kR + D}. \tag{4.4}$$

Thus, the evolution of a precipitate consisting of N atoms is given by the growth rate

$$\frac{dN}{dt} = -\oint \vec{j}|_{r=R} d\vec{S} = -\frac{4\pi R^2 kD}{kR + D}\left[c^{GT}(R) - c_u\right]. \tag{4.5}$$

Obviously, a shrinking NC acts as a source of monomers and thus feeds the surrounding concentration field $c(\vec{r},t)$. Therefore, a precipitate is characterized by its source strength, given by $Q = -\mathrm{d}N/\mathrm{d}t$, which is defined as the number of atoms it puts into solution per second. Thus Eq. (4.2) can be expressed as

$$c(r \geq R) = c_\mathrm{u} + \frac{1}{4\pi D}\frac{Q}{r}. \tag{4.6}$$

As a result, for a single NC one obtains for the interface monomer concentration and source strength in the two limiting regimes:

Diffusion control: $kR \gg D$

$$\hat{c}(R) = c^\mathrm{GT}(R), \qquad Q = 4\pi DR\left[c^\mathrm{GT}(R) - c_\mathrm{u}\right]. \tag{4.7}$$

Reaction control: $kR \ll D$

$$\hat{c}(R) = c_\mathrm{u}, \qquad Q = 4\pi R^2 k\left[c^\mathrm{GT}(R) - c_\mathrm{u}\right]. \tag{4.8}$$

4.2.2 Evolution of an ensemble of nanoclusters

An ensemble of NCs is described by the time-dependent PRD $f(R,t)$, where $f(R,t)\mathrm{d}R$ denotes the number of particles per unit volume which have a radius between R and $R+\mathrm{d}R$. Accordingly, the NC density, normalized to unit volume, is given by $n(t) = \int f(R,t)\mathrm{d}R$.

In the limiting case of a highly dilute system, a growth law can be derived, where all NCs are embedded in the *same* average concentration $\bar{c}$. This growth law is given by Eq. (4.5) after substituting $\bar{c}$ for c_u

$$\frac{\mathrm{d}R}{\mathrm{d}t} = -\frac{kDV_\mathrm{a}}{kR+D}\left[c^\mathrm{GT}(R) - \bar{c}\right]. \tag{4.9}$$

According to the GT relation [Eq. (2.23)], for a given (materials-dependent) capillary length R_c the mean concentration $\bar{c}$ is associated with a specific NC radius $R^\star$

$$R^\star = \frac{R_\mathrm{c}}{\ln(\bar{c}/c_\infty)}. \tag{4.10}$$

This radius is called the critical radius because precipitates larger than $R^\star$ will grow, whereas those being smaller will shrink. With the help of the linearized GT equation

$$c^\mathrm{LSW}(R) = c_\infty(1 + R_\mathrm{c}/R), \tag{4.11}$$

Eq. (4.9) can be written as

$$\frac{\mathrm{d}R}{\mathrm{d}t} = -\frac{kDV_\mathrm{a}}{kR+D}\frac{c_\infty R_\mathrm{c}}{R}\left(1 - \frac{R}{R^\star}\right). \tag{4.12}$$

The evolution of NCs can be expressed as a continuity equation for f in size space

$$\frac{\partial f(R,t)}{\partial t} - \frac{\partial}{\partial R}\left(f(R,t)\frac{\partial R}{\partial t}\right) = 0. \tag{4.13}$$

For closed systems, the amount c_0 per unit volume of minority phase (impurities) consists of dissolved monomers and precipitates. Both parts are related according to material conservation

$$c_0 = \phi(t)c_{\mathrm{NC}} + [1-\phi(t)]\bar{c}(t) = \text{const.}, \tag{4.14}$$

where $\phi(t) = 4\pi/3 \int R^3 f(R,t)\mathrm{d}R$ denotes the precipitated volume fraction per unit volume and c_{NC} is the concentration of monomers within a NC.

Combining Eqs. (4.12)-(4.14) and introducing a normalized radius $\rho = R/R^\star$, LIFSHITZ, SLYOZOV [104] and WAGNER [105] have derived the following distribution functions, characteristic time constants and time dependences of the critical radius $R^\star(t)$ (the mean radius $\bar{R}$, respectively) and the NC density $n(t)$:

Diffusion control

$$f(\rho,t) \propto \begin{cases} \frac{\rho^2}{\left(1+\frac{t}{\tau_{\mathrm{diff}}}\right)^{4/3}} \left(\frac{3}{3+\rho}\right)^{7/3} \left(\frac{\frac{3}{2}}{\frac{3}{2}-\rho}\right)^{11/3} \exp\left\{-\frac{\rho}{\frac{3}{2}-\rho}\right\} & 0 \le \rho \le \rho_{\max}^{\mathrm{LSW}} = \frac{3}{2} \\ 0 & \rho > \rho_{\max}^{\mathrm{LSW}} \end{cases} \tag{4.15}$$

$$R^\star(t) = R^\star(t=0)\left(1+\frac{t}{\tau_{\mathrm{diff}}}\right)^{1/3}, \qquad \tau_{\mathrm{diff}} = \frac{9[R^\star(t=0)]^3}{4c_\infty D V_{\mathrm{a}} R_{\mathrm{c}}}, \qquad R^\star = \bar{R} \tag{4.16}$$

$$n(t) \propto t^{-1} \quad \text{for} \quad t \gg \tau_{\mathrm{diff}} \tag{4.17}$$

Reaction control

$$f(\rho,t) \propto \begin{cases} \frac{\rho}{\left(1+\frac{t}{\tau_{\mathrm{reac}}}\right)^2} \left(\frac{2}{2-\rho}\right)^5 \exp\left\{-\frac{3\rho}{2-\rho}\right\} & 0 \le \rho \le \rho_{\max}^{\mathrm{LSW}} = 2 \\ 0 & \rho > \rho_{\max}^{\mathrm{LSW}} \end{cases} \tag{4.18}$$

$$R^\star(t) = R^\star(t=0)\left(1+\frac{t}{\tau_{\mathrm{reac}}}\right)^{1/2}, \qquad \tau_{\mathrm{reac}} = \frac{2[R^\star(t=0)]^2}{c_\infty k V_{\mathrm{a}} R_{\mathrm{c}}}, \qquad R^\star = \frac{9}{8}\bar{R} \tag{4.19}$$

$$n(t) \propto t^{-3/2} \quad \text{for} \quad t \gg \tau_{\mathrm{reac}} \tag{4.20}$$

Both PRDs are shown in Fig. 4.2a. Note, that theoretical descriptions of OR for non-vanishing volume fraction ϕ predict $\rho_{\max} > \rho_{\max}^{\mathrm{LSW}}$. Furthermore, it should be stressed, that the LSW theory is based on the linearization of the GT relation [see Eq. (4.9)]. Thus care has to be taken by applying the LSW theory to systems, where $\bar{R} \gg R_{\mathrm{c}}$ is not valid. As Fig. 4.3 indicates, the exact GT relation gives much higher equilibrium concentrations for $R \lesssim R_{\mathrm{c}}$, thus NCs in this regime tend to dissolve more rapidly than the LSW theory predicts. As a consequence NC ensembles with $\bar{R} \lesssim R_{\mathrm{c}}$ can *not* be described by Eqs. (4.15)-(4.20). Rather, they will exhibit a quite different dynamics (see Section 6.1).

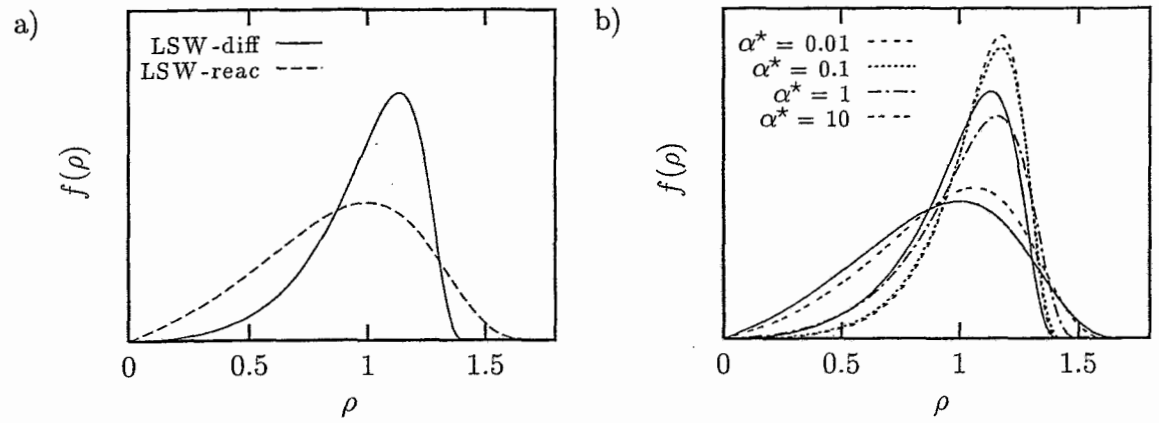

Figure 4.2: In a) the normalized PRDs of both limiting cases of the LSW theory are shown. In b) the normalized PRDs of four intermediate cases according to Eq. (4.21) are plotted [for comparison both LSW-PRDs (solid lines) of Fig. a) have been added].

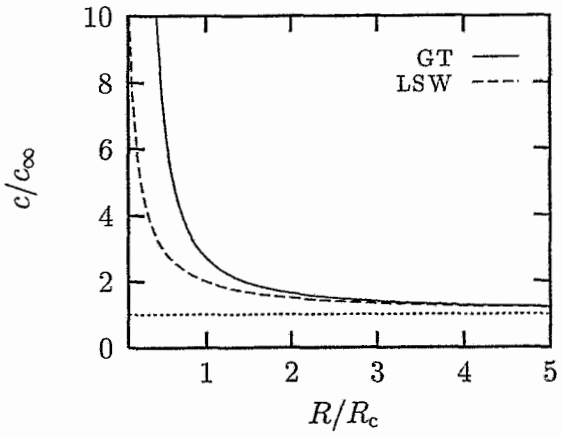

Figure 4.3: Comparison of the equilibrium monomer concentration of a NC of radius R according to the exact [Eq. (2.23)] and linearized [Eq. (4.11)] GT relation.

Intermediate regime

Using the parameterization $\alpha^* = R_r/R^*$, where $R_r = D/k$, WHITE [180] derived an expression for the PRD in the intermediate regime between pure diffusion and reaction controlled OR

$$f(\rho) \propto \rho(\alpha^* + \rho)(a - \rho)^\gamma(-c - \rho)^\delta \exp\left\{\frac{b(a+\alpha^*)}{a-c}\frac{\rho}{a-\rho}\right\}, \tag{4.21}$$

where the parameters are given by $\gamma = [ba(a-2c)-2(a-c)^2-bc\alpha^*]/(a-c)^2$, $\delta = [bc(c+\alpha^*)-(a-c)^2]/(a-c)^2$, $a = 2\zeta/(2+\zeta)$, $b \approx -3$, $c = -\zeta/2$, and $\zeta = 3+\alpha^*+\sqrt{(9+\alpha^*)(1+\alpha^*)}$. Here, the parameter a denotes the maximum allowed NCs size.

In the above description, the quasi-stationary PRD depends on $\alpha^\star$, and thus changes shape during OR. Thus Eq. (4.21) is only valid, if changes within the distribution occur much more rapidly than changes in $\alpha^\star$. It should be noted, that in the limiting cases $\alpha^\star \to 0$ and $\alpha^\star \to \infty$ Eq. (4.21) reduces to the LSW limits Eqs. (4.15) and (4.18), respectively.

In Fig. 4.2b the PRDs of the LSW theory are plotted as well as four PRDs characterized by various values of $\alpha^\star$ according to Eq. (4.21). Distributions with parameters $\alpha^\star \gtrsim 100$ are essentially indistinguishable from the PRD of the reaction controlled limit. Interestingly, for small but finite $\alpha^\star$ the relative contribution of NCs smaller than $R^\star$ to the PRD first decreases with respect to the LSW distribution for the diffusion limited case. This property (not discussed in [180]) might be due to the approximations made for deriving $f(\rho)$ in closed form and will be discussed in Section 4.5.

4.3 Local mean-field approach to diffusion and reaction controlled Ostwald ripening

As mentioned above, for non-vanishing volume fractions the LSW theory is no longer strictly valid simply because the long-range diffusion fields start to overlap. As a result, the monomer concentration around one NC is influenced by the presence of neighboring precipitates. Thus an appropriate framework for simulation studies of OR is a local mean-field description. The following derivation is in line with the VG approach and is aimed as an extension to the work of REISS [182] and REISS *et al.* [171, 172] towards a full coverage of the LSW theory.

As in the single NC case, the starting point for this approach to model the evolution of coarsening NCs is to seek a solution of the stationary diffusion equation $\vec{\nabla}^2 c(\vec{r},t) = 0$ defined in the multiply connected space outside the precipitated phase [equivalent to Eq. (4.1)]. Considering an ensemble of N NCs, the BCs for the monomer concentration at each phase boundary $c(\vec{r})|_{|\vec{r}-\vec{r}_i|=R_i} = \hat{c}_i$ are now a function of c and therefore have to be determined self-consistently.

Like in electrostatics, an exact solution to the stationary diffusion equation subject to N BCs may be found by the method of mirror sources. Replacing the (infinite) number of mirror sources inside the precipitates by an (infinite) series of multipole moments at each center gives an equivalent solution. Thus the concentration field can be expressed as a sum over the individual multipole expansions (with multipole moments M_{il}^m)

$$c(\vec{r}) = c_u + \frac{1}{4\pi D} \sum_{i=1}^{N} \sum_{l=0}^{\infty} \sum_{m=-l}^{l} \frac{Y_l^m(\theta_i,\phi_i) M_{il}^m}{|\vec{r}-\vec{r}_i|^{l+1}} \tag{4.22}$$

using the common notation Y_l^m to denote the spherical harmonics. It should be noted, that in the case of a single isolated isotropic NC all but the monopole term $Q = Y_0^0 M_0^0$ vanish and Eq. (4.6) is retained.

The actual boundary values $\hat{c}_i$ can be derived by equating the reaction current [Eq. (4.3)] with the diffusion current evaluated at the i-th interface, $\vec{j}_{\text{diff}}^{(i)} = \vec{j}_{\text{reac}}^{(i)}$, from which

immediately follows

$$\hat{c}_i = \frac{D}{k}\left(\vec{\nabla}c(\vec{r})\right)\Big|_{|\vec{r}-\vec{r}_i|=R_i} \cdot \vec{e}_i^{(r)} + c^{\mathrm{GT}}(R_i). \tag{4.23}$$

The multipole moments M_{il}^m can be obtained by integration of Eq. (4.22) over the (spherical) surface of the i-th precipitate using the orthogonal properties of the spherical harmonics involved. However, in order to keep things simple, only monopole terms are considered, which is a reasonable approximation for small volume fractions of the second phase (usually the monopole approximation is acceptable as long as $\phi < 0.1$ [183]). After some straightforward algebra (see Appendix B) one ends up with a coupled system of N linear equations for the N source strengths $Q_i = Y_0^0 M_{i0}^0$

$$Q_i = \frac{4\pi D R_i^2}{R_i + R^\star\alpha^\star}\left[c^{\mathrm{GT}}(R_i) - \frac{1}{4\pi D}\sum_{j\neq i}^{N}\frac{Q_j}{|\vec{r}_i-\vec{r}_j|}\left(1+\frac{R^\star\alpha^\star}{|\vec{r}_i-\vec{r}_j|}\right) - c_\mathrm{u}\right]. \tag{4.24}$$

Here, the dimensionless parameter $\alpha^\star = D/(kR^\star)$ denotes the degree of diffusion and reaction control during ripening. In the case $\alpha^\star = 0$, i.e. the diffusion controlled coarsening mode, Eq. (4.24) is equivalent to formerly derived expressions [39, 172].

The local mean-field character of this approach is clearly seen in Eq. (4.24), since the source strength of the i-th precipitate is proportional to the difference between its own equilibrium concentration and the superposition of the external concentration c_u and the concentration fields caused by all other NCs. The evolution of individual precipitates is mainly determined by the diagonal elements of Eq. (4.24), whereas the off-diagonal elements account for the coupling of NCs. Thus the onset of reaction control primarily reduces the absolute value of the source strengths, while additional modifications of the NC coupling become only relevant for large $\alpha^\star$. More precisely, the influence of reaction control on mutual NC interactions can not be neglected if D/k is of the same order as the average distance d between NCs. However, in the course of OR the NC density decreases, thus the ratio of both types of coupling decreases like $1/d$. As other studies suggest [113], the correct treatment of off-diagonal terms influences the time behavior of the ensemble. It should be noted that in the limit $\phi \to 0$, i.e. $|\vec{r}_i - \vec{r}_j| \to \infty$, the LSW growth law is obtained.

Within the monopole approximation, the concentration field is given by

$$c(\vec{r}) \simeq c_\mathrm{u} + \frac{1}{4\pi D}\sum_{i=1}^{N}\frac{Q_i}{|\vec{r}-\vec{r}_i|}, \tag{4.25}$$

and the individual source strengths Q_i determine the evolution of the precipitates

$$\frac{4\pi}{V_\mathrm{a}}R_i^2(t)\frac{\mathrm{d}R_i(t)}{\mathrm{d}t} = -Q_i. \tag{4.26}$$

Eq. (4.26) together with the diffusion equation form a coupled system of differential equations controlling the evolution of the precipitates. Considering the characteristic time scales

one generally loses no information in neglecting the time derivative of the diffusion equation. This is due to the fact that the time scale involved in the precipitate growth is usually much larger than that of the diffusional accommodation of the impurity concentration to the existing precipitate pattern.

4.4 Numerical implementation

Here, a short sketch of the numerical implementation will be given; are more detailed discussion can be found in [182].

At the beginning of the simulation, geometrical (e.g. shape of basic simulation cell, assignment of physical properties of ensemble boundaries, like periodic, absorbing, or reflecting boundaries, respectively) and physical (materials parameters, NC size and space distributions) aspects have to be specified. In order to obtain dimensionless quantities, the following (to some extent arbitrary) transformations are performed: all lengths are scaled by the ensemble size L_{ens} (in the case of a cubic geometry L_{ens} is the size of the unit cell of the simulation); a supersaturation $\Theta = (c - c_\infty)/c_\infty$ according to VG is defined; a time scale is introduced via $\tau_{\mathrm{sim}} = L_{\mathrm{ens}}^2/(V_{\mathrm{a}} D c_\infty)$. Within the scaled system of equations, the only remaining explicit dependence on physical parameters is the capillary length R_{c}.

Since besides the N unknown quantities Q_i also the BC c_{u} has to be specified, one has to solve a linear system of equations of dimension $N+1$. Several choices for c_{u} are possible: (i) via the closure condition $\sum Q_i = Q_{\mathrm{ext}}$ (material conservation), where Q_{ext} is an external source strength, c_{u} is determined self-consistently; (ii) c_{u} can be defined directly. In case (ii) the choice $c_{\mathrm{u}} = c_\infty$ together with the linearized GT relation [Eq. (4.11)] allows to transform $R_{\mathrm{c}}/L_{\mathrm{ens}}$ into the time scale. Thus, in this special case, OR depends just on geometry $(\{\vec{r}_i\}, \{R_i\})$, whereas all physical constants only influence the time scale of coarsening. Note, that if not otherwise indicated, in simulations presented in this work the exact GT relation [Eq. (2.23)] has been used.

Usually, the generation of the initial ensemble is to a large extent arbitrary. The simulation input, the NC density and mean radius, are by definition average values and thus do not provide any specification of spatial correlation between precipitates. A reasonable setting algorithm [182] starts by randomly distributing non-overlapping spheres (halos) with a constant radius ($R_{\mathrm{halo}} > R_{\mathrm{max}}$) throughout the simulation volume, i.e. the unit cell. Then the NCs are placed into the centers of the halos and their radii are chosen statistically according to a predefined PRD. This procedure tries to mimic the nucleation of precipitates during IBS, since a new nucleus decreases the supersaturation of impurities in its vicinity and thus decreases the probability of a close second nucleus to come into existence.

With respect to the generation of the initial ensemble the transfer of K3DLMC simulation results to the rate-equation approach to OR seems to be a promising option [184] (see Chapter 6). Although there remains an ambiguity about the minimal NC size to be transferred, K3DLMC generated input data have the advantage, that they already characterize a coarsening system. If initial data have been chosen solely statistically, the artificial

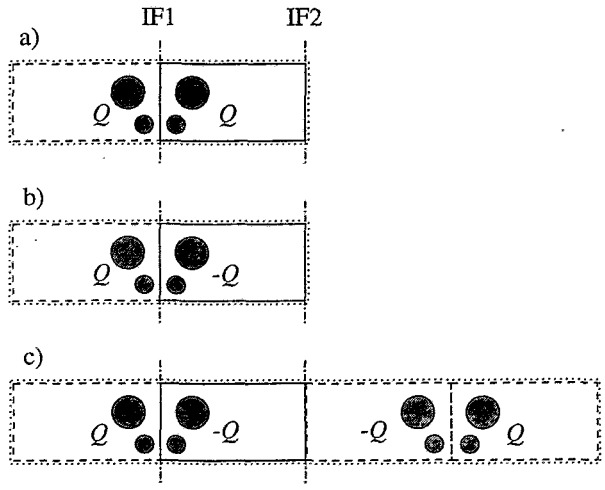

Figure 4.4: Construction of basic unit cell for EWALD summation for various BCs of interfaces IF1 and IF2. In (a) both interfaces are reflecting (i.e. prevent monomer flow out of the system), in (b) both interfaces are fixed to c_u, and in (c) IF1 is fixed to c_u, whereas IF2 is reflecting. In each figure, the solid box denotes the physical NC ensemble, the dashed boxes contain auxiliary ensembles and the dotted box is the resulting unit cell for 3D EWALD summation.

system will nevertheless evolve toward a state conform with the LSW or extended theories. This has been proven by CHEN *et al.* [162], who showed that for homogeneous systems the LSW distributions represent attractors in the space of all possible distributions. The more artificial the initial distribution the longer is the transient time this unphysical system needs to converge to the behavior of real systems. This may lead to bad statistics of the remaining independent precipitates. In the case of inhomogeneous systems, however, an unphysical choice of initial data may have a major influence on the evolution of coarsening precipitates (see also Section 6.2)

In OR simulations BCs deserve a closer investigation. For fundamental studies one wishes to use ensembles which are not distorted by boundary effects. Thus a natural choice are periodic BCs. As demonstrated earlier by other groups [39], EWALD'S summation method provides an analytical way to incorporate $1/r$ interactions between precipitates in spatially periodic unit cells. However, as already pointed out, the description of ion beam synthesized NCs requires the correct treatment of a heterogeneous NC distribution as well as absorbing and reflecting interfaces. For instance, in Si^+ implantation into a thin SiO_2 film on a flat Si substrate, the SiO_2/Si interface absorbs the Si monomer supersaturation in SiO_2, because the bulk Si maintains the solidus concentration c_∞ at the interface. On the other hand, if the implanted impurities do not segregate on the surface or are non-volatile, the surface prohibits any monomer flow out of the system and is thus equivalent to a reflecting interface. Both BCs can be achieved by the proper use of mirror sources (see Fig. 4.4). While the 2D EWALD summation with respect to a unit cell containing mirror

sources by REISS *et al.* [172] allowed them to describe one absorbing interface (analogous to Fig. 4.4b), they remarked, that the second interface has not been treated correctly. This shortcoming is circumvented simply by a full 3D extension of the appropriately extended simulation cell.

However, the EWALD summation method fails to treat $1/r^2$ interaction terms [Eq. (4.24)], which are present in the case $\alpha^\star \neq 0$. But considering the effective screening by surrounding precipitates [112], the actual range of influence of one NC is restricted and quantitatively described by the diffusional screening length λ_D [111] given by Eq. (3.18). Based on this property of the system, YUKAWA-like interaction terms among the precipitates can be applied, i.e. the expression for the source strengths [Eq. (4.24)] is modified according to the substitutions

$$\frac{1}{|\vec{r}_i - \vec{r}_j|^n} \longrightarrow \frac{\exp\{-|\vec{r}_i - \vec{r}_j|/l_{\mathrm{scr}}\}}{|\vec{r}_i - \vec{r}_j|^n}, \quad n = 1, 2. \tag{4.27}$$

Choosing for the YUKAWA screening length $l_{\mathrm{scr}} > \lambda_D$ this model gives in the diffusion controlled limit physically reasonable results comparable to results obtained by EWALD'S summation method (for a discussion, see Section 4.5). Additionally, it provides a method to incorporate higher order interactions. Since the interaction matrix is calculated once at the beginning of the simulation and because of the increase of $\lambda_D(t)$ during the ripening process,[1] the initial value for l_{scr} has to be chosen high enough to ensure $l_{\mathrm{scr}} > \lambda_D$ during the whole simulation. One shortcoming of this approach is the relative increase of damping during the simulation due to the increase of the average NC distance d. An improved, but computationally more extensive approach would be to keep the ratio d/l_{scr} fixed by subsequently updating the interaction matrix for an appropriately increased screening length.

In practice, only a finite number s of surrounding shells of unit cells can numerically be included to achieve quasi-3D periodic BCs. For the simulation results presented in the next section $s = 6$ has been used.

The simulation is discrete in time, i.e. at each time step Δt first the linear system of equations (4.24) extended by one equation fixing c_u is solved. Then the change in radius due to the actual value of the source strengths is evaluated with the help of a linear approximation of Eq. (4.26). With the new radii obtained the procedure is repeated. The time interval Δt can be chosen to some extent arbitrarily. However, it should be noted, that special care has to be taken not to violate material conservation. This situation easily arises, if an almost dissolved NC would lose in the next time interval more material than it contains. An effective solution is first to check all NCs which will dissolve, and in a second step to adjust their computed source strengths by their total remaining material content. For further details concerning second order corrections see [182].

[1] Combining Eqs. (3.18), (4.16) and (4.17) one obtains $\lambda_D(t) \propto t^{1/3}$ in the asymptotic limit.

4.5 Computer simulation of diffusion and reaction controlled Ostwald ripening

In this section the evolution of homogeneously distributed ensembles of NCs is simulated for various values of $\alpha^\star$. In particular, the parameter set $\alpha^\star = \{0, 1, 100\}$ is used to study the ripening regimes of pure diffusion control, intermediate mixed processes, and reaction control, respectively. Typical ensembles consist of up to several thousand precipitates located randomly in a cubic unit cell and periodic BCs are applied in three dimensions.

As a first check of the validity of YUKAWA-like screened interactions [Eq. (4.27)], simulations have been performed for $\alpha^\star = 0$. Starting with an ensemble described by the stationary PRD of the diffusion limited case [Eq. (4.15)] no deviations have been observed with respect to the evolution of the number of particles, $N(t)$, and the critical radius, $R^\star(t)$, as compared to numerical results using EWALD's summation method. In particular, the time dependences of the critical radius and the NC density are observed to be in accordance with the LSW predictions [Eqs. (4.16) and (4.17)]. However, the proportionality between these quantities and the time t depends on the choice of the screening length l_{scr}. This is illustrated for the evolution of $R^\star(t)$, where the relative difference to the analytical result is given by the coefficient γ

$$R^{\star\,3}(t) - R^{\star\,3}(t_0) = \gamma \frac{R^{\star\,3}(t_0)}{\tau_{\text{diff}}} t. \tag{4.28}$$

In the case $\alpha^\star = 0$ the results are shown in Table 4.1 for four different values of l_{scr} and EWALD's summation method. Due to finite volume effects mentioned above, in general the observed coarsening rates are larger than the value $\gamma = 1$ predicted by the LSW theory. This increase is systematic with decreasing l_{scr} and can be physically understood by noting, that the YUKAWA-like screening causes a damping of the mutual interactions.

The implication of reaction control, i.e. $\alpha^\star \neq 0$, on the ripening kinetics is pointed out for a simple 1D model system in Fig. 4.5. A plot of the scaled concentration field is shown for two precipitates with different radii in an effective field $c_{\text{u}} = 1.2 c_\infty$, e.g. generated by other clusters of an ensemble not visible in Fig. 4.5. For this pair of NCs the concentration field is evaluated using Eqs. (4.22) and (4.24) with arbitrary materials parameters. Obviously, the larger the value of $\alpha^\star$ the weaker is the gradient of the concentration field.

From the point of view of simulations, for a fixed diffusion coefficient D the higher the parameter $\alpha^\star$ is chosen, the slower will the evolution of the system takes place. This is

Table 4.1: Relative coarsening rate γ [see Eq. (4.28)] of precipitates during diffusion controlled ripening for four different ratios of the YUKAWA screening length l_{scr} [see Eq. (4.27)] to the system size L_{ens} and in the case of using EWALD's summation method (ESM).

$l_{\text{scr}}/L_{\text{ens}}$	0.25	0.5	1.0	1.5	ESM
γ	1.143	1.193	1.237	1.297	1.273

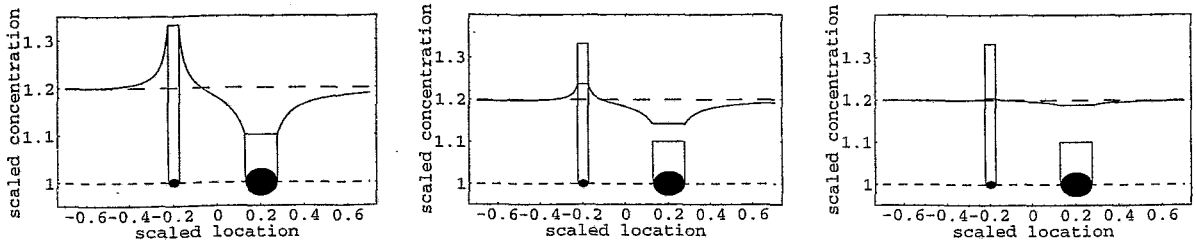

Figure 4.5: Scaled monomer concentration field of two interacting NCs embedded in a global field $c_u = 1.2\,c_\infty$ for three different degrees of diffusion and reaction control. From left to right, the NC pairs are characterized by $\alpha^\star = \{0, 1, 10\}$. The equilibrium concentrations c^{GT} are indicated by the corresponding columns.

based on the fact that individual IAs have to overcome a finite reaction barrier, which obviously hinders their redistribution. This effect is clearly seen in Eq. (4.24), because for high values of $\alpha^\star$ the source strengths are roughly proportional to $1/\alpha^\star$.

In order to compare systems characterized by different values of $\alpha^\star$ it is useful to scale the ripening time by a time constant $\tau(\alpha^\star)$. Since analytical expressions for characteristic ripening times [Eqs. (4.16) and (4.19)] are only known in the LSW limits [105], a reciprocal interpolation should serve as a reasonable approximation for the intermediate range

$$\tau = \frac{8}{9}\left(\frac{R_0^\star}{\bar{R}_0}\right)^3 \left[\alpha_0^\star + \frac{9}{8}\left(\frac{\bar{R}_0}{R_0^\star}\right)^3\right] \tau_{\text{diff}}. \tag{4.29}$$

Thus for $\alpha^\star \gg 1$ the ripening time scale is proportional to $\alpha^\star \tau_{\text{diff}}$, which implies that an ensemble characterized by $\alpha^\star = 100$ ripens approximately 100 times slower in real time than it would in the diffusion controlled regime.

The dependence of the evolution of homogeneous ensembles of precipitates on the degree of diffusion and reaction control is shown in Fig. 4.6. In each of six runs of a series of simulations the coarsening of $N = 3600$ nanoclusters has been studied, where their initial PRDs obeyed the stationary PRD of the diffusion limited case. The volume fraction of the precipitated material is $\eta = 0.076$, with a mean radius $\bar{R}_0 = 11.5\,\text{nm}$ at $t = 0$. In the logarithmic plot of Fig. 4.6a the averaged remaining number of ripening precipitates is shown in the cases $\alpha^\star = \{0, 1, 100\}$. In the case $\alpha^\star = 0$, i.e. pure diffusion controlled ripening, $N(t)$ tends to be proportional to $1/t$ as predicted by the LSW theory. The ensembles characterized by $\alpha^\star = 1$ and $\alpha^\star = 100$, respectively, exhibit a stronger time dependence. In particular, in the limit $\alpha^\star \to \infty$, coarsening systems are found to have a time dependence $N(t) \propto 1/t^{3/2}$. The evolution of the critical radius is pointed out in Fig. 4.6b. Depending on $\alpha^\star$, the time dependence for $t \gg \tau$ for $R^\star(t)$ lies in between the two asymptotic results $R^\star(t) \propto t^{1/3}$ for diffusion limited coarsening and $R^\star(t) \propto t^{1/2}$ for the reaction limited process, respectively.

The differences in the ripening behavior for the three ensembles are also visible in their PRDs. In the case $\alpha^\star = 0$, the PRD does not change its scaled shape during the

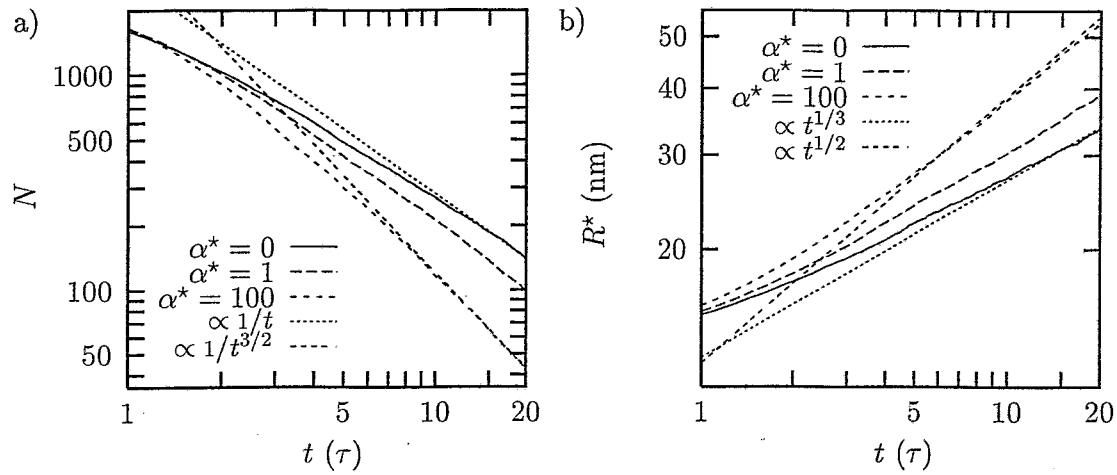

Figure 4.6: Time dependence of the number of coarsening particles (a) and the critical radius (b) in the time interval $\tau \leq t \leq 20\tau$ for the three ensembles discussed in the text. For comparison, the corresponding analytically derived results (Section 4.2.2) for the two limiting cases of diffusion and reaction controlled ripening are plotted as well.

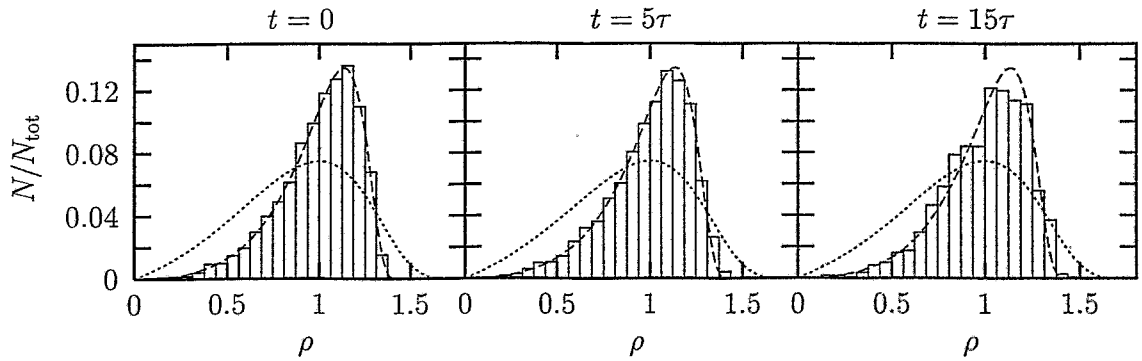

Figure 4.7: Evolution of the PRD in the case of diffusion controlled OR ($\alpha^* = 0$). Here, the normalized number of NCs belonging to a size interval is plotted versus the normalized radius $\rho = R/R^*$. For comparison the two stationary PRDs of the LSW theory are included (dashed: diffusion control, dotted: reaction control).

simulation in accordance with the LSW theory. This can be seen in Fig. 4.7, where for comparison also the analytically derived LSW distributions [Eqs. (4.15) and (4.18)] are shown. As expected, the shape of the PRD starts to deviate from this specific initial choice for systems having a non zero degree of reaction control. This is visible in Fig. 4.8, where the evolution of the PRD in the case $\alpha^* = 1$ is shown. With increasing reaction control, the simulated distribution becomes broader and less peaked than in the pure diffusion limited case. Especially the fraction of NCs with $\rho < 1$ starts to increase with respect to the PRD of the diffusion limited case. This behavior is not predicted by Eq. (4.21). Moreover, the

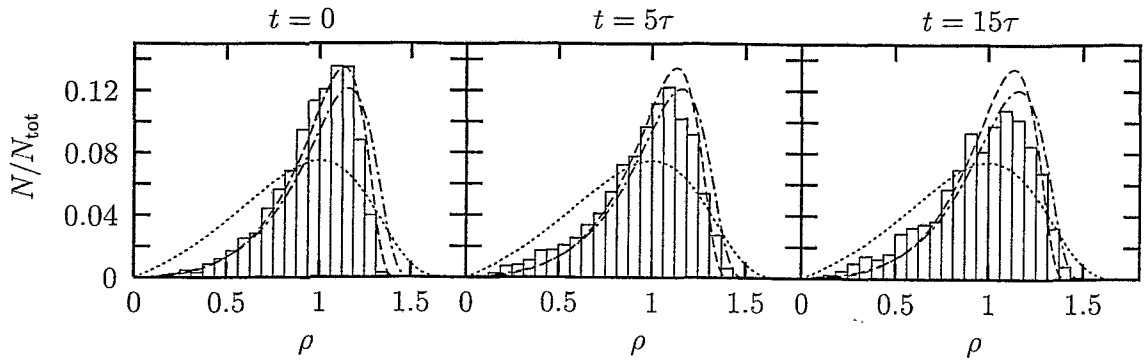

Figure 4.8: Evolution of the PRD for competing influences of diffusion and reaction controlled OR ($\alpha^\star = 1$). Additionally to the stationary PRDs of the LSW theory (dashed: diffusion control, dotted: reaction control), the PRD for $\alpha^\star = 1$ according to Eq. (4.21) is plotted (dashed-dotted line).

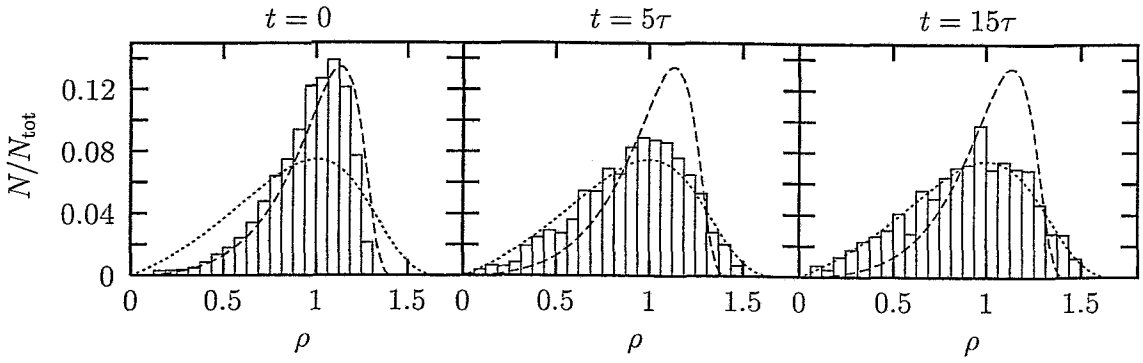

Figure 4.9: Evolution of the PRD in the case of (basically) reaction controlled OR ($\alpha^\star = 100$).

scaled maximum size of the precipitates increases, as may be seen more clearly in Fig. 4.9, where coarsening is shown for $\alpha^\star = 100$. Obviously, in the limit $\alpha^\star \to \infty$, the PRD is found to match the stationary PRD of the reaction controlled limit derived by WAGNER [105].

The coarsening of precipitates can also be monitored with respect to the evolution of the width ω of the PRD defined as

$$\omega(t) = \sqrt{\left\langle (R/\bar{R}(t) - 1)^2 \right\rangle}. \tag{4.30}$$

The time behavior of ω can be seen in Fig. 4.10 for three values of $\alpha^\star$. After a coarsening duration of a few time constants $\tau(\alpha^\star)$, also systems being initially in an artificial state reach a stationary OR stage. This observation is in accordance to findings of CHEN *et al.* with respect to attractor states in the space of size distributions [162]. However, as already indicated in Fig. 4.8, the simulated PRD for $\alpha^\star = 1$ is significantly broader as compared

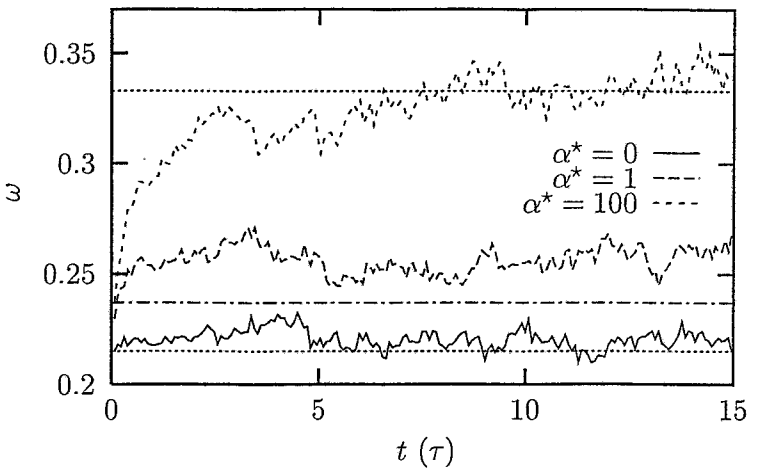

Figure 4.10: Averaged widths ω of the PRDs for a set of ensembles characterized by $\alpha^\star = \{0, 1, 100\}$, which possess initially the LSW size distribution of diffusion control. The two dotted lines denote the analytic results for the stationary PRDs of the diffusion and reaction controlled limit of the LSW theory, which read $\omega_{\text{diff}} = 0.215$ and $\omega_{\text{reac}} = 0.333$, respectively. The dashed-dotted line is obtained from the analytic form of the intermediate PRD [Eq. (4.21)].

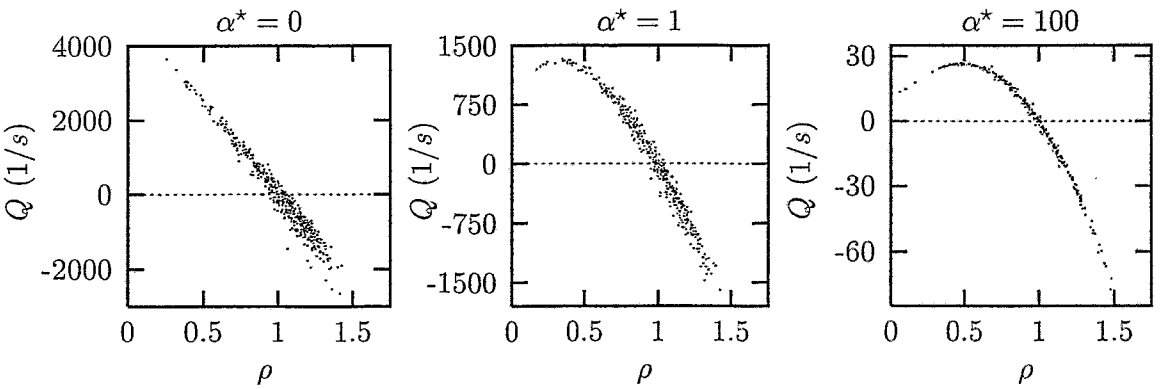

Figure 4.11: Source strengths Q_i of precipitates plotted versus the scaled radius $\rho = R/R^\star$ for the set of NC ensembles characterized by $\alpha^\star = \{0, 1, 100\}$ after coarsening for a time $t = 5\tau$. Note that positive source strengths belong to shrinking, whereas negative ones belong to growing precipitates.

to the prediction of WHITE [180].

Additional insight into the physics of OR is gained by plotting the source strengths Q_i versus the scaled radius $\rho(t) = R/R^\star(t)$ for the three characteristic ensembles of coarsening precipitates (see Fig. 4.11). While in a global mean-field theory the source strengths have to lie on a single curve, the scattered data for particular cluster sizes reveal the local

interaction character of the simulation approach. The concentration field at the site of a precipitate depends considerably on the specific configuration of neighboring precipitates. As can be seen in Fig. 4.11 the effect of mutual interactions due to overlapping diffusion fields decreases with increasing degree of interface controlled OR. This can be understood due to the weaker concentration gradients between neighboring NCs of different sizes, since for basically reaction controlled OR the detailed nearest-neighbor configuration tend to be smeared out by the fast diffusion.

Another interesting point is the size of the NC characterized by the largest source strength. In the diffusion controlled limit there is a linear dependence of the source strength with respect to the NC size. Thus precipitates about to vanish have the largest detachment rate. However, if reaction control becomes important, intermediate shrinking precipitates show a larger dissolution potential than very small ones. Within the global mean-field approximation the maximum source strength $Q_{\max}$ can be determined by combining Eqs. (4.12) and (4.26), taking the derivative with respect to ρ, and solving the equation $\rho^2 + 2\alpha^\star\rho - \alpha^\star = 0$, from which follows

$$Q_{\max} = 4\pi D c_\infty R_c \left(1 + 2\alpha^\star - 2\sqrt{\alpha^\star(\alpha^\star+1)}\right) \quad \text{for} \quad \rho = \sqrt{\alpha^\star(\alpha^\star+1)} - \alpha^\star. \quad (4.31)$$

In the reaction controlled limit, i.e. $\alpha^\star \to \infty$, NCs of half the critical size have the largest monomer detachment rate, which, in turn, tends to zero.

The fact, that within this local mean-field description for finite $\alpha^\star$ the maximum dissolution rate is associated with a finite precipitate size, interesting consequences arise with respect to the validity of Eq. (4.21). The deceleration of dissolution of NCs being smaller than the size corresponding to $Q_{\max}$ causes them to remain slightly longer alive. Thus the consequence of this small retardation of dissolution should be a tendency of accumulation of small NCs. This, in turn, explains the relative abundance of small NCs in the simulated PRD with respect to the PRD of the diffusion controlled limit of the LSW theory and is in clear contrast to the prediction of Eq. (4.21). Thus it can be concluded, that the approximations made by WHITE [180] for $\alpha^\star \lesssim 5$ deserve a closer inspection.

All of the results presented above have been obtained on the assumption, that the reaction rate k does not depend on size. However, it is reasonable to assume, that the monomer flux through the precipitate/matrix phase boundary is a function of the local curvature. A more detailed study of these effects remains to be given in future approaches.

Essentially all experimental data for aging of second-phase particles are in accordance with the time dependence of diffusion limited OR [185, 161]. Good candidates for the observation of reaction controlled coarsening are solid-solid systems, which possess incoherent phase boundaries and/or very high diffusion coefficients for impurity monomer diffusion.

Recently, evidence has been reported for 2D ripening of 3D self-assembled quantum dots located on a substrate according to the reaction controlled limit [186]. In this experiment the density of CdSe quantum dots grown on ZnSe showed a time dependence of $n(t) \propto t^{-1}$ rather than $n(t) \propto t^{-3/4}$ as would be expected for ripening in the diffusion controlled regime for this geometry [30].

Chapter 5

Nanocluster formation and evolution during high-dose ion implantation

The formation of second-phase domains in systems transferred to the thermodynamically metastable region of the phase diagram is usually described by classical nucleation theory (see Section 2.3). As pointed out earlier, the application of this standard theory to IBS is not straightforward, because in this process precipitation is due to a depth- and time-dependent supersaturated solid solution of IAs. Furthermore, for nucleation occurring during implantation, a correct treatment should take into account the effects of CM, not to mention the influence of radiation damage, e.g. the depth-dependent interaction of IAs with point defects and defect clusters. This Chapter first presents K3DLMC results of simplified (neglecting CM) simulations of NC formation at constant and varying implantation conditions and discusses corresponding experiments for the Au-SiO_2 system [187]. Then, in the last section, the effect of CM on the state of a single NC is described and consequences of CM on the evolution of NC ensembles are pointed out.

5.1 Nucleation and growth of NCs at constant implantation conditions

General considerations

The basic physical stages of IBS briefly introduced at the beginning of Chapter 2 can easily be identified in K3DLMC simulations. Fig. 5.1 presents results of a model simulation of a finite homogeneous system, where monomers have been added at a constant (volume) deposition rate up to a total dose of F_0. For constant (implantation) parameters the evolution of the system is governed by:

Accumulation/Saturation (I): Immediately after the start of ion deposition, the first IAs can be found as (dissolved) monomers. Depending mainly on the substrate temperature, the implanted atoms either remain "frozen" in their final position, or they may diffuse through the substrate. Initially, the concentration of monomers

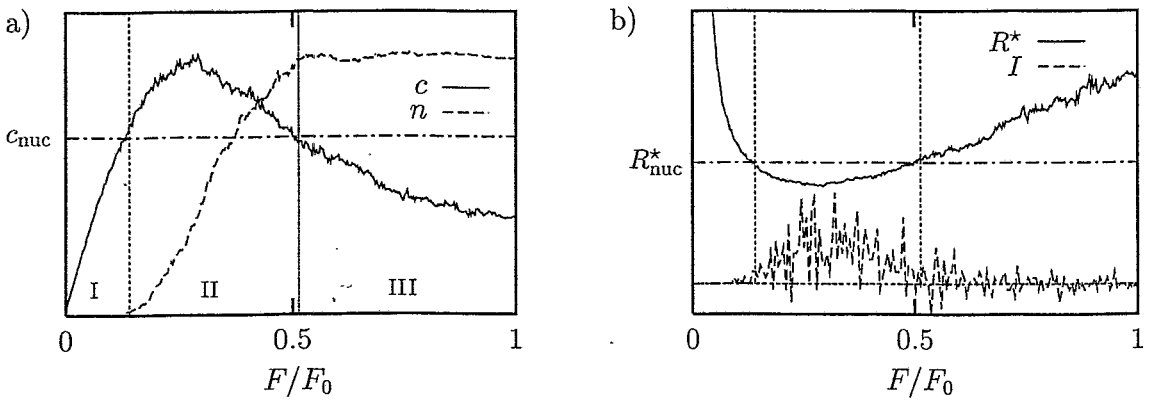

Figure 5.1: K3DLMC simulation of homogeneous phase transformation indicating the physical regimes of accumulation/saturation (I), nucleation (II), and growth (III). In a) the evolution of the monomer concentration c and the NC density n is shown. The effective concentration threshold for nucleation c_{nuc} is indicated for clarity. In b) the (discrete) nucleation rate I is directly compared to the critical radius $R^\star$ given by the inverse GT relation [Eq. (4.10)].

c increases linearly with time (or, equivalently, with fluence F). In the case of sufficient impurity mobility, as c increases further and reaches the solubility threshold (saturation is given by $\delta\mu = 0$), small agglomerations of IAs (i.e. dimers, trimers, ...) start to form by thermal fluctuations. The appearance of these subcritical nuclei slows down the increase of c.

Supersaturation/Nucleation (II): Supersaturation sets in, when c exceeds the solubility limit (i.e. $\delta\mu > 0$). By thermal fluctuations some subcritical nuclei start to grow beyond the critical size $i^\star$ forming stable precipitates. At later times, these supercritical precipitates act as sinks for diffusing monomers, which reduces the volume available for nucleation [70]. Despite the continuing deposition of IAs c starts to decrease, thus eventually dropping below the threshold for nucleation. Further NC formation becomes very unlikely.

Growth (III): No additional NCs are formed and the existing ones grow by attachments of newly implanted IAs rather than competitive ripening. Hence, the density of precipitates essentially remains constant, while the concentration of monomers further decreases.

In Fig. 5.1b the nucleation rate I is given by the derivative of the NC density n with respect to the implanted fluence, which is proportional to t (the discrete implementation $I = \Delta n/\Delta F$ of the results of this single run for a finite system explains the observed oscillations of the nucleation rate).

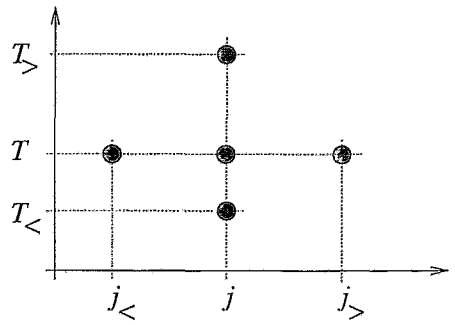

Figure 5.2: Scheme of parameter range of ion flux and implantation temperature of K3DLMC study of NC formation during ion implantation.

The appearance of the three stages relative to the implanted fluence depends on the implantation parameters and the materials constants. For instance, for very low fluences the monomer concentration might completely remain below the nucleation threshold. For very low T_{imp} the monomer mobility might be negligible, thus, although a considerable degree of supersaturation might have been reached, nucleation is essentially retarded to a subsequent heat treatment. Furthermore, due to the depth-dependent deposition profile, the above described sequence of stages sets in first around R_{p} and shifts later on gradually to the tails.

Simulation of NC formation during implantation

In order to understand the evolution of NCs during implantation, the dependence of the (depth-dependent) size distribution on the main implantation parameters, i.e. the implantation temperature T_{imp} and the ion current j, was studied qualitatively for a fixed ion energy E (see Fig. 5.2). In a series of simulations for a fixed ion fluence $F_0 \approx 30\, a_{\mathrm{fcc}}^{-2}$ (in the case of Co implantation into c-Si, this would correspond to a fluence of $F_0 \approx 10^{16}\,\mathrm{cm}^{-2}$), the NC formation was studied at three different implantation temperatures $\{T_<, T, T_>\}$ for a fixed ion flux j and at three different ion fluxes $\{j_<, j, j_>\}$ for a fixed T_{imp}. The three ion currents $\{j_<, j, j_>\}$ differed one another by one order of magnitude, whereas the implantation temperatures were chosen according to the K3DLMC parameters $\epsilon_{\mathrm{fcc}} = \{2, 3, 4\}$.

Here a few comments should be made concerning the corresponding physical values of the simulation parameters chosen for this general study. The ion current in the case of the reference parameter pair was $j_{(T,j)} = 2.44 \times 10^{-4}\, a_{\mathrm{fcc}}^{-2} \tau^{-1}$. Since the physical time scale of a MCS is temperature-dependent [see Eq. (3.12)], simulations for constant j at different T have to be specified with respect to a particular value of the activation energy for diffusion E_{A}. Taking for this study (the arbitrarily chosen, but typical values) $E_{\mathrm{A}} = 0.5\,\mathrm{eV}$ and $E_{\mathrm{S}} = 1.5\,\mathrm{eV}$, the simulation currents are related approximately by (in units of $a_{\mathrm{fcc}}^{-2}\tau^{-1}$): $j_{(T_<,j)} : j_{(T,j)} : j_{(T_>,j)} = 7 : 1 : (1/7)$. It should be noted, that the higher E_{A} the higher are the ratios of the simulation currents normalized with respect to a MCS. The corresponding physical ion currents, however, depend still on the preexponential D_0 of the diffusion

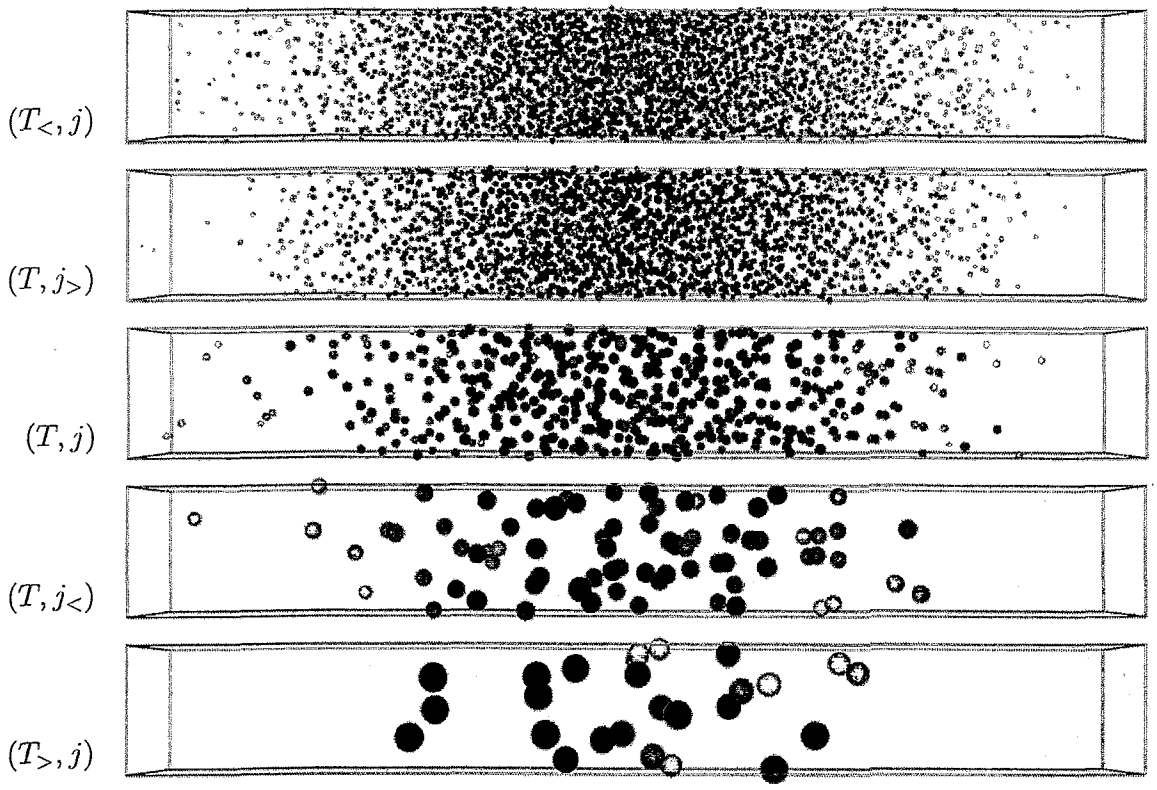

Figure 5.3: K3DLMC simulation results of NC formation during implantation as recorded immediately at the end of ion deposition. All NCs are represented as spheres (see Fig. 3.4) and the blue (grey) scale is chosen according to their size (within each figure the blue (grey) scale increases with size).

constant.

In a simulation volume of size $64 \times 64 \times 512$ fcc unit cells (about 1.7×10^7 lattice sites) IAs have been deposited symmetrically according to a Gaussian with $R_\mathrm{p} = 256\, a_\mathrm{fcc}$ and $\Delta R_\mathrm{p} = 75\, a_\mathrm{fcc}$. For this particular series of simulations reflecting BCs have been applied at $z = 0$, whereas the opposite boundary acts as an absorbing interface.[1] However, as the results to be presented will indicate, this specific choice of BCs has no pronounced influence on the nucleation results due to diffusional screening effects and the restricted diffusion length during implantation (it will be shown in Section 6.2, however, that BCs do have an influence during long time annealing.). In this simulation series CM was not included.

For the five parameter pairs $\{(T_<, j), (T, j_>), (T, j), (T, j_<), (T_>, j)\}$ Fig. 5.3 shows the corresponding NC distributions. Increasing the implantation temperature or decreasing the

[1] For non-periodic BCs in the z direction used in this work, positive depths point to the right.

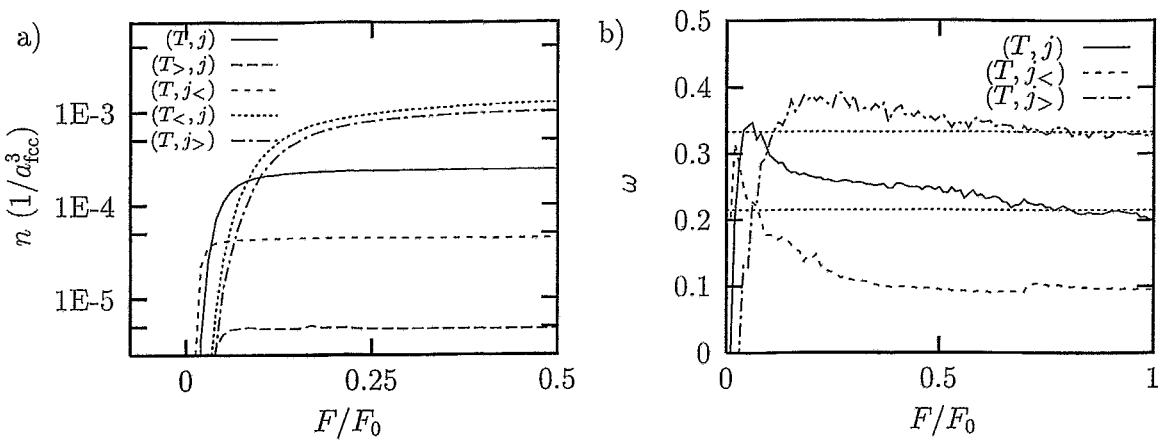

Figure 5.4: In a) the evolution of the NC densities (normalized with respect to the simulation volume) for the five parameter pairs is shown. In b) the evolution of the widths ω of the PRDs is plotted. Here, the widths of the LSW distributions (see Fig. 4.10) have been added for comparison.

ion flux with respect to the reference parameter pair results in similar NC distributions. This observation is also reflected in Fig. 5.4a, where the evolution of the NC density in the first half of the respective implantations is shown. The evolution of the width ω [see Eq. (4.30)] referring to three parameter pairs can be seen in Fig. 5.4b.

Experimental observations and discussion

The IBS of Au nanoclusters in SiO_2 is well-suited for fundamental precipitation studies, because (i) Au does not tend to form an oxide or silicide [188] (Au atoms are chemically inert with respect to the constituents of the host material), (ii) Au is observed to precipitate during the implantation stage, and (iii) no collective shift of the implanted IAs influences the NC formation.[2] The temperature dependence of Au nanocrystal formation in fused silica can be seen in Fig. 5.5. Here, Au NC distributions recorded immediately after 2.75 MeV Au^+ implantations (projected range about 0.9 μm) at current densities of approximately 1 $\mu A/cm^2$ are shown. The K3DLMC simulations for a fixed ion current presented in Fig. 5.3 reproduce these observations. This qualitative dependence of the NC distribution on T_{imp} has been reported also for other NC/substrate systems [189]. For a fixed T_{imp} the increase of the NC density with increasing ion current has been observed, for instance, in the case of Co implantation into Si [106].

Both simulated and experimentally observed NC distributions can be understood in terms of the classical nucleation theory presented in Section 2.3 (neglecting for a moment inhomogeneities due to the implantation profile). However, in contrast to standard studies

[2]For instance in the case of Ag implantation into fused silica at elevated temperatures, a net movement of the IAs towards the surface has been observed [6].

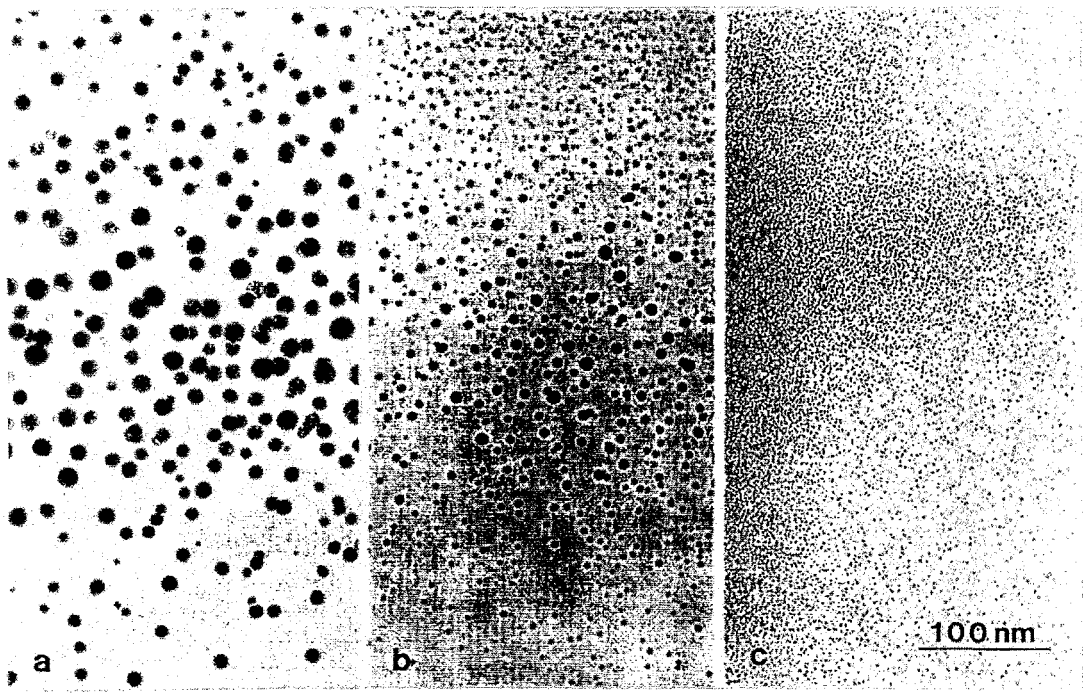

Figure 5.5: Cross-section TEM micrographs of 2.75 MeV Au^+ implantation into fused silica for a fluence of 1.5×10^{17} cm^{-2} (from Ref. [187]). Figs. a) – c) refer to implantation temperatures of 600 °C, 400 °C and room temperature, respectively.

of nucleation phenomena starting with a particular supersaturation level, here in addition the dynamical concentration increase has to be considered.

Constant implantation current: *Given* a specific supersaturation $\delta\mu$, Eqs. (2.7) and (2.10) state, that the nucleation probability increases with increasing temperature (BOLTZMANN-factor). Therefore, the decay velocity of a supersaturated state also increases with increasing temperature (transient effects). While for a fixed implantation current the supersaturation increase is temperature-independent, the decay of the metastable state into precipitates *does* depend on T_{imp}. Thus an increased thermal activity leads for high T_{imp} to nucleation on a lower supersaturation scale, with a correspondingly larger critical NC size.

After growing beyond the critical size, a NC acts as permanent sink for diffusing monomers, thus decreasing the monomer concentration in its vicinity. The ratio of the deposition to diffusion rate then determines the range of the effective depletion zone around each NC, where the nucleation of an additional precipitate is unlikely. Since both the critical size of nucleation increases and diffusion becomes more effective with increasing temperature, less stable NCs will be formed, onto which the subsequently implanted impurities condense (see Figs. 5.3 and 5.5).

Constant implantation temperature: For a given T_{imp} it is obvious, that supersaturation increases more slowly as j decreases. This implies, that the systems remains the longer at a specific supersaturation level the lower the ion flux is (for constant temperature the time lag of nucleation depends on $\delta\mu$). Thus on the average larger NCs are nucleated for low j than for high j.

The corresponding ratio of deposition to diffusion defines again the range of the depletion zone around a successful precipitation. Since here the size of the depletion zone, where no additional nucleation is expected, is proportional to $1/j$, the smallest NC density is observed for the lowest ion current (see Fig. 5.3).

As Fig. 5.4a indicates, the NC density essentially remains constant after the end of the nucleation stage. During the ongoing implantation all NC can be expected to grow approximately at the same rate, because both the deposition and NC density distributions are similar (Gaussian-like). This is reflected in the evolution of the widths of the PRDs shown in Fig. 5.4b, which tend to decrease during the growth stage.

From the viewpoint of homogeneous nucleation similar NC size distributions can be obtained either by increasing the implantation temperature or by decreasing the ion flux (or vice versa) (see Fig. 5.3 and also Fig. 5.6 below). This behavior suggests, that the mean NC size can be described according to a function $f(G/D(T))$, where D is the (strongly temperature-dependent) diffusion coefficient and G the generation rate of IAs per unit volume, which is proportional to j. No unique form of f could be deduced from the K3DLMC results, which might be related to the depth-dependence of G.

The ratio G/D also explains the observed vertical spread of the nucleation region. A small deposition to diffusion ratio prevents a significant increase of the impurity concentration in the very tails of the implantation profile. In this case the nucleation region lies close to R_{p} (compare microstructures in the cases $(T_<, j)$ and $(T_>, j)$ of Fig. 5.3).

5.2 Nucleation and growth of NCs at varying implantation conditions

Simulation of NC formation at varying implantation conditions

Most studies of IBS of NCs reported so far have been conducted for constant implantation parameters (excluding here multi-energy implantations). Therefore, K3DLMC studies have been performed in order to give predictions of NC distributions to be expected for a controlled variation of parameters *during* implantation. Fig. 5.6 shows simulation results, where one parameter (either T_{imp} or j) has been (instantaneously) changed for the second half of the implantation. The results for the changes $(T_<, j) \rightarrow (T, j)$, $(T, j) \rightarrow (T_<, j)$, $(T, j_>) \rightarrow (T, j)$, and $(T, j) \leftrightarrow (T, j_>)$ not shown here yield qualitatively similar results with respect to the direction of the parameter variation. Fig. 5.7 shows the NC density evolution during implantation and relates the observed bimodal PRDs to the onset of a second nucleation stage after an appropriate parameter change.

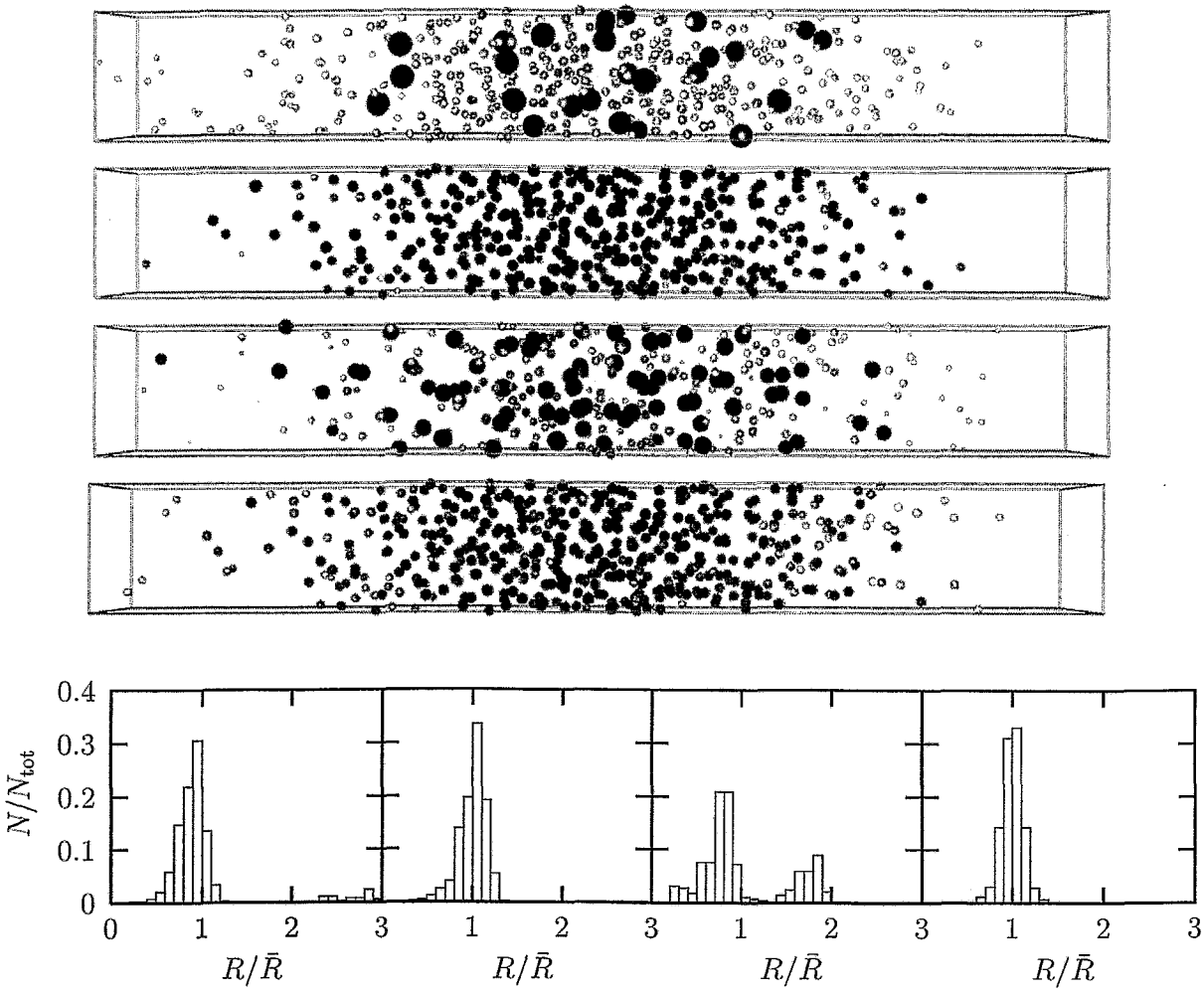

Figure 5.6: K3DLMC simulations of NC formation for the following changes of parameters at $F = F_0/2$ (from top to bottom): $(T_>, j) \rightarrow (T, j)$, $(T, j) \rightarrow (T_>, j)$, $(T, j_<) \rightarrow (T, j)$, and $(T, j) \rightarrow (T, j_<)$. All NCs are represented as spheres (see Fig. 3.4). The corresponding NC size distributions are shown from left to right in the lower row.

The predicted bimodal PRD (for the implantation sequences $(T_>, j) \rightarrow (T, j)$ and $(T, j_<) \rightarrow (T, j)$, respectively) has not previously been observed. Therefore, a set of experiments was conducted to verify these results.

Experimental observations and discussion

The TEM micrographs of Fig. 5.8 show the effect of changing T_{imp} during Au^+ implantation into SiO_2. Clearly, the size distribution depends on the sequence of the temperature change. A rather broad PRD (possibly the overlap of two individual distributions as suggested by

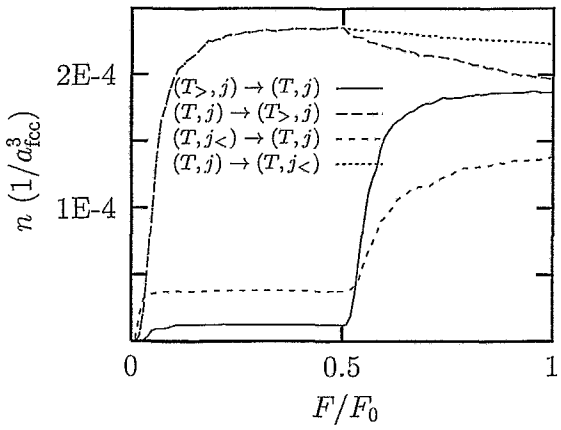

Figure 5.7: Evolution of the NC densities for a parameter variation during implantation.

the simulation results of Fig. 5.6) is obtained by decreasing T_{imp} in the second implantation period. The change in size distribution due to a significant change in j has not been measured in this experiment.

Like in Section 5.1 the simulation results of Fig. 5.6 can be explained in terms of classical nucleation theory. For a given monomer concentration c the transition to a lower temperature increases the effective supersaturation $\delta\mu$, which, in turn, corresponds to a smaller critical radius R^* [Eq. (2.10)]. Furthermore, due to the larger ratio G/D, the effective monomer flux to the NCs is reduced, which causes an increase in c. Thus c might now again exceed the nucleation threshold and a second generation of NCs can form leading to a bimodal size distribution. On the other hand, by increasing T_{imp} during implantation, a narrow PRD is observed with very tiny NCs missing. A reasonable explanation for this behavior is the corresponding shift of R^* (the higher temperature increases the monomer flux to the NCs, thus c decreases), which can be so large, that previously formed NCs are now smaller than the critical size and thus dissolve.

Variations in the ion current j cause changes in the ratio G/D opposite to the respective temperature changes. Like in Section 5.1 increasing (decreasing) j during implantation results qualitatively in the same microstructure as decreasing (increasing) T_{imp}.

Considerable changes of the implantation parameters can lead to even more dramatic effects. For instance, if a Au^+ implantation into SiO_2 at 600°C is followed by a second implantation at room temperature, no large Au precipitates, which have been certainly formed in the first part of the experiment (see also Fig. 5.5a), can be detected [150]. Rather, the resulting NC size distribution resembles the distribution obtained by the experiment, where the complete fluence was implanted at room temperature (see also Fig. 5.5c). Therefore it can be concluded, that in the experiment shown in Fig. 5.8a the previously formed NCs probably decreased in size by ballistic losses during the second implantation step concurrently with the development of new NCs precipitating from the supersaturation. Thus CM, which will be discussed in the next Section, might prevent the

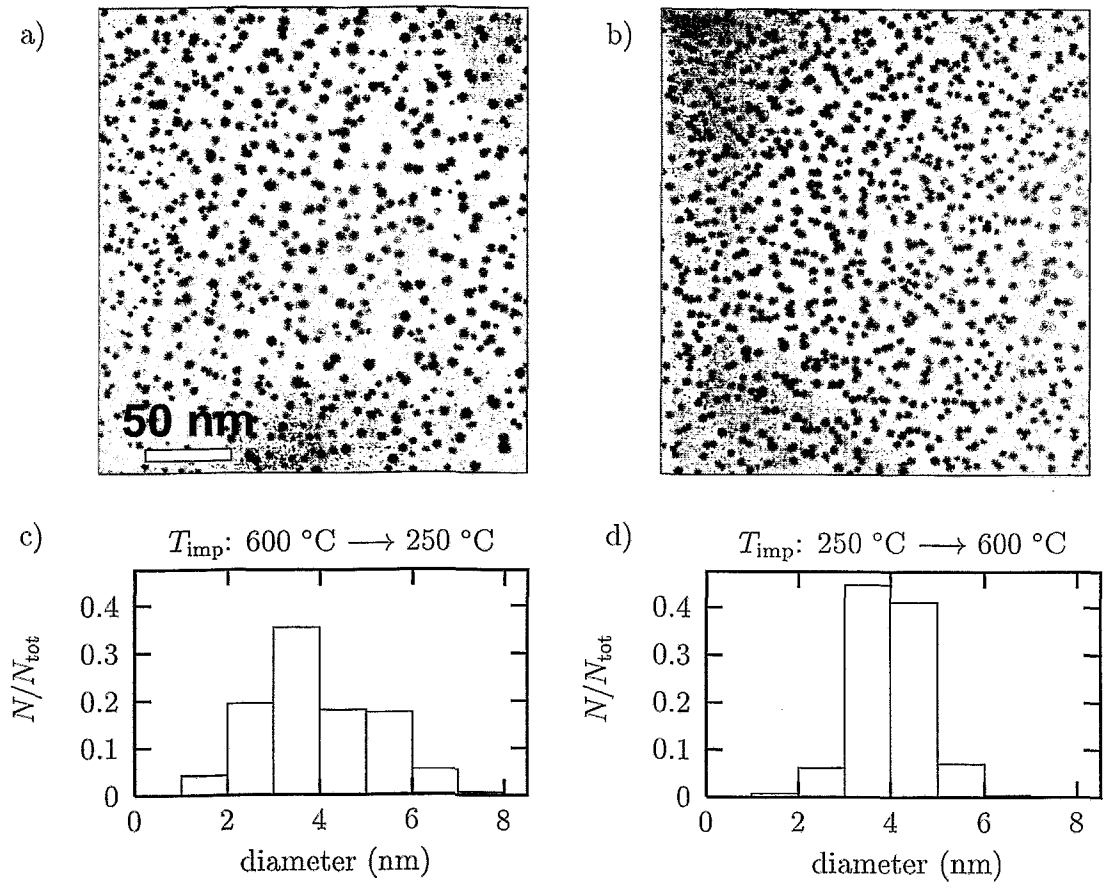

Figure 5.8: TEM micrographs for 2.75 MeV Au^+ implantation into SiO_2: a) 3×10^{16} cm^{-2} at 600 °C + 3×10^{16} cm^{-2} at 250 °C, b) 3×10^{16} cm^{-2} at 250 °C + 3×10^{16} cm^{-2} at 600 °C (from Ref. [187]). The corresponding size distributions are shown in Figs. c) and d).

formation of a clearly separated double-peaked PRD.

5.3 On the influence of collisional mixing

For systems, where NCs are forming during implantation, the continuous ion bombardment not only causes damage to the substrate, but also interacts with previously formed precipitates. For each impact in a NC by a decelerating ion or an associated recoil, IAs may be knocked out and deposited in the surrounding matrix according to a distribution function. This has not been taken into account in the simplified procedure of ion deposition used for the simulations described in the previous two sections. A promising approach to describe irradiation influences on the NC evolution is the concept of CM briefly introduced in Section 3.6.

5.3.1 Collisional mixing of a single nanocluster

K3DLMC simulation and results

In order to obtain a qualitative understanding of the effect of CM, in a series of simulations similar to the determination of the GT relation in the pure thermal case (see Section 3.5.3), the steady-state monomer concentration c as a function of NC size is studied in the presence of temperature-independent ballistic jumps.[3] For this isothermal series of simulations (for $\epsilon_{\mathrm{fcc}} = 1.75$) the mixing length λ (an isotropic displacement distribution $\propto \exp\{-r/\lambda\}$ is assumed; see also Section 3.6) as well as the number Ω of displacement attempts per IA per MCS is varied. In the following, Ω will be given in units of $[\tau^{-1}]$, where τ denotes the duration of one MCS [see Eq. (3.12)]. Regardless of the chosen value of λ, due to the lattice nature of the model the smallest possible discrete displacement $r_{if} = |\vec{r}_i - \vec{r}_f|$ is given by $r_0 = (\sqrt{2}/2)\, a_{\mathrm{fcc}}$ (i.e. a nearest-neighbor displacement) in the case of a fcc lattice. Since the continuously chosen displacement length is projected onto the lattice,[4] the minimum radial distance of a successful jump attempt is $r_{\mathrm{m}} = 0.35\, a_{\mathrm{fcc}} \approx \sqrt{0.25^2 + 0.25^2 + 0^2}\, a_{\mathrm{fcc}}$ causing a nearest-neighbor displacement of length r_0.

Within the K3DLMC method the length of a displacement is determined by $r = -\lambda \ln w$, $w \in [w_0, 1]$, where the cut-off parameter w_0 corresponds to a maximum distance of a ballistic jump. For the simulations to be presented in this Section the (arbitrarily chosen) cut-off value $w_0 = 10^{-6}$ has been used. Therefore, the probability of a discrete displacement of length r_{if} is given by

$$P = \begin{cases} 0 & , \quad r < r_{\mathrm{m}} \\ \Omega \mathcal{P}(r \to r_{if})(1 - C_f) & , \quad r \geq r_{\mathrm{m}}, \end{cases} \tag{5.1}$$

where the projection operator $\mathcal{P}$ determines the final lattice site $\vec{r}_f$. The last factor in Eq. (5.1) takes into account that a displacement to an occupied lattice site (i.e. $C_f = 1$) is not performed. In the case of a fcc lattice Fig. 5.9 shows the normalized displacement distributions for three mixing lengths. In general, the assumed exponentially decaying displacement distribution for jump attempts will differ from the (continuous) distribution of performed jumps, which cause discrete displacements within the K3DLMC model.

Fig. 5.10 shows the dependence of the steady-state monomer concentration on the NC size for various mixing lengths and mixing intensities. Obviously, also in the presence of competing dynamics a GT-like behavior [see Eq. (2.23)] is observed

$$c^{(\mathrm{CM})}(R) = c_{\infty}^{(\mathrm{CM})} \exp\left\{ \frac{R_{\mathrm{c}}^{(\mathrm{CM})}}{R} \right\}. \tag{5.2}$$

[3]Note, that in this study for each simulation the number of IAs within the simulation volume is kept constant. This corresponds to irradiating a NC consisting of impurities of type A with ions of type B.

[4]The final lattice site of a displacement attempt is determined by the coordinate transformation $\vec{r}_f(r, \theta, \phi) \to \vec{r}_f(x, y, z)$ and subsequent rounding to the next nearest integers, i.e. projection onto the next nearest lattice site. If $\vec{r}_f$ belongs to the shifted second fcc lattice (see Fig. 3.1), this jump attempt is discarded and, retaining r, a new pair (θ, ϕ) is chosen.

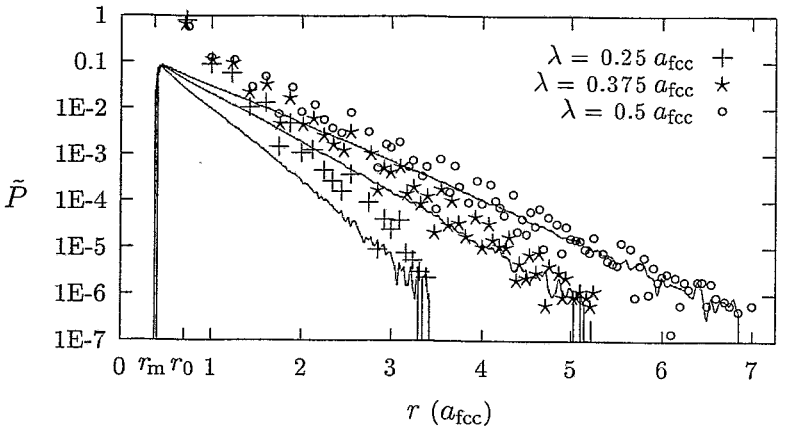

Figure 5.9: For three values of λ the normalized radial distributions $\tilde{P}$ of discrete displacements are plotted for CM simulations of a single NC of radius $R \approx 4.75\, a_{fcc}$. The underlying continuously chosen displacement distances ($r \geq r_m$) of these successful ballistic jumps have been included (solid lines). Furthermore, the distance r_0 of a nearest-neighbor jump is indicated.

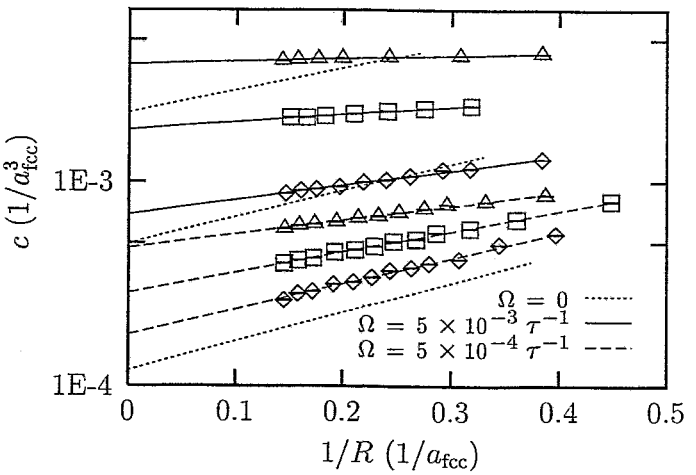

Figure 5.10: For isothermal conditions ($\epsilon_{fcc} = 1.75$) the GT-like $c(R)$ behavior is shown for various mixing parameters ($\diamond$: $\lambda = 0.25\, a_{fcc}$, $\square$: $\lambda = 0.375\, a_{fcc}$, $\triangle$: $\lambda = 0.5\, a_{fcc}$). For comparison results for pure thermally activated processes ($\Omega = 0$) are added [dotted lines; from bottom to top: $\epsilon_{fcc} = (1.75, 1.5, 1.25)$; see Fig. 3.8b].

However, as compared to the pure thermal case (see Fig. 3.8), in addition to an overall solubility increase $\Delta c_\infty^{(CM)} = c_\infty^{(CM)} - c_\infty$ also the effective capillary length $R_c^{(CM)}$ changes as a function of the CM parameters.

An analysis of the effect of mixing can be done by determining the slope (i.e. $R_c^{(CM)}$) and the intersection in the limit $R \to \infty$ (i.e. $c_\infty^{(CM)}$) employing least-square fits. Table 5.1

summarizes the simulation results. As one would intuitively guess, the higher the mixing intensity Ω, the larger is the solubility increase, whereas simultaneously the capillary length decreases. For a fixed value of Ω, the results depend furthermore on the mixing length λ. In real systems the mixing length λ of an atomic component X is fixed with respect to irradiation by ions Y^- at a given energy E. The mixing intensity Ω depends then on the irradiation flux. For instance, assuming a displacement probability $\propto \exp\{-r/\lambda\}$ a fit to TRIM (SRIM) calculations of 50 keV Co^+ irradiation of a thin $CoSi_2$ layer buried in Si yields a mixing length $\lambda \approx 0.28\,\mathrm{nm} \approx 0.52\,a_{\mathrm{fcc}}$ with respect to Co displacements [190].

It should be noted, that SOISSON *et al.* [191] have performed similar simulations for a bcc binary alloy in an essentially two-dimensional model (system sizes up to 80×80 bcc unit cells). Restricting their ballistic jumps to nearest-neighbor XY exchanges, they also derive a GT-like $c(R)$ relation. However, although an overwhelming fraction of successful ballistic jumps is to nearest-neighbor sites (in the regime $\lambda \lesssim a_{\mathrm{fcc}}$, see Fig. 5.9), the tails of the displacement distribution have a considerable influence on the (dynamical) equilibrium conditions (see Table 5.1).

According to an idea of MARTIN [72] the effect of CM can be approximated by assigning a higher temperature $T^{(\mathrm{CM})} > T$ to the system. Assuming that the changes in the observed capillary lengths with respect to the pure thermal case are completely due to a higher temperature (i.e. $R_{\mathrm{c}}^{(\mathrm{CM})} = R_{\mathrm{c}} T/T^{(\mathrm{CM})} = R_{\mathrm{c}}\epsilon_{\mathrm{fcc}}^{(\mathrm{CM})}/\epsilon_{\mathrm{fcc}}$), Fig. 5.11a shows the corresponding results for the solubilities $c_\infty^{(\mathrm{CM})}$. Since the simulation data are located far off the theoretical solubility curve [Eq. (3.14)] the assumption of MARTIN does not explain the observed decrease of the capillary length. Nevertheless it is interesting to determine an effective temperature on the basis of the solubility increase rather than the change in R_{c}. Using the relation $\epsilon_{\mathrm{fcc}}^{(\mathrm{eff})} = -\ln(c_\infty^{(\mathrm{CM})}/A_{\mathrm{fcc}})/B_{\mathrm{fcc}}$ [see Eq. (3.14) and Table 3.6], which with respect to Fig. 5.11a corresponds to shifting the observed solubilities on iso-concentration lines onto the solubility curve, Table 5.2 lists the relative temperature changes. For instance, the solubility increase in the case of the highest mixing efficiency ($\Omega = 5 \times 10^{-3}\,\tau^{-1}$, $\lambda = 0.5\,a_{\mathrm{fcc}}$) corresponds to a pure thermal system, where the temperature is increased about a factor 1.5.

Table 5.1: Analysis of GT-like behavior of CM of a single NC shown in Fig. 5.10 (the uncertainty of the last given digit is indicated in parenthesis). For comparison, the respective results for the capillary length and the solubility in the pure thermal case ($\Omega = 0$) derived according to Eqs. (3.16) and (3.14) are added.

Ω (τ^{-1})	0	5×10^{-3}			5×10^{-4}		
λ (a_{fcc})	0	0.25	0.375	0.5	0.25	0.375	0.5
$R_{\mathrm{c}}^{(\mathrm{CM})}$ (a_{fcc})	3.51	1.65(4)	0.86(3)	0.32(2)	2.88(6)	2.32(3)	1.58(5)
$c_\infty^{(\mathrm{CM})}$ ($10^{-3}/a_{\mathrm{fcc}}^3$)	0.11	0.69(1)	1.80(0)	3.79(2)	0.18(0)	0.28(0)	0.47(1)

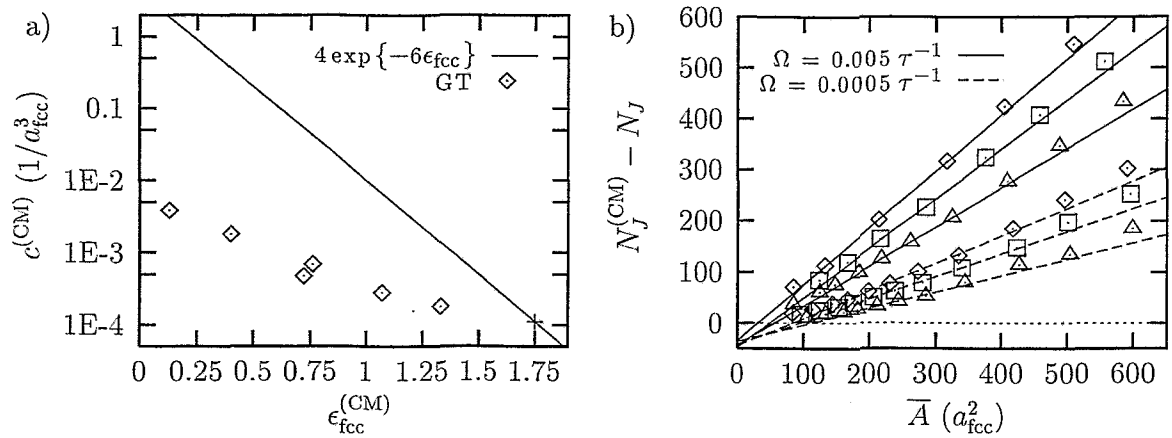

Figure 5.11: In a) the solubilities (intersections in the limit $R \to \infty$, 'GT') are plotted versus the effective temperatures as determined by $\epsilon_{\rm fcc}^{\rm (CM)} = \epsilon_{\rm fcc} R_{\rm c}^{\rm (CM)}/R_{\rm c}$. In b) the difference between the average number of broken bonds N_J of NCs with or without CM is plotted versus the average surface area $\overline{A} = 4\pi\overline{R^2}$.

Assuming an *unchanged* temperature the solubility increase can also be interpreted in terms of an effectively reduced binding energy. In the absence of CM according to Eq. (3.14) on the average $B_{\rm fcc} = 6$ nearest-neighbor bonds J have to be broken for an IA to go into solution. Under irradiation, this number is supposed to decrease, i.e. $B_{\rm fcc} \to B_{\rm fcc} - \delta B_{\rm fcc}$, because due to the ballistic assistance less bonds have to be broken thermally. Writing the CM-induced solubility increase as

$$c_\infty^{\rm (CM)} = c_\infty^0 \exp\{-(B_{\rm fcc} - \delta B_{\rm fcc})\epsilon_{\rm fcc}\} = c_\infty \exp\{\delta B_{\rm fcc}\epsilon_{\rm fcc}\}, \tag{5.3}$$

Table 5.2 lists the corresponding values for $\delta B_{\rm fcc}$.

Besides assuming an artificially increased temperature, in the equation for $R_{\rm c}$ [Eq. (2.23)] the surface tension is the only other quantity changing in the presence of CM.

Table 5.2: Analysis of CM of a single NC with respect to the effective temperature $T^{\rm (eff)}$ on the basis of the solubility increase, the corresponding number of ballistically broken bonds $\delta B_{\rm fcc}$, and surface tension $\sigma_{\rm I}$.

$\Omega\ (\tau^{-1})$	0	5×10^{-3}			5×10^{-4}		
$\lambda\ (a_{\rm fcc})$	0	0.25	0.375	0.5	0.25	0.375	0.5
$T^{\rm (eff)}/T$	1	1.21	1.36	1.51	1.05	1.10	1.16
$\delta B_{\rm fcc}$	0	1.04	1.59	2.03	0.29	0.55	0.83
$\sigma_{\rm I}^{\rm (CM)}\ (J/a_{\rm fcc}^2)$	7.43(1)	8.20(1)	8.40(1)	8.53(2)	7.75(1)	7.87(2)	7.97(2)

Irradiated interfaces are in general rougher than non-irradiated ones. In the ISING model more broken bonds per unit area are observed, which increases the internal energy part σ_{I} of the surface tension. The influence of CM on σ_{I} can be seen in Fig. 5.11b. In this plot in comparison to the pure thermal case the excess number of dangling bonds of the cluster atoms is given as a function of the (assumed spherical[5]) surface of the NC. In the chosen regime of CM the effective surface tensions $\sigma_{\mathrm{I}}^{(\mathrm{CM})}$ exhibit a linear dependence on the NC surface (the observed standard deviation is below 0.3% of the value $\sigma_{\mathrm{I}}^{(\mathrm{CM})}$, whereas nonlinearities become only obvious for determining the difference to the assumed *linear* surface dependence in the pure thermal case). Furthermore, for the range of the considered CM parameters, the least-square fits indicate a negative offset in the limit $\overline{A} \to 0$, which is a few times above the standard deviation. The meaning of this offset is not clear, but might be related to the size dependence of the surface tension for NCs consisting of $\mathcal{O}(10^1)$ atoms [192, 193]. The change in σ_{I} (the observed values are listed in Table 5.2) is in line with the observed solubility increase. However, since the entropic part $\sigma_{\mathrm{E}}^{(\mathrm{CM})}$ of the surface tension has not been determined, the change of R_c due to the modified surface tension $\sigma^{(\mathrm{CM})}$ is not clear.

In this context it is interesting to note, that corresponding CM simulations of a flat interface yield approximately the same effective solubilities as the asymptotic values in the limit $R \to \infty$ of the GT relation (see Table 5.3). Fig. 5.12a shows a snapshot of the microstructure indicating the increased surface roughening. A measure of CM effects on the surface morphology is the mean interface width, which can be seen in Fig. 5.12b. The preliminary results of this simulation series seem to indicate a saturation of the surface width. Using a similar model, but restricting ballistic jumps to nearest-neighbor exchanges, BELLON [194] has also reported a saturation of the interface width of (100) surfaces under irradiation. However, more simulations are needed to study the response of a flat phase boundary on (isotropic) CM, e.g. the parameter regime of a transition of a flat (100) surface to (111) facets, for which some evidence is present in the data.

[5]The NC shape parameter δ [Eq. (3.8)] for the most intensive CM conditions is only approximately two percent higher than in the pure thermal case.

Table 5.3: Steady-state solubilities in the case of CM of a flat interface.

Ω (τ^{-1})	0	5×10^{-3}			5×10^{-4}		
λ (a_{fcc})	0	0.25	0.375	0.5	0.25	0.375	0.5
$c_{\infty}^{(\mathrm{CM})}$ $(10^{-3}/a_{\mathrm{fcc}}^3)$	0.11	0.67(0)	1.84(0)	3.75(0)	0.18(0)	0.29(0)	0.49(0)

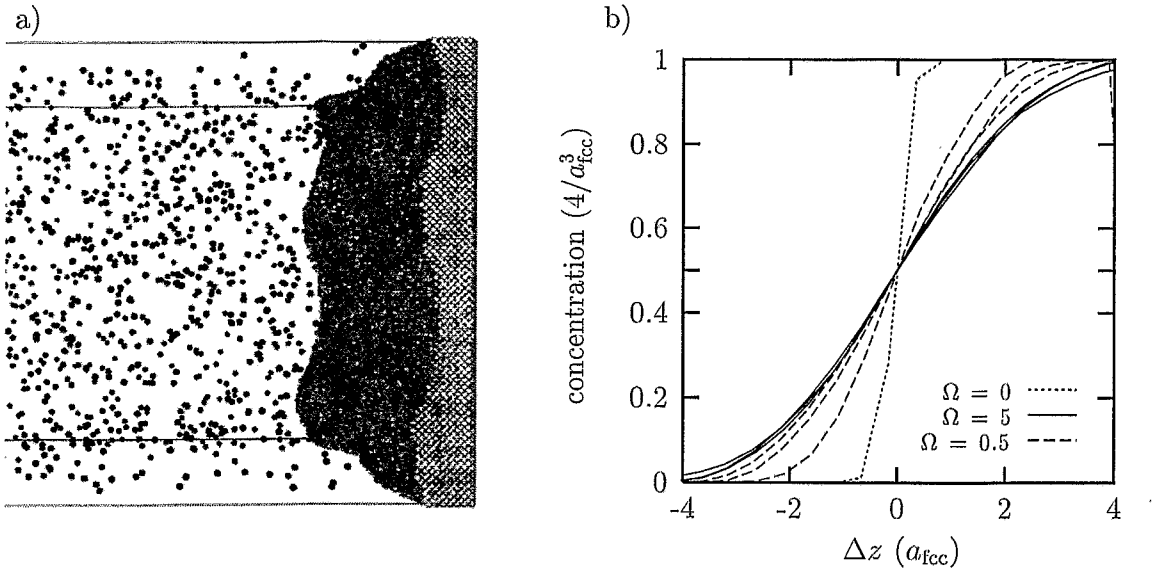

Figure 5.12: Isotropic CM of a flat phase boundary. In a) the microstructure exhibiting the induced surface roughening is shown in the case $\Omega = 5 \times 10^{-3}\,\tau^{-1}$ and $\lambda = 0.5\,a_{\rm fcc}$. In b) the effective interface profile is shown for the set of six CM parameters (Ω is given in units of $10^{-3}\,\tau^{-1}$) corresponding to Table 5.1 and the pure thermal case (see Fig. 3.6).

Discussion

From the results presented above, it can be concluded, that the decrease of the capillary length with respect to the thermal value involves additional CM-dependent factors. According to recent analytical work by HEINIG [190] (who by integrating the isotropic, exponentially decaying, continuous displacement distribution over a spherical NC determined the profile of atoms mixed out, which enters then the radial diffusion equation as a source term), the steady-state monomer concentration of spherical NCs subjected to irradiation is given by

$$c^{(\rm CM)}(R) \;\cong\; c_\infty^{(\rm CM)} \exp\left\{\frac{R_{\rm c}^{(\rm CM)}}{R}\right\}, \quad c_\infty^{(\rm CM)} = c_\infty + \tilde{q}\lambda^2 \tag{5.4}$$

$$R_{\rm c}^{(\rm CM)} \;=\; \frac{\hat{R}_{\rm c} c_\infty - (5\lambda/4)\tilde{q}\lambda^2}{c_\infty + \tilde{q}\lambda^2}. \tag{5.5}$$

Here the notation $\tilde{q} = q/D$ has been used with the mixing amplitude q expressed in units of number of displaced atoms per nm^3 per second. The MC mixing intensity Ω is related to q via the atomic density, i.e. $\Omega N_{\rm a} = q$. It should be noted, that q is the product of the ion current j times the number Θ of displaced atoms per nm per incident ion, and Θ is a function of the deposited nuclear energy per unit length.

The analytical model predicts that the curvature-independent solubility increase depends linearly on the product $\tilde{q}\lambda^2$. However, in the derivation of Eqs. (5.4) and (5.5)

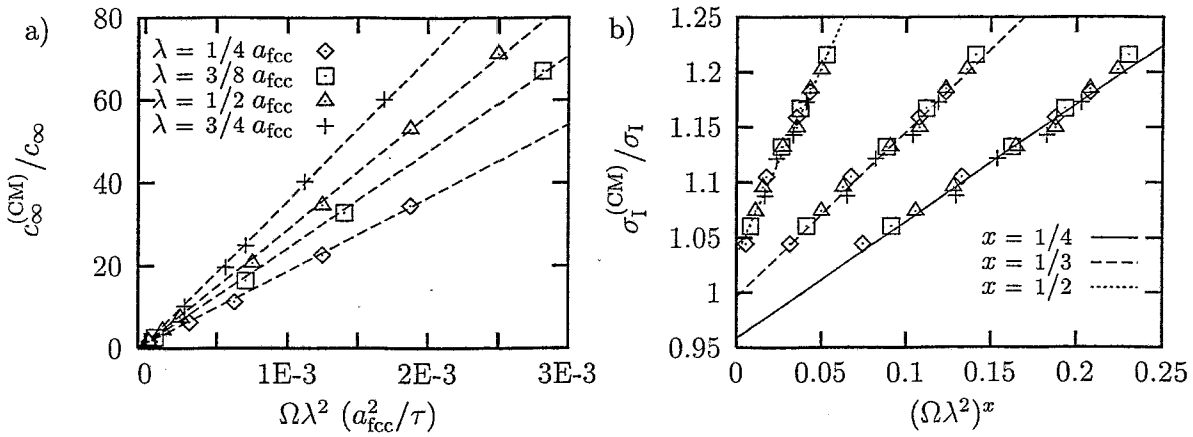

Figure 5.13: In a) the observed solubilities $c_\infty^{(CM)}$ of the GT-like simulations are plotted versus the CM parameter $\Omega\lambda^2$. In b) the enhancement of the internal energy part σ_I of the surface tension is plotted versus various roots of $\Omega\lambda^2$ [same symbols as in Fig. a)].

it has been assumed that every possible displacement of an IA out of a spherical NC is performed, which includes infinitesimal small ballistic jumps. Due to the discrete character of the K3DLMC model, only a fraction of successful displacements contributes to the CM-induced modifications [see Eq. (5.1)].

According to this derivation, the effective capillary length $R_c^{(CM)}$ is an explicit function of the CM parameters. However, while Eq. (5.5) gives an explanation for the observed reduced capillary lengths under irradiation, care has to be taken with respect to the intrinsic value of $\hat{R}_c$.[6] The unperturbed pure thermal value R_c is supposed to be a reasonable choice only in the limit $\tilde{q}\lambda^2 \ll c_\infty$. For considerable CM levels the intrinsic capillary length has to be modified appropriately, i.e. $\hat{R}_c = R_c\sigma^{(CM)}/\sigma$.

Plotting the observed solubilities $c_\infty^{(CM)}$ versus $\Omega\lambda^2$ (see Fig. 5.13a) allows to check the simulation results with the curvature-independent part of Eq. (5.4). For this purpose, in addition to the results of Table 5.1 further simulations have been performed for other values of the mixing intensity Ω as well as for a fourth mixing length $\lambda = 0.75\, a_{fcc}$. A reasonable linear dependence is observed for each value of λ. Assuming the ansatz

$$c_\infty^{(CM)} = c_\infty + \eta'_\lambda \Omega\lambda^2 = c_\infty + \eta_\lambda \frac{\Omega N_a}{D}\lambda^2 = c_\infty + \eta_\lambda \tilde{q}\lambda^2 \tag{5.6}$$

and using $D = a_{fcc}^2/\xi_{fcc}\,\tau^{-1}$ [see Eq. (3.9)] and $N_a = 4\,a_{fcc}^{-3}$, the proportionality constants η_λ can be obtained (see Table 5.4). Here, however, a λ-dependence not present in Eq. (5.4) is observed. This behavior is easily explained by taking into account the lattice character of the MC model. The smaller the ratio λ/a_{fcc} the larger is the fraction of (i) displacements with $r < r_m$, which do not contribute at all (see Fig. 5.9), and (ii) nearest-neighbor

[6] In Ref. [190] no prediction is given for the changes of the intrinsic capillary length $\hat{R}_c$ due to CM.

Table 5.4: Dependence of the proportionality constant η_λ of Eq. (5.6) on the mixing length λ (the uncertainty of the last given digit is indicated in parenthesis).

λ (a_{fcc})	0.25	0.375	0.5	0.75
η	0.0403(4)	0.0531(4)	0.0635(5)	0.0797(6)

displacements of length r_0. Since only a fraction of nearest-neighbor displacements corresponds to a detachment event (within the simulation ballistic jumps of surface atoms to an adatom position are the majority of these nearest-neighbor displacements), the observed values of η_λ seem to be reasonable.

Furthermore, a ballistic diffusion coefficient can be derived as

$$D_{\mathrm{b}} = \frac{q\lambda^2}{c_\infty}. \tag{5.7}$$

The last equation allows to express the observed solubility increase due to CM as the ratio of ballistic to thermal diffusion coefficients, i.e. $c_\infty^{(\mathrm{CM})} = c_\infty(1 + \eta_\lambda D_{\mathrm{b}}/D)$.

As can be seen by the least-square fits of Fig. 5.13b, the observed increase of the internal energy part of the surface tension $\sigma^{(\mathrm{CM})} = \sigma_{\mathrm{I}}^{(\mathrm{CM})} + \sigma_{\mathrm{E}}^{(\mathrm{CM})}$ is best described by

$$\frac{\sigma_{\mathrm{I}}^{(\mathrm{CM})}}{\sigma_{\mathrm{I}}} = 1 + \alpha_{\mathrm{I}} \left(\Omega\lambda^2\right)^{1/3}. \tag{5.8}$$

In contrast to Fig. 5.13a, no λ-dependence of the proportionality constant α_{I} is observed [an analysis with respect to individual mixing lengths yields values (in units of $(\Omega\lambda^2)^{-1/3}$; dropping the subscript I for convenience): $\alpha_{0.25} = 1.48$, $\alpha_{0.375} = 1.54$, $\alpha_{0.5} = 1.46$, and $\alpha_{0.75} = 1.50$, respectively]. For this empirically obtained relation between the increase of the internal energy part of the surface tension and the CM parameters, a derivation in the framework of (non-equilibrium) statistical mechanics remains to be given.

The values of the capillary lengths plotted versus $\Omega\lambda^2$ can be seen in Fig. 5.14a. Here, for all four mixing lengths the mixing intensity Ω has been increased until the regime of metastability (i.e. the CM-induced nucleation of new NCs; see also Section 5.3.2) has been approximately reached. In the case of $\lambda = 0.75\, a_{\mathrm{fcc}}$ for high mixing intensities even a negative capillary length is observed. The change in the sign of R_{c} with increasing mixing intensity can clearly be seen in Fig. 5.14b. A negative capillary length implies, that small NCs possess a lower steady-state equilibrium concentration than large ones. As a consequence, a new regime of NC evolution is expected, which will be discussed in Section 5.3.2.

Rewriting Eq. (5.5) the capillary length is given by

$$R_{\mathrm{c}}^{(\mathrm{CM})} = \frac{R_{\mathrm{c}}\sigma^{(\mathrm{CM})}/\sigma - (5\lambda/4)\tilde{q}\lambda^2/c_\infty}{1 + \tilde{q}\lambda^2/c_\infty}. \tag{5.9}$$

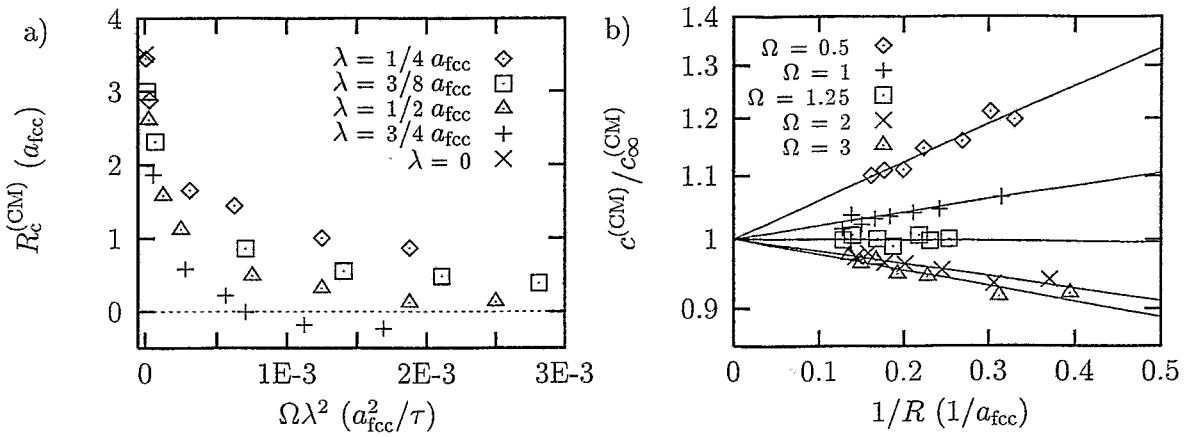

Figure 5.14: In a) the fitted capillary lengths are plotted versus $\Omega\lambda^2$. In b) the normalized GT-like $c(R)$ relation for a single NC subjected to CM in the case of a mixing length $\lambda = 0.75\, a_{fcc}$ (the values of Ω are given in units of $10^{-3}\,\tau^{-1}$) is displayed. The solid lines indicate the results of least-square fits.

Combining Eqs. (5.4) and (5.5) and using a dimensionless CM-induced solubility $u = c_\infty^{(CM)}/c_\infty - 1$ (which serves also as a measure of ballistic forcing) one obtains for the normalized effective capillary length

$$\frac{R_c^{(CM)}}{R_c} = \frac{\sigma^{(CM)}/\sigma - \lambda'\left(c_\infty^{(CM)}/c_\infty - 1\right)}{1 + \left(c_\infty^{(CM)}/c_\infty - 1\right)} = \frac{\sigma^{(CM)}/\sigma - \lambda' u}{1+u}, \quad \lambda' = \frac{5\lambda}{4R_c}. \tag{5.10}$$

The last equation expresses the CM-dependence of the effective capillary length as a function of the solubility increase. Fig. 5.15a shows the CM behavior of $R_c^{(CM)}/R_c$ according to the analytical model [190], i.e. Eq. (5.10) in the case $\sigma^{(CM)} = \sigma$ (see footnote 6). Plotting the simulated values of the effective capillary length versus the relative solubility increase (see Fig. 5.15b) it is observed, that within the K3DLMC model a higher ballistic forcing is needed to obtain the regime $R_c^{(CM)}/R_c < 0$ as predicted by the analytical model. This suggests, that in order to describe the simulation results in the framework of the analytical model [190], the ballistic forcing has to be scaled appropriately, i.e. $u \to \chi_\lambda u$, with a free, λ-dependent parameter. However, while the lattice character of the MC model gives a reasonable explanation for the proportionality constant η_λ between the predicted and simulated solubility increase [see Eq. (5.6)], the origins of the differences with respect to the capillary length are presently not clear.

It remains to describe the surface tension under CM completely, for which only the relative change of the internal energy part (see Fig. 5.13b) is known. Due to the lack of an appropriate non-equilibrium thermodynamic expression and inspired by Eq. (5.8), the relative change of the total surface tension under CM conditions is expanded in powers of

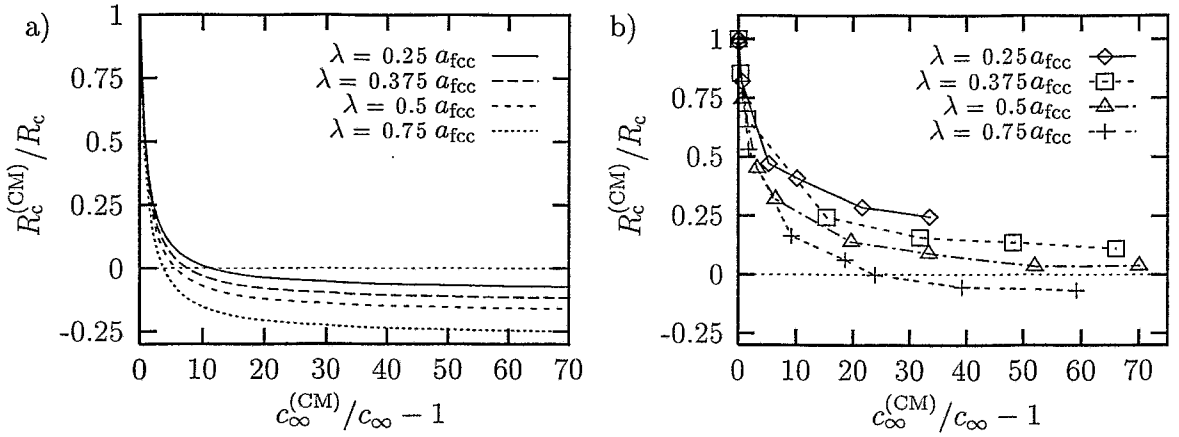

Figure 5.15: In a) the theoretical dependence of $R_c^{(CM)}/R_c$ on the ballistic forcing $u = c_\infty^{(CM)}/c_\infty - 1$ (as predicted in [190]) is plotted according to Eq. (5.10) in the case $\sigma^{(CM)} = \sigma$. In b) the simulation results for the effective capillary length are plotted as a function of the observed solubility increase.

$u^{1/3}$

$$\frac{\sigma^{(CM)}}{\sigma} = 1 + \sum_{n=1}^{\infty} \alpha_n (u^{1/3})^n. \tag{5.11}$$

Inserting the last expression into Eq. (5.10), taking only the first term of the expansion ($\alpha_{n\geq 2} = 0$) into account, and performing the substitution $u \to \chi_\lambda u$, one yields the following equation

$$\frac{R_c^{(CM)}}{R_c} = \frac{1 + \alpha_1 (\chi_\lambda u)^{1/3} - \lambda'(\chi_\lambda u)}{1 + (\chi_\lambda u)}. \tag{5.12}$$

Fitting the parameters α_1 and χ_λ with respect to the simulation results (see Table 5.5) seems to give a reasonable description of the simulation data (see Fig. 5.16a). However, as the errors of the fitted parameters are in the order of the values itself, this description is not satisfying.

Table 5.5: Values for the surface tension parameter α_1 and the ballistic scaling parameter χ for fits of Eq. (5.12) with respect to the simulation data (see Fig. 5.16).

λ (a_{fcc})	0.25	0.375	0.5	0.75
α_1	-1.1 ± 1.4	-0.68 ± 0.53	-0.36 ± 0.48	-0.43 ± 0.51
χ	0.0088 ± 0.0251	0.023 ± 0.028	0.085 ± 0.091	0.084 ± 0.085

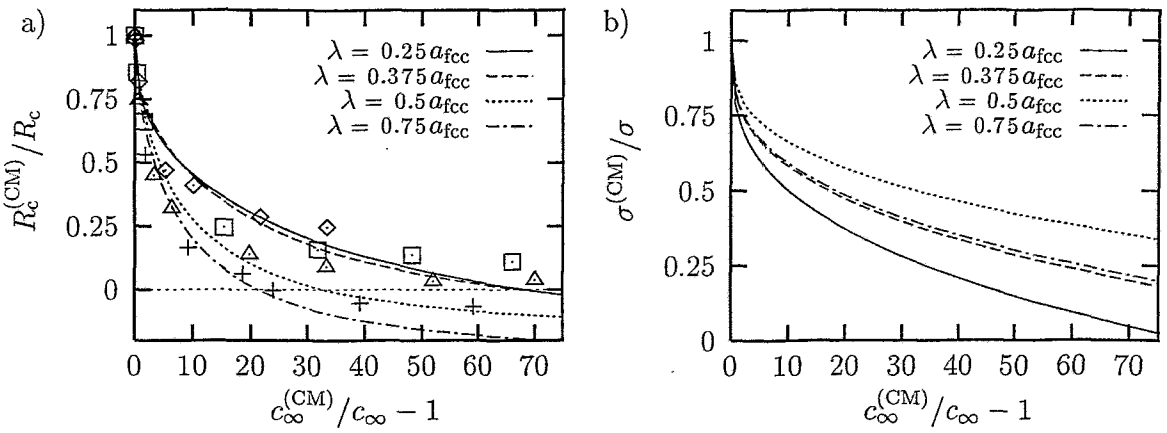

Figure 5.16: In a) the fitted dependence of $R_{\mathrm{c}}^{(\mathrm{CM})}/R_{\mathrm{c}}$ [see Eq. (5.12)] is plotted versus the ballistic forcing $u = c_\infty^{(\mathrm{CM})}/c_\infty - 1$. In b) the corresponding fitted surface tensions are shown.

The corresponding behavior of the normalized surface tensions is shown in Fig. 5.16b. According to this derivation a λ-dependence not observed for $\sigma_{\mathrm{I}}^{(\mathrm{CM})}$ (see Fig. 5.13b) is obtained. The decrease of $\sigma^{(\mathrm{CM})}$ under mixing conditions implies, that the entropic part σ_{E} decreases faster than the internal energy part σ_{I} increases. Since in the limit $u \to \infty$ no stable second-phase domains exist, which is equivalent to a vanishing surface tension [this corresponds to the pure thermal case in the regime $T > T_{\mathrm{c}}$; see Eq. (3.17)], the fitted behavior of $\sigma^{(\mathrm{CM})}/\sigma$, although derived not quite convincingly, is physically reasonable.

In an ion beam mixing experiment one can easily control the magnitude of the ballistic forcing by varying the ion current and/or the implantation temperature, whereas the mixing length is given by the ion-NC-substrate system. Therefore, in a series of simulations for a fixed mixing length $\lambda = 0.5\,a_{\mathrm{fcc}}$, the dependence of the solubility and the capillary length on the mixing intensity Ω and the temperature (i.e. ϵ) has been studied. Fig. 5.17 shows the results for the normalized capillary length as a function of $\Omega\lambda^2$. Obviously, for high temperatures ($\epsilon \propto 1/T$) the capillary length remains positive until the regime of metastability is reached.

Based on Eq. (5.5), Eq. (5.12) provides a reasonable qualitative description of the observed dependence of the effective capillary length on the CM parameters. Combining Eqs. (5.6) and (5.12) the condition $R_{\mathrm{c}}^{(\mathrm{CM})}/R_{\mathrm{c}} = 0$ is approximately given by $\sigma^{(\mathrm{CM})}/\sigma = \lambda'\chi_\lambda\eta_\lambda(\bar{q}\lambda^2/c_\infty)$. Thus in the range $\lambda/a_{\mathrm{fcc}} < 1$ the necessary ballistic forcing is roughly more than an order of magnitude larger than predicted by the analytical model. Knowing precisely $\sigma^{(\mathrm{CM})}(\bar{q},\lambda)$ promises to provide a better correspondence between the predicted and simulated behavior of the effective capillary length and would allow to determine analytically the parameter window, for which $R_{\mathrm{c}}^{(\mathrm{CM})} < 0$ holds. While this has not been performed in this work, the general requirements are nevertheless clear. Basically, the ratio λ/R_{c} defines the range of decrease of the effective capillary length. Therefore, a large mixing length (see Fig. 5.14) and/or a small intrinsic capillary length (see Fig. 5.17),

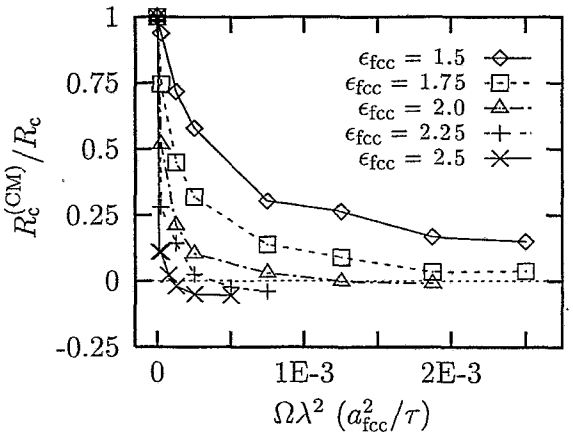

Figure 5.17: Temperature-dependence of the simulation results of the normalized capillary length in the case $\lambda = 0.5\, a_{fcc}$.

which according to Eq. (3.16) in this parameter range is roughly proportional to $1/T$, support the decrease of $R_c^{(CM)}$.

In the above analysis it has been assumed, that the solubility enhancement (i) is completely due to ballistic effects and (ii) depends, accordingly, linearly on the product $\tilde{q}\lambda^2$ [190]. However, higher order powers of $\tilde{q}\lambda^2$ might become important for very large mixing intensities (in the above study Ω has been varied for some orders of magnitude). It is also not clear, how the inevitably modified surface tension (not considered in [190]) influences the observed solubility properties (for instance, thermally driven monomer detachment from an interface roughened by CM is facilitated with respect to a smooth one). Furthermore, it remains to be shown, how the lattice character of this CM model is compatible with the continuum description of displacements used in Ref. [190].

5.3.2 Nucleation, growth, and Ostwald ripening in the presence of collisional mixing

Effects during implantation

As already pointed out in Section 2.3.3 nucleation of precipitates during ion implantation can be described by appropriately modifying the rate equation (2.21) of cluster growth [64] and determining the modified kinetic coefficients. As a consequence, a shift of the critical NC size is predicted, i.e. $i^*_{CM} > i^*$. Therefore, the onset of nucleation is delayed roughly by a factor of the order of $c_\infty^{(CM)}/c_\infty$ as compared to the hypothetical case of impurity accumulation without ballistic side effects. After the end of the nucleation stage, also in the presence of CM all stable NCs are supposed to grow as essentially isolated precipitates as described in Section 2.4.

During implantation a steady-state equilibrium should set in between monomer absorption and ballistically enhanced detachment like a thermal equilibrium establishes in the

absence of ballistic forcing. Thus, for constant conditions throughout the implantation, the concept of an effectively higher T_{imp} may give a reasonable description of the NC evolution. Although it does not describe precisely the modifications due to CM (see Section 5.3.1), it might explain the similarities between experiment and results of K3DLMC simulations without including CM (see Section 5.1).

After a variation of implantation parameters the system transforms to a new steady-state. For instance, lowering the implantation temperature (or, equivalently, increasing the ion current) increases the value of the ballistic forcing u. Since now the monomer flux back to the NCs is reduced with respect to deposition of new impurities and CM-induced detachments, an overall increase of the monomer concentration is expected. As predicted by the pure thermal K3DLMC simulations a new nucleation stage may be initiated. Note however, that while stable NCs in the pure thermal case do not shrink in the case of a temperature decrease, in the case of CM the ratio of unchanged ballistic monomer detachment to reduced thermal condensation is supposed to support an overall NC shrinkage. This might explain, why no distinct bimodal size distribution has been observed in the Au implantation experiment described in Section 5.2.

Effects during irradiation I. Inverse Ostwald ripening

Irradiating a pre-existing ensemble of NCs with a different kind of ions (e.g. with atoms building up the matrix) can cause a pronounced change of its steady-state properties. The resulting solubility increase towards a modified steady-state equilibrium [depending on the ballistic forcing from a few times c_∞ to some orders of magnitude (see Fig. 5.13a)] has to be fed by the NCs themselves. This causes initially a simultaneous size decrease of all irradiated NCs, where the smallest ones are expected to disintegrate, until modified coarsening sets in.

From the behavior of a single NC in the presence of CM some conclusions can be drawn with respect to OR of an ensemble of NCs under irradiation. Assuming that NCs under irradiation remain spherical, for a fixed λ and mixing intensities below the disintegration threshold (or, as will be shown below, the threshold for CM-induced nucleation of further NCs) $u_{\max}$, different physical regimes should exist with respect to the minimum value $R_{\mathrm{c,min}}^{(\mathrm{CM})}$ of the effective capillary length:

$R_{\mathrm{c,min}}^{(\mathrm{CM})} > 0$: The capillary length remains positive for all mixing intensities below $u_{\max}$. Thus ordinary OR occurs, which proceeds, however, on a modified time scale (the CM-induced relative changes of the solubility and capillary length determine the modified velocity of OR; see below).

$R_{\mathrm{c,min}}^{(\mathrm{CM})} = 0$: For a specific mixing intensity u_0 the capillary length vanishes. This implies that all stable NCs possess the same steady-state equilibrium concentration. Therefore, no OR occurs.

$R_{\mathrm{c,min}}^{(\mathrm{CM})} < 0$: Within the parameter window $u_0 < u < u_{\max}$, the effective capillary length becomes negative [190]. As a consequence, in this regime small NCs (in the range

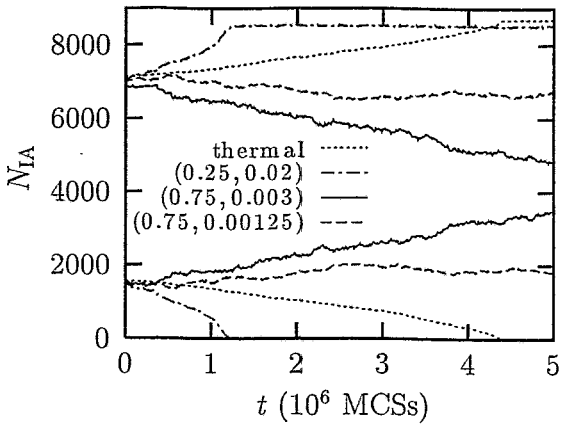

Figure 5.18: Analysis of the evolution of a model system of two diffusionally interacting NCs with respect to the NC sizes (given as number of IAs N_{IA} per NC). The corresponding mixing length λ (in $[a_{fcc}]$) and the mixing intensity Ω (in $[\tau^{-1}]$) are indicated in parenthesis.

of stable ones) have a lower steady-state equilibrium concentration than large ones. Such a dependence prevents coarsening and gives rise to a delta-like PRD, because the effective driving force and the resulting monomer flux reduce any size dispersion $\Delta R_i = |R_i - \bar{R}|$ [this becomes obvious by the substitution $R_c \rightarrow -R_c$ in the single-NC growth law Eq. (4.5)]. Therefore, in the following ballistically driven impurity redistribution towards equal-sized NCs will be referred to as inverse OR.

The above discussed modifications of OR are demonstrated with respect to the evolution of two NCs diffusionally interacting in a closed box (volume of simulation cell: $32 \times 32 \times 64\, a_{fcc}^3$) with periodic BCs.[7] For four different conditions the detailed evolution of both NC sizes can be seen in Fig. 5.18. Taking the pure thermally driven OR as a reference (whose evolution can be seen in four snapshots in Figs. 5.19a – d), the range of modifications due to CM can be seen. For mixing conditions favoring more the solubility increase than the decrease of the effective capillary length, accelerated OR is observed, i.e. the small NC dissolves within 1.2×10^6 MCSs (dashed-dotted curve in Fig. 5.18). No OR occurs for CM parameters leading to a vanishing capillary length (dashed curve in Fig. 5.18; despite the considerable fluctuations of both NC sizes CM *stabilizes* this thermodynamically metastable system). Finally inverse OR occurs for negative $R_c^{(CM)}$ (solid curve in Fig. 5.18). The growth of the small NC at the expense of the large one can be seen in Figs. 5.19e – h. It should be noted, that while in the pure thermal case both NCs maintain their quasi-equilibrated octahedral form, here the faceting is smeared out due to CM. Although the surfaces are rough the NCs remain compact.

Since the characteristic time constant of coarsening τ_{diff} is proportional to $1/(R_c c_\infty)$ [see Eq. (4.16)], the relative change of the velocity of coarsening can be obtained by inserting

[7] This simple model system is certainly affected by self-interactions. Nevertheless the governing physics should be clear.

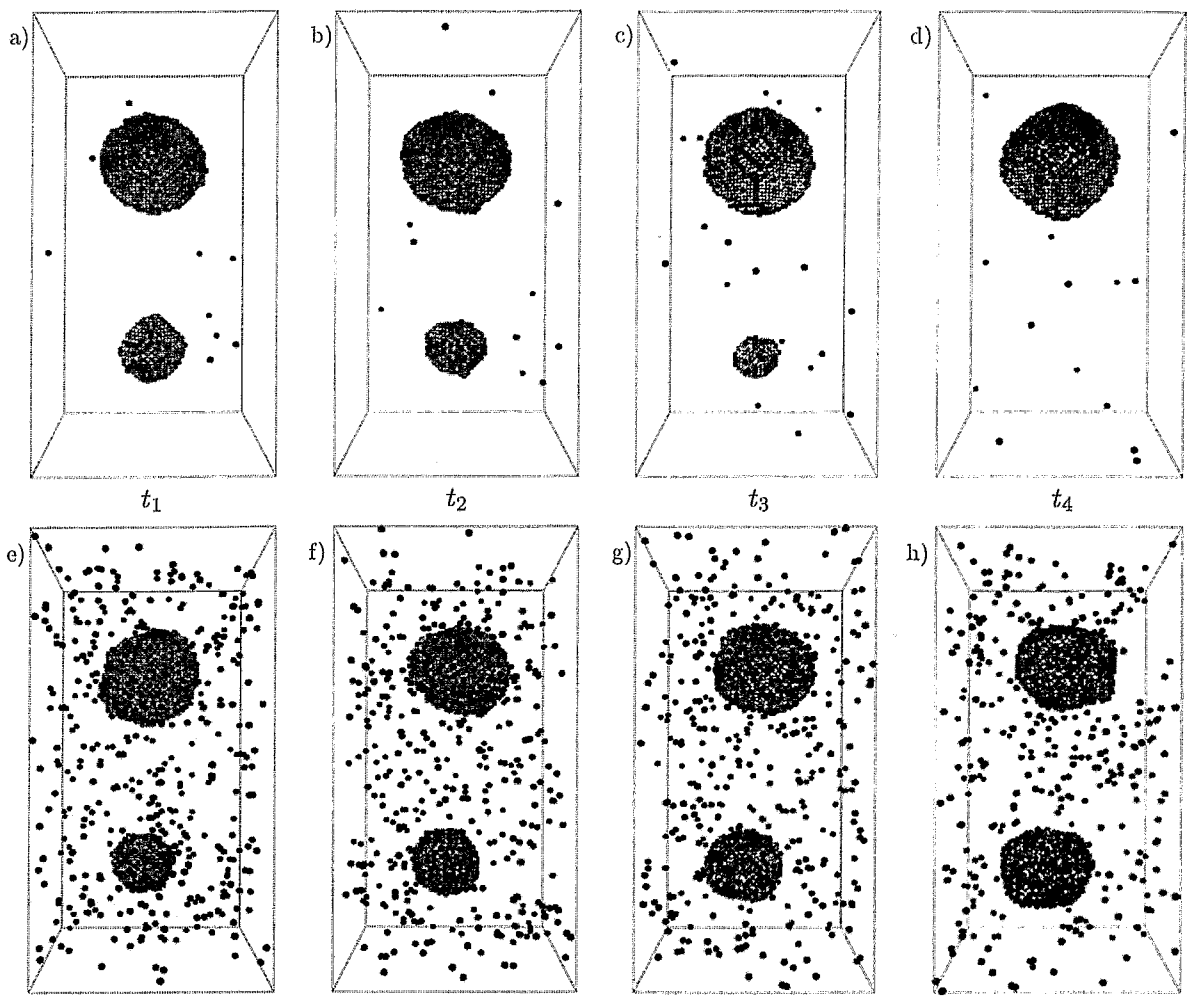

Figure 5.19: Evolution of two NCs in a closed box with periodic BCs for $\epsilon_{\text{fcc}} = 1.75$. Starting with identical initial systems $[R_1(t_0) \approx 4.5\, a_{\text{fcc}},\ R_2(t_0) \approx 7.5\, a_{\text{fcc}}]$ in the top row ordinary, i.e. thermally driven, OR can be seen (no ballistic jumps), whereas in the bottom row for the CM parameters $\Omega = 0.005\, \tau^{-1}$ and $\lambda = 0.75\, a_{\text{fcc}}$ inverse OR is shown. Referring to Fig. 5.18 the snapshots have been recorded at $t_1 = 1 \times 10^5$, $t_2 = 1.6 \times 10^6$, $t_3 = 3.6 \times 10^6$, and $t_4 = 4.9 \times 10^6$ MCSs, respectively.

the respective values under CM. Fig. 5.20 shows the modified time constants. Assuming a constant diffusion coefficient (neglecting within this analysis a change in D due to the additional ballistic jumps per MCS as well as a concentration dependence, i.e. $D \neq D(c)$) an acceleration of ripening up to a factor of eight is predicted within the parameter regime of this study. It is interesting to note, that the largest acceleration of OR is obtained for the smallest mixing length. This can be understood in terms of the different mixing

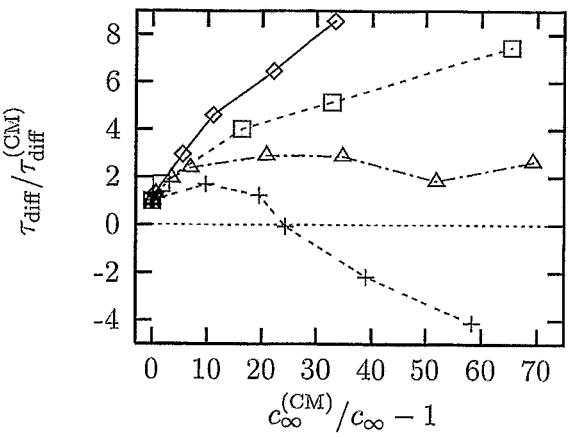

Figure 5.20: Variation of the characteristic time constant for OR $\tau_{\rm diff}$ for various CM parameters (for the data points of Figs. 5.13 and 5.14).

dependences of the solubility and capillary length. The change in the coarsening velocity is given by (expressed in terms of the ballistic forcing $u = c_\infty^{\rm (CM)}/c_\infty - 1$)

$$\frac{\tau_{\rm diff}}{\tau_{\rm diff}^{\rm (CM)}} = \frac{R_{\rm c}^{\rm (CM)} c_\infty^{\rm (CM)}}{R_{\rm c} c_\infty} = \frac{\sigma^{\rm (CM)}/\sigma - \lambda' \chi_\lambda u}{1 + \chi_\lambda u}(1+u), \tag{5.13}$$

where Eq. (5.12) has been used. In addition to a negative effective capillary length, inverse OR is characterized by a negative time constant, the meaning of which is, however, presently not clear.

Although NCs lose their faceted octahedral shape under CM, they essentially remain spherical. Within this CM model no evidence for a dynamical shape transition has been observed below the disintegration threshold. In this context it is interesting to note that applying his mixing model BELLON [194] has reported for a fcc NC a faceting transition from octahedral to cuboidal shape for a high ratio of ballistic to thermal nearest-neighbor diffusion steps.

Effects during irradiation II. Collisional mixing-induced nucleation

For a better understanding of the modifications of the impurity-substrate system due to ion irradiation the (c, T, Ω, λ) phase diagram has to be determined. While some trivial limits are clear, e.g. the absence of CM or the limit $u \to \infty$, which corresponds to a completely random system free of thermal effects, the range of the metastable part of the phase diagram is presently not clear. In particular, a definition of the modified supersaturation $\delta\mu^{\rm (CM)}$ has to be given. In this context it should be noted, that after the solubility increase $c_\infty^{\rm (CM)}/c_\infty$ has exceeded a temperature-dependent threshold, nucleation of new NCs is observed. This can be seen in Fig. 5.21a, where for a model system analogous to Fig. 5.19 the evolution of the individual NCs is plotted. Whereas for the mixing intensity $\Omega = 0.003\,\tau^{-1}$ only

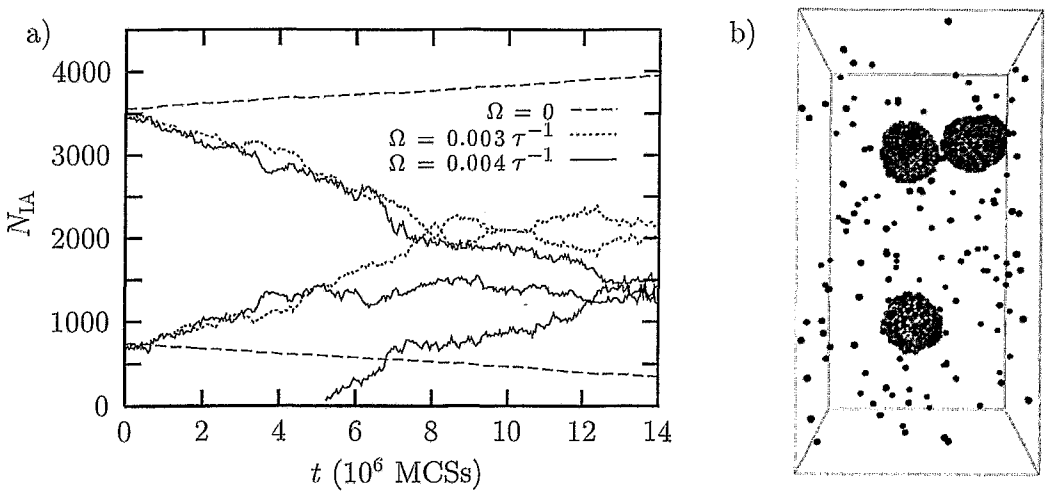

Figure 5.21: Analogous to the model system of Fig. 5.19 [here: $R_1(t_0) \approx 3.5\,a_{\rm fcc}$, $R_2(t_0) \approx 6.0\,a_{\rm fcc}$] for the parameters $\epsilon_{\rm fcc} = 2.25$ and $\lambda = 0.5\,a_{\rm fcc}$ the evolution of individual NCs is displayed in a) for various mixing intensities. The dashed lines indicate the pure thermal case. Inverse OR can be seen for $\Omega = 0.003\,\tau^{-1}$ and $\Omega = 0.004\,\tau^{-1}$, where at $t \approx 5 \times 10^6$ MCSs an additional NC forms. In the case $\Omega = 0.004\,\tau^{-1}$ in b) a snapshot of the microstructure at $t = 1.3 \times 10^7$ MCSs is shown indicating three essentially equal-sized NCs.

inverse OR[8] of the existing NCs is observed (at least during the finite simulation time), for a mixing intensity $\Omega = 0.004\,\tau^{-1}$ the system is clearly transformed to the metastable state, because an additional NC is formed at $t \approx 5 \times 10^6$ MCSs. For this system inverse OR is then observed among three NCs. Although Fig. 5.21b suggests at a first glance, that the large NC has disintegrated, Fig. 5.21a rules out this possibility.

The tendency for CM-induced nucleation can be understood as follows: From a thermodynamical point of view an increasing CM intensity drives the system to a higher energetic state, because more IAs are found as dissolved monomers [see Eq. (5.4)]. As already pointed out in Section 5.3.1, in the regime of a negative capillary length small NCs have a lower steady-state monomer concentration than large ones. This implies that the nucleation of new NCs is energetically favorable, if the effective solubility decrease due to the decreasing average precipitate size over-compensates the additional energy to be spent to create new phase boundaries. Thus it can be concluded, that beyond the limit of inverse OR at a constant NC density the higher the ballistic forcing u the more additional NCs will be nucleated. This, in turn, decreases the mean-radius of the NC ensemble, because the precipitated amount of impurities will be equally shared among more clusters.

[8]In the case of the parameters $\epsilon_{\rm fcc} = 2.25$ and $\lambda = 0.5\,a_{\rm fcc}$, the capillary length becomes negative slightly above $\Omega = 0.001\,\tau^{-1}$ (see Fig. 5.17).

General discussion

One of the major approximations of this CM model is the neglect of matrix atoms mixed into the second-phase domains. This process is supposed to enhance the interface roughness, because it makes the phase boundary more diffuse. While in the current model a vacancy is left after a ballistic jump of a bulk atom close to the interface into the matrix, the reverse process introduces matrix atoms into the NCs. This should promote the disintegration of small NCs, thus causing an additional shift in i^* not observable in the current description. Thus the above model should give a reasonable description for NC/substrate systems, where (i) the solubility of matrix atoms in the NCs is high (no precipitation within the second-phase domains) and (ii) the diffusion coefficient of matrix atoms in the second-phase domains is high (they can quickly reach the phase boundary and rejoin the matrix).

For a complete description of the NC evolution during implantation/irradiation also dwell time effects of the ion beam have to be considered. Since in CBII the substrate is scanned by the ion beam at a defined frequency, for a particular area periods of ion deposition accompanied with CM take place alternately with (in general larger) periods of basically thermally activated impurity redistribution. Dwell time effects have been rather extensively studied in the area of buried silicide layer formation using a FIB [195, 196], but are usually not even mentioned in IBS of NCs.

Chapter 6

Combination of K3DLMC and RDE simulation methods

As already pointed out in Chapter 4, the RDE approach to OR needs as essential input the coordinates $\{\vec{r}_i\}$ and radii $\{R_i\}$ of NCs. Although some setting algorithms have been developed which try to cover some properties of real NC distributions (e.g. mean radius, volume fraction, density, size distributions, and spatial correlations) [172, 182], statistically generated input data are always to some extent artificial. For infinite homogeneous systems this is not much a problem, because all ensembles evolve towards an attractor state [162] regardless how unphysical the initial conditions were chosen. However, the main problem in simulations of OR of inhomogeneous (finite) systems remains the choice of the initial conditions. In finite systems small fluctuations may have a strong effect on the (spatial) evolution [41], thus a reliable knowledge of the initial conditions is crucial for a RDE approach to OR.

On the other hand, as shown in Chapter 5, the K3DLMC method covers the basic mechanisms of nucleation and growth of NCs. In principal, this atomic model allows to study consistently all basic processes of IBS of NCs including OR. However, due to the restricted power of current computer systems, it is in general not the method of choice for predictions of large scale and long time phenomena. Thus it is tempting to combine both simulation approaches via the transfer of data $(\{\vec{r}_i\}, \{R_i\})$ in order to study the evolution of NC ensembles from the very beginning of nucleation to the late stage of coarsening [184]. Before applying the combined simulation scheme to finite inhomogeneous systems, e.g. layers of NCs formed by IBS, first the results of K3DLMC simulations of homogeneous coarsening have to be studied and discussed.

6.1 K3DLMC and RDE simulations of homogeneous OR

Using the KIM (usually restricted to nearest-neighbor interactions) MC studies in two (mostly on a square lattice) [197]-[200] and three (mostly on a sc lattice) [91]-[94] dimen-

sions of the growth of minority phase domains in systems with conserved and non-conserved order parameter have been performed for many years (see, e.g. GUNTON *et al.* [61] for a comprehensive review of the work up to 1983). As a consequence of the scaling hypothesis [Eq. (2.42)] and the LSW theory (see Chapter 4) in the late stage of phase separation all physical quantities should depend only on a single length scale L, i.e. the average domain size or, equivalently, the average distance between domains (see e.g. the reviews of FURUKAWA [96] and BRAY [97]). Usually, one assumes a power law for growth of the form $L \propto t^m$ (or, equivalently, $k_\mathrm{m} \propto t^{-m}$ for the value of the wave number, which maximizes the structure function $S(\vec{k},t)$ [Eq. (2.32)]), and tries to determine the coefficient m.

Additional to extensive MC studies of the properties of the structure function $S(\vec{k},t)$, the evolution of NCs was also followed directly by an analysis of individual NCs and the mean cluster size. For instance, using a sc lattice gas model, PENROSE *et al.* [100] simulated cluster growth after a quench ($T = 0.59\,T_\mathrm{c}$) below the coexistence curve into the metastable region. For a system with $c = 0.075\,a_\mathrm{sc}^{-3}$ they reported a linear dependence of the critical NC size $i^\star$ on time for a run of 6000 MCSs. Further MC studies in three dimensions with explicit analysis according to the droplet model have been performed, for instance, by LEBOWITZ *et al.* [94], KALOS *et al.* [98], and PENROSE *et al.* [99], who concentrated on a detailed kinetic description of the phase transition. Surprisingly, since the middle eighties further work on domain coarsening in three dimensions using the KIM is very hard to find [201].

6.1.1 K3DLMC simulations of homogeneous OR

In order to analyze the properties of the K3DLMC model with respect to OR, in a series of simulations on a fcc lattice systems with volume fractions $\phi = 0.01$ have been studied. For a system size of $128 \times 128 \times 128$ unit cells (using periodic BCs) the evolution of the IAs has been monitored over a period of 4×10^6 MCSs.

Nucleation stage

Quenching the statistically distributed IAs to five finite temperatures well below T_c (i.e. assuming $c(t_0 = 0) = 4\phi\, a_\mathrm{fcc}^{-3}$), the initial dimensionless supersaturations $\delta\mu\beta = \ln(c(t_0)/c_\infty(\epsilon))$ are listed in Table 6.1. Combining Eqs. (2.10) and (3.17) the energy barriers W_min for homogeneous nucleation

$$W_\mathrm{min} = \frac{8\pi}{3}\frac{\epsilon_\mathrm{fcc}^2}{(\delta\mu\beta)^2}\left(\frac{R_\mathrm{c0}^\mathrm{(fcc)}}{a_\mathrm{fcc}\epsilon_\mathrm{fcc}} + \zeta_\mathrm{fcc}\right)^3 J_\mathrm{fcc} \tag{6.1}$$

and the corresponding (continuous) critical NC sizes

$$i^\star = \frac{16\pi}{3}\left[\frac{\epsilon_\mathrm{fcc}}{(\delta\mu\beta)}\left(\frac{R_\mathrm{c0}^\mathrm{(fcc)}}{a_\mathrm{fcc}\epsilon_\mathrm{fcc}} + \zeta_\mathrm{fcc}\right)\right]^3 \tag{6.2}$$

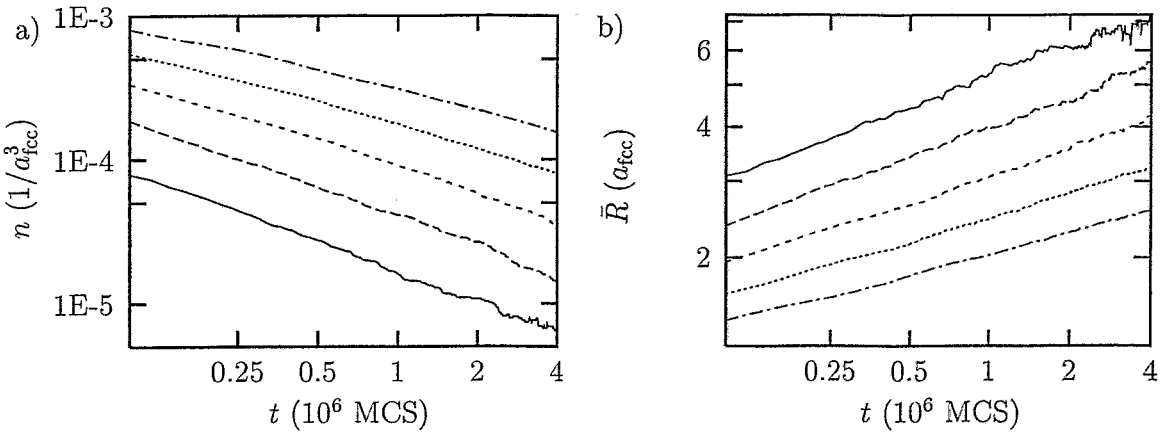

Figure 6.1: Using double-logarithmic scales the evolution of the density of NCs and of the mean radius are shown in a) and b), respectively. In the $\ln(n)$-$\ln(t)$ plot, from bottom to top the curves correspond to $\epsilon_{fcc} = \{1.25, 1.5, 1.75, 2.0, 2.25\}$, whereas the reversed order is valid in the $\ln(\bar{R})$-$\ln(t)$ plot.

as given by classical nucleation theory are listed in Table 6.1 as well (note, however, the sensitivity of Eqs. (6.1) and (6.2) with respect to the derived expression for the surface tension σ; see Section 3.5.3). Due to the high supersaturation levels the critical NC sizes are extremely small (in the case $\epsilon_{fcc} = 2.25$ even a dimer can be regarded as a critical nucleus). It is, however, questionable, if the capillarity approximation, and thus the classical nucleation theory, provides reliable results in a regime with no distinct surface and bulk energy states.

Coarsening stage

The further evolution of the NC density $n(t)$ and the mean radius $\bar{R}(t)$ is shown in Fig. 6.1. In these plots for each value of ϵ_{fcc} the average of two independent runs has been

Table 6.1: Temperature-dependence of the initial supersaturation $\delta\mu$, the critical NC size i^* [Eq. (6.2)] and the energy barrier W_{min} for nucleation [Eq. (6.1)] with respect to an initial monomer concentration $c(t_0) = 0.04\ a_{fcc}^{-3}$.

ϵ_{fcc}	1.25	1.5	1.75	2.0	2.25
$\delta\mu\beta$	2.89	4.39	5.89	7.39	8.89
i^*	9.8	5.2	3.6	2.8	2.3
W_{min}/J_{fcc}	11.3	7.6	6.0	5.1	4.6

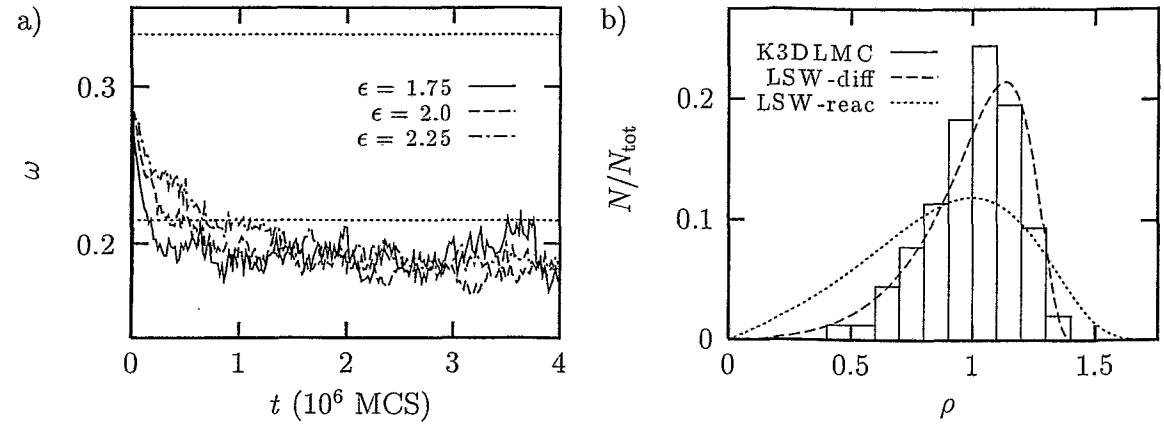

Figure 6.2: In a) the evolution of the widths ω of PRDs corresponding to the simulations for the three lowest temperatures of Fig. 6.1 are shown. As a reference the results of the both limiting LSW distributions (see Fig. 4.10) are added. In b) the PRD of a single run for $\epsilon = 2$ obtained after 2×10^6 MCSs is shown.

used. Size-dependent effects should not have influenced these simulations, since the largest diffusional screening length of this series [as obtained by Eq. (3.18)] for $\epsilon_{\text{fcc}} = 1.25$ is $\lambda_{\text{D}} \approx 42\, a_{\text{fcc}}$. This value is considerably below the linear dimension of the simulation volume, thus self-interaction effects are negligible.

Care has to be taken in order to extract the growth behavior, since a fit assuming $\bar{R} \propto t^m$ is only justified for late times of phase separation. According to Eq. (4.16) this implies that the relation $\bar{R}(t) \gg \bar{R}_0$ must be valid. Due to the quench the initial system consisted entirely of monomers, thus for application of the LSW theory the mean radius has to be large with respect to $R_0 \approx 0.39\, a_{\text{fcc}}$.[1] Assuming that this requirement is fulfilled (at least in the end of the simulations), least-square fits performed in the time interval $1 \times 10^6 < t < 4 \times 10^6$ MCSs yield growth exponents $m(\epsilon_{\text{fcc}} = 1.25) = 0.19$, $m(\epsilon_{\text{fcc}} = 1.5) = 0.26$, $m(\epsilon_{\text{fcc}} = 1.75) = 0.23$, $m(\epsilon_{\text{fcc}} = 2.0) = 0.19$, and $m(\epsilon_{\text{fcc}} = 2.25) = 0.17$, respectively. These results would indicate a temperature-dependence of ripening (the data for $\epsilon_{\text{fcc}} = 1.25$ show a very bad statistics), which is not predicted in the LSW theory [Eq. (4.16)].

More insight into the dynamics of the K3DLMC method is gained by plotting the widths w [Eq. (4.30)] of the PRDs as can be seen in Fig. 6.2a. Fig. 6.2b shows the PRD for $\epsilon_{\text{fcc}} = 2$ obtained after 2×10^6 MCSs. While the size distribution is in reasonable accordance with the stationary form (LSW) of the PRD of diffusion limited OR [Eq. (4.15)], it is on the average somewhat smaller (see also Fig. 4.10) and seems to be more symmetric. Since the quasi-stationary form of the PRD is directly coupled to the growth law, the on the average smaller width ω as compared to the result of the diffusion controlled LSW regime is consistent with the observation $m < 1/3$.

However, a more careful analysis reveals, that the simulated coarsening data can not be

[1] Using $a_{\text{fcc}}^3 = 4V_{\text{a}}$.

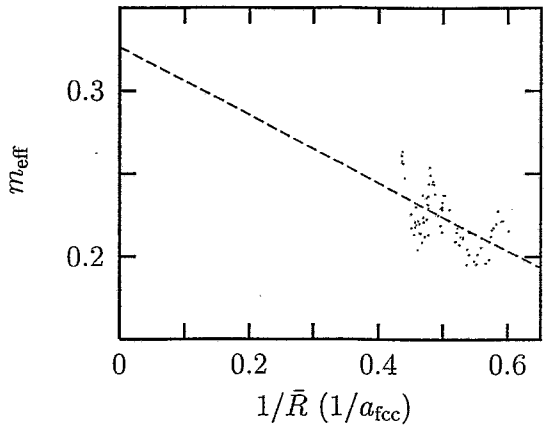

Figure 6.3: The effective domain growth exponent m_{eff} of the K3DLMC model is shown for the parameter $\epsilon_{\text{fcc}} = 1.75$ according to Eq. (6.3) with data points in the range $t \geq 5 \times 10^5$ MCSs.

analyzed in the framework of the standard LSW theory, because Eq. (4.12) is based on the linearization of the GT equation (i.e. use of Eq. (4.11) rather than Eq. (2.23); see also Fig. 4.3). This is, however, not justified for the rather small NCs of the current simulations, which becomes obvious by comparing the range of the mean NC radius $\bar{R}$, as obtained by the simulations, to the corresponding capillary lengths. According to Eq. (3.16) the capillary length varies between $R_c(\epsilon_{\text{fcc}} = 1.25) \approx 2.42\, a_{\text{fcc}}$ and $R_c(\epsilon_{\text{fcc}} = 2.25) \approx 4.61\, a_{\text{fcc}}$. Thus for the lowest temperature of the simulation series ($\epsilon_{\text{fcc}} = 2.25$), the mean domain size has only grown up to the order of the capillary length, whereas for the highest temperature ($\epsilon_{\text{fcc}} = 1.25$) the ratio $R_c/\bar{R}$ has become small at the end of the simulation; a linearization of the GT relation would be justified in modeling this ensemble at *later* times.

Since in all simulation of this series the LSW requirement $R_c/\bar{R} \ll 1$ is not satisfied, coarsening should be analyzed with respect to an effective growth exponent according to the growth law $\bar{R}(t) = A + Bt^{1/3}$ [note the difference to Eq. (4.16)!]. This approach has been motivated by domain growth studies in the two-dimensional case [199, 200]. Without discussing the capillary length of the square lattice, these authors proposed an effective growth exponent

$$m_{\text{eff}} = \frac{1}{3} - \frac{C}{\bar{R}(t)} := \frac{\mathrm{d}\{\ln[\bar{R}(t)]\}}{\mathrm{d}[\ln(t)]}. \tag{6.3}$$

Thus an analysis of the growth behavior has been performed using an appropriate implementation of Eq. (6.3), i.e. $m_{\text{eff}}(t_f) = \ln[\bar{R}(t_f)/\bar{R}(t_i)]/\ln(t_f/t_i)$ with, e.g. $t_f/t_i = 2$.[2] Fig. 6.3 shows the result of the analysis for $\epsilon_{\text{fcc}} = 1.75$ and the corresponding least-square fit. Here, the effective growth exponent approaches the LSW prediction $m = 1/3$, but, as the

[2]This (arbitrary) ratio should exclude fluctuations, but guarantee 'local' time in this discrete implementation of the derivative of Eq. (6.3) [200].

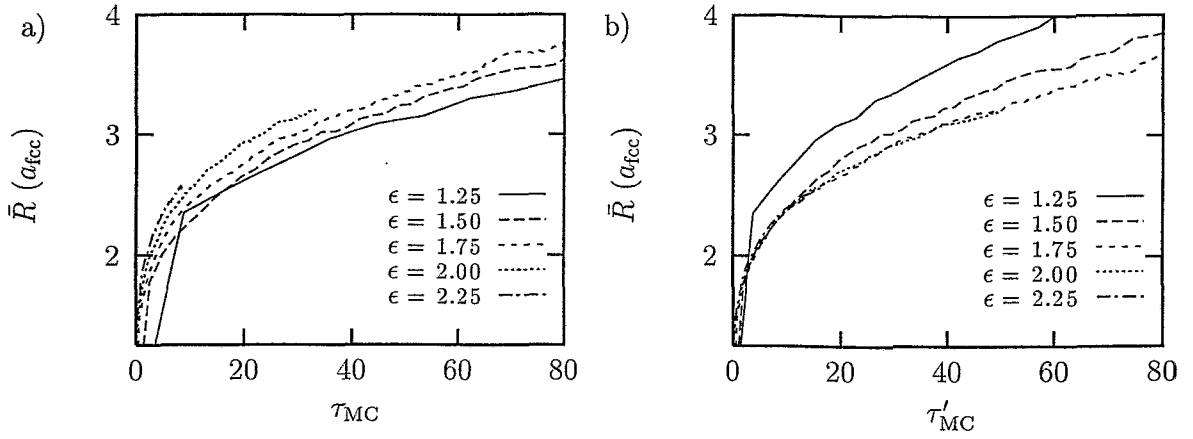

Figure 6.4: In a) the results of Fig. 6.1b are replotted by scaling according to Eq. (6.4). In b) the modified time constants $\tau'_{\rm MC} = [R(i^*)^3/V_{\rm a}]\tau_{\rm MC}$ have been used.

large scatter of the data indicates, this particular results seems to depend on the range of included data (the considerable scatter in the data points for the other four simulation parameters gives partly even a negative $m_{\rm eff}$). Thus a good statistics is needed in order to obtain a smooth dependence of $\bar{R}$ on t (AMAR *et al.* [200] used 100 independent runs in their study of the two-dimensional case). With more reliable data, the constant C in Eq. (6.3) can be determined, which should exhibit a temperature dependence proportional to the capillary length.

Since all simulations of this series started from the same initial state (basically just dissolved monomers) followed coarsening of the nucleated NCs, it is interesting to check if a common scaling behavior can be extracted. Therefore, inspired by the LSW approach [Eq. (4.16)] a dimensionless MC time scale is introduced,

$$\tau_{\rm MC} = \frac{1}{D_{\rm sim} c_\infty R_{\rm c}} = \frac{1}{\frac{1}{\xi_l} a_l^2 A_l \exp\{-(\xi_l/2)\epsilon_l\}(R_{\rm c0}^{(l)} + \zeta_l a_l \epsilon_l)} \overset{\rm fcc}{\approx} \frac{3\exp\{6\epsilon_{\rm fcc}\}}{(-0.32 + 2.19\epsilon_{\rm fcc})}, \quad (6.4)$$

where Eqs. (3.10), (3.14), and (3.16) have been combined (normalizing, as usually, a MCS). As Fig. 6.4a indicates, this approach does not scale the K3DLMC results, rather a systematic deviation is observed. This is, however, not a surprise, because according to the LSW theory scaling should only occur, if OR is governed by a stationary dynamics. This can not be expected here, since for all parameters $R_{\rm c}/\bar{R} \ll 1$ is not given. Furthermore, the LSW approach assumes a ripening system, whereas in these simulations the nucleation stage is included. This suggests to derive a scaling constant $\tau'_{\rm MC} = [R(i^*)^3/V_{\rm a}]\tau_{\rm MC}$, which is modified by the critical nucleation size. Using Eq. (6.2) in order to obtain i^*, Fig. 6.4b shows the result of the modified scaling attempt. While there is an excellent agreement for $\epsilon \geq 1.75$ (the curves are hardly distinguishable) the other two cases deviate (with respect to Fig. 6.4a an overcompensation for high temperatures is observed). Having in mind the

uncertainties related to Eq. (6.2) and that the LSW regime of coarsening could not be reached with the available computer capacities, a more detailed study of the K3DLMC scaling behavior remains to be done in future approaches.

6.1.2 Comparison of K3DLMC and RDE simulations of OR

The RDE approach to OR verifies the LSW predictions provided that $R_c/\bar{R} \gg 1$ holds [40, 149], thus it is interesting to apply the RDE method to systems characterized by $R_c/\bar{R} \approx 1$. The direct comparison to the K3DLMC method reveals, furthermore, the similarities and differences of the atomic and thermodynamic descriptions of domain growth.

Therefore, after a K3DLMC run for 4×10^5 MCSs of a system quenched to $\epsilon_{fcc} = 1.75$, the further evolution of the NC ensemble was followed also in parallel with the RDE description in the diffusion controlled regime. Fig. 6.5 shows the corresponding results after 3.6×10^6 MCSs, where the RDE parameters have been chosen such as to give identical capillary lengths. At a first glance both simulation results seem to be very similar, but a closer inspection reveals certain differences of the microscopic evolution (positions and sizes of remaining NCs).

In order to compare the dynamics of both simulation methods, Fig. 6.6 shows the evolution of the NC densities, which obey a quite similar behavior. The additional plot of n obtained by the RDE method using the linearized GT equation [LSW approximation, Eq. (4.11)] exhibits the influence of the choice of the driving force on the dynamics of OR. The differences in the dynamics of both RDE simulations is also reflected in the time scales of coarsening. For this particular comparison the durations of ripening [measured in units of τ_{diff}, Eq. (4.16)] are related by $\Delta t_{\text{LSW}} \approx 3\Delta t_{\text{GT}}$. In general, this time difference is a function of the ratios $\bar{R}_i/R_c$ and $\bar{R}_f/R_c$ for the initial and final mean radii and vanishes for $\bar{R}/R_c \to \infty$. Since the K3DLMC method excellently reproduces the GT relation (see Fig. 3.8) it is obvious, that a parallel or subsequent RDE approach should use the same dynamical description.

As already pointed out, a more detailed analysis reveals, that the sequence of dissolving NCs depends on the simulation approach. Fig. 6.7a shows the differences of the evolution of the NC ensemble in the parallel treatments by directly comparing the sizes. These differences with respect to the detailed evolution within each simulation method is not really surprising, because the RDE simulation is deterministic once the input data ($\{\vec{r}_i\}$, $\{R_i\}$) have been fixed, while the K3DLMC simulation is stochastic in nature.

A further analysis with respect to the movement of NCs inherently included in the K3DLMC method is shown in Fig. 6.7b. In this plot for each surviving NC of the MC simulation the nearest remaining NC in the RDE simulation is determined (note that the monopole approximation used in the RDE method does not allow for NC diffusion; they remain fixed at their positions). While a majority of the NCs has moved at most $\Delta r = |\vec{r}_f - \vec{r}_i| \approx 4\, a_{\text{fcc}}$, the few with no close remaining counterpart can easily be explained by the difference in the sequence of NC dissolution of both descriptions.

Although the dependence of the effective coarsening dynamics on the ratio $R_c/\bar{R}$ seems to offer a reasonable explanation for the observed growth exponents, there might be ad-

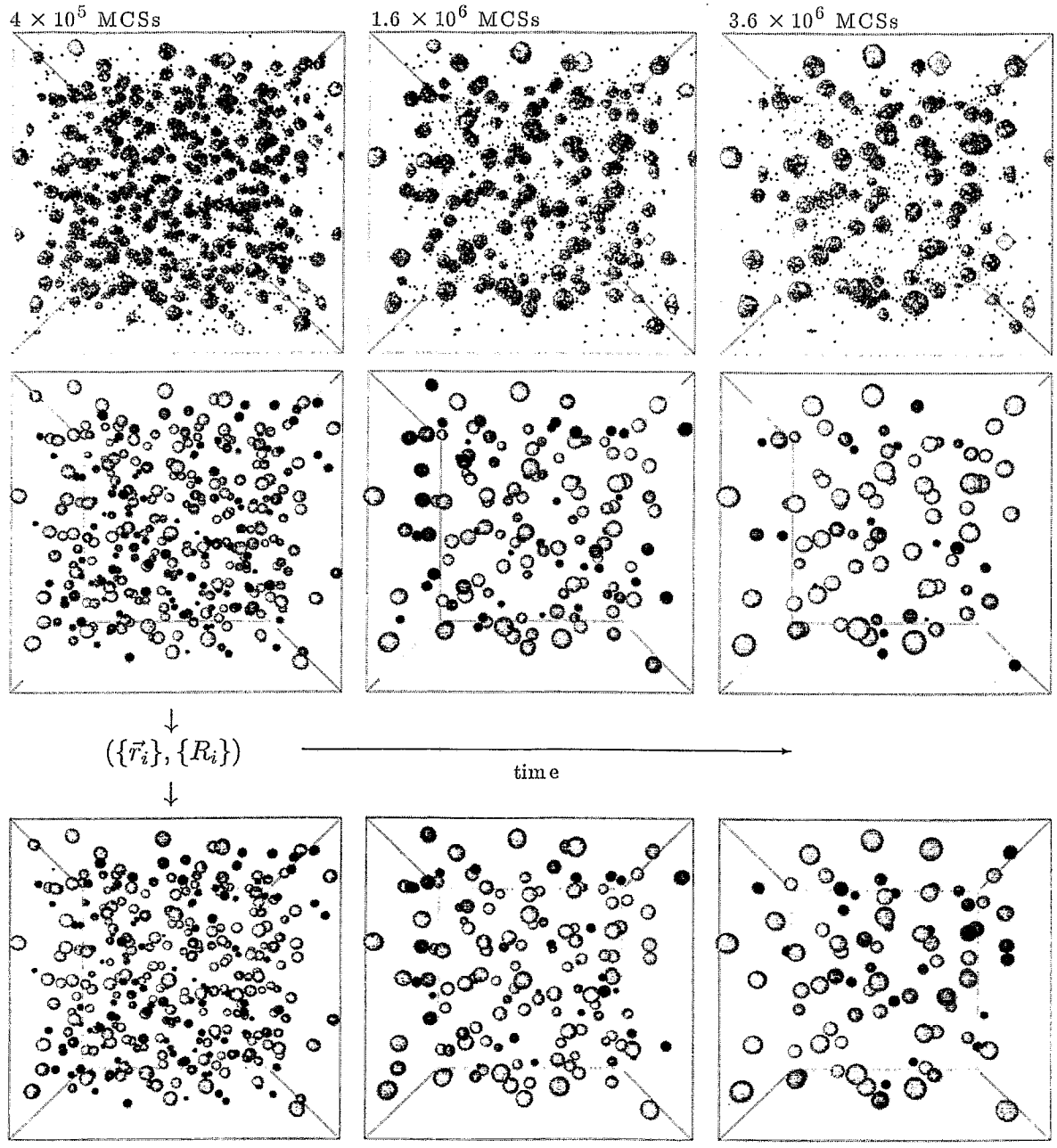

Figure 6.5: Comparison of OR simulations with K3DLMC and RDE methods of a fcc system with volume fraction $\phi = 0.01$ quenched to $\epsilon_{\text{fcc}} = 1.75$. Upper row: snapshots from the K3DLMC simulation; middle row: the corresponding spherical cluster representation. The RDE simulation starts with K3DLMC input data as recorded at $t = 4 \times 10^5$ MCSs. Lower row: the ensemble is shown at equal NC densities, i.e. $n_{\text{RDE}} = n_{\text{MC}}$.

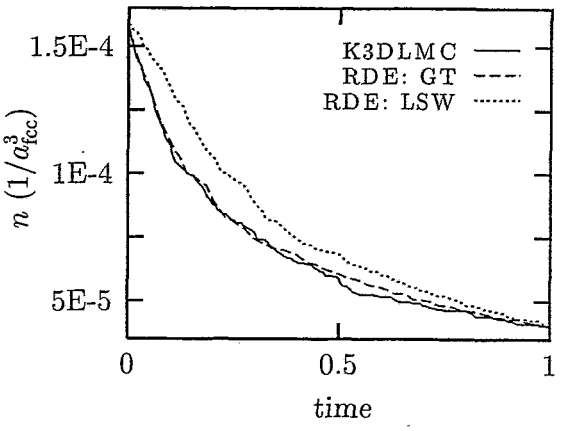

Figure 6.6: Comparison of the evolution of the density of NCs obtained by the K3DLMC and RDE methods in the normalized time interval between $t = 4 \times 10^5$ and $t = 3.6 \times 10^6$ MCSs (see Fig. 6.5).

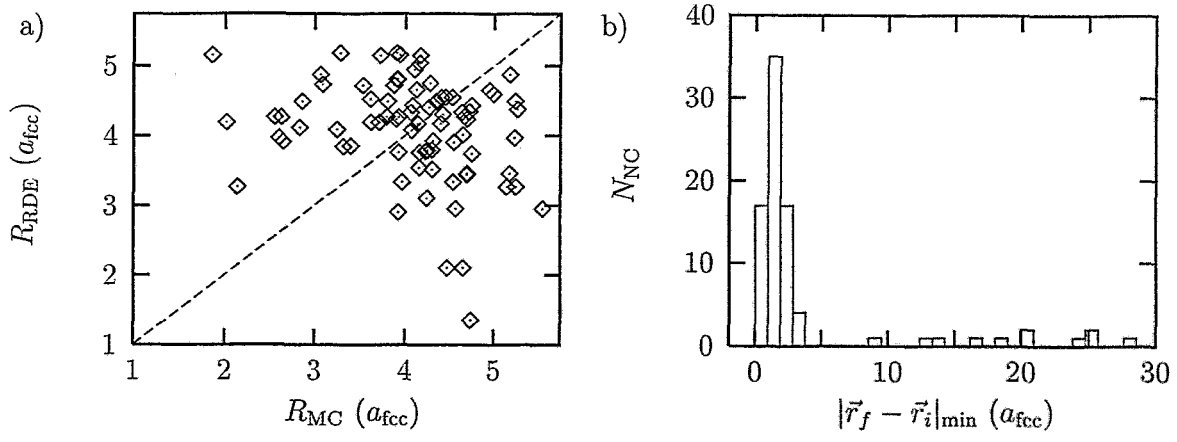

Figure 6.7: Comparison of the evolution of NCs obtained by the K3DLMC and RDE (with GT) methods. In a) the radii as obtained by both methods are directly compared. In b) for each remaining NC of the K3DLMC ensemble the distance to the nearest remaining NC of the RDE ensemble is determined.

ditional factors influencing the phase transformation. Since the K3DLMC method automatically includes the migration of NCs, it is tempting to analyze, if the NC dynamics can be brought into accordance with the BINDER-STAUFFER theory of cluster growth [202, 203, 78]. In their model the cluster evolution proceeds mainly via coagulation rather than monomer evaporation and condensation. Therefore, coarsening occurs via coalescence of diffusing NCs and is thus determined by the effective diffusion coefficient $D_{\mathrm{NC}}(i)$ of NCs. Depending on the detailed atomic mechanism, by which the center of mass of a NC moves (e.g. surface diffusion, diffusion of a vacancy within the NC or evaporation of a monomer

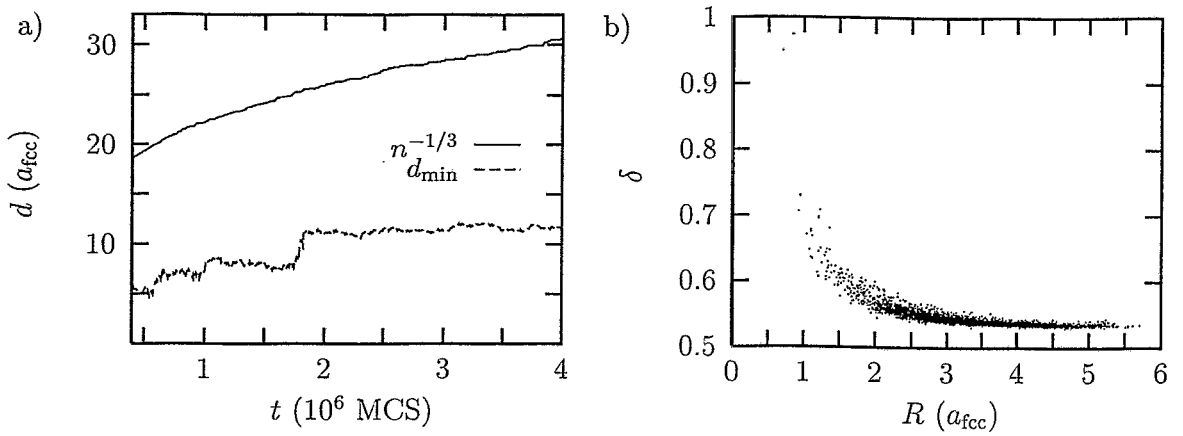

Figure 6.8: In a) the evolution of the mean NC distance given by the inverse cubic root of the density is compared to the minimum NC distance in the ensemble. In b) the spectrum of the NC shape parameter δ during OR ($4 \times 10^5 < t < 4 \times 10^6$ MCSs) as recorded every 2×10^5 MCSs is plotted.

and re-condensation at a different surface site) a growth law is derived, which in three dimensions varies between the regimes $\bar{R} \propto t^{1/6}$, $\bar{R} \propto t^{1/5}$, and $\bar{R} \propto t^{1/4}$, respectively. For instance, TORAL and MARRO [204] interpreted the change of the evolution of the excess energy $\Delta E/J \propto \bar{R}^{-1}$ from a 1/6 to a 1/3 growth regime with a change from the cluster coagulation to the OR coarsening mechanism.

In order to proof, whether this cluster growth mode explains the observed time dependences, the K3DLMC results have to be checked for the motion of NCs and for deviations from the quasi-equilibrated shape of faceted octahedras due to coalescence events. This is done by measuring in intervals of $\Delta t = 5000$ MCSs the minimum distance between any two precipitates defined as $d_{\min} = |\vec{r}_i - \vec{r}_j|_{\min} - R_i - R_j$. As the plateau-like behavior of $d_{\min}$ in Fig. 6.8a indicates, no evidence for diffusional encounters of NCs can be detected [the minimum observed distance of $\approx 5\, a_{\mathrm{fcc}}$ is larger than the maximum analyzed diffusion length $\Delta r_{\max} \approx 4\, a_{\mathrm{fcc}}$ (see Fig. 6.7b) for the whole coarsening process]. The slight negative slope of the plateaus is not necessarily due to NC diffusion; also NC growth (see definition of $d_{\min}$) can explain this observation. Consequently, in the recorded data of the NC shape parameter δ [Eq. (3.8)] no significant deviations can be observed except for the smallest NCs shortly to their dissolution (see Fig. 6.8b).

To summarize this subsection it should be noted, that both the atomic and mesoscopic simulation models result in the same cluster dynamics, provided the same driving forces are applied [use of the appropriate (i.e. exact or linearized) GT relation in the RDE approach]. This implies that the K3DLMC method would model the late stage of phase separation according to the LSW predictions if the computation power would allow for long lasting simulations (although here K3DLMC simulations of OR in three dimensions have been extended for two orders of magnitude in time (MCSs) compared to earlier studies, the LSW regime has not been reached for the chosen temperatures). With respect to

the movement of NCs observed in the K3DLMC simulations it would be interesting to check the range of NCs diffusion of corresponding RDE approaches extended to the dipole approximation (which take into account NC migration as well as shape deviation) [166].

6.2 Late stage evolution of as-implanted samples

Background

Self-organization is a well known phenomenon occurring in nature on several time and length scales [54]. In the area of IBS of nanostructures the observation of layers of NCs aligned parallel to substrate interfaces, for instance in the SIMOX process [205]-[208], can be explained by self-organization. The underlying dynamics in such finite systems may be determined by OR [209], and spatial inhomogeneities (e.g. the presence of interfaces or concentration gradients) are believed to be the reason for the modulated arrangement of NCs.

Computer simulations based on the RDE approach successfully described the occurrence of bands of NCs [41, 113] using a model, where an absorbing interface initiated the self-organization. Additionally the structure wavelength λ was determined as the characteristic interlayer distance, which is proportional to the diffusional screening length λ_D [111] [see also Eq. (3.18)]

$$\lambda(t) = \alpha\lambda_D(t) = \frac{\alpha}{\sqrt{4\pi n(t)\bar{R}(t)}}, \qquad \alpha \approx 3. \tag{6.5}$$

The discussions of Refs. [41, 113] have assumed the rather artificial initial condition of equal-sized precipitates across the implantation profile. Though experimental evidence supports this assumption [210], simulations beyond this approximation are needed to clarify the physics of this process. Especially the competition between the coarsening of NCs, which is initially suppressed in the studies of Refs. [41, 113], and the self-organization of NC layers have to be considered in more detail.

With the combination of both simulation tools, it is possible to consistently describe the evolution of IAs implanted into a substrate. In particular, the influence of an absorbing interface on the impurity redistribution can be included from the very beginning, which allows to trace back the origins of the observed spatial patterns to the NC nucleation stage [184]. From such K3DLMC simulations one obtains consistent NC distributions as input data for the RDE modeling. Within the framework of OR it is then studied how BCs and internal ripening interfere during the evolution of these structures.

K3DLMC simulations

Here, the study is restricted to systems, where the physical conditions during implantation prevent a significant redistribution of the deposited atoms before annealing. As an example, the evolution of an as-implanted Gaussian-like depth profile for a fluence of $F_0 \approx 30\ a_{fcc}^{-2}$ IAs has been simulated in a volume of $128 \times 128 \times 256$ fcc unit cells for $\epsilon_{fcc} = 1.75$. The

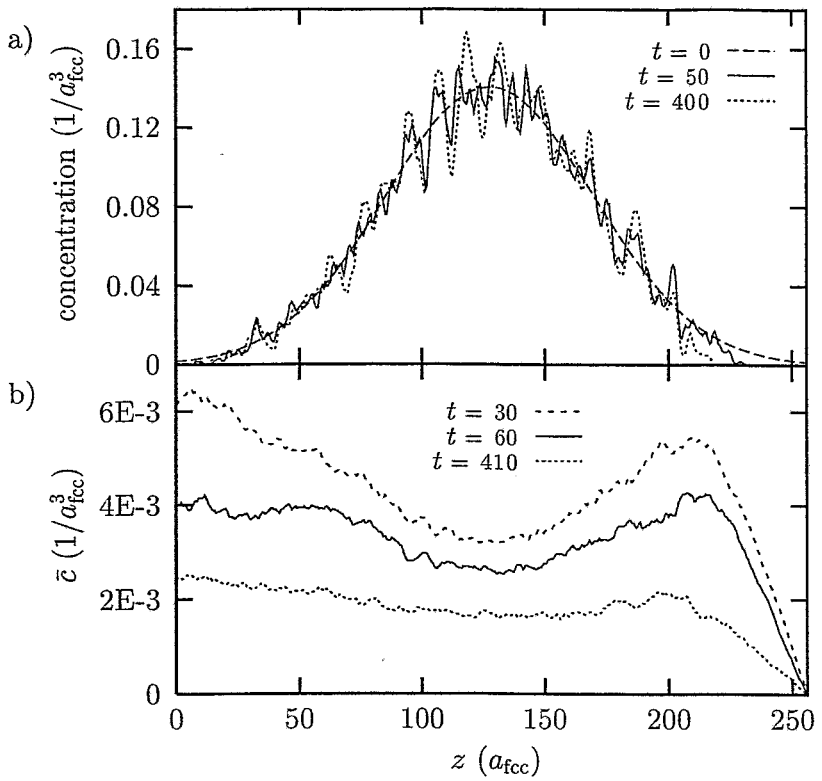

Figure 6.9: In the top plot the evolution of the impurity profile during the K3DLMC simulation is shown. Times are given in units of 10^3 MCSs. In the bottom plot, the monomer concentration $\bar{c}$ averaged over the last 10^4 MCSs with respect to the indicated MC times can be seen.

projected range of the peak concentration is $R_p = 128\, a_{fcc}$ (with $\Delta R_p = 42\, a_{fcc}$), and at a depth of $L_z = 256\, a_{fcc}$ an absorbing interface is set up. This corresponds to a symmetric implantation into a thin layer A on a substrate B, where either the impurities are volatile (diffuse out through the surface) or B acts a sink for the IAs.

The influence of the absorbing BC is clearly seen in Fig. 6.9a, where MC simulation results of the evolution of the depth distribution of implanted IAs are plotted. The absorbing interface causes an asymmetry of the profile with a NC free region spreading out towards the center. Across the profile, some structuring occurs as indicated by the evolving peaks.[3] More insight in the mechanisms of impurity redistribution is gained by plotting the monomer concentration versus depth (see Fig. 6.9b). Whereas the reflecting interface at $z = 0$ is characterized by a vanishing concentration gradient at a finite value of c, the concentration gradient at $z = L_z$ is proportional the the monomer flow out of the system. The overall concentration decrease with time is due to the increase of the average radius

[3]Note, that this local structuring is only visible due to the finite lateral dimension of the simulation volume.

(GT relation) during coarsening. Since the velocity of OR depends on the volume fraction ϕ of impurities (the higher ϕ the less is monomer diffusion length between shrinking and growing NCs), the minimum of c around R_p is in accordance with the observation, that the largest NCs can be found there (see also Fig. 6.10 below).

It should be noted, that despite diffusional screening effects the monomer concentration profile of Fig. 6.9b indicates a net flow of impurities from the tails of the profile towards the center. These concentration gradients give an explanation of experimentally observed accumulation of implanted impurities close to R_p in terms of ordinary rather than "up-hill" diffusion.

RDE simulations

In order to discriminate between internal ripening effects and boundary-induced structuring, two different sets of input parameters have been extracted from the K3DLMC method. In both cases, the positions of the NCs have been transferred. Then for one run of the RDE simulation the atomically derived radii have been used [case (i)], whereas in the other case (ii) the mean radius $\bar{R}$ has been assigned to each NC. The long time behavior of both systems can be seen in Fig. 6.10. In both RDE simulations the absorbing interface was described by the BC[4] $c(L_z) = c_\infty$ (as used in Ref. [41]). Obviously, for case (i), the BC has only a minor influence on the impurity redistribution. Pronounced self-organization into layers of NCs is only observed using the rather artificial condition $R_i(t_{\mathrm{RDE}} = 0) = \bar{R}$.

Discussion

Right from the beginning of thermally activated impurity diffusion, nucleation of NCs starts beginning in the center of the profile, where the highest supersaturation is found. After the monomer concentration has dropped considerably, local OR is initiated by small size differences. Since according to the GT equation the equilibrium monomer concentration decreases with increasing cluster size, precipitates slightly larger than the average become a more effective sink to diffusing monomers. Thus small fluctuations initiate a self-amplifying coarsening process over the whole implantation profile.

Assuming an approximately constant mean NC radius across the profile (this should be a reasonable assumption for the early phase separation process), the diffusive screening length λ_D, and thus the structure wavelength λ [Eq. (6.5)], varies with depth and is smallest in the center of the profile, where the density of precipitates is highest. During annealing the diffusive screening length evolves (in the case of diffusion controlled coarsening) proportional to $t^{1/3}$ according to the time dependences of $n(t)$ and $\bar{R}(t)$ [LSW theory, see Eqs. (4.16) and (4.17)]. This is the reason, why spatial structures, which are in phase with λ (i.e. self-amplifying) during a certain time, grow out of phase for later times and then start a competitive growth among each other.

[4]Noting the value $c_\infty(\epsilon_{\mathrm{fcc}} = 1.75) = 0.11 \times 10^{-3}\, a_{\mathrm{fcc}}^{-3}$, the choice $c(L_z) = 0$ used in the K3DLMC simulation (see Fig. 6.9) obviously has had a negligible influence on the early stage of impurity redistribution.

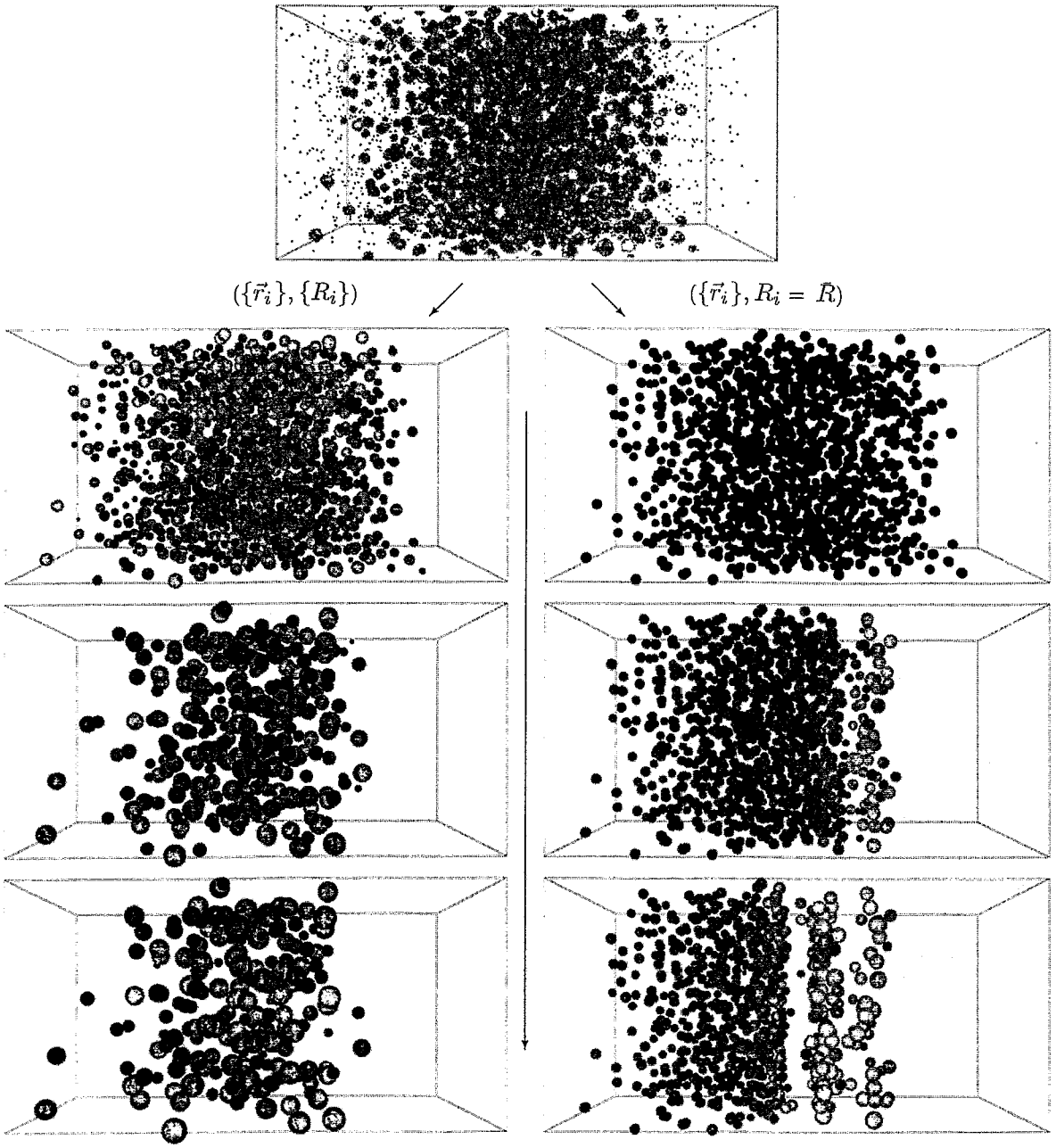

Figure 6.10: Combined K3DLMC and RDE simulations of the redistribution of IAs during annealing in the presence of an absorbing interface. In the top row, the microstructure of an as-deposited profile is shown after 4×10^5 MCSs for $\epsilon_{\mathrm{fcc}}=1.75$. For the left column the sets $(\{\vec{r}_i\},\{R_i\})$ are used as input for the RDE simulations. For the right column only the positions are transferred, whereas the mean radius $\bar{R}$ is assigned to each NC.

It should be noted, that while the spatial inhomogeneity due to the (Gaussian) concentration profile influences all NCs, the diffusional interaction with the absorbing interface is screened by the precipitates located in the tail towards the interface. For the K3DLMC simulation the effective depth of this interaction range can be associated with the z coordinate breaking the symmetry of the monomer concentration field (see Fig. 6.9b). Thus self-structuring across the profile starts before diffusional interaction between the interfaces and the main fraction of NCs sets in.

However, as can be concluded from the RDE simulations of system (i), internal OR does not necessarily induce the formation of bands of NC. Yet the signature of this internal coarsening is pronounced enough to dominate over the disturbance present due to the absorbing BC. As can be seen in the right column of Fig. 6.10, only suppressing internal OR by assigning all NCs the same initial radius (i.e. all precipitates possess the same equilibrium concentration, thus no monomer concentration gradients are present) allows the formation of periodic layers induced by the absorbing interface.

From the simulations presented above it can be concluded, that the observed tendency towards self-organization in systems modeled consistently beginning from the nucleation stage does not necessarily result in equal-spaced layers of precipitates. Thus it is very likely, that in ion-implanted systems besides the driving force of phase separation further physical effects (e.g. inhomogeneities due to radiation damage) influence the impurity evolution.

6.3 Focused ion beam synthesis of NC arrays

In CBII the formation of NCs can be controlled to some extent with respect to ensemble properties like the average depth or the mean radius. Furthermore, a specific dispersion of the size distribution seems to be inevitable, which is in contrast to the need of monodisperse sizes in certain applications. The use of a finely focused ion beam (FIB) [48] promises to open new methods of NC synthesis by a precise control of the lateral deposition pattern as well as of the implanted fluence. Besides forming buried structures by "writing" the desired pattern with the FIB directly onto the substrate, an interesting application is the defined synthesis of a single nanocrystal at a chosen position on the substrate.

A straightforward extension would be the synthesis of a regular array of nanocrystals [211, 44], which would possess a monodisperse size distribution due to (ideally) identical implantation conditions at each spot. For appropriate NC-substrate systems, the two-dimensional periodic array can be regarded as a photonic-bandgap material [212, 213] specifically influencing the properties of light transmission. While such structures have been designed with lattice spacings in the range of several μm or larger, photonic band-gap materials in the range of visible light are difficult to synthesize. In this area, the formation of periodic arrays of NCs by FIB implantation might provide a promising alternative.

It is, however, a priori not clear if the deposited fluence per spot coalesces into a single NC, or if losses into the surrounding substrate dominate the evolution. Furthermore, in a periodic array of precipitates, there is necessarily diffusional interaction among the spots. In this context it is interesting to explore, if the spots first coalesce into single NCs and

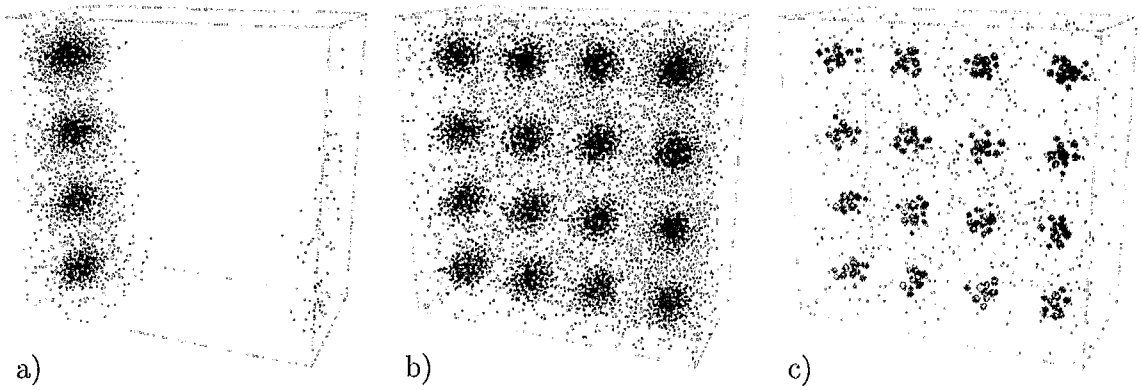

Figure 6.11: K3DLMC simulation of FIB implantation for a periodic array of implantation spots. Figs. a) and b) refer to stages during implantation, whereas Fig. c) shows the microstructure during annealing.

then, on a quite different time scale, start to ripen, or if inter-spot ripening dominates over intra-spot ripening right from the beginning of impurity redistribution.

In a preliminary simulation series of idealized FIB synthesis of NCs, the evolution of a 4×4 array of implantation spots has been studied. Using system dimensions of $256 \times 256 \times 128$ fcc unit cells, per spot $N_{\text{spot}} = 5000$ IAs have been deposited according to a Gaussian depth distribution with $R_{\text{p}} = 37\, a_{\text{fcc}}$ and $\Delta R_{\text{p}} = 8\, a_{\text{fcc}}$. Two lateral distributions have been considered, each defined by a radial Gaussian with $\Delta R_{\text{r}} = 8\, a_{\text{fcc}}$ and $\Delta R_{\text{r}} = 12\, a_{\text{fcc}}$, respectively (recently SAKAGUCHI *et al.* [214] reported a beam size of 5-8 nm for a Ga metal ion source operating at an ion energy of some tens of keV[5]). In what follows, these radial distributions are referred to as 'high' and 'low' focused implantations. Fig. 6.11 shows snapshots during and at the end of the simulation procedure of implantation in the case of the high-focused system at $\epsilon_{\text{fcc}} = 3$ using periodic BCs in lateral directions. The corresponding cluster distribution obtained after 8×10^5 MCSs for $\epsilon_{\text{fcc}} = 2$ can be seen in Fig. 6.11c. Once a characteristic NC distribution has been developed the computational efficiency of the RDE approach with respect to OR can be used to model the further evolution of the samples.

Figs. 6.12 and 6.13 show simulation results of the late stage evolution for the high and low focused systems, where in both cases material conservation was assumed. Although within one sample the implantation conditions were identical, the evolution for each spot seems to be governed by the statistical process of precipitation. While in some spots a large NC forms very early and thus mainly dominates intra-spot OR, other spots are characterized by a few nearly equal-sized NCs, which compete in coarsening. This can considerably slow down the intra-spot redistribution and thus inter-spot OR becomes important. As can be clearly seen for the low-focused sample (Fig. 6.13), the influence of inter-spot coars-

[5]The effective radial impurity distribution within the substrate is given by the convolution of the beam profile and the radial straggling, which depends on the ion energy and the substrate composition.

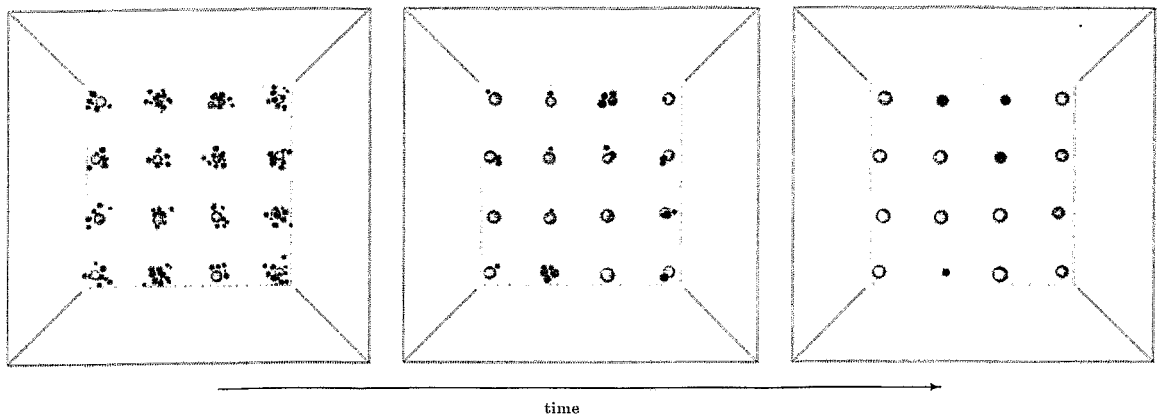

Figure 6.12: Evolution of the high-focused sample obtained by the RDE approach using K3DLMC input data.

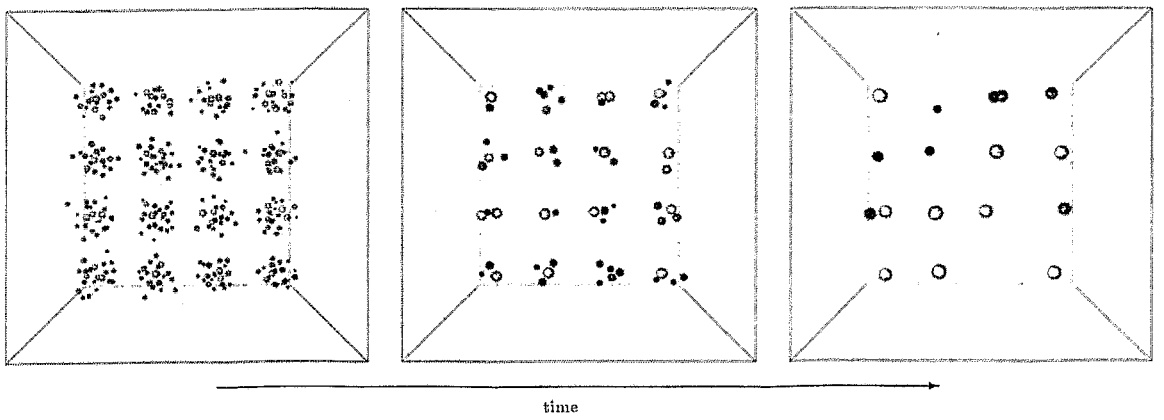

Figure 6.13: Evolution of the low-focused sample obtained by the RDE approach using K3DLMC input data.

ening can be so large, that spots disappear before the impurities within other spots have condensed to a single NC. A clear requirement for the formation of periodic arrays of dots is the absence of impurity losses, for instance evaporation through the surface or diffusion into deeper parts of the substrate. For instance, in simulations assuming an absorbing interface at $z = L_z$ (not shown here), even in the high-focused sample NCs within certain spots completely dissolved before in other spots condensation into one single NC was achieved.

The redistribution of IAs observed for annealing at low to moderate temperatures seems not to guarantee the condensation of the complete fluence per spot into a single NC. Even in the high-focused example, where one NC per spot was temporarily obtained, there is a considerable dispersion in the size distribution due to diffusional interaction between

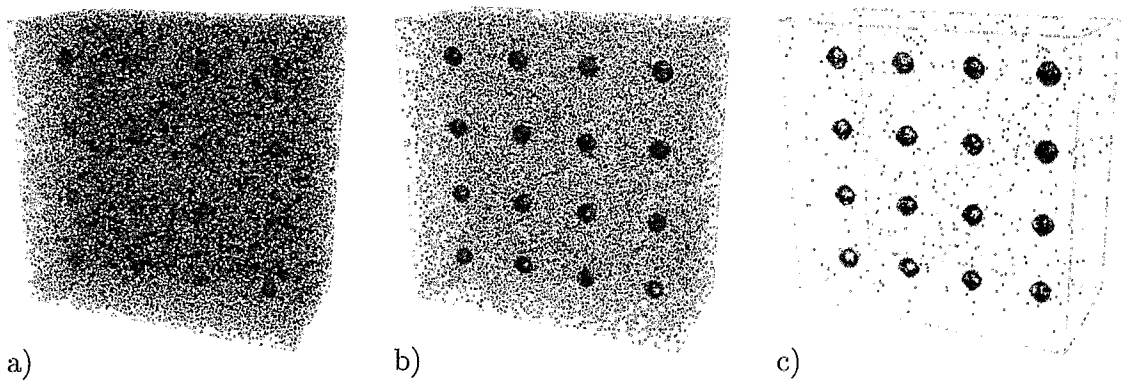

Figure 6.14: K3DLMC simulation of rapid high-temperature annealing of a periodic array of implantation spots (the microstructure prior to annealing is similar to the one shown in Fig. 6.11b). Here, $N_{\mathrm{spot}} = 10^4$ IAs per spot are initially annealed at $\epsilon_{\mathrm{fcc}} = 1$. Increasing ϵ_{fcc} every 5×10^4 MCSs about $\Delta\epsilon_{\mathrm{fcc}} = 0.25$, Figs. a) – c) show the evolution after 5×10^4 ($\epsilon_{\mathrm{fcc}} = 1$), 1.5×10^5 ($\epsilon_{\mathrm{fcc}} = 1.5$), and 2.5×10^5 ($\epsilon_{\mathrm{fcc}} = 2$) MCSs, respectively.

spots. The uncertainty in real experiments about the actually implanted fluence per spot is supposed to increase this size dispersion even further. Although the spots are spaced regularly (an assumption, which can not expected to be met in experiments), the centers of mass of the remaining NCs do not coincide with the centers of the implantation spots.

A more promising method seems to be rapid annealing to high temperatures followed by a controlled cooling as suggested by the simulation results of Fig. 6.14. Provided that material conservation holds within a thin film of thickness s (e.g. ideally $s \approx 2R_{\mathrm{p}}$), the underlying idea is to tune the effective supersaturation in such a way, that only one large NC nucleates, onto which the impurities within the spot collapse. As a consequence of the high temperature needed for this method a considerable fraction $\eta(T)$ of the N_{spot} impurities will be found dissolved as monomers. Assuming a two-dimensional spot density of n_{spot}, the following equilibrium monomer concentration according to the GT relation [Eq. (2.23)] will be found

$$\hat{c} = \frac{\eta N_{\mathrm{spot}}}{s n_{\mathrm{spot}}^{-1}} = c_\infty \exp\left\{\frac{R_{\mathrm{c}}}{R^*}\right\}, \quad R^* = \left[\frac{3}{4\pi}(1-\eta)N_{\mathrm{spot}}V_{\mathrm{a}}\right]^{1/3}. \tag{6.6}$$

The NC size R^* associated with $\hat{c}$ has to be larger than the critical size $R^*_{\mathrm{nuc}}(T)$ for this temperature in order to prevent a complete dissolution.

After the high-temperature anneal the subsequently applied cooling rate should be chosen such that secondary nucleation is hindered in the sample. This guarantees that essentially the whole fraction ηN_{spot} of impurities diffuses back to and condenses onto the central NC. According to Fig. 6.14 this methods supports the formation of a nearly monodisperse, highly periodic two-dimensional array of precipitates.

Chapter 7

Application of the K3DLMC method to special topics in IBS

Besides describing the evolution of a single implanted impurity species in a neutral matrix, the K3DLMC method can be applied to a variety of other systems. In this Chapter simulation results of the influence of an oxidizing annealing atmosphere on the redistribution of impurities are shown [215]. Furthermore, the K3DLMC method is extended to include two types of interacting IAs in order to study various aspects of compound NC formation by IBS.

7.1 Influence of the annealing atmosphere on the redistribution of impurities

Nanocrystals of elemental semiconductors (Si, Ge, Sn) in SiO_2 are particularly interesting due to their electro- and photo-luminescence (see e.g. [22, 23, 216]) and their potential use for non-volatile memory devices (see e.g. [217]-[219]). Besides various preparation methods based on thin-film deposition techniques (e.g. by chemical vapor deposition (CVD) [24] or by sputtering [220]), IBS of such NC/substrate systems is a promising option, because of its compatibility with standard microelectronics process technologies.

The impurity redistribution and nanocrystal evolution can be strongly influenced by the annealing ambient as has been reported for Ge implanted SiO_2 layers [22]. The origin of this behavior is in-diffusion of an oxidant from the annealing atmosphere, which changes substantially the Ge depth profile and NC distribution. In order to study systematically the influence of the annealing ambient on the microstructure of Ge implanted SiO_2, samples have been annealed in N_2, Ar or dry O_2 atmospheres [215], which have different concentrations of chemical reactive components (H_2O, O_2).

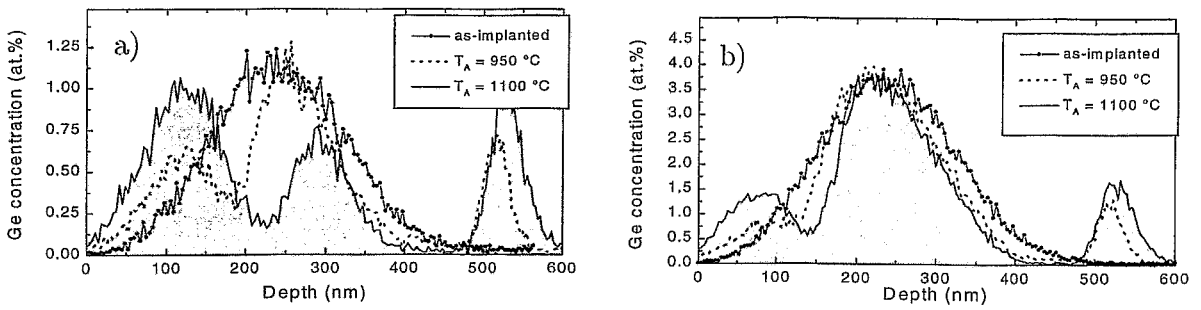

Figure 7.1: Ge concentration profiles obtained from RBS spectra (taken from Ref. [215]) of 500 nm thick SiO_2 layers on Si which were implanted with 350 keV Ge^+ and subsequently annealed in N_2 for one hour. (a) Fluence: 1.5×10^{16} cm^{-2}, (b) Fluence: 5.0×10^{16} cm^{-2}.

7.1.1 Experimental observations

Experimental setup

In a series of experiments aimed at studying the properties of ion beam synthesized semiconducting NCs in SiO_2, 350 keV Ge^+ ions have been implanted into 500 nm thick SiO_2 layers, which were thermally grown at 1100 °C by wet oxidation of [100] oriented Si wafers. Implantations have been performed at "room temperature" (sample heating up to 90-100 °C at current densities of 1-2 $\mu A/cm^2$) in a fluence range between 5×10^{15} and 5×10^{16} cm^{-2}, which results in peak concentrations of implanted Ge of 0.4-4 atomic percent. The annealing was performed at 950, 1000 and 1100 °C in a standard furnace for 15 to 180 min using the "inert" gases of N_2, Ar or the "reactive" gas of dry O_2 (all of 5.0 purity). The Ge depth distribution in the SiO_2 layer after each annealing was measured by standard RBS (1.7 MeV $^4He^+$, backscattering angle 170°), while the precipitate structures were studied by XTEM.

Annealing in "inert" gases N_2 or Ar

In Fig. 7.1 RBS measurements of Ge depth distributions are shown. The as-implanted Ge profiles are located inside the SiO_2 layer, i.e. the Ge concentrations at the surface and the SiO_2/Si interface are below 1% of the peak concentration. For both fluences the RBS analysis shows unusual changes in the Ge depth distributions after annealing at 950 °C in N_2. In general, three well-separated peaks are found, whose separation from each other increases with increasing annealing temperature. The width and height of the central Ge peak decrease and the two satellite peaks grow. As it has been shown by STEM-EDX analysis [71], the Ge at the SiO_2/Si interface is located within a thin Si layer adjacent to the SiO_2 layer, where it forms a few monolayers of a Si-Ge alloy.

In the as-implanted samples no Ge clusters could be detected by TEM as evidenced by Fig. 7.2a. However, after annealing (see Figs. 7.2b-c), in the center of the SiO_2 layer Ge

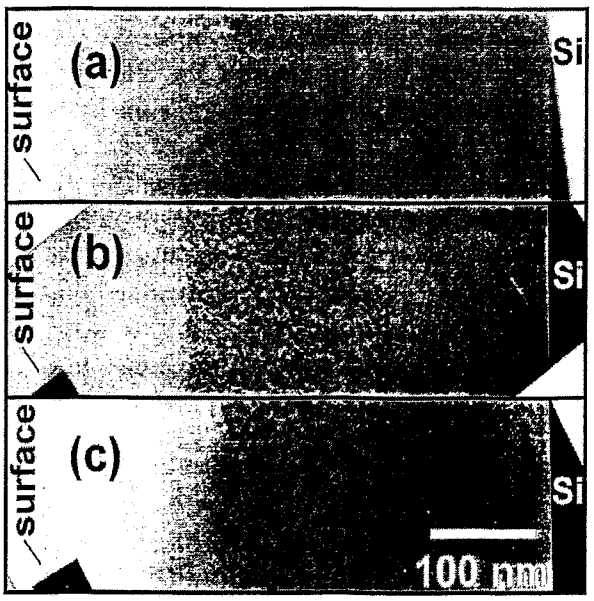

Figure 7.2: XTEM micrographs (taken from Ref. [215]) of 500 nm thick SiO_2 layers on Si implanted with Ge (fluence 5.0×10^{16} cm^{-2} at 350 keV) prior to annealing (a) as well as after annealing for one hour at 950 °C (b) and 1100 °C (c).

NCs appear which are related to the central peak in the RBS spectrum (see Fig. 7.1b).

For the Ge NC distribution of Fig. 7.2c, a mean cluster size of 6 nm is observed, which is in good agreement with the mean cluster size of 6.4 ± 0.7 nm measured by X-ray diffraction (XRD) [22]. Towards the SiO_2 surface, the Ge cluster band is terminated by a very narrow (11 ± 1 nm) edge region, which is in contrast to the smooth tail of NCs facing the Si substrate. Surprisingly no Ge clusters were found between the sharp edge of the cluster band and the SiO_2 surface, where a pronounced sub-surface peak of Ge was observed by RBS (see Fig. 7.1). X-ray photoemission spectroscopy (XPS) measurements [215] reveal that Ge $2p_{3/2}$ photoelectrons coming from the central, cluster-related peak and from the interface peak can be attributed to a large extent to Ge–Ge and Ge–Si bonds respectively, whereas the energy of photoelectrons from the sub-surface peak is shifted indicating Ge–O bonds. The Ge redistribution and NC evolution of identically implanted but Ar annealed SiO_2 layers are quite similar to the samples annealed in N_2. However, the Ge redistribution can be largely suppressed by the deposition of a 20 nm thick film of Si_3N_4 on top of the SiO_2 layer before implantation.

Annealing in dry O_2

In order to study systematically the influence of an reactive ambient, annealing of 5.0×10^{16} cm^{-2} Ge implanted 500 nm thick SiO_2 layers has been also carried out in dry oxygen at 950

°C. After annealing for 15 min the general features of the NC depth and size distribution appear to be similar to samples annealed in N_2 or in Ar. In particular, elemental Ge nanocrystals form in the center of the profile and the RBS spectrum shows a sub-surface peak of Ge in a region where no nanocrystals can be seen by XTEM. At longer annealing times (30 and 45 min) the sharp edge of the cluster band of elemental Ge shifts progressively into the depth of the layer. In contrast to annealing in N_2 or Ar, on the rearside of the moving sharp edge of the Ge NC band a layer of diffuse precipitates is observed. Since (i) in TEM micrographs these NCs exhibit a weaker Z-contrast than elemental Ge nanocrystals and (ii) under high-resolution conditions no lattice planes could be found, they are assumed to be oxidized (disordered or glassy) Ge clusters. After annealing for 90 min the elemental Ge clusters disappeared completely, and a region of GeO_2 precipitates remains.

Discussion

The following model for the Ge redistribution and NC evolution is proposed: The Ge^+ ion implantation forms a highly supersaturated solid solution of Ge in SiO_2. At the initial stage of annealing most of the Ge nucleates to tiny Ge NCs, whereas a small fraction of Ge remains dissolved in SiO_2 (inserting the mean radius $\bar{R}$ into the GT relation [Eq. (2.23)] yields a good measure of the average supersaturation, provided that the materials parameters entering the capillary length are known). During annealing an oxidant (e.g. moisture being present with an extremely low concentration in the annealing atmosphere) can diffuse into SiO_2, where it oxidizes dissolved Ge. Assuming for both species comparable monomer fluxes (i.e. $D_{ox}c_{ox} \approx D_{Ge}c_{Ge}$), the zone of GeO_2 formation should lie between the surface and the cluster band.

This explains immediately two features of the experiments. (i) As the oxidant reacts with Ge dissolved in SiO_2, the resulting GeO_2 does not form clusters, rather it is transformed to become part of the glassy SiO_2 matrix. Thus, the Ge accumulated there as GeO_2 can be seen as a peak in the RBS spectra, however not as clusters in XTEM images. (ii) The small distance between the sink (the zone of GeO_2 formation) and the source (the layer of Ge clusters) of Ge monomers leads to a steep gradient of dissolved Ge. Therefore, an effective dissolution of clusters occurs only within a narrow layer of the cluster band whose width is in the order of the diffusional screening length λ_D [see Eq. (3.18)]. Estimating the mean cluster radius $\bar{R}$ from Fig. 7.2 and calculating the corresponding cluster density n according to the implanted fluence, the diffusional screening length can be calculated to be $\lambda_D \approx 10$ nm. This value is in excellent agreement with the width of the edge of the NC band (see Fig. 7.2).

The disappearance of the drastic Ge redistribution during annealing in samples protected by a diffusion barrier (Si_3N_4 capping layer) underlines the strong influence of tiny oxidant concentrations in the annealing ambient. An interaction of N_2 of the annealing ambient with the Ge implanted into the SiO_2 layer can be ruled out as annealing in an inert Ar atmosphere results in a similar Ge redistribution. Thus, it can be concluded that the few ppm of oxidizing impurities in the high-purity annealing gases N_2 and Ar cause the strong impact on the Ge profile in SiO_2. The main impurity in these gases is moisture

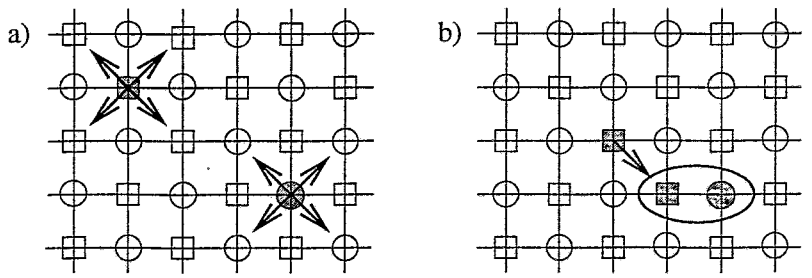

Figure 7.3: Using a two-dimensional scheme in a) the impurity (○) and oxidant (□) diffusion on both fcc sublattices are shown. An oxidation event can be seen in b), which occurs upon a nearest-neighbor encounter ($\Delta r = |\vec{r}_{\mathrm{IA}} - \vec{r}_{\mathrm{ox}}| = a_{\mathrm{fcc}}/2$) of IA and oxidant.

(H_2O), which dissolves and diffuses readily in SiO_2 [221].

In comparison to annealing in N_2 or Ar, annealing in dry O_2 increases the surface concentration of the oxidant by orders of magnitudes which over-compensates the smaller diffusivity of O_2 compared to H_2O [221]. Thus, the zone of GeO_2 formation shifts towards the edge of the NC band. Finally, the arriving oxidant cannot be consumed completely by dissolving Ge which results in direct oxidation of Ge nanocrystals.

At the SiO_2/Si interface the concentration c of Ge dissolved in SiO_2 is lower than c_∞ because the Ge–Si bond strength is more than 10% larger than the Ge–Ge bond strength [222]. In the NC region c is higher than c_∞ due to the convex interface curvature. The resulting concentration gradient leads to a diffusion flux and to an accumulation of Ge at the interface. There, Ge can either grow epitaxially on top of the Si substrate, or, for sufficiently high annealing temperatures, it can diffuse into the Si substrate.

7.1.2 Modeling of redistribution of implanted Ge in the presence of an oxidizing atmosphere

Modifications of the K3DLMC method

Modeling the evolution of implanted impurities in a reactive ambient requires the introduction of a second atomic species into the K3DLMC program. Defining the IAs on a fcc lattice, the second fcc lattice [shifted by $(1/2, 0, 0)a_{\mathrm{fcc}}$] of the bit-array not used so far is taken to accommodate the oxidant (see Fig. 7.3a) without the need to change the efficient bit encoding procedures. For this application, the evolution of the IAs (here Ge; in the following referred to as species X) is determined by their solubility [established by the bond strength J^{XX}; see Eq. (3.14)) and diffusion coefficient (the activation energy E_{A}^{X}). For simplicity, the oxidant (species Y) is not allowed to cluster, i.e. $J^{YY} = 0$. In this model, an oxidation event occurs upon a nearest-neighbor encounter of both impurity species (see Fig. 7.3b), which is a simple estimate of the capture radius entering the recombination term of a corresponding rate-equation description. By assuming an infinite bond strength between IA and oxidant ($J^{XY} \to \infty$) the reverse reaction (reduction of an

oxidized impurity) is suppressed. The oxidation site is recorded, and the reaction partners removed from the list of active atoms. Therefore, the oxidized impurities are not allowed to perform further diffusion or reactions.

For the simulations to be presented below it is assumed, that the use of an absorbing BC at $z = z_{SiO_2/Si}$ opposite to the surface describes the physics at the SiO_2/Si interface. This approach lowers the impurity concentration ($c = 0$ rather than $c = \tilde{c}_\infty$ due to the evolving SiGe alloy) at the interface, but is not supposed to distort the impurity evolution considerably.[1] Thus in the course of the simulation the evolving decoration of the SiO_2/Si interface with Ge is approximated by counting the number of IAs diffusing across the interface (and recording the site of the crossing).

The frequency of diffusional jumps of IAs (Ge) and the oxidant is according to their (assumed) diffusion coefficients D_{Ge} and D_{ox}. In each single diffusion step for an IA (an oxidant), the sc neighborhood of the final site is checked for the presence of an oxidant (an IA).

K3DLMC simulations

In order to obtain a qualitative understanding of the observed impurity redistribution, the evolution of an as-implanted profile was studied. Having in mind that Ge nanocrystals have diamond structure, the length scale a_{fcc} is gauged according to the Ge density ($\rho_{Ge} = 5.32$ g/cm^3 $\Rightarrow$ $a_{fcc} = 0.45$ nm). Rather than seeking on the atomic scale an exact geometrical matching of the simulation box with the experiment (for this problem a computationally favored simulation volume of $64 \times 64 \times 1024$ fcc unit cells does not pose any significant problem on computer memory but requires a very powerful CPU in order to achieve diffusional transport) a model system of dimension $64 \times 64 \times 256$ fcc unit cells was studied. Using a fluence of $F_0 \approx 15\, a_{fcc}^{-2}$ the initial sample was characterized by a Gaussian distribution with $R_p = 127\, a_{fcc}$ and $\Delta R_p = 40\, a_{fcc}$, and its evolution was followed at $\epsilon_{fcc} = 1.8$ for 10^6 MCSs. (In order to match the annealing at, say, 1000 °C, this would correspond to an activation energy for solution of $E_S \approx 1.18$ eV (see Section 3.5.3). However, since no reliable data of solubility properties of Ge in SiO_2 have been available, the simulation has to remain qualitative in nature.)

A snapshot of the corresponding microstructure obtained after 10^6 MCSs can be seen in Fig. 7.4a. For this simulation the oxidizing species were continuously deposited by keeping their concentration fixed in the surface layer ($c_{ox}|_{z=0} = 0.004\, a_{fcc}^{-3}$) and assuming a ratio of the diffusion coefficients $D_{ox}/D_{Ge} = 0.05$. While close to the surface the oxidized Ge accumulates, in the center of the deposited profile NCs have been formed. The interface decoration at $z = z_{SiO_2/Si}$ marks the impurity flow out of the system, which approximately corresponds to the evolving SiGe alloy.

The driving forces of the impurity redistribution can be seen in Fig. 7.4b, which shows the respective monomer concentration profiles after 1.1×10^5 MCSs. Since both the

[1] In a more advanced treatment one would set up a thin bulk layer of a third atom type Z (Si) at $z = z_{SiO_2/Si}$ additionally to the implanted impurities of type X (Ge) and use appropriate bond strengths $\{J^{XX}, J^{XZ}, J^{ZZ}\}$ in order to describe the SiGe alloy.

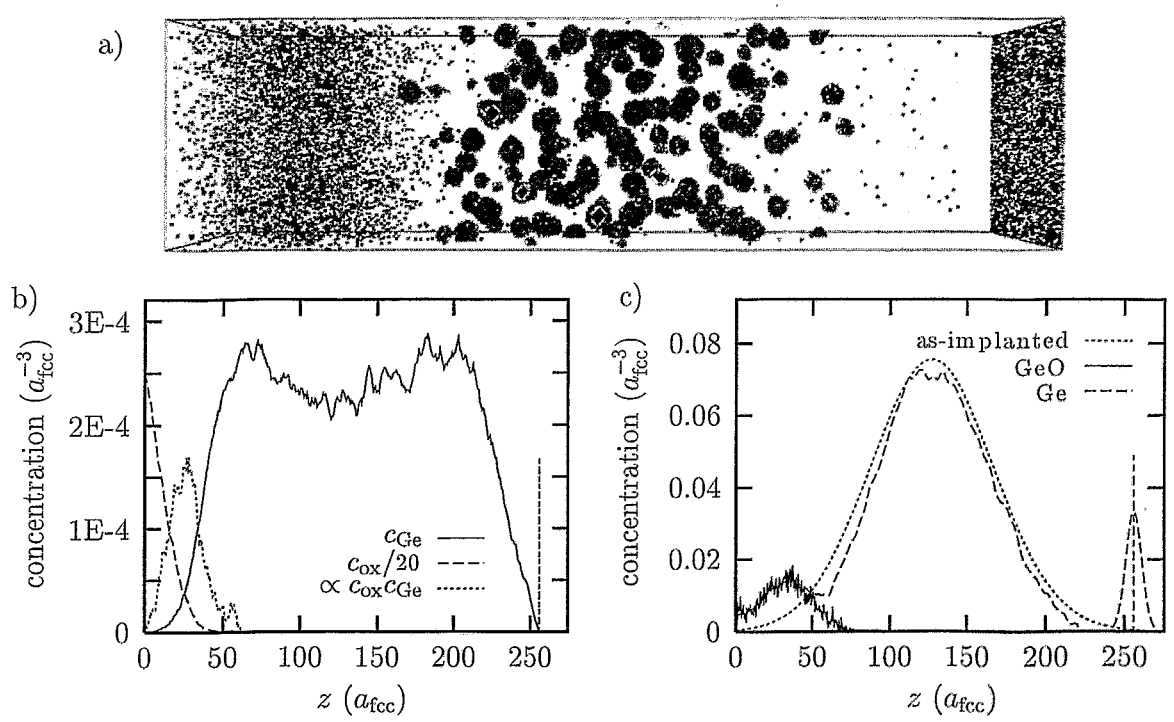

Figure 7.4: In a) the microstructure decomposed into oxidized Ge, Ge NCs and the interface decoration is displayed after a simulation period of 1.1×10^5 MCSs. In b) the corresponding impurity monomer concentration c_{Ge} (averaged over the last 10^4 MCSs) and the profile of the in-diffusing oxidant are plotted indicating the reaction zone. In c) the (smoothed) impurity profile as obtained after 10^6 MCSs is shown (the interface decoration has been artificially broadened).

SiO_2/Si interface and the sub-surface oxidizing region are sinks for dissolved Ge atoms, steep concentration gradients at both tails of the NC region reflect the resulting impurity flow. However, due to diffusional screening only the NCs in the very tails of the profile are subjected to the driving forces, whereas around R_p undisturbed coarsening is observed (see also Fig. 6.9).

The total Ge profile of the K3DLMC simulation (see Fig. 7.4c) is in excellent qualitative agreement with the RBS spectrum (see Fig. 7.1). In particular, the concomitant formation of a sub-surface peak of oxidized Ge, coarsening of NCs, and the evolving interface decoration have been observed. Furthermore, the steepening of the Ge profile towards the oxidizing zone is reproduced. However, also certain differences to the experiment should be mentioned. For instance, both tails of the simulated NC region appear to be similar, i.e. the K3DLMC simulation of Fig. 7.4 does not show a sharp edge of the cluster band towards the surface.

Additional to these simulations featuring the qualitative understanding of the observed Ge redistribution, more quantitative simulations are needed to understand the influence of

the level of oxidant concentration at the surface (related to the partial pressure of oxidant in the atmosphere) and to estimate the ratio of impurity and oxidant diffusion coefficients. Also the role of hydrogen supposed to be set free upon Ge oxidation (i.e. $H_xO + Ge \leftrightarrows GeO + H_x$) and its further influence on the system remains to be explored (upon otherwise identical conditions a Si_3N_4 capping layer not only suppresses the formation of a sub-surface region of GeO_2, but also, surprisingly, *modifies* the amount of Ge transferred to the SiO_2/Si interface [215]).

As a summary it is found that in Ge implanted SiO_2 layers the kinetics of Ge redistribution and NC evolution depends strongly on the annealing ambient. Atmospheres having oxidant (moisture) concentrations as low as a few ppm can cause a sequence of complex processes of diffusion and chemical reactions. Due to the low concentration of the moisture, the oxidant reacts with dissolved Ge monomers only (not with Ge clusters) in a zone between the surface and the cluster band and forms GeO_2 which is built homogeneously into the glassy SiO_2 network. Annealing in dry O_2 increases the surface concentration of the oxidant by orders of magnitudes which shifts the reaction zone into the band of Ge NCs, i.e. non-crystalline GeO_2 clusters are formed. The accumulation of Ge at the SiO_2/Si interface is due to the lower solubility at a flat interface and the relatively strong Ge–Si bonds.

7.2 Ion beam synthesis of compound nanoclusters

As already mentioned in the introduction, a large class of compound NCs has been synthesized in various substrate types by co- and sequential implantation of two or more species of IAs. In order to apply the K3DLMC method for multi-component systems, it has to be modified appropriately. Rather than applying the q-state POTTS model [152] with spin variables $q \geq 1$ in order to have the necessary degrees of freedom to define the occupation state of a lattice site,[2] two spatially identical l-lattices are used, which are mutually occupied by either X or Y species. While the efficient bit encoding of the single-component lattice gas can still be used, the computational effort for each jump attempt now more than doubles, because the nearest-neighbor sites of the jump configuration have to be checked in both the X and Y lattices. Whereas a restriction to the fcc and bcc lattices would have allowed to define the second species on a free sublattice, the above choice was motivated by the wish to have a common implementation for all three lattice types.

7.2.1 K3DLMC model for two types of interacting IAs

The decomposition of supersaturated multi-component solid solutions can be described in terms of classical nucleation theory [223]-[225]. Restricting the current study to two types X, Y of IAs and assuming like in Section 2.3.2 that NC growth and shrinkage proceeds by

[2] In a $q = 1$ POTTS model the occupation states $C_i = -1$, $C_i = 0$, and $C_i = 1$ can be used to represent a X particle, a vacancy, or a Y particle, respectively.

bimolecular steps only, the suitable extension of Eq. (2.11) reads

$$\frac{\partial U(i_X, i_Y, t)}{\partial t} = \sum_{j=1}^{2} [I(i_j) - I(i_j + 1)], \quad j \in \{X, Y\}. \tag{7.1}$$

The rate factors are now given by

$$I(i_j) = k_+(i_j - 1, i_l) U(i_j - 1, i_l, t) - k_-(i_j, i_l) U(i_j, i_l, t), \quad j, l \in \{X, Y\}. \tag{7.2}$$

The attachment and detachment coefficients $k_\pm(i_X, i_Y)$ are in general complicated functions of the local impurity concentrations as well as of NC composition.

Like in Chapter 3 a modeling approach is sought within the effective particle picture rather than via the determination of the coefficients $k_\pm(i_j, i_l)$. Assuming that the substrate is chemically inert with respect to both types of IAs, the complex interactions between an IA and the atoms of the host matrix as well as with other IAs of the same and/or of different kind are expressed in a set of effective nearest-neighbor bond strengths $\{J_l^{XX}, J_l^{XY}, J_l^{YY}\}$. For instance, the energetics of an IA of type X is given by the sum $nJ_l^{XX} + mJ_l^{XY}$ over all nearest-neighbor interactions, where n and m are the corresponding numbers of alike or different bonds. The diffusion of monomers of types X or Y is determined by their individual activation energies E_A^X and E_A^Y, respectively, for a single diffusional jump. Using the METROPOLIS algorithm [81] for the jump kinetics, the transition probability W_{if}^X for atoms of type X to jump from the initial site i to the final site f is

$$W_{if}^X = (\tau_0^X)^{-1} \exp\left\{-\left(\varepsilon^X + E_\mathrm{A}^X\right)\beta\right\}, \quad \varepsilon^X = (n_i - n_f) J_l^{XX} + (m_i - m_f) J_l^{XY}. \tag{7.3}$$

The jump probability reduces to $W_{if}^X = (\tau_0^X)^{-1} \exp\left\{-E_\mathrm{A}^X \beta\right\}$ in all cases for which $\varepsilon^X \beta \leq 0$. For simplicity, the (constant) rates of jump attempts $\{(\tau_0^X)^{-1}, (\tau_0^Y)^{-1}\}$ are assumed not to depend on the particular chemical neighborhood.

The corresponding single-component impurity-substrate systems can be used to determine the activation energies E_A and the bond strength J_l via proper adjustments to measured diffusion coefficients and solubilities. The mixed bond strength J_l^{XY} can then be derived from tabulated values of chemical bond strengths (see e.g. [222]).

The ratio of the numbers of MCSs of both subsystems is proportional to the ratio of the diffusion coefficients. Since in this K3DLMC model both impurity types are defined on the same lattice, effects of a possible lattice mismatch between the pure X and Y phases can not be taken into account. The length scale of the two-component K3DLMC model is defined by the lattice constant a_l of the bulk phase of the compound system.

Three major regimes of NC systems can be defined if the nearest-neighbor bond strengths obey specific relations:

- for $J_l^{XY} \ll J_l^{XX}, J_l^{YY}$ there is essentially no interaction between the two kinds of IAs. In this case, two virtually independent subsystems of NCs will evolve;
- for $J_l^{XY} \gg J_l^{XX}, J_l^{YY}$ the formation of an ordered compound phase is highly favored. Hence, fairly stoichiometric NCs are expected to evolve in cases of equal fluences and sufficient overlap of both implantation profiles;

- for $J_l^{XY} \approx J_l^{XX} \approx J_l^{YY}$ mainly kinetic reasons and the local concentration of both impurity components determine the cluster (alloy) formation and composition.

7.2.2 On core/shell NC formation by sequential ion implantation

Background

Core/shell NCs [a NC of composition A (the core) is coated by a few nanometer thick film of composition B (the shell)][3] represent an interesting nanocrystalline state of matter. For instance, if both materials (A and B) are semiconductors and the shell has a slightly larger energy band gap than the core, then a very interesting behavior with respect to excitons is observed. In this case, the hole is confined to the core, whereas the electron is delocalized throughout the entire structure [33]. This property considerably reduces non-radiative transitions and thus very high luminescence efficiencies have been measured [226]. These unique luminescence properties have made them very interesting in detecting and analyzing biological processes [227, 228]. A variety of II-IV semiconducting core/shell nanocrystals has been synthesized by means of colloidal chemistry, e.g. CdSe/CdS [33] or CdSe/ZnS [228].

So far there have been no direct attempts to synthesize core/shell nanocrystals in an inert matrix by IBS via the scheme of coating the previously formed NCs by subsequently implanted impurities. However, HOSONO [229] has found Cu NCs coated by a CuO layer embedded in SiO_2 for an implantation sequence of Cu^+ followed by F^+ ions, but not vice versa. In this case ballistic and chemical effects are used to explain the core/shell formation. Very recently, CATTARUZZA *et al.* [230] reported Ag/Ag_2S core/shell NCs in silica for sequential implantation of first Ag^+ and then S^+ ions. Additionally, MELDRUM *et al.* [231] found evidence for voids within CdS precipitates in silica formed by IBS, which represent a special core/shell structure.

It is worth noting that in most publications about co- or sequential implantation aimed at the formation of compound NCs, the compound phase is detected by X-ray diffraction measurements. However, this type of analysis provides averaged information for a large ensemble of NCs with possibly differing nanocomposition but is not suited to detect core/shell NCs. Neglecting lattice distortions at the core/shell interface, these nanostructures would be analyzed as two elemental phases. Only analyzing methods sensitive to single NCs like high-resolution TEM, electron energy loss spectroscopy (EELS) or EDX can reveal information of their spatial structure and composition.

K3DLMC simulations

In the case of a sequential implantation of two ion species, some light should be shed on how nucleation, CM and coarsening affects core/shell NC formation. In a series of preliminary simulations the evolution of a X-type NC is studied in presence of a source of Y monomers.

[3] Both A and B can be mono- or multi-component materials.

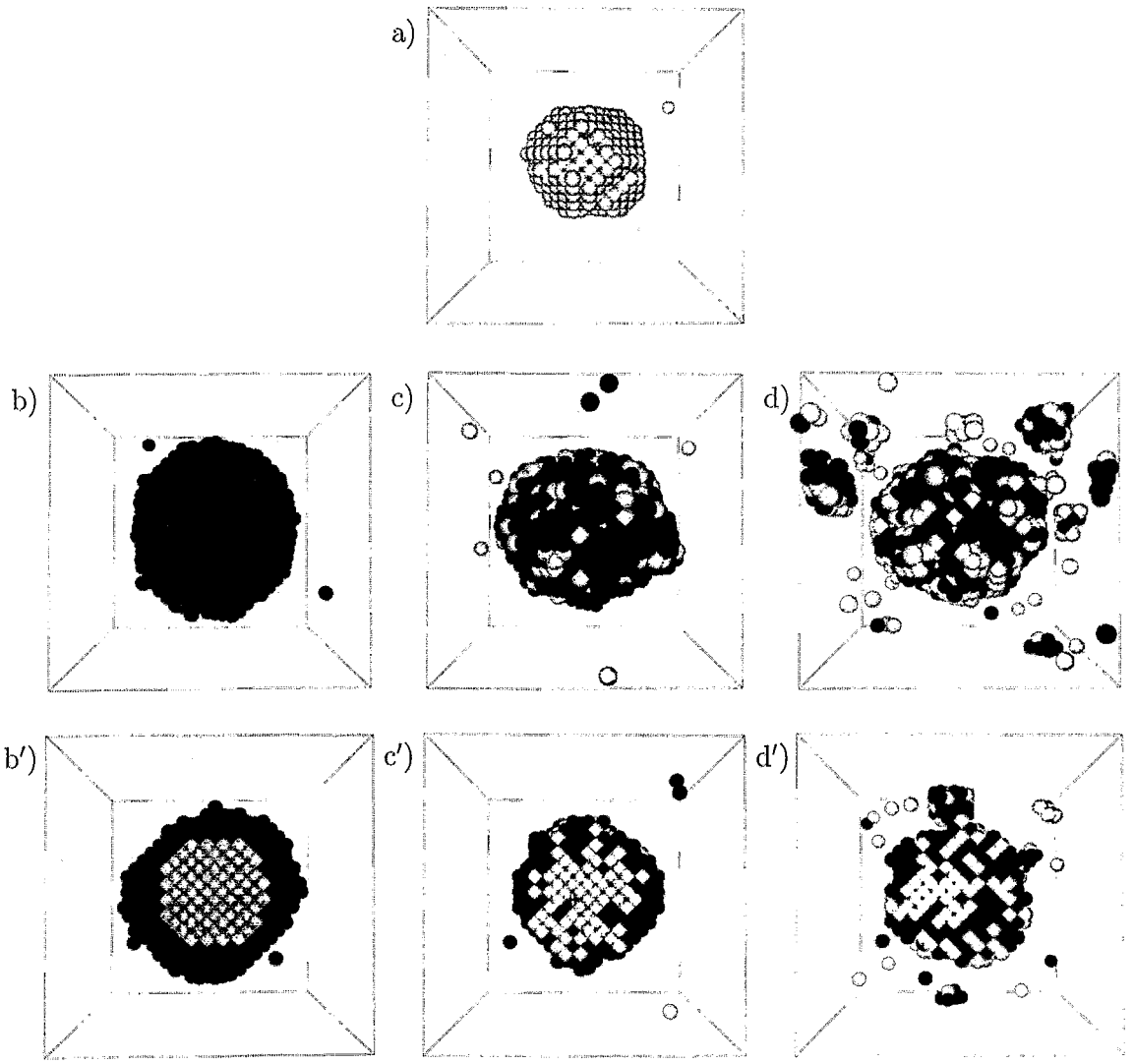

Figure 7.5: Sequence of snapshots from K3DLMC simulations of core/shell NC formation. Fig. a) shows the X-type "core" NC. The microstructure of the compound NC after the deposition of $N^Y = 2N^X$ impurities is shown in the cases of b) no mixing, c) low intensity and d) high intensity of mixing. In b') – d') corresponding cuts through the NCs (perpendicular to the plane of view) are shown.

For this purpose the initial setup is a quasi-equilibrated NC consisting of atoms of type X in a simulation box with periodic BCs (see Fig. 7.5a).

However, ion implantation of Y atoms causes CM (see Section 5.3), which can hinder pure core/shell formation. For this study the following (arbitrarily chosen) ratios of bond

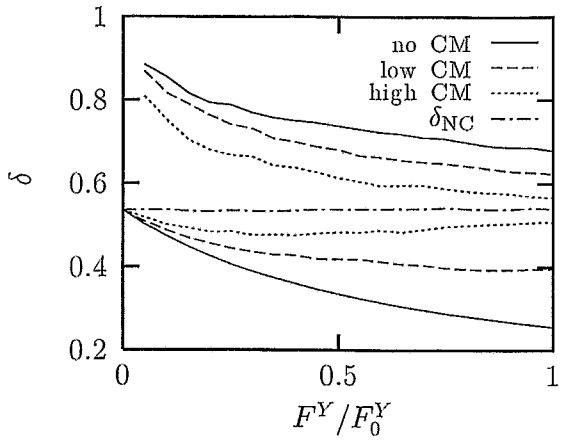

Figure 7.6: Evolution of the mean square radial X and Y distributions during the deposition of the Y component plotted versus the fraction of the implanted total Y fluence. In each of the three cases the upper curve shows the evolution of δ_Y, whereas the lower one shows δ_X. For comparison, in the case of no CM δ_{NC} represents the homogeneous ($X = Y$) NC.

strength have been used: $J_l^{XX}/J_l^{XY} = 9/8$ and $J_l^{YY}/J_l^{XY} = 7/8$ (the relation $J_l^{XX} > J_l^{XY}, J_l^{YY}$ energetically stabilizes NCs having a X-type core covered by a Y-type shell against an internal, thermodynamically driven mixing). The Y deposition rate was kept low enough to prevent satellite nucleation in the case of no mixing. In order to allow for a reasonable coating of the pre-existing core $N^Y = 2N^X$ was chosen. The evolution of this model system has been studied in the case of no CM during deposition of the Y component and for two different intensities of CM corresponding to ≈ 0.9 displacements per atom (dpa) of X impurities and ≈ 2 dpa, respectively, recorded during the period of deposition of Y atoms.

Results and Discussion

The spatial inhomogeneity of the X and Y components within a core/shell NC can be analyzed with respect to the radial concentration profiles. For this purpose, in an extension of Eq. (3.8), the normalized mean square distance of an impurity component from the center of mass of the NC can be used

$$\delta_i = \frac{1}{M_i R^2} \int r^2 \mathrm{d}m_i, \quad i \in \{X, Y\}. \tag{7.4}$$

The evolution of δ_X and δ_Y during "implantation" of species Y without and with CM can be seen in Fig. 7.6.

Figs. 7.5b – 7.5d show the resulting microstructure of the compound NC if CM is neglected (b) and if two different degrees of CM are included (c,d). The corresponding cuts through the NC (Figs. 7.5b′ – 7.5d′) reveal more clearly the composition. Whereas in case (b) the chosen energetics and kinetics leads to a pure core/shell formation, the X and

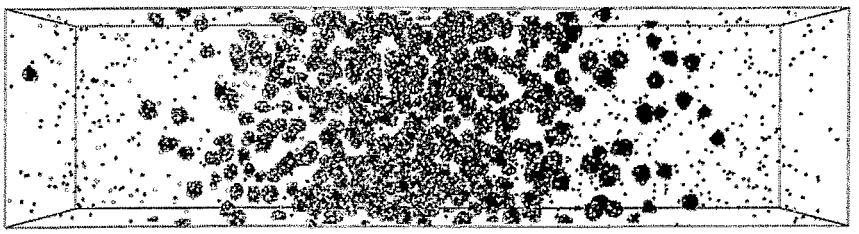

Figure 7.7: Large-scale simulation of the evolution of a sequentially implanted two component system in the presence of CM. The snapshot shows the microstructure right at the end of the second implantation.

Y replacements caused by CM lead to a random distribution of both components within the NC. As can be seen in Fig. 7.6 the more effective the mixing the more homogeneous is the resulting radial distribution of both components. Additionally, depending on the level of CM, the pronounced faceting (octahedral-like shape) of the NC tends to be smeared out.

CM enhances also the impurity monomer concentration in the vicinity of a NC. These monomers can diffuse back to the NC and reattach, but if this enhanced supersaturation exceeds a critical value, small satellite NCs may form, as is indicated in Fig. 7.5d. For high ion fluxes j^Y even the complete dissolution of pre-existing NCs can be achieved.

After the Y implantation a compound NC is characterized by a random X-Y composition due to the collisional displacements and the random attachment of X or Y monomers. An isolated NC would then evolve to an energetically more favorable state by local X-Y rearrangements mediated most effectively by vacancy as well as by X or Y interstitial diffusion within the NC or by direct X-Y site changes. Depending on the X-Y energetics an isolated NC would then tend either to an ordered or segregated composition, which in the latter case could be a core/shell structure.

Obviously, CM competes with the coating of a X NC with Y impurities, which makes core/shell NCs unlikely to be found in as-implanted samples. Fig. 7.7 shows the typical microstructure after the implantation of the second component ($F_0^Y = 2F_0^X$) into a substrate having a pre-implanted ensemble of X-"core" NCs for a reasonable overlap of the implantation profiles ($R_p^X = 120\,a_{fcc}$, $\Delta R_p^X = 32\,a_{fcc}$, $R_p^Y = 135\,a_{fcc}$, $\Delta R_p^Y = 40\,a_{fcc}$). Obviously, no reasonably coated X-type NCs are observed.

NCs formed by IBS interact with each other due to their size and space distribution (OR). Due to their metastability (GT relation) small NCs are continuously dissolving and there is always a certain degree of supersaturation of monomers, which mediate the diffusional transport from the small to the large NCs. Generally the dynamics is governed by the diffusion and solubility properties as well as the phase diagrams and the local concentration of both components. The evolution of the compound NCs, e.g. in a subsequent annealing step, depends then on the ratio of the time scales of ensemble-like (coarsening) and NC-like (local ordering mechanisms) processes.

Since ion implantation is inevitably accompanied by a specific level of CM, for sequential implantation of two ion types there is a competition between a coating of the pre-implanted NCs and a random arrangement of X and Y impurities. As a rule of thumb core/shell formation is favored if (i) the solubility of Y exceeds the solubility of X in the matrix, i.e. $J_l^{XX} > J_l^{YY}$ for reasonable J_l^{XY}, if (ii) the atomic mass of Y is small, i.e. low CM, and (iii) for rather low ion flux j^Y and/or high second implantation temperature, which favors a compensation of displacements by thermodynamically driven atomic movements.

7.2.3 Shifted-profile compound NC synthesis

Compound NC formation by co- and/or sequential implantation of two or more ion species is a highly complex process much less understood than the governing physics in the single-component case. Restricting this study two types of impurities in a neutral matrix the evolution is governed by two diffusion coefficients and three solubilities (besides the compound phase also the single-component phases have to be considered), not to mention the modifications arising due to nontrivial interactions with point defects or other damage structures caused by the implantations. Essentially all experimental studies on IBS of compound NCs in chemically neutral substrates reported so far have been based on achieving a rather good overlap of both implantation profiles. The spirit of these experiments was to demonstrate, that compound NCs can be synthesized by ion implantation [14, 15, 232, 233]. However, rather than presenting simulation results of the standard approach to compound NC formation, in this Section some preliminary predictions are given for implanted systems with only partly overlapping impurity profiles. With the help of K3DLMC results of a few exemplifying model systems, the physics of impurity redistribution and compound NC formation in a homogeneous environment is qualitatively discussed.

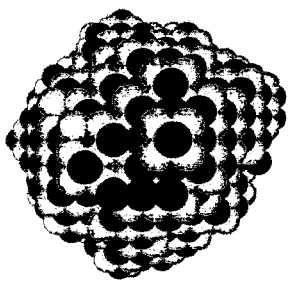

Figure 7.8: Compound NC of bcc structure consisting of roughly 1400 IAs.

Without referring to a specific materials system, simulations have been performed for two interacting types of IAs on a bcc lattice. Fig. 7.8 shows the typical microstructure of such a compound NC. In a series of simulations the evolution of an as-implanted sample corresponding to two shifted impurity profiles (simulation volume $64 \times 64 \times 256$ bcc unit cells, absorbing interface at $z = L_z$, fluences of $F^X = F^Y \approx 2.4 a_{\mathrm{bcc}}^{-2}$, Gaussian profiles characterized by $R_{\mathrm{p}}^X = 75\, a_{\mathrm{bcc}}$, $\Delta R_{\mathrm{p}}^X = 17.5\, a_{\mathrm{bcc}}$, $R_{\mathrm{p}}^Y = 155\, a_{\mathrm{bcc}}$, $\Delta R_{\mathrm{p}}^Y = 25\, a_{\mathrm{bcc}}$) is studied. Within the K3DLMC model, the evolution depends on five parameters, namely the two diffusion coefficients D^X and D^Y and the three bond strengths J_l^{XX}, J_l^{XY}, and J_l^{YY}. Table 7.1 lists the parameter relations for three model systems, which in the following serve to discuss the physics of compound NC formation in this approach.

Fig. 7.9a shows the as-implanted initial sample, which in implantation experiments may be qualitatively achieved be suitably tuning the ion energies. In the left column of Fig.

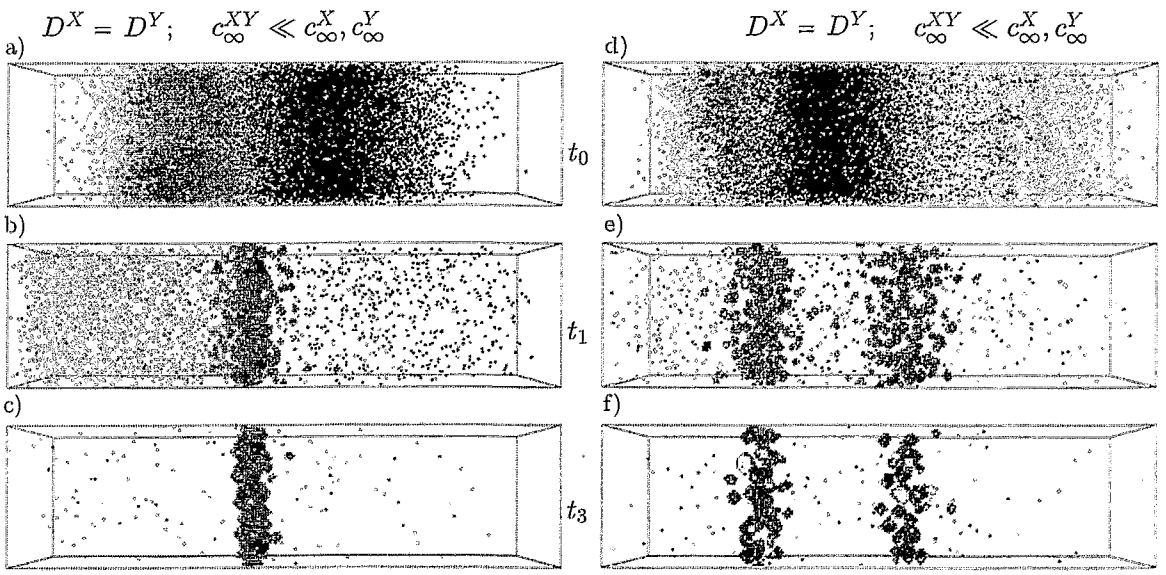

Figure 7.9: For model system A compound NC synthesis is shown in the case of double (X, Y) or triple (X, Y, X) implantations with shifted profiles. The further evolution of the initial states is shown at times $t_1 = 5 \times 10^4$ MCSs and $t_3 = 1.9 \times 10^6$ MCSs, respectively.

7.9 the evolution of model system A (equal diffusion coefficients and an energetics strongly favoring compound NC formation) can be seen. Obviously, in this highly symmetric case, a band of NCs starts to form at the region of the overlap of the implantation profiles.

Assuming a physical system can be found (two species X and Y with approximately equal diffusion coefficients, for which in an inert substrate the compound phase XY is favored due to the driving chemical forces), which tends to form a NC band in the overlapping region, a straightforward extension would be a triple implantation. Figs. 7.9d-f show such a model simulation, where the initial distributions are described by $R_\mathrm{p}^{X_1} = 50\,a_\mathrm{bcc}$, $\Delta R_\mathrm{p}^{X_1} = 12.5\,a_\mathrm{bcc}$, $R_\mathrm{p}^{Y} = 110\,a_\mathrm{bcc}$, $\Delta R_\mathrm{p}^{Y} = 20\,a_\mathrm{bcc}$, $R_\mathrm{p}^{X_2} = 175\,a_\mathrm{bcc}$, $\Delta R_\mathrm{p}^{X_2} = 30\,a_\mathrm{bcc}$. The

Table 7.1: Parameter relations for three exemplifying model systems of compound NC formation.

system	$\epsilon_\mathrm{bcc}^{XX}$	$\epsilon_\mathrm{bcc}^{XY}$	$\epsilon_\mathrm{bcc}^{YY}$	D^Y/D^X
A	0	3	0	1
B	2	3	2.5	1
C	2	3	2.5	10

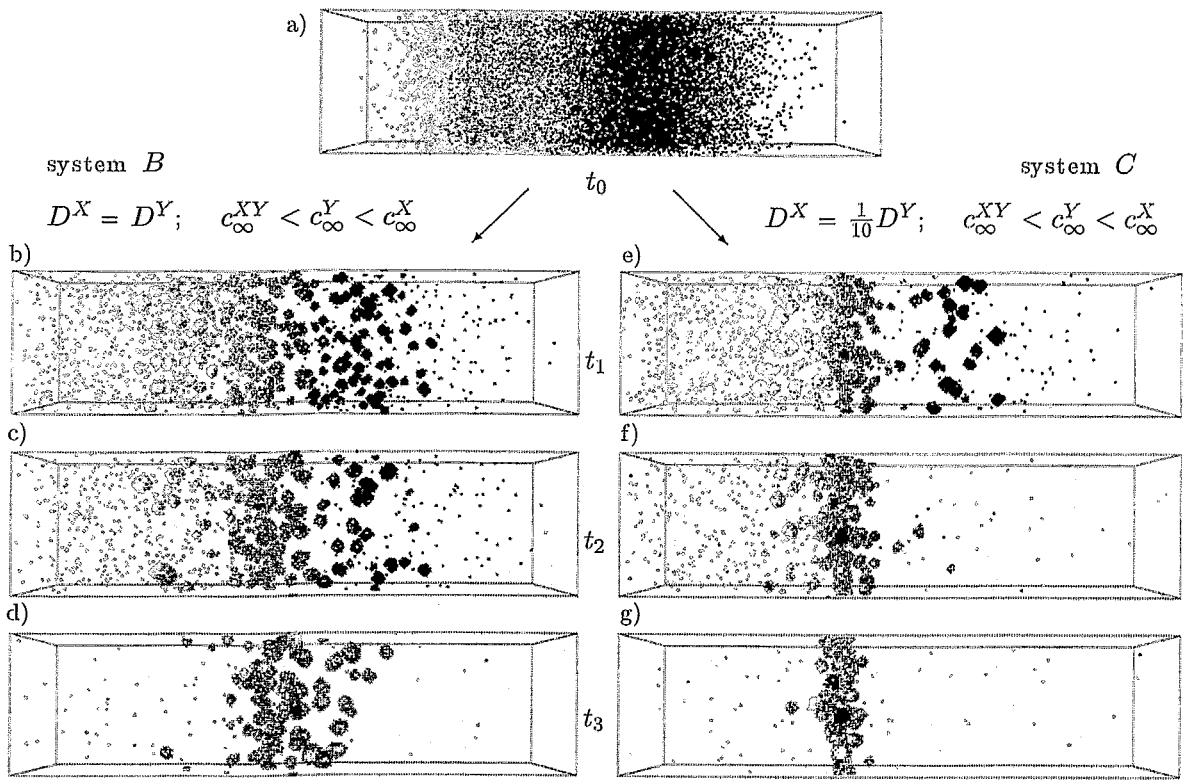

Figure 7.10: In the top row, the initial sample can be seen (as-implanted state). The further evolution for the model systems B and C is shown at times (given for the X-component) $t_1 = 5 \times 10^4$ MCSs, $t_2 = 2.5 \times 10^5$ MCSs, and $t_3 = 1.9 \times 10^6$ MCSs, respectively.

deposited fluences $F^{X_1} \approx 1.3\, a_{\mathrm{bcc}}^{-2}$, $F^{X_2} \approx 1.6\, a_{\mathrm{bcc}}^{-2}$, and $F^Y \approx 2.4\, a_{\mathrm{bcc}}^{-2}$ have been chosen such as to have an excess amount of X impurities on order to compensate for the absorbing interface at $z = L_z$. Here, two planar NC layers should evolve, whose distance is given as a function of the respective implantation energies, and can thus be changed by a proper choice of implantation parameters.

In the case of model system B the influence of the solubilities can be seen in Fig. 7.10. Here, additional to the compound NC formation, due to the finite solubilities c_∞^X and c_∞^Y single-component NCs of both species start to form. In the course of the simulation, the NCs with the highest solubilities (i.e. the lowest bond strength J) start to dissolve, since concentration gradients to spatial regions with lower solubility will build up. The impurity redistribution can be monitored with the help of the monomer concentration profiles. Fig. 7.11a shows the corresponding depth-dependence of c^X and c^Y. Clearly, the region of compound NC formation acts as sink for both types of impurities. Furthermore, the difference in the single-component solubilities is reflected in the respective monomer concentration levels.

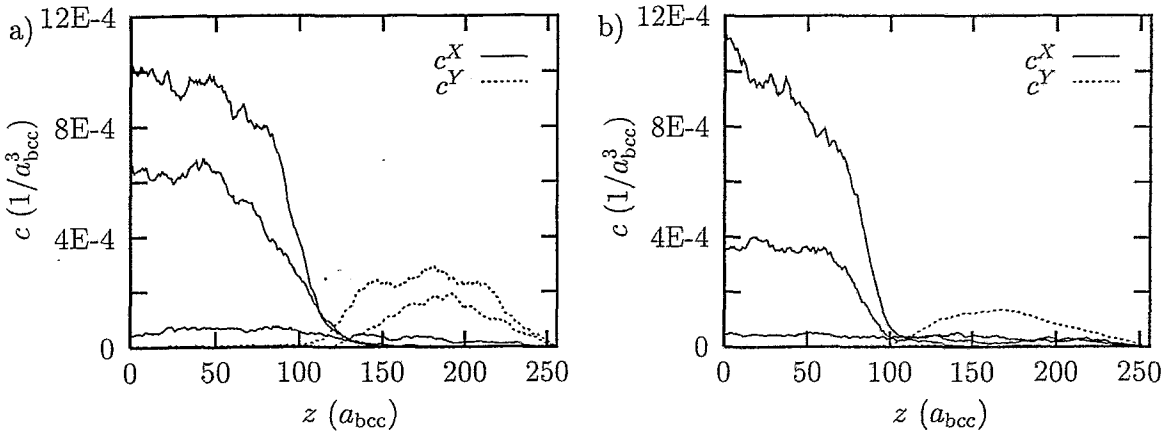

Figure 7.11: Monomer concentrations averaged over the last 10^4 MCSs as recorded at times (from top to bottom) t_1, t_2, and t_3 of Fig. 7.10 (on this scale c^Y essentially vanishes for late times). Figs. a) and b) correspond to systems B and C, respectively.

The evolution of both single-component NC subsystems can be understood with the help of the time scale of OR $\tau_{\rm diff}$, which is proportional to $1/(DR_{\rm c}c_\infty)$ [Eq. (4.16)]. Assuming, that as in the case of the fcc lattice the capillary length is given by $R_{\rm c} = R_{\rm c0}^{\rm (bcc)} + \zeta_{\rm bcc}a_{\rm bcc}\epsilon_{\rm bcc} \approx \zeta_{\rm bcc}a_{\rm bcc}\epsilon_{\rm bcc}$ (see Section 3.5.3; omitting the term $R_{\rm c0}^{\rm (bcc)}$ should be a reasonable approximation in the current parameter range), the following relation can be derived

$$\frac{\tau_{\rm diff}^X}{\tau_{\rm diff}^Y} \approx \frac{D^Y J^{YY}}{D^X J^{XX}} \exp\{-4(\epsilon_{\rm bcc}^{YY} - \epsilon_{\rm bcc}^{XX})\}. \tag{7.5}$$

Besides characterizing OR, $\tau_{\rm diff}$ furthermore gives a measure of the time a system of NC needs to interact with an external disturbance, for instance a nearby region with a different solubility. Accordingly, a small value of $\tau_{\rm diff}$ (i.e. a large product Dc_∞) implies an efficient impurity redistribution by diffusional mass transport. For system B (equal diffusion coefficients, but considerable solubility difference), the evolving asymmetry of the NC distribution with respect to the overlapping region is thus simply a consequence of the relation $\tau_{\rm diff}^X \approx 0.17\,\tau_{\rm diff}^Y$.

A more general situation is represented by model system C, whose evolution can be seen in the left column of Fig. 7.10. Here, in addition to differing solubilities, the diffusion coefficients differ by one order of magnitude. The time constants are, however, similar, i.e. $\tau_{\rm diff}^X \approx 1.7\,\tau_{\rm diff}^Y$. Thus both single-component subsystems show similar response to the effective sink created by the small region of compound NC formation. This explains, why the formation of a pronounced NC band in the overlapping region is very similar to model system A (see Fig. 7.9), for which $\tau_{\rm diff}^X = \tau_{\rm diff}^Y$ trivially holds.

Furthermore, it is instructive to analyze the NC evolution on the basis of the numbers and compositions of the nearest-neighbor bonds [see Eq. (7.3)]. As can be seen in Fig. 7.12 the fraction of compound bulk IAs ($n + m = 8$) increases for both impurity components,

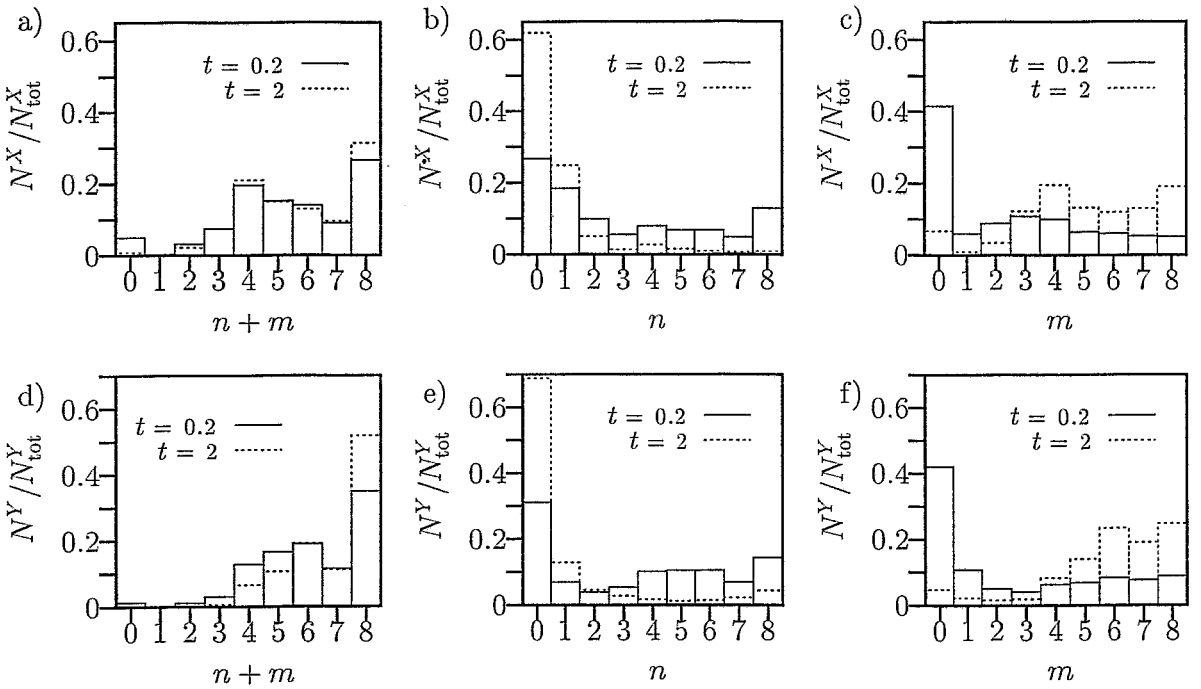

Figure 7.12: Analysis of number and type of nearest-neighbor bonds during the evolution of system B (times are given in units of 10^6 MCSs, see Fig. 7.10). For the X-type IAs the normalized histograms in the top row show the complete neighborhood ($n+m$), and the distributions of X–X (n) and X–Y (m) bonds, respectively. The corresponding analysis for the Y-type IAs is shown in the bottom row.

whereas the fraction of single-component bulk atoms ($n = 8$) decreases. The formation of the energetically favored compound phase is also reflected in the increasing number of atoms having $m = 8$ nearest-neighbor bonds to the other impurity component.

It is interesting to note, that in model system B a large fraction of Y atoms is in a bulk state ($n + m = 8$), whereas a significant fraction of X atoms can be found to be part of the surface of the compound NCs (see peak at $n + m = 4$ in Fig. 7.12a). The effect of the flow of X-type atoms into the region of the Y profile can be interpreted as a tendency of core/shell NC formation. This can be understood as follows: The evolving predominantly Y-type NCs within the Y profile close to the overlapping region represent a diffusion barrier for X-type monomers (the mean undisturbed penetration depth can be estimated with the help of the diffusional screening length). Thus the first arriving X-type monomers will be able to form energetically most favored X–Y bonds by condensing on these predominantly Y-type NCs. Later on, subsequently arriving monomers find essentially X-type coated NCs. Although these NCs still act as monomer traps, the detachment rate is accordingly higher (note, that these lately arriving monomers have basically formed only X–X bonds), and hence they may readily diffuse further into the Y region.

The above introduced method of shifted-profile compound NC synthesis should in prin-

ciple work also for an interchange in the ion types (i.e. $X \leftrightarrow Y$). While it is clear, that due to the mass-dependent straggling the profiles can not simply be reversed, at least qualitatively the same impurity redistributions should occur after achieving a mirror image with respect to the overlapping region of the as-implanted profiles.

Obviously, the presented results rely on homogeneous conditions throughout the simulation volume. However, radiation damage can significantly alter the redistribution e.g. by inhomogeneous nucleation. Therefore, it would be very interesting to conduct corresponding shifted-profile implantation experiments in order to explore the predictability of the K3DLMC results.

Chapter 8

Summary and outlook

In this work various aspects of the ion beam synthesis of nanostructures, in particular nanoclusters, have been studied by atomic and mesoscopic computer simulation methods. Nucleation of precipitates out of (in general depth-dependent) supersaturated solid solutions, their subsequent growth and the early stages of coarsening phenomena have been studied using a kinetic three-dimensional lattice Monte-Carlo method based on the nearest-neighbor ISING model (also known as lattice gas model). For all simulations the impurity atoms have been regarded as effective particles defined in an inert and homogeneous matrix (i.e. no depth-dependent inhomogeneities due to irradiation damage have been considered). The late stage of phase separation of isolated second-phase domains, i.e. OSTWALD ripening, is modeled by a mesoscopic approach. This has been done by the stepwise numerical integration of the reaction-diffusion equations of coarsening nanoclusters formulated in the framework of a local mean-field theory.

The first purpose was to give a solid foundation of the intrinsic properties of the K3DLMC model with respect to the governing physics of nanocluster evolution. For the three major lattices implemented (fcc, bcc, and sc lattices, respectively), ARRHENIUS-like laws for the solubility have been derived, which allows a coupling to thermodynamic data. Furthermore, the GIBBS-THOMSON relation, which by establishing the curvature-dependence of the equilibrium monomer concentration defines the dynamical properties of coarsening systems, has been proven to be valid down to nanocluster sizes of a few tens of atoms, i.e. on a nanometer scale. Based on the GIBBS-THOMSON relation an explicit expression for the surface tension has been derived in the temperature range well below the roughening transition.

An existing computer model for diffusion limited OSTWALD ripening has been extended to be applicable for an arbitrary degree of diffusion and reaction control. Based on the approximation of a radius-independent interface reaction rate, it has been shown that the mesoscopic method successfully reproduces the basic results of the LSW theory in the two limiting cases. For the intermediate parameter regime, the simulation results of OSTWALD ripening have been compared to an alternative description and the observed differences have been discussed.

In the case of nanocluster formation during implantation (typical for high-dose metal

implantations into insulators) the basic dependence of the size distribution on substrate temperature and ion current has been studied. A comparison of K3DLMC simulation results with experiments (MeV Au^+ implantation into SiO_2 for varying temperatures) has been presented. A good qualitative correspondence has been observed even though ballistic effects have not been taken into account in this particular study. Additional Monte-Carlo simulations predict that a controlled variation of the implantation conditions (decreasing the implantation temperature or increasing the ion current) can initiate a second nucleation regime, thus leading to a bimodal size distribution. Corresponding Au^+ implantations into SiO_2 are discussed with respect to these predictions.

On the basis of an isotropic collisional mixing model, temperature-independent ballistic jumps of impurity atoms have been added to the K3DLMC method, which are typical for irradiation effects. In particular, the modifications of the GIBBS-THOMSON relation in the presence of collisional mixing have been studied. The simulation results indicate, that irradiation-induced modifications of nanocluster properties cannot merely be explained by the concept of an effectively higher temperature. As predicted recently it has been shown, that collisional mixing (i) increases the solubility and (ii) causes a decrease of the effective capillary length, which can even result in negative values for specific parameter regimes. Based on these observations, K3DLMC simulations show the predicted modifications of OSTWALD ripening under irradiation, especially inverse coarsening (i.e. the growth of small nanoclusters on the expense of large one). It is demonstrated, that inverse OSTWALD ripening leads to a delta-like size distribution. Furthermore, for very high mixing intensities or low diffusivities, the nucleation of additional precipitates is predicted, which in combination with inverse OSTWALD ripening causes a decrease of the mean nanocluster size.

The atomic and mesoscopic computer simulation methods have been combined to perform a multi-process and multi-scale modeling of the evolution of nanoclusters. It has been found, that the ratio of the mean nanocluster radius to the capillary length determines the dynamics of phase separation. For equivalent dynamical descriptions the differences in the evolution of an nanocluster ensemble have been shown to be due to the stochastic and deterministic characters of the atomic and mesoscopic methods, respectively. As an application the competition of internal OSTWALD ripening and boundary-induced self-organization has been investigated with respect to the evolution of as-implanted samples. Furthermore, simulation results regarding the synthesis of periodic two-dimensional arrays of nanoclusters by focused ion implantation are presented, where the competition between intra-spot and inter-spot OSTWALD ripening has been discussed. It is predicted that for the formation of nanocluster arrays high-temperature rapid thermal annealing followed by a well-controlled cooling-down stage is superior to conventional annealing techniques.

Extending the K3DLMC method to two types of interacting species, various specific phenomena encountered in ion beam synthesis have been modeled. For instance, the redistribution of implanted impurities has been studied taking into account the influence of a reactive annealing atmosphere. A comparison to experimental results of annealing of a Ge-implanted SiO_2 layer in various ambients (N_2, Ar, or O_2) has been given. In the area of compound nanocluster synthesis by means of ion implantation, some aspects of perspectives

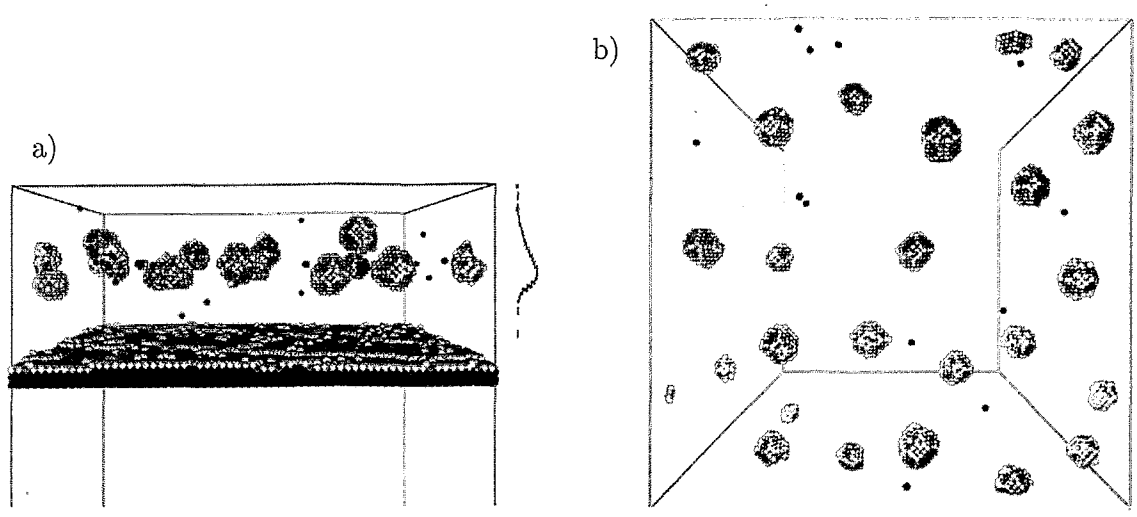

Figure 8.1: K3DLMC modeling of ultralow energy Si implantation into a thin gate oxide on (100) silicon (the silicon structure is approximated by the fcc lattice). The simulated redistribution of implanted Si^+ (partly nucleating into nanoclusters and partly condensing onto the flat Si layer) can be seen in Fig. a) as a cross-section view and in Fig. b) as a plane view (omitting here the Si substrate for clarity).

on core/shell nanocluster formation by sequential ion implantation have been discussed. It has been shown that collisional mixing seems to be a major obstacle concerning ion beam synthesis of core/shell nanoclusters. Furthermore, predictions have been made concerning the formation of a narrow layer of compound nanoclusters by shifted-profile implantation of two ion species.

As an atomic model describing efficiently the evolution of impurities within a chemically neutral matrix, the K3DLMC method has the potential to enlarge our understanding of basic physical processes on length scales up to mesoscopic dimensions. Noting potential applications of this modeling approach also outside implantation-specific phenomena, two more interesting areas related to the ion beam synthesis of nanostructures should be briefly mentioned. From the technological point of view a very promising option is ultralow energy implantation into thin gate-oxides (thickness $\approx$ 10 nm) in order to position nanoclusters within the tunneling length in the gate oxide of a transistor. From the modeling point of view, the implantation of Si^+ into a thin SiO_2 layer on Si [42] can be described consistently by considering only a single atom type (see Fig. 8.1). In this process the formed nanoclusters are in a highly metastable state due to the close flat Si interface. Thus an essentially two-dimensional layer of Si nanoclusters will evolve, whose stability is expected to be very sensitive to the applied heat budget.

Furthermore, aspects of buried layer formation can be addressed (see Fig. 8.2). While these simulation results are obtained starting with a (from the modeling point of view) simple initial configuration, the observed microstructures are very similar to experimental

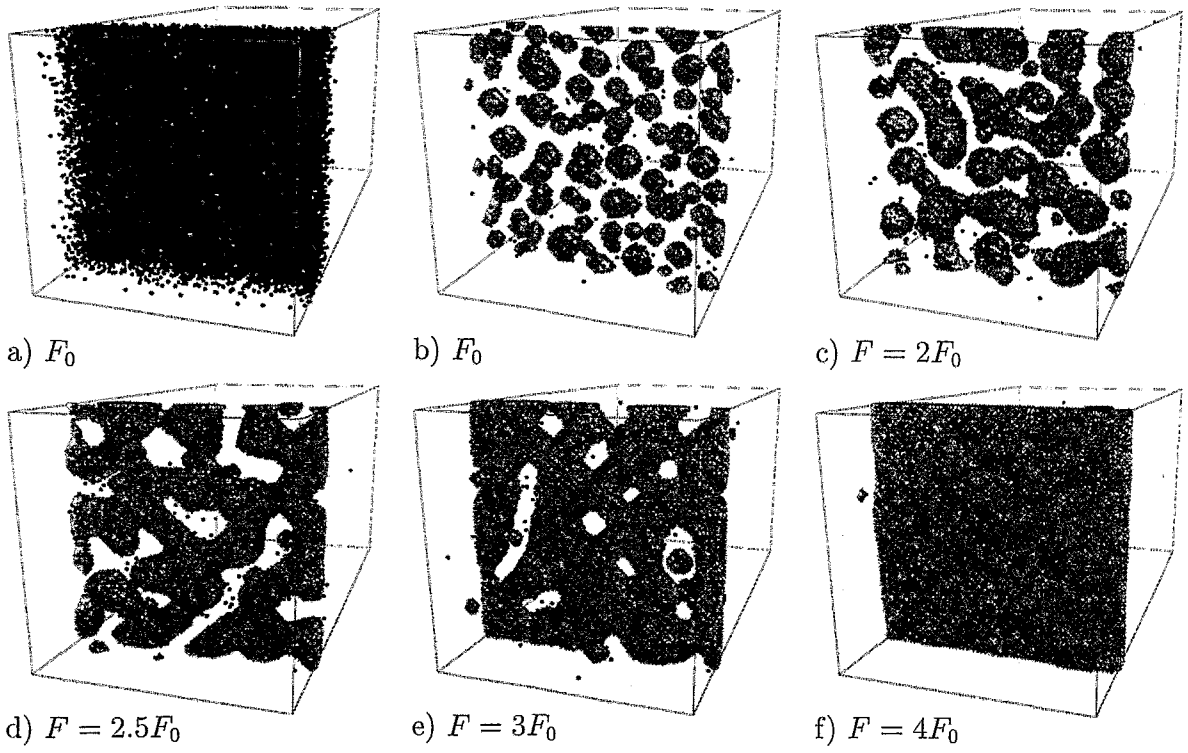

Figure 8.2: K3DLMC simulations of the dose-dependence of buried layer formation starting from as-implanted Gaussian profiles [see Fig. a)]. Figs. b) – f) show the microstructures obtained after 4.5×10^5 MCSs for the indicated multiples of the reference fluence $F_0 \approx 7.4\, a_{\mathrm{fcc}}^{-2}$.

observations (see e.g. [234, 235]). Especially the transition between isolated spherical-like nanoclusters and meandering interconnected structures can be seen. The closed layer of Fig. 8.2f as obtained by the K3DLMC method is trivially mono-crystalline, because all impurity atoms are defined on one lattice.

Besides taking into account basic statistical mechanical properties and isotropic collisional mixing effects, by extending the K3DLMC method properly further improvements of simulation results, and thus more reliable predictions, are expected. For instance, the forward anisotropy of displaced atoms under irradiation has to be considered in order to obtain a more precise description of ballistic effects. This extension would allow to model the observed asymmetries of the disintegration of buried (multi-) layer systems under irradiation (see e.g. [236, 26, 27]).

Other peculiarities in ion beam synthesis of nanoclusters, for instance the observed collective drift of impurity atoms towards the surface (found for some metal-ion/substrate systems [6]), remain to be explored. This problem can be accessed by introducing a drift term into the K3DLMC method, which influences the diffusion of implanted monomers.

Depending on the assumed physical origin of the drift term (e.g. due to charging effects) and its proposed interaction with the impurity atoms, more could be learned about these systems.

Promising options for future modeling approaches of the ion beam synthesis of nanostructures include a coupling of the K3DLMC method to a binary collision approximation description of the slowing-down of implanted impurity atoms as well as to Molecular Dynamics simulations, which allow to study the kinetics of the interactions of impurity atoms with point and extended defects. This would provide a consistent description from the very beginning of ion-solid interactions to the late stage of annealing.

Appendix A

Bit encoding of MC lattice

With the availability of "fast computing machines" in the early fifties, MC simulations have become an important method in statistical physics, especially in the area of phase transitions and critical phenomena [38]. A variety of special purpose (vector of parallel) computers has been designed, which hardware was optimized with respect to sophisticated spin-flip, spin-exchange or cluster updating algorithms [237, 80]. However, in recent years the tremendous increase of computing power of general purpose computers allows reasonable MC simulations without the need of supercomputers. Nevertheless, there is always the need for optimized algorithms.

A simple but ineffective implementation of a jump attempt would randomly pick one out of N IAs and then for all relevant positions of the jump geometry [14 for the fcc (see Fig. 3.1) and bcc and 10 for the sc lattices, respectively] search for nearest-neighbors in the remaining set of $(N-1)$ IAs. A more efficient method is to keep track of the neighborhood of each IA once it has been determined. One possibility widely used for instance in MD simulations is the use of neighboring lists, which, however, still requires computing intensive updating after a certain number of time steps.

For the single-component lattice gas, a different approach is advantageous. Since in this model each lattice site can either be empty or occupied, just a single bit is needed to characterize the occupation state. Thus during the jump attempt of one particular IA, only the *known* nearest-neighbor sites have to be checked for the presence of further IAs (bit on or off). While the necessary computations can be performed completely on the bit level, the mapping of the coordinate onto the bit space proves to be very important for the efficiency of the K3DLMC method [114].

In a double book-keeping approach the positions of the IAs are stored in coordinate as well as in bit space. While the coordinates of the IAs are stored in an array of dimension $N \times 3$, for the bit representation an integer array of rank one is used. For a given position $\vec{r} = (x, y, z)$ of an IA within the simulation box of size $2^{n_x} \times 2^{n_y} \times 2^{n_z}$, two procedures to address the corresponding bit have been developed.

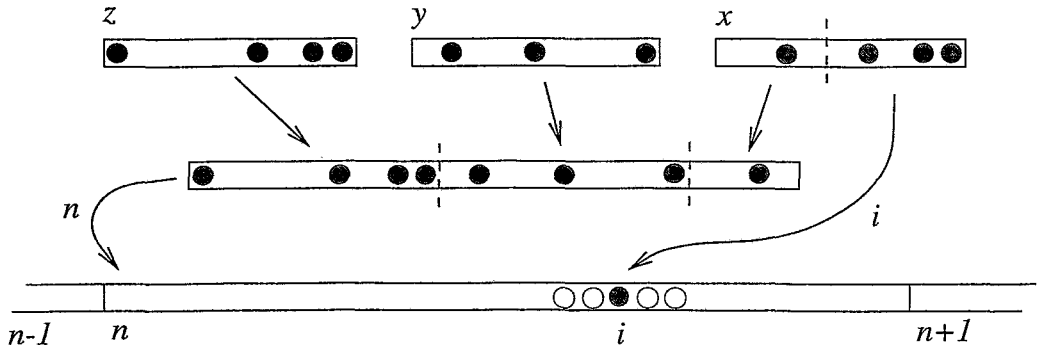

Figure A.1: Scheme of coordinate-to-bit transformation in the case of the vector algorithm. The k lower bits of the x coordinate are used to address the i-th bit within component n of an array of rank one.

Vector algorithm

One possibility to map the lattice space onto the bit space is to cut rods of length $l = 8I_{\text{byte}}$ out of the lattice, where I_{byte} is the number of bytes the integer consists of. For this purpose, the last k bits (with the constraint $2^k = 8I_{\text{byte}}$) of the (arbitrarily chosen) x coordinate are used to address the bit within the integer $n = n(x, y, z)$ (see Fig. A.1). The remaining bits (if any) of the x as well as the y and z coordinates are used to address the specific element within the integer array. The following FORTRAN 90 code segments show parts of this algorithm, where `i` and the one-dimensional array `latt_1d(:)` are of integer type $I_{\text{byte}} = 4$.

```
INTEGER   n_x,n_y,n_z,x,y,z,y_shift,z_shift,bit_mask,n
INTEGER, PARAMETER ::  k = 5
   :
bit_mask = 2**k - 1
y_shift = n_x - k
z_shift = n_x + n_y - k
   :
i = ISHFT(1,IAND(x,bit_mask))
n = IOR(IOR(ISHFT(x,-k),ISHFT(y,y_shift)),ISHFT(z,z_shift))
latt_1d(n) = IOR(latt_1d(n),i)
```

Only specifying I_{byte}, this algorithm can be implemented using programming languages, where the largest supported integer is of length I_{byte} bytes. However, a disadvantage of this particular bit representation is the fact, that for each jump attempt 12 components of the one-dimensional integer array `latt_1d(:)` have to be loaded into the CPU from somewhere out of the cache and memory hierarchy, which usually slows down the computation.

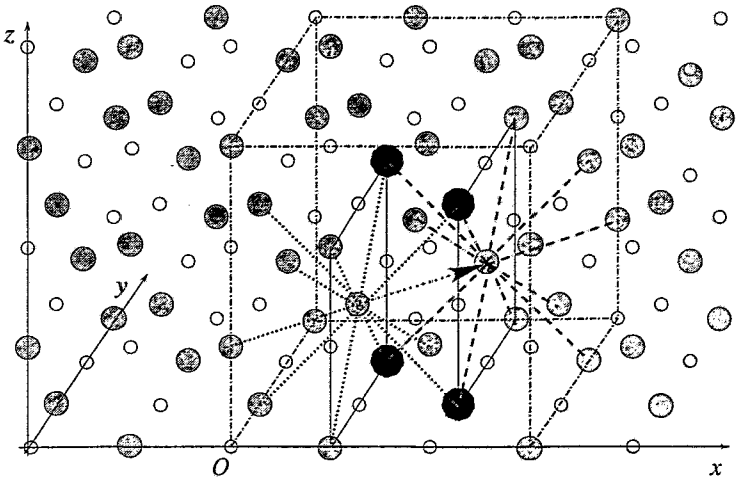

Figure A.2: Representation of a nearest-neighbor jump configuration within the fcc lattice (grey circles). This particular jump with coordinates $\vec{r}_i = (1,1,1)$ and $\vec{r}_f = (2,2,1)$ with respect to the origin O of a $4 \times 4 \times 4$ cube is one example, where all relevant positions can be addressed within one 8-byte integer.

Cube algorithm

An alternative, more efficient method is to divide the real space into rectangular pieces, where now more positions are likely to be found in one array component. Especially for computer systems supporting integers of length $I_{\text{byte}} = 8$ bytes, it is advantageous to divide the lattice into small cubes of size (4 bits) $\times$ (4 bits) $\times$ (4 bits) (see Fig A.2). Here, the last $k = 2$ bits of each coordinate are used to compute the bit representing a particular lattice site. The remaining parts of the coordinates determine the index within the integer array. For `i` and the one-dimensional array `latt_3d(:)` being of integer type $I_{\text{byte}} = 8$, the corresponding FORTRAN 90 code reads:

```
INTEGER   n_x,n_y,x,y,z,y_shift,z_shift,n
INTEGER, PARAMETER ::  k = 2
INTEGER, PARAMETER ::  bit_mask = 3
INTEGER, PARAMETER ::  y_bit_shift = 2
INTEGER, PARAMETER ::  z_bit_shift = 4
   :
y_shift = n_x - y_bit_shift
z_shift = n_x + n_y - z_bit_shift
   :
i = ISHFT(1_8,IOR(IOR(IAND(x,bit_mask),
&  ISHFT(IAND(y,bit_mask),y_bit_shift)),
&  ISHFT(IAND(z,bit_mask),z_bit_shift)))
n = IOR(IOR(ISHFT(x,-k),ISHFT(ISHFT(y,-k),y_shift)),
```

```
&  ISHFT(ISHFT(z,-k),z_shift))
 latt_3d(n) = IOR(latt_3d(n),i)
```

Although the number of calls of basic bit-manipulating procedures more than doubles (15:7), the great advantage of this algorithm is the fact, that a large number of nearest-neighbor sites is now addressable within the same integer. This considerably reduces the simulation time, since now the scan of the physical state of the vicinity of a specific site can be performed loading only a few integers into the processor (one component of the array in the ideal and eight in the worst case, respectively). The needed data are very highly to be found in the cache hierarchy instead of the RAM memory, and are thus quickly accessible for the CPU.

Appendix B

Derivation of nanocluster source strengths

B.1 General formulation

In Section 4.2.1 the solution for the monomer concentration field caused by the presence of a single isolated NC has been derived

$$c(\vec{r}) = c_\mathrm{u} + \frac{1}{4\pi D}\frac{\tilde{Q}_1}{|\vec{r}-\vec{r}_1|}. \tag{B.1}$$

Here the source strength $\tilde{Q}_1$ is chosen such as to fulfill the BCs [Eqs. (2.25) and (2.26)].

However, in the case of an interacting ensemble of N precipitates the concentration field $c(\vec{r})$ is not simply the superposition of N single-NC solutions [Eq. (B.1)]. Rather, the BCs are determined according to the diffusional influence of all other precipitates and do thus depend on the form of $c(\vec{r})$. In the most general case the BCs can depend also on a continuous source density $G(\vec{r})/D$ defined in the space $\mathcal{G}$ outside of the precipitates. This situation is encountered during ion deposition (neglecting modifications due to the presence of collisional mixing), where $G(\vec{r})$ denotes a depth-dependent volume generation term of monomers.

Like in electrostatics the effect of interacting NCs and a continuous source term on the BCs can be compensated by appropriately located mirror sources $Q_{i\nu}$ and mirror source densities g_i (direct compensation of G in NC i) and $g_{i\mu}$ (compensation of g_μ in NC μ) within the NCs. Since every mirror source gives rise to additional mirror sources, an infinite number of them is needed to fix the BCs.

An equivalent approach is to place one mirror source in the center of a particular precipitate, which by its angular-dependent multipole moments also fulfills the BCs. In this case the general solution is given by

$$c(\vec{r}) = c_\mathrm{u} + \frac{1}{4\pi D}\left[\int_{\mathcal{G}}\frac{G(\vec{r}\,')}{|\vec{r}-\vec{r}\,'|}\mathrm{d}^3r' + \sum_{i=1}^{N}\sum_{l=0}^{\infty}\sum_{m=-l}^{l}\frac{Y_l^m(\theta_i,\phi_i)}{|\vec{r}-\vec{r}_i|^{l+1}}(A_{il}^m + B_{il}^m)\right], \tag{B.2}$$

where Y_l^m are spherical harmonics. In the last equation the term

$$A_{il}^m = \frac{4\pi}{2l+1}\left(\int_{\mathcal{P}_i}\overline{Y_l^m}(\Theta_i,\Phi_i)g_i(\vec{r}_i')|\vec{r}_i'-\vec{r}_i|^l\mathrm{d}^3r_i' + \sum_\mu\int_{\mathcal{P}_i}\overline{Y_l^m}(\Theta_{i\mu},\Phi_{i\mu})g_{i\mu}(\vec{r}_{i\mu})|\vec{r}_{i\mu}-\vec{r}_i|^l\mathrm{d}^3r_{i\mu}\right) \tag{B.3}$$

accounts for influences of a continuous source strength $G(\vec{r})$, where the quantities $g_i(\vec{r}_i')$ and $g_{i\mu}(\vec{r}_{i\mu})$ denote appropriately mirrored images of G, and the integration is performed within the volume $\mathcal{P}_i$ of the i-th precipitate. The term

$$B_{il}^m = \tilde{Q}_i\delta_{0l} + \frac{4\pi}{2l+1}\sum_\nu\overline{Y_l^m}(\Theta_{i\nu},\Phi_{i\nu})Q_{i\nu}|\vec{r}_{i\nu}-\vec{r}_i|^l \tag{B.4}$$

describes the mutual interaction between NCs. In the following $C_{il}^m = A_{il}^m + B_{il}^m$.

In order to calculate the multipole moments Eq. (B.2) is multiplied with $\overline{Y_{l'}^{m'}}(\theta_{i'},\phi_{i'})$ and integrated over the surface of the i'-th precipitate

$$\begin{aligned}\oint_{\mathcal{P}_{i'}} c'(\theta_{i'},\phi_{i'})\overline{Y_{l'}^{m'}}(\theta_{i'},\phi_{i'})\mathrm{d}S_{i'} &= \frac{4\pi}{\sqrt{4\pi}}R_{i'}^2c_\mathrm{u}\delta_{0l'} \\ &+ \frac{1}{4\pi D}\oint_{\mathcal{P}_{i'}}\left(\sum_{i=1}^N\sum_{l=0}^\infty\sum_{m=-l}^l\frac{1}{|\vec{r}-\vec{r}_i|^{l+1}}Y_l^m(\theta_i,\phi_i)C_{il}^m\right)\overline{Y_{l'}^{m'}}(\theta_{i'},\phi_{i'})\mathrm{d}S_{i'} \\ &= \frac{4\pi}{\sqrt{4\pi}}R_{i'}^2c_\mathrm{u}\delta_{0l'} + \frac{R_{i'}^2}{4\pi D}\left(\frac{C_{i'l'}^{m'}}{R_{i'}^{l'+1}} + \sum_{i\neq i'}^N\sum_{l=0}^\infty\sum_{m=-l}^l C_{il}^m g_{i'il'l}^{m'm}\right),\end{aligned} \tag{B.5}$$

where the orthogonality properties of the spherical harmonics have been used together with the fact that the contribution of the source density G on the i'-th surface is canceled by definition of the mirrored source density $g_{i'}$. The purely geometrical quantities

$$g_{i'il'l}^{m'm} = \frac{1}{R_{i'}^2}\oint_{\mathcal{P}_{i'}}\frac{Y_l^m(\theta_i,\phi_i)\overline{Y_{l'}^{m'}}(\theta_{i'},\phi_{i'})}{|\vec{r}-\vec{r}_i|^{l+1}}\mathrm{d}S_{i'} \tag{B.6}$$

can be interpreted as interaction terms between NCs i and i'.

In the case of diffusion control one would insert the BC $\hat{c} = c^\mathrm{GT}(R)$ [Eq. (4.7)] into the lhs of Eq. (B.5) and straightforwardly proceed to determine the coupling constants $g_{i'il'l}^{m'm}$ to the desired order [182]. However, in the general case considered here, $\hat{c}$ is a function of the concentration field itself. This can be seen by equating the reaction and diffusion currents on the surface of the i-th NC

$$\vec{\jmath}_\mathrm{reac} = \vec{\jmath}_\mathrm{diff} \quad\Rightarrow\quad k\left[c^\mathrm{GT}(R_i) - \hat{c}(\theta_i,\phi_i)\right] = -D\left(\vec{\nabla}c(\vec{r})\right)\Big|_{|\vec{r}-\vec{r}_i|=R_i}\cdot\vec{e}_i^{(r)}, \tag{B.7}$$

where k denotes the surface-averaged and radius-independent reaction constant in the linear ansatz for $\vec{j}_{\mathrm{reac}}$ and $\vec{e}_i^{(r)}$ is the unit vector in radial direction. After solving for c' one gets

$$\hat{c}(\theta_i,\phi_i) = \frac{D}{k}\left(\vec{\nabla}c(\vec{r})\right)\Big|_{|\vec{r}-\vec{r}_i|=R_i}\cdot\vec{e}_i^{(r)} + c^{\mathrm{GT}}(R_i). \tag{B.8}$$

By substituting the last expression into Eq. (B.5) one gets

$$\oint_{\mathcal{P}_{i'}} \hat{c}(\theta_{i'},\phi_{i'})\overline{Y_{l'}^{m'}}(\theta_{i'},\phi_{i'})\mathrm{d}S_{i'} = \frac{D}{k}\oint_{\mathcal{P}_{i'}}\left(\vec{\nabla}c(\vec{r})\right)\vec{e}_{i'}^{(r)}\overline{Y_{l'}^{m'}}(\theta_{i'},\phi_{i'})\mathrm{d}S_{i'} + c^{\mathrm{GT}}(R_{i'})\sqrt{4\pi}R_{i'}^2. \tag{B.9}$$

Using the general solution for the concentration field [Eq. (B.2)] the first term on the rhs of Eq. (B.9) reads

$$\begin{aligned}
&\frac{D}{k}\oint_{\mathcal{P}_{i'}}\vec{\nabla}\left(\frac{1}{4\pi D}\sum_{i=1}^{N}\sum_{l=0}^{\infty}\sum_{m=-l}^{l}\frac{1}{|\vec{r}-\vec{r}_i|^{l+1}}Y_l^m(\theta_i,\phi_i)C_{il}^m\right)\vec{e}_{i'}^{(r)}\overline{Y_{l'}^{m'}}(\theta_{i'},\phi_{i'})\mathrm{d}S_{i'}\\
&= \frac{-(l+1)}{4\pi k}\left[\oint_{\mathcal{P}_{i'}}\sum_{l=0}^{\infty}\sum_{m=-l}^{l}\frac{\vec{r}-\vec{r}_{i'}}{|\vec{r}-\vec{r}_{i'}|^{l+3}}\vec{e}_{i'}^{(r)}Y_l^m(\theta_{i'},\phi_{i'})C_{i'l}^m\overline{Y_{l'}^{m'}}(\theta_{i'},\phi_{i'})\mathrm{d}S_{i'}\right.\\
&\quad\left.+\oint_{\mathcal{P}_{i'}}\sum_{i\neq i'}^{N}\sum_{l=0}^{\infty}\sum_{m=-l}^{l}\frac{\vec{r}-\vec{r}_i}{|\vec{r}-\vec{r}_i|^{l+3}}\vec{e}_{i'}^{(r)}Y_l^m(\theta_i,\phi_i)C_{il}^m\overline{Y_{l'}^{m'}}(\theta_{i'},\phi_{i'})\mathrm{d}S_{i'}\right]\\
&= -\frac{R_{i'}^2}{4\pi k}\left(\frac{l'+1}{R_{i'}^{l'+2}}C_{i'l'}^{m'} + (l+1)C_{il}^m h_{i'il'l}^{m'm}\right),
\end{aligned} \tag{B.10}$$

containing the purely geometrical quantities

$$h_{i'il'l}^{m'm} = \frac{l+1}{R_{i'}^2}\oint_{\mathcal{P}_{i'}}\left(\frac{\vec{r}-\vec{r}_i}{|\vec{r}-\vec{r}_i|^{l+3}}\vec{e}_{i'}^{(r)}\right)Y_l^m(\theta_i,\phi_i)\overline{Y_{l'}^{m'}}(\theta_{i'},\phi_{i'})\mathrm{d}S_{i'}, \tag{B.11}$$

which like $g_{i'il'l}^{m'm}$ are NC interaction terms.

By equating the corresponding expressions on the rhs and lhs of Eq. (B.5), one gets after interchanging primed and unprimed quantities the following system of equations

$$\begin{aligned}
&\frac{4\pi}{\sqrt{4\pi}}\left[c^{\mathrm{GT}}(R_i) - c_{\mathrm{u}}\right]\delta_{0l} =\\
&\quad\frac{1}{4\pi}\frac{C_{il}^m}{R_i^{l+1}}\left(\frac{1}{D}+\frac{l+1}{kR_i}\right) + \frac{1}{4\pi}\sum_{i'\neq i}^{N}\sum_{l'=0}^{\infty}\sum_{m'=-l'}^{l'}C_{i'l'}^{m'}f_{ii'll'}^{mm'},
\end{aligned} \tag{B.12}$$

where

$$f_{ii'll'}^{mm'} = \left(\frac{1}{D}g_{ii'll'}^{mm'} + \frac{l'+1}{k}h_{ii'll'}^{mm'}\right) \tag{B.13}$$

defines the coupling between multipole moments. The degree of mutual interaction of precipitates is given by the geometrical terms $f_{ii'll'}^{mm'}$.

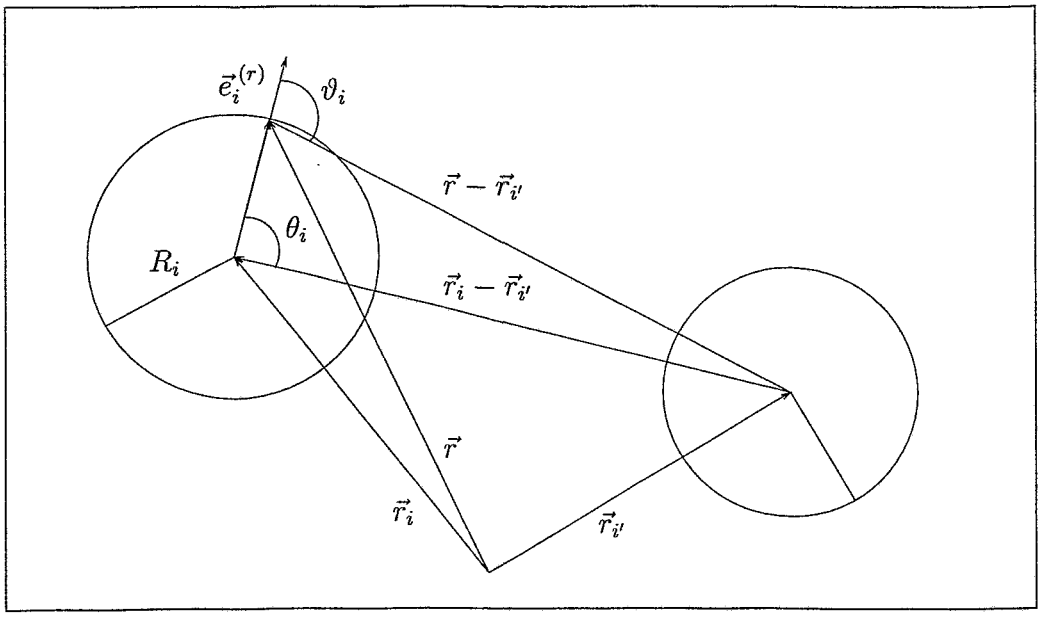

Figure B.1: Geometric relations for calculating coupling elements $f_{ii'00}$

B.2 Monopole approximation

In Eq. (B.12) the terms C_{il}^m are of the order of $\mathcal{O}\left(R^l\right)$ [Eqs. (B.3) and (B.4)], where R denotes a typical NC radius. The modified geometrical coupling terms $g_{ii'll'}^{mm'}/D$ and $h_{ii'll'}^{mm'}/k$ are of the order of $\mathcal{O}\left((1/d)^{l+1}/D\right)$, and $\mathcal{O}\left((1/d)^{l+2}/k\right)$, respectively, where d is an averaged distance between precipitates. Although both terms are of different order with respect to d, the re-weighting due to factors $1/D$ and $1/k$ may change their relative magnitudes considerably. In particular, if D/k is of the order of d, both terms are approximately of same order.

For the purpose of a basic rate-equation approach to diffusion and reaction controlled OR, the multipole expansion is truncated after the first term ($l'=0$: monopole approximation). Thus $h_{ii'00}$ is given by

$$h_{ii'00}=\frac{1}{R_i^2}\oint_{\mathcal{P}_i}\frac{\vec{r}-\vec{r}_{i'}}{|\vec{r}-\vec{r}_{i'}|^3}\vec{e}_i^{(r)}Y_0^0(\theta_{i'},\phi_{i'})\overline{Y_0^0}(\theta_i,\phi_i)\mathrm{d}S_i. \tag{B.14}$$

Using the cosine relation (see Fig. B.1) the scalar product can be written as

$$(\vec{r}-\vec{r}_{i'})\vec{e}_i^{(r)}=|\vec{r}-\vec{r}_{i'}|\frac{|\vec{r}_i-\vec{r}_{i'}|^2-R_i^2-|\vec{r}-\vec{r}_{i'}|^2}{2R_i|\vec{r}-\vec{r}_{i'}|}. \tag{B.15}$$

Therefore one gets

$$h_{ii'00}=\frac{1}{4\pi}\frac{1}{2R_i}\int_0^{2\pi}\mathrm{d}\phi\int_0^{\pi}\left(\frac{|\vec{r}_i-\vec{r}_{i'}|^2-R_i^2}{|\vec{r}-\vec{r}_{i'}|^3}-\frac{1}{|\vec{r}-\vec{r}_{i'}|}\right)\sin\theta\mathrm{d}\theta. \tag{B.16}$$

Using (see Fig. B.1)

$$|\vec{r}-\vec{r}_{i'}| = \sqrt{|\vec{r}_i-\vec{r}_{i'}|^2 + R_i^2 - 2R_i|\vec{r}_i-\vec{r}_{i'}|\cos\theta_i} \tag{B.17}$$

and applying the substitutions

$$\begin{aligned} u &= \cos\theta_i \\ A &= |\vec{r}_i-\vec{r}_{i'}|^2 - R_i^2 \\ a &= |\vec{r}_i-\vec{r}_{i'}|^2 + R_i^2 \\ b &= 2R_i|\vec{r}_i-\vec{r}_{i'}| \end{aligned} \tag{B.18}$$

the geometry factor is given by

$$\begin{aligned} f_{ii'00} &= \frac{1}{2R_ib}\left(\frac{A}{\sqrt{a-bu}}\Big|_0^1 + \sqrt{a-bu}\Big|_0^1\right) \\ &= \frac{1}{2R_ib}\frac{\left[A(\sqrt{a}-\sqrt{a-b}) + (a-b)\sqrt{a} - a\sqrt{a-b}\right]}{\sqrt{a(a-b)}}. \end{aligned} \tag{B.19}$$

Substituting back one gets

$$\begin{aligned} f_{ii'00} = \frac{1}{4R_i^2|\vec{r}_i-\vec{r}_{i'}|}\frac{1}{\sqrt{|\vec{r}_i-\vec{r}_{i'}|^2+R_i^2}} \\ \times\Big\{(|\vec{r}_i-\vec{r}_{i'}|+R_i)\left[\sqrt{|\vec{r}_i-\vec{r}_{i'}|^2+R_i^2} - (|\vec{r}_i-\vec{r}_{i'}|-R_i)\right] \\ + \sqrt{|\vec{r}_i-\vec{r}_{i'}|^2+R_i^2}\,(|\vec{r}_i-\vec{r}_{i'}|-R_i) - (|\vec{r}_i-\vec{r}_{i'}|^2+R_i^2)\Big\}. \end{aligned} \tag{B.20}$$

After some straightforward algebra the last equation reads

$$f_{ii'00} = -\frac{1}{2R_i^2}\left[\frac{|\vec{r}_i-\vec{r}_{i'}|}{\sqrt{|\vec{r}_i-\vec{r}_{i'}|^2+R_i^2}} - 1\right]. \tag{B.21}$$

Rewriting the square root and expanding in terms of $R_i^2/|\vec{r}_i-\vec{r}_{i'}|^2$, one gets

$$f_{ii'00} = \frac{1}{|\vec{r}_i-\vec{r}_{i'}|^2}. \tag{B.22}$$

Combining the last result with the result $g_{ii'00} = 1/|\vec{r}_i-\vec{r}_{i'}|$ [182], the complete geometry factor is given by

$$f_{ii'00} = \frac{1}{|\vec{r}_i-\vec{r}_{i'}|}\left(\frac{1}{D} + \frac{1}{k|\vec{r}_i-\vec{r}_{i'}|}\right). \tag{B.23}$$

B.3 Source strengths in monopole approximation

Within the monopole approximation, the concentration field is given by

$$c(\vec{r}) = c_{\mathrm{u}} + \frac{1}{\sqrt{4\pi}^3 D} \sum_{i=1}^{N} \frac{C_{i0}}{|\vec{r} - \vec{r}_i|}, \tag{B.24}$$

where the quantities C_{i0} are defined as

$$\frac{1}{\sqrt{4\pi}^3}\left[\frac{C_{i0}}{R_i}\left(\frac{1}{D}+\frac{1}{kR_i}\right) + \sum_{i'\neq i}^{N} \frac{C_{i'0}}{|\vec{r}_i - \vec{r}_{i'}|}\left(\frac{1}{D}+\frac{1}{k|\vec{r}_i - \vec{r}_{i'}|}\right)\right] = c^{\mathrm{GT}}(R_i) - c_{\mathrm{u}}. \tag{B.25}$$

The source strengths Q_i can be obtained by integration of the material current given by FICKs law $\vec{j} = -D\left(\vec{\nabla} c(\vec{r})\right)$ at the i-th precipitate

$$\begin{aligned} Q_i &= -D \oint_{\mathcal{P}_i} \vec{j}|_{|\vec{r}-\vec{r}_i|=R_i} \cdot \vec{e}_i^{(r)} \mathrm{d}S_i = \frac{1}{\sqrt{4\pi}^3} \sum_{i'}^{N} C_{i'0} \oint_{\mathcal{P}_i} \frac{(\vec{r}-\vec{r}_{i'})}{|\vec{r}-\vec{r}_{i'}|^3} \vec{e}_i^{(r)} \mathrm{d}S_i \\ &= \frac{1}{4\pi} C_{i0} + \mathcal{O}\left(\left(\frac{R}{d}\right)^2\right). \end{aligned} \tag{B.26}$$

Thus the following system of equations for the source strengths is obtained in the case of no external source term

$$\frac{1}{4\pi}\left[\frac{Q_i}{R_i}\left(\frac{1}{D}+\frac{1}{kR_i}\right) + \sum_{i'\neq i}^{N} \frac{Q_{i'}}{|\vec{r}_i - \vec{r}_{i'}|}\left(\frac{1}{D}+\frac{1}{k|\vec{r}_i - \vec{r}_{i'}|}\right)\right] = c^{\mathrm{GT}}(R_i) - c_{\mathrm{u}}, \tag{B.27}$$

which can be rewritten as

$$Q_i = 4\pi \frac{R_i}{\frac{1}{D}+\frac{1}{kR_i}}\left[c^{\mathrm{GT}}(R_i) - \frac{1}{4\pi}\sum_{i'\neq i}^{N} \frac{Q_{i'}}{|\vec{r}_i - \vec{r}_{i'}|}\left(\frac{1}{D}+\frac{1}{k|\vec{r}_i - \vec{r}_{i'}|}\right) - c_{\mathrm{u}}\right]. \tag{B.28}$$

In the limit of diffusion and reaction control the last equation reduces to:

Diffusion control: $D \ll kR < kd$:

$$Q_i = 4\pi D R_i \left[c^{\mathrm{GT}}(R_i) - \frac{1}{4\pi D}\sum_{i'\neq i}^{N} \frac{Q_{i'}}{|\vec{r}_i - \vec{r}_{i'}|} - c_{\mathrm{u}}\right], \tag{B.29}$$

Reaction control: $D \gg kd > kR$:

$$Q_i = 4\pi k R_i^2 \left[c^{\mathrm{GT}}(R_i) - \frac{1}{4\pi k}\sum_{i'\neq i}^{N} \frac{Q_{i'}}{|\vec{r}_i - \vec{r}_{i'}|^2} - c_{\mathrm{u}}\right]. \tag{B.30}$$

It should be noted, that a full treatment of interactions up to order $1/d^2$ involves the expansion of Eq. (B.12) to dipole order ($l' = 1$). However, this quadruples the number of involved multipole moments and thus terms are introduced, which account for migration and/or spherical shape deformation of precipitates [166].

List of Figures

List of Tables

Bibliography

[1] J.F. Ziegler, *Ion implantation physics*, in *Handbook of ion implantation technology*, edited by J.F. Ziegler (Elsevier Science Publishers, Amsterdam, 1992), p. 1.

[2] E. Chason, S.T. Picraux, J.M. Poate, J.O. Borland, M.I. Current, T. Diaz de la Rubia, D.J. Eaglesham, O.W. Holland, M.E. Law, C.W. Magee, J.W. Mayer, J. Melngailis and A.F. Tasch, *Ion beams in silicon processing and characterization*, J. Appl. Phys. **81**, 6513 (1997).

[3] A.M. Vredenberg, F.Z. Cui, F.W. Saris, N.M. Van der Pers and P.F Colijn, *Microstructure and hardness of titanium and iron surfaces after megaelectronvolt nitrogen implantation*, Mat. Sci. Eng. A **115**, 297 (1989).

[4] G.W. Arnold, *Near-surface nucleation and crystallization of an ion-implanted lithia-alumina-silica glass*, J. Appl. Phys. **46**, 4466 (1975).

[5] C.W. White, D.S. Zhou, J.D. Budai, R.A. Zuhr, R.H. Magruder and D.H. Osborne, *Colloidal Au nanoclusters formed in fused silica by MeV ion implantation and annealing*, Mat. Res. Soc. Symp. Proc. **316**, 499 (1994).

[6] C.W. White, D.S. Zhou, R.A. Zuhr and R.H. Magruder, *Formation of colloidal Ag precipitates in fused silica by MeV ion implantation*, Trans. Mat. Res. Soc. Jpn. **17**, 553 (1994).

[7] R.H. Magruder III, R.F. Haglund Jr., L. Yang, J.E. Wittig and R.A. Zuhr, *Physical and optical properties of Cu nanoclusters fabricated by ion implantation in fused silica*, J. Appl. Phys. **76**, 708 (1994).

[8] T. Isobe, R.A. Weeks and R.A. Zuhr, *Magnetic properties of nanosize nickel particles produced in silica glasses by ion-implantation and subsequent annealing*, Solid State Comm. **105**, 469 (1998).

[9] P. Mazzoldi, G.W. Arnold, G. Battaglin, R. Bertoncello and F. Gonella, *Peculiarities and application perspectives of metal-ion implants in glasses*, Nucl. Instr. & Meth. B **91**, 478 (1994).

[10] H.A. Atwater, K.V. Shcheglov, S.S. Wong, K.J. Vahala, R.C. Flagan, M.L. Brongersma and A. Polman, *Ion beam synthesis of luminescent Si and Ge nanocrystals in a silicon dioxide matrix*, Mat. Res. Soc. Symp. Proc. **316**, 409 (1994).

[11] S. Mantl, *Ion beam synthesis of epitaxial silicides: Fabrication, characterization and applications*, Mater. Sci. Rep. **8**, 1 (1992).

[12] J.G. Zhu, C.W. White, J.D. Budai, S.P. Withrow and Y. Chen, *Growth of Ge, Si, and SiGe nanocrystals in SiO_2 matrices*, J. Appl. Phys. **78**, 4386 (1995).

[13] C.W. White, J.D. Budai, J.G. Zhu, S.P. Withrow, R.A. Zuhr, Y. Chen, D.M. Hembree Jr., R.H. Magruder and D.O. Henderson, *Compound semiconductor nanocrystals formed by sequential ion implantation*, Mat. Res. Soc. Symp. Proc. **358**, 169 (1995).

[14] C.W. White, J.D. Budai, J.G. Zhu, S.P. Withrow and M.J. Aziz, *Ion-beam synthesis and stability of GaAs nanocrystals in silicon*, Appl. Phys. Lett. **68**, 2389 (1996).

[15] R.A. Zuhr, R.H. Magruder III, T.A. Anderson and J.E. Wittig, *Nanosize metal alloy particle formation in Ag and Cu sequentially implanted silica*, Mat. Res. Soc. Symp. Proc. **316**, 457 (1994).

[16] *Proceedings of the E-MRS 1998 Spring Meeting, Symp. J: Ion implantation into semiconductors, oxides and ceramics*, Vol. 147 of *Nucl. Instr. & Meth. B*, edited by J.K.N. Lindner, B.G. Svenson, P.L.F. Hemment and H.A. Atwater (Elsevier Science Publishers, Amsterdam, 1999).

[17] *Proceedings of the 11th International Conference on Ion Beam Modifications of Matrials*, Vol. 148 of *Nucl. Instr. & Meth. B*, edited by A.M. Vredenberg, A. Polman, P.A. Stolk, E. Snoeks and M.L. Brongersma (Elsevier Science Publishers, Amsterdam, 1999).

[18] A.P. Alivisatos, *Semiconductor clusters, nanocrystals, and quantum dots*, Science **271**, 933 (1996).

[19] K.S. Min, K.V. Shcheglov, C.M. Yang, H.A. Atwater, M.L. Brongersma and A. Polman, *The role of quantum-confined excitons vs defects in the visible luminescence of SiO_2 films containing Ge nanocrystals*, Appl. Phys. Lett. **68**, 2511 (1996).

[20] A.P. Alivisatos, *Scaling law for structural metastability in semiconductor nanocrystals*, Ber. Bunsenges. Phys. Chem. **101**, 1573 (1997).

[21] C. Flytzanis, F. Hache, M.C. Klein, D. Ricard and Ph. Roussignol, *Semiconductor and metal crystallites in dielectrics*, in *Progress in optics XXIX*, edited by E. Wolf (Elsevier Science Publishers, Amsterdam, 1991), p. 321.

[22] J. von Borany, R. Grötzschel, K.-H. Heinig, A. Markwitz, W. Matz, B. Schmidt and W. Skorupa, *Multimodal impurity redistribution and nanocluster formation in Ge implanted silicon dioxide films*, Appl. Phys. Lett. **71**, 3215 (1997).

[23] M.L. Brongersma, A. Polman, K.S. Min, E. Boer, T. Tambo and H.A. Atwater, *Tuning the emission wavelength of Si nanocrystals in SiO_2 by oxidation*, Appl. Phys. Lett. **72**, 2577 (1998).

[24] S. Tiwari, F. Rana, H. Hanafi, A. Hartstein and E.F. Crabbé, *A silicon nanocrystals based memory*, Appl. Phys. Lett. **68**, 1377 (1996).

[25] D.L. Klein, R. Roth, A.K.L. Lim, A.P. Alivisatos and P.L. McEuen, *A single-electron transistor made from a cadmium selenide nanocrystal*, Nature **389**, 699 (1997).

[26] L. Thomé, J. Jagielski, G. Rizza, F. Garrido and J.C. Pivin, *Formation of metallic nanophases in silica by ion-beam mixing Part I: Mixing mechanisms*, Appl. Phys. A **66**, 327 (1998).

[27] L. Thomé, G. Rizza, F. Garrido, M. Gusso, L. Tapfer and A. Quaranta, *Formation of metallic nanophases in silica by ion-beam mixing Part II: cluster formation*, Appl. Phys. A **67**, 241 (1998).

[28] A.P. Alivisatos, *Perspectives on the physical chemistry of semiconductor nanocrystals*, J. Phys. Chem. **100**, 13226 (1996).

[29] G. De, L. Tapfer, M. Catalano, G. Battaglin, F. Caccavale, F. Gonella, P. Mazzoldi and R.F. Haglund Jr., *Formation of copper and silver nanometer dimension clusters in silica by the sol-gel process*, Appl. Phys. Lett. **68**, 3820 (1996).

[30] M. Zinke-Allmang, L.C. Feldman and M.H. Grabow, *Clustering on surfaces*, Surf. Sci. Rep. **16**, 377 (1992).

[31] G.H. Gilmer, P.H. Huang and C. Roland, *Thin film deposition: Fundamentals and modeling*, Comp. Mat. Sci. **12**, 354 (1998).

[32] S.A. Empedocles, D.J. Norris and M.G. Bawendi, *Photoluminescence spectroscopy of single CdSe nanocrystallite quantum dots*, Phys. Rev. Lett. **77**, 3873 (1996).

[33] X. Peng, M.C. Schlamp, A.V. Kadavanich and A.P. Alivisatos, *Epitaxial growth of highly luminescent CdSe/CdS core/shell nanocrystals with photostability and electronic accessibility*, J. Am. Chem. Soc. **119**, 7019 (1997).

[34] R. Wagner and R. Kampmann, *Homogeneous second phase precipitation*, in *Phase transformations in materials*, Vol. 5 of *Materials Science and Technology*, edited by P. Haasen (VCH, Weinheim, 1991), p. 213.

[35] C. Sagui, D.S. O'Gorman and M. Grant, *Nucleation and growth: Decay of a metastable state*, Phys. Rev. E **56**, R21 (1997).

[36] C. Sagui and M. Grant, *Theory of nucleation and growth during phase separation*, Phys. Rev. E **59**, 4175 (1999).

[37] K. Binder and D.W. Heermann, *Monte Carlo simulation in statistical physics*, Vol. 80 of *Springer Series in Solid-State Sciences*, 2nd Ed. (Springer, Berlin, 1992).

[38] *The Monte Carlo method in condensed matter physics*, Vol. 71 of *Topics in Applied Physics*, edited by K. Binder (Springer, Berlin, 1992).

[39] P.W. Voorhees and M.E. Glicksman, *Solution to the multi-particle diffusion problem with applications to Ostwald ripening - I. Theory*, Acta Metall. **32**, 2001 (1984).

[40] P.W. Voorhees and M.E. Glicksman, *Solution to the multi-particle diffusion problem with applications to Ostwald ripening - II. Computer simulations*, Acta Metall. **32**, 2013 (1984).

[41] S. Reiss and K.-H. Heinig, *Computer simulations of mechanisms of the SIMOX process*, Nucl. Instr. & Meth. B **102**, 256 (1995).

[42] P. Normand, D. Tsoukalas, E. Kapetanakis, J.A. Van Den Berg, D.G. Armour, J. Stoemenos and C. Vieu, *Formation of 2-D arrays of silicon nanocrystals in thin SiO_2 films by very-low energy Si^+ ion implantation*, Electrochem. Solid-State Lett. **1**, 88 (1998).

[43] J.K.N. Lindner, T. Klassen and E.H. te Kaat, *Ion beam synthesis of deep buried $NiSi_2$ layers in silicon by 6 MeV Ni implantation*, Nucl. Instr. & Meth. B **59/60**, 655 (1991).

[44] R.A. Zuhr, J.D. Budai, P.G. Datskos, A. Meldrum, K.A. Thomas, R.J. Warmack, C.W. White, L.C. Feldman, M. Strobel and K.-H. Heinig, *Nanostructured arrays formed by finely focused ion beams*, Mat. Res. Soc. Symp. Proc. **536**, 251 (1999).

[45] P.K. Chu, S. Qin, C. Chan, N.W. Cheung and L.A. Larson, *Plasma immersion ion implantation – a fledgling technique for semiconductor processing*, Mat. Sci. Eng. R **17**, 207 (1996).

[46] J.F. Ziegler, J.P. Biersack and U. Littmark, *The stopping and range of ions in solids* (Pergamon Press, Oxford, 1984), Vol. 1.

[47] J.P. Biersack and L.G. Haggmark, *A Monte Carlo computer program for the transport of energetic ions in amorphous targets*, Nucl. Instr. & Meth. **174**, 257 (1980).

[48] J. Orloff, *High-resolution focused ion beams*, Rev. Sci. Instrum. **64**, 1105 (1993).

[49] T. Aign, P. Meyer, S. Lemerle, J.P. Jamet, J. Ferré, V. Mathet, C. Chappert, J. Gierak, C. Vieu, F. Rousseaux, H. Launois and H. Bernas, *Magnetization reversal in arrays of perpendicularly magnetized ultrathin dots coupled by dipolar interaction*, Phys. Rev. Lett. **81**, 5656 (1998).

[50] Y. Ishikawa, N. Shibata and S. Fukatsu, *Fabrication of [110]-aligned Si quantum wires embedded in SiO_2 by low-energy oxygen implantation*, Nucl. Instr. & Meth. B **147**, 304 (1999).

[51] G.H. Kinchin and R.S. Pease, *The displacement of atoms in solids by radiation*, Rep. Prog. Phys. **18**, 1 (1955).

[52] P. Sigmund, *On the number of atoms displaced by implanted ions or energetic recoil atoms*, Appl. Phys. Lett. **14**, 114 (1969).

[53] R.S. Averback and T. Diaz de la Rubia, *Displacement damage in irradiated metals and semiconductors*, Solid State Physics **51**, 281 (1998).

[54] J. Schmelzer, G. Röpke and R. Mahnke, *Aggregation phenomena in complex systems* (Wiley-VCH, Weinheim, 1999).

[55] J.W. Cahn, *Spinodal decomposition*, Trans. Metall. Soc. AIME **242**, 166 (1968).

[56] J.S. Langer, *An introduction to the kinetics of first-order phase transitons*, in *Solids far from equilibrium*, edited by C. Godréche (Cambridge University Press, Cambridge, 1992), p. 297.

[57] K. Binder, *Spinodal decomposition*, in *Phase transformations in materials*, Vol. 5 of *Materials Science and Technology*, edited by P. Haasen (VCH, Weinheim, 1991), p. 405.

[58] M. Volmer and A. Weber, *Keimbildung in übersättigten Gebilden*, Z. Phys. Chem. (Leipzig) **119**, 277 (1926).

[59] R. Becker and W. Döring, *Kinetische Behandlung der Keimbildung in übersättigten Dämpfen*, Ann. Phys. **24**, 719 (1935).

[60] K.F. Kelton, *Crystal nucleation in liquids and glasses*, Solid State Physics **45**, 75 (1991).

[61] J.D. Gunton, M. San Miguel and P.S. Sahni, *The dynamics of first-order phase transitions*, in *Phase transitions and critical phenomena*, edited by C. Domb and J.L. Lebowitz (Academic Press, London, 1983), Vol. 8, p. 267.

[62] K. Binder, *Theory of first-order phase transitions*, Rep. Prog. Phys. **50**, 783 (1987).

[63] D.T. Wu, *Nucleation theory*, Solid State Physics **50**, 38 (1997).

[64] C. Spinella, S. Lombardo and F. Priolo, *Crystal grain nucleation in amorphous silicon*, J. Appl. Phys. **84**, 5383 (1998).

[65] J.W.P. Schmelzer, I. Gutzow and J. Schmelzer Jr., *Curvature-dependent surface tension and nucleation theory*, J. Colloid Interf. Sci. **178**, 657 (1996).

[66] J.B. Zeldovich, *On the theory of new phase formation; Cavitation*, Acta Physicochimica URSS **18**, 1 (1943).

[67] D. Turnbull and J.C. Fisher, *Rate of nucleation in condensed systems*, J. Chem. Phys. **17**, 71 (1949).

[68] K.C. Russell, *Nucleation in solids: The induction and steady state*, Adv. Colloid Interf. Sci. **13**, 205 (1980).

[69] K.F. Kelton, A.L. Greer and C.V. Thompson, *Transient nucleation in condensed systems*, J. Chem. Phys. **79**, 6261 (1983).

[70] M. Avrami, *Granulation, phase change, and microstructure: Kinetics of phase change. III*, J. Chem. Phys. **9**, 177 (1941).

[71] A. Markwitz, B. Schmidt, W. Matz, R. Grötzschel and A. Mücklich, *Microstructural investigation of ion beam synthesized germanium nanoclusters embedded in SiO_2 layers*, Nucl. Instr. & Meth. B **142**, 338 (1998).

[72] G. Martin, *Phase stability under irradiation: Ballistic effects*, Phys. Rev. B **30**, 1424 (1984).

[73] *The modern theory of capillarity*, edited by F.C. Goodrich and A.I. Rusanov (Akademie-Verlag, Berlin, 1981).

[74] M. Posselt, *CRYSTAL-TRIM and its application to investigations on channeling effects during ion implantation*, Rad. Eff. Def. Solids **130/131**, 87 (1994).

[75] W. Möller and W. Eckstein, *TRIDYN – A TRIM simulation code including dynamic composition changes*, Nucl. Instr. & Meth. B **2**, 814 (1984).

[76] W. Möller and W. Eckstein, *Ion mixing and recoil implantation simulations by means of TRIDYN*, Nucl. Instr. & Meth. B **7/8**, 645 (1985).

[77] J.S. Langer, M. Bar-on and H.D. Miller, *New computational method in the theory of spinodal decomposition*, Phys. Rev. A **11**, 1417 (1975).

[78] K. Binder, *Theory for the dynamics of "clusters". II. Critical diffusion in binary systems and the kinetics of phase separation*, Phys. Rev. B **15**, 4425 (1977).

[79] D.W. Heermann, *Computer simulation methods in theoretical physics*, 2nd Ed. (Springer, Berlin, 1990).

[80] M.E.J. Newman and G.T. Barkema, *Monte Carlo methods in statistical physics* (Oxford University Press, Oxford, 1999).

[81] N. Metropolis, A.W. Rosenbluth, M.N. Rosenbluth, A.H. Teller and E. Teller, *Equation of state calculations by fast computing machines*, J. Chem. Phys. **21**, 1087 (1953).

[82] W. Janke, *Monte Carlo simulations of spin systems*, in *Computational Physics*, edited by K.H. Hoffmann and M. Schreiber (Springer, Berlin, 1996), p. 10.

[83] A.C. Levi and M. Kotrla, *Theory and simulation of crystal growth*, J. Phys. Condens. Mat. **9**, 299 (1997).

[84] E. Ising, *Beitrag zur Theorie des Ferromagnetismus*, Z. Physik **31**, 253 (1925).

[85] T.D. Lee and C.N. Yang, *Statistical theory of equations of state and phase transitions. II. Lattice gas and Ising model*, Phys. Rev. **87**, 410 (1952).

[86] R.J. Glauber, *Time-dependent statistics of the Ising model*, J. Math. Phys. **4**, 294 (1963).

[87] K. Kawasaki, *Diffusion constants near the critical point for time-dependent Ising models. I*, Phys. Rev. **145**, 224 (1966).

[88] K. Binder, *Statistical theories of phase transitions*, in *Phase transformations in materials*, Vol. 5 of *Materials Science and Technology*, edited by P. Haasen (VCH, Weinheim, 1991), p. 143.

[89] A.L. Talapov and H.W.J. Blöte, *The magnitization of the 3D Ising model*, J. Phys. A **29**, 5727 (1996).

[90] S. Kobe, *Das Ising-Modell – gestern und heute*, Phys. Bl. **54**, 917 (1998).

[91] J. Marro, A.B. Bortz, M.H. Kalos and J.L. Lebowitz, *Time evolution of a quenched binary alloy. II. Computer simulation of a three-dimensional model system*, Phys. Rev. B **12**, 2000 (1975).

[92] A. Sur, J.L. Lebowitz, J. Marro and M.H. Kalos, *Time evolution of a quenched binary alloy. IV. Computer simulation of a three-dimensional model system*, Phys. Rev. B **15**, 3014 (1977).

[93] J. Marro, J.L. Lebowitz and M.H. Kalos, *Computer simulation of the time evolution of a quenched model alloy in the nucleation region*, Phys. Rev. Lett. **43**, 282 (1979).

[94] J.L. Lebowitz, J. Marro and M.H. Kalos, *Dynamical scaling of structure function in quenched binary alloys*, Acta Metall. **30**, 297 (1982).

[95] P. Fratzl and J.L. Lebowitz, *Universality of scaled structure functions in quenched systems undergoing phase separation*, Acta Metall. **37**, 3245 (1989).

[96] H. Furukawa, *A dynamic scaling theory for phase separation*, Adv. Phys. **34**, 703 (1985).

[97] A.J. Bray, *Theory of phase-ordering kinetics*, Adv. Phys. **43**, 357 (1994).

[98] M.H. Kalos, J.L. Lebowitz, O. Penrose and A. Sur, *Clusters, metastability, and nucleation: Kinetics of first-order phase transitions*, J. Stat. Phys. **18**, 39 (1978).

[99] O. Penrose, J.L. Lebowitz, J. Marro, M.H. Kalos and J. Tobochnik, *Kinetics of a first-order phase transition: Computer simulations and theory*, J. Stat. Phys. **34**, 399 (1984).

[100] O. Penrose, J.L. Lebowitz, J. Marro, M.H. Kalos and S. Sur, *Growth of clusters in a first-order phase transition*, J. Stat. Phys. **19**, 243 (1978).

[101] H.E. Cook, *Brownian motion in spinodal decomposition*, Acta Metall. **18**, 297 (1970).

[102] R. Toral, A. Chakrabarti and J.D. Gunton, *Numerical study of the Cahn-Hilliard equation in three dimensions*, Phys. Rev. Lett. **60**, 2311 (1988).

[103] A. Chakrabarti, R. Toral and J.D. Gunton, *Late stages of spinodal decomposition in a three-dimensional model system*, Phys. Rev. B **39**, 4386 (1989).

[104] I.M. Lifshitz and V.V. Slyozov, *The kinetics of precipitation from supersaturated solid solutions*, J. Phys. Chem. Solids **19**, 35 (1961).

[105] C. Wagner, *Theorie der Alterung von Niederschlägen durch Umlösen*, Z. Elektrochem. **65**, 581 (1961).

[106] S. Reiss, M.O. Ruault, J. Clayton, O. Kaitasov, K.-H. Heinig and H. Bernas, *Nucleation, growth and Ostwald ripening of $CoSi_2$ precipitates during Co ion implantation*, Mater. Res. Soc. Symp. Proc. **354**, 183 (1995).

[107] F.-P. Ludwig and J. Schmelzer, *On von Weimarn's law in nucleation theory*, J. Colloid Interf. Sci. **181**, 503 (1996).

[108] V.V. Slezov, J. Schmelzer and Y.Y. Tkatch, *Number of clusters formed in nucleation-growth processes*, J. Chem. Phys. **105**, 8340 (1996).

[109] J. Schmelzer, G. Röpke and F.-P. Ludwig, *Nuclear multifragmentation processes and nucleation theory*, Phys. Rev. C **55**, 1917 (1997).

[110] O. Penrose, *The Becker-Döring equations at large times and their connection with the LSW theory of coarsening*, J. Stat. Phys. **89**, 305 (1997).

[111] A.D. Brailsford, *Diffusion to a random array of identical spherical sinks*, J. Nucl. Mat. **60**, 257 (1976).

[112] V.A. Borodin, *Generalized rate theory for spatially inhomogeneous systems of point defect sinks*, Physica A **211**, 279 (1994).

[113] V.A. Borodin, K.-H. Heinig and S. Reiss, *Self-organization kinetics in finite precipitate ensembles during coarsening*, Phy. Rev. B **56**, 5332 (1997).

[114] K.-H. Heinig, 1995, unpublished.

[115] K. Binder, *Ordering of the face-centered-cubic lattice with nearest-neighbor interaction*, Phys. Rev. Lett. **45**, 811 (1980).

[116] S. Wolfram, *Statistical mechanics of cellular automata*, Rev. Mod. Phys. **55**, 601 (1983).

[117] W. Kinzel, *Phase transitions of cellular automata*, Z. Phys. B **58**, 229 (1985).

[118] S.G. Brush, *History of the Lenz-Ising model*, Rev. Mod. Phys. **39**, 883 (1967).

[119] D. Stauffer, *Computer simulations of cellular automata*, J. Phys. A **24**, 909 (1991).

[120] S. Mantl, L. Kappius, A. Antons, M. Löcken, F. Klinkhammer, M. Dolle, Q.T. Zhao, S. Mesters, C. Buchal, H.L. Bay, B. Kabius, H. Trinkaus and K.-H. Heinig, *Growth, patterning, and microelectronic applications of epitaxial cobaltdisilicide*, Mat. Res. Soc. Symp. Proc. **514**, 145 (1999).

[121] M.F. Sykes, D.S. Gaunt, P.D. Roberts and J.A. Wyles, *High temperature series for the susceptibility of the Ising model. Three dimensional lattices*, J. Phys. A **5**, 640 (1972).

[122] J.W. Essam and M.E. Fisher, *Padé approximant studies of the lattice gas and Ising ferromagnet below the critical point*, J. Chem. Phys. **38**, 802 (1963).

[123] C. Domb, *Ising model*, in *Phase transitions and critical phenomena*, edited by C. Domb and M.S. Green (Academic Press, London, 1974), Vol. 3, p. 357.

[124] C. Jayaprakash and W.F. Saam, *Thermal evolution of crystal shapes: The fcc crystal*, Phys. Rev. B **30**, 3916 (1984).

[125] K.L. Murphy and C. Rottman, *Low-index interfaces in Ising models: Macroscopic faceting, roughening, and phase diagrams*, Phys. Rev. B **42**, 680 (1990).

[126] *Physics of solid surfaces*, Vol. III/24a of *Landolt-Börnstein*, edited by G. Chiarotti (Springer, Berlin, 1993).

[127] P. Nozières, *Shape and growth of crystals*, in *Solids far from equilibrium*, edited by C. Godréche (Cambridge University Press, Cambridge, 1992), p. 1.

[128] H. Huang, G.H. Gilmer and T. Diaz de la Rubia, *An atomistic simulator for thin film deposition in three dimensions*, J. Appl. Phys. **84**, 3636 (1998).

[129] J. Philibert, *Atom movements, diffusion and mass transport in solids* (Les Editions de Physique, Les Ulis, 1991).

[130] H.J. Leamy, G.H. Gilmer, K.A. Jackson and P. Bennema, *Lattice-gas interface structure: A Monte Carlo study*, Phys. Rev. Lett. **30**, 601 (1973).

[131] K.K. Mon, S. Wansleben, D.P. Landau and K. Binder, *Monte Carlo studies of anisotropic surface tension and interfacial roughening in the three-dimensional Ising model*, Phys. Rev. B **39**, 7089 (1989).

[132] K.K. Mon, D.P. Landau and D. Stauffer, *Interface roughening in the three-dimensional Ising model*, Phys. Rev. B **42**, 545 (1990).

[133] *Impurities and defects in group IV elements and III-V compounds*, Vol. III/22b of *Landolt-Börnstein*, edited by M. Schulz (Springer, Berlin, 1989).

[134] H. Meirovitch and Z. Alexandrowicz, *Estimation of the pressure with computer simulation: The lattice gas model*, Mol. Phys. **34**, 1027 (1977).

[135] H. Furukawa and K. Binder, *Two-phase equilibria and nucleation barrieres near a critical point*, Phys. Rev. A **26**, 556 (1982).

[136] M. Strobel, K.-H. Heinig and W. Möller, *Computer simulation of precipitate coarsening: An unified treatment of diffusion and reaction controlled Ostwald ripening*, Rad. Def. Eff. Solids **141**, 99 (1997).

[137] M. Palard, Ph.D. thesis, Universite de Paris-Sud, 1997.

[138] K. Binder, *Monte Carlo calculation of the surface tension for two- and three-dimensional lattice-gas models*, Phys. Rev. A **25**, 1699 (1982).

[139] M. Hasenbusch and K. Pinn, *Surface tension, surface stiffness, and surface width of the three-dimensional Ising model on a cubic lattice*, Physica A **192**, 342 (1993).

[140] D. Stauffer, A. Coniglio and D.W. Heermann, *Monte Carlo experiment for nucleation rate in the three-dimensional Ising model*, Phys. Rev. Lett. **49**, 1299 (1982).

[141] D.W. Heermann, A. Coniglio, W. Klein and D. Stauffer, *Nucleation and metastability in three-dimensional Ising models*, J. Stat. Phys. **36**, 447 (1984).

[142] Y.T. Cheng, *Thermodynamic and fractal geometric aspects of ion-solid interactions*, Mat. Sci. Rep. **5**, 45 (1990).

[143] W. Bolse, *Ion-beam induced atomic transport through bi-layer interfaces of low- and medium-Z metals and their nitrides*, Mat. Sci. Eng. R **12**, 53 (1994).

[144] E. Salomons, P. Bellon, F. Soisson and G. Martin, *Dynamical lattice models for binary alloys under irradiation: Mean-field solutions and Monte Carlo simulations*, Phys. Rev. B **45**, 4582 (1992).

[145] G. Martin and P. Bellon, *Driven Alloys*, Solid State Physics **50**, 189 (1997).

[146] P. Sigmund and A. Gras-Marti, *Theoretical aspects of atomic mixing by ion beams*, Nucl. Instr. & Meth. **182/183**, 25 (1981).

[147] P. Fratzl and O. Penrose, *Ising model for phase separation in alloys with anisotropic elastic interaction – I. Theory*, Acta metall. mater. **43**, 2921 (1995).

[148] P. Fratzl and O. Penrose, *Ising model for phase separation in alloys with anisotropic elastic interaction – II. A computer experiment*, Acta metall. mater. **43**, 3227 (1995).

[149] M. Strobel, S. Reiss and K.-H. Heinig, *Evolution of nanocluster ensembles: Computer simulation of diffusion and reaction controlled Ostwald ripening*, Nucl. Instr. & Meth. B **120**, 216 (1996).

[150] C.W. White, 1997, unpublished.

[151] P. Fratzl and O. Penrose, *Kinetics of spinodal decomposition in the Ising model with vacancy diffusion*, Phys. Rev. B **50**, 3477 (1994).

[152] G.S. Grest, M.P. Anderson and D.J. Srolovitz, *Domain-growth kinetics for the Q-state Potts model in two and three dimensions*, Phys. Rev. B **38**, 4752 (1988).

[153] J.-M. Liu, *A Monte-Carlo approach to domain boundary precipitation in binary alloys*, J. Appl. Phys. **84**, 6582 (1998).

[154] W. Ostwald, *Über die vermeintliche Isomerie des roten und gelben Quecksilberoxyds und die Oberflächenspannung fester Körper*, Z. Phys. Chem. **34**, 495 (1900).

[155] A.D. Brailsford and P. Wynblatt, *The dependence of Ostwald ripening kinetics on particle volume fraction*, Acta Metall. **27**, 489 (1979).

[156] K. Tsumraya and Y. Miyata, *Coarsening models incorporating both diffusion geometry and volume fraction of particles*, Acta Metall. **31**, 437 (1983).

[157] J.A. Marqusee and J. Ross, *Theory of Ostwald ripening: Competitive growth and its dependence on volume fraction*, J. Chem. Phys. **80**, 536 (1984).

[158] M. Marder, *Correlations and Ostwald ripening*, Phys. Rev. A **36**, 858 (1987).

[159] P.W. Voorhees, *The theory of Ostwald ripening*, J. Stat. Phys. **38**, 231 (1985).

[160] J.H. Yao, K.R. Elder, H. Guo and M. Grant, *Theory and simulation of Ostwald ripening*, Phys. Rev. B **47**, 14110 (1993).

[161] J. Alkemper, V.A. Snyder, N. Akaiwa and P.W. Voorhees, *Dynamics of late-stage phase separation: A test of theory*, Phys. Rev. Lett. **82**, 2725 (1999).

[162] M.K. Chen and P.W. Voorhees, *The dynamics of transient Ostwald ripening*, Mod. Sim. Mat. Sci. Eng. **1**, 591 (1993).

[163] C.W.J. Beenakker, *Numerical simulation of diffusion-controlled droplet growth: Dynamical Correlation Effects*, Phys. Rev. A **33**, 4482 (1986).

[164] Y. Enomoto, K. Kawasaki and M. Tokuyama, *Computer modeling of Ostwald ripening*, Acta Metall. **35**, 907 (1987).

[165] T. Imaeda and K. Kawasaki, *Theory of morphological evolution in Ostwald ripening*, Physica A **186**, 359 (1992).

[166] N. Akaiwa and P.W. Voorhees, *Late-stage phase separation: Dynamics, spatial correlations, and structure functions*, Phys. Rev. E **49**, 3860 (1994).

[167] D. Feinn, P. Ortoleva, W. Scalf, S. Schmidt and M. Wolff, *Spontaneous pattern formation in precipitating systems*, J. Chem. Phys. **69**, 27 (1978).

[168] R. Feeney, S.L. Schmidt, P. Strickholm and P. Ortoleva, *Periodic precipitation and coarsening waves: Applications of the competitive particle growth model*, J. Chem. Phys. **78**, 1293 (1983).

[169] G. Venzl, *Pattern formation in precipitation processes. I. The theory of competitive coarsening*, J. Chem. Phys. **85**, 1996 (1986).

[170] G. Venzl, *Pattern formation in precipitation processes. II. A post-nucleation theory of Lisegang bands*, J. Chem. Phys. **85**, 2006 (1986).

[171] S. Reiss and K.-H. Heinig, *Ostwald ripening during ion beam synthesis - A computer simulation for inhomogeneous systems*, Nucl. Instr. & Meth. B **84**, 229 (1994).

[172] S. Reiss and K.-H. Heinig, *Self-structuring of buried SiO_2 precipitate layers during IBS: A computer simulation*, Nucl. Instr. & Meth. B **112**, 223 (1996).

[173] N. Akaiwa and D.I. Meiron, *Numerical simulation of two-dimensional late-stage coarsening for nucleation and growth*, Phys. Rev. E **51**, 5408 (1995).

[174] B. Levitan and E. Domany, *Ostwald ripening in two dimensions: Correlations and scaling beyond mean field*, Phys. Rev. E **57**, 1895 (1998).

[175] B. Burton and M.V. Speight, *The coarsening and annihilation of dislocation loops*, Phil. Mag. A **53**, 385 (1986).

[176] C. Bonafos, D. Mathiot and A. Claverie, *Ostwald ripening of end-of-range defects in silicon*, J. Appl. Phys. **83**, 3008 (1998).

[177] W.C. Johnson, T.A. Abinandanan and P.W. Voorhees, *The coarsening kinetics of two misfitting particles in an anisotropic crystal*, Acta metall. mater. **38**, 1349 (1990).

[178] C. Sagui, D. Orlikowski, A.M. Somoza and C. Roland, *Three-dimensional simulations of Ostwald ripening with elastic effects*, Phys. Rev. E **58**, R4092 (1998).

[179] R.J. White and S.B. Fisher, *The precipitation and growth kinetics of γ' in nimonic PE16*, Mat. Sci. Eng. **33**, 149 (1978).

[180] R.J. White, *The particle size distributions in systems evolving from interface-controlled to diffusion-controlled coarsening kinetics*, Mat. Sci. Eng. **40**, 15 (1979).

[181] J.P. Lavine and G.A. Hawkins, *Numerical studies of precipitate coarsening phenomena*, Mat. Res. Soc. Symp. Proc. **205**, 345 (1992).

[182] S. Reiss, Ph.D. thesis, Technische Universität Dresden, 1996.

[183] C.W.J. Beenakker and J. Ross, *Monte Carlo study of a model of diffusion-controlled reactions*, J. Chem. Phys. **84**, 3857 (1986).

[184] M. Strobel, K.-H. Heinig and W. Möller, *A combination of atomic and continuum computational models describing the evolution of nanoclusters*, Comp. Mat. Sci. **10**, 457 (1998).

[185] C.S. Jayanth and P. Nash, *Factors affecting particle-coarsening kinetics and size distribution*, J. Mat. Sci. **24**, 3041 (1989).

[186] S. Lee, I. Daruka, C.S. Kim, A.-L. Barabasi, J.L. Merz and J.K. Furdyna, *Dynamics of ripening of self-assembled II-VI semiconductor quantum dots*, Phys. Rev. Lett. **81**, 3479 (1998).

[187] M. Strobel, K.-H. Heinig, W. Möller, A. Meldrum, D.S. Zhou, C.W. White and R.A. Zuhr, *Ion beam synthesis of gold nanoclusters in SiO_2: Computer simulations versus experiments*, Nucl. Instr. & Meth. B **147**, 343 (1999).

[188] H. Hosono and H. Imagawa, *Ion-solid chemistry in implanted amorphous SiO_2*, Nucl. Instr. & Meth. B **91**, 510 (1994).

[189] E.H.A. Dekempeneer, J.J.M. Ottenheim, D.E.W. Vandenhoudt, C.W.T. Bulle-Lieuwma and E.G.C. Lathouwers, *Ion beam synthesis of cobalt silicide: Effect of implantation temperature*, Nucl. Inst. & Meth. B **55**, 769 (1991).

[190] K.-H. Heinig, 1999, to be published.

[191] F. Soisson, P. Bellon and G. Martin, *Two-phase equilibria driven by irradiation in ordered alloys*, Phys. Rev. B **46**, 11332 (1992).

[192] R.C. Tolman, *The effect of droplet size on surface tension*, J. Chem. Phys. **17**, 333 (1949).

[193] K.F. Kelton and A.L. Greer, *Test of classical nucleation theory in condensed systems*, Phys. Rev. B **38**, 10089 (1988).

[194] P. Bellon, *Nonequilibrium roughening and faceting of interfaces in driven alloys*, Phys. Rev. Lett. **81**, 4176 (1998).

[195] S. Hausmann, L. Bischoff, J. Teichert, M. Voelskow, D. Grambole, F. Herrmann and W. Möller, *Dose rate effects in focused ion beam synthesis of cobalt disilicide*, Appl. Phys. Lett. **72**, 2719 (1998).

[196] S. Hausmann, L. Bischoff, M. Voelskow, J. Teichert, W. Möller and H. Fuhrmann, *Dwell-time effects in focused ion beam synthesis of cobalt disilicide: Reflectivity measurements*, Nucl. Instr. & Meth. B **148**, 610 (1999).

[197] A.B. Bortz, M.H. Kalos, J.L. Lebowitz and M.A. Zendejas, *Time evolution of a quenched binary alloy. Computer simulation of a two-dimensional model system*, Phys. Rev. B **10**, 535 (1974).

[198] M. Rao, M.H. Kalos, J.L. Lebowitz and J. Marro, *Time evolution of a quenched binary alloy. III. Computer simulation of a two-dimensional model system*, Phys. Rev. B **13**, 4328 (1976).

[199] D.A. Huse, *Corrections to late-stage behavior in spinodal decomposition: Lifshitz-Slyozov scaling and Monte Carlo simulation*, Phys. Rev. B **34**, 7845 (1986).

[200] J.G. Amar, F.E. Sullivan and R.D. Mountain, *Monte Carlo study of growth in the two-dimensional spin-exchange kinetic Ising model*, Phys. Rev. B **37**, 196 (1988).

[201] O. Penrose, J.L. Lebowitz and J. Marro, 1998, private communication.

[202] K. Binder and D. Stauffer, *Theory for the slowing down of the relaxation and spinodal decomposition of binary mixtures*, Phys. Rev. Lett. **33**, 1006 (1974).

[203] K. Binder and D. Stauffer, *Statistical theory of nucleation, condensation and coagulation*, Adv. Phys. **25**, 343 (1976).

[204] R. Toral and J. Marro, *Scaling of the excess energy in thermodynamically unstable solutions*, Phys. Rev. Lett. **54**, 1424 (1985).

[205] P.L.F. Hemment, K.J. Reeson, J.A. Kilner, R.J. Chater, C. Marsh, G.R. Booker, G.K. Celler and J. Stoemenos, *Ion beam synthesis of thin buried layers of SiO_2 in silicon*, Vacuum **36**, 877 (1986).

[206] H. Yang, R.F. Pinizotto, F. Namavar and E. Cortesi, *Effect of implantation current density and anneal time on the microstructure of SIMOX*, Nucl. Instr. & Meth. B **56/57**, 668 (1991).

[207] S. Nakashima and K. Izumi, *Analysis of buried oxide layer formation and mechanism of threading dislocation generation in the substoichiometric oxygen dose region*, J. Mater. Res. **8**, 523 (1993).

[208] G.F. Cerofolini, S. Betoni, P. Fumagalli, L. Meda and C. Spaggiari, *SiO_2 precipitation in highly supersaturated oxygen-implanted single-crystal silicon*, Phys. Rev. B **47**, 10174 (1993).

[209] L.A. Maksimov, A.I. Ryazanov, K.-H. Heinig and S. Reiss, *Self-organization of precipitates during Ostwald ripening*, Phys. Lett. A **213**, 73 (1996).

[210] R. Weber, R. Yankov, R. Müller, W. Skorupa, S. Reiss and K.-H. Heinig, *Experimental study of precipitation processes in oxygen implanted silicon*, Mater. Res. Soc. Symp. Proc. **316**, 729 (1994).

[211] R.L. Kubena, R.J. Joyce, J.W. Ward, H.L. Garvin, F.P. Stratton and R.G. Brault, *Dot lithography for zero-dimensional quantum wells using focused ion beams*, Appl. Phys. Lett. **50**, 1589 (1987).

[212] P.M. Hui and N.F. Johnson, *Photonic band-gap materials*, Solid State Physics **49**, 151 (1995).

[213] A. Birner, K. Busch and F. Müller, *Photonische Kristalle*, Phys. Bl. **55(4)**, 27 (1999).

[214] K. Sakaguchi and T. Sekine, *Focused ion beam optical column design and consideration on minimum attainable beam size*, J. Vac. Sci. Technol. B **16**, 2462 (1998).

[215] K.-H. Heinig, B. Schmidt, A. Markwitz, R. Grötzschel, M. Strobel and S. Oswald, *Precipitation, ripening and chemical effects during annealing of Ge^+ implanted SiO_2 layers*, Nucl. Instr. & Meth. B **148**, 969 (1999).

[216] L. Rebohle, J. von Borany, R.A. Yankov, W. Skorupa, I.E. Tyschenko, H. Fröb and K. Leo, *Strong blue and violet photoluminescence and electroluminescence from germanium-implanted and silicon-implanted silicon-dioxide layers*, Appl. Phys. Lett. **71**, 2809 (1997).

[217] M.Y. Hao, H. Hwang and J.C. Lee, *Memory effects of silicon-implanted oxides for electrically erasable programmable read-only memory applications*, Appl. Phys. Lett. **62**, 1530 (1993).

[218] H.I. Hanafi, S. Tiwari and I. Khan, *Fast and long retention-time nanocrystal memory*, IEEE Trans. Electron Devices **43**, 1553 (1996).

[219] J. von Borany, R. Grötzschel, K.-H. Heinig, A. Markwitz, B. Schmidt, W. Skorupa and H.-J. Thees, *The formation of narrow nanocluster bands in Ge-implanted SiO_2-layers*, Solid State Electr. **43**, 1159 (1999).

[220] H. Seifarth, R. Grötzschel, A. Markwitz, W. Matz, P. Nitzsche and L. Rebohle, *Preparation of SiO_2 films with embedded Si nanocrystals by reactive r.f. magnetron sputtering*, Thin Solid Films **330**, 202 (1998).

[221] *The physics and chemistry of SiO_2 and Si-SiO_2 interface*, edited by C.R. Helms and B.E. Deal (Plenum Press, New York, 1993).

[222] *CRC Handbook of Chemistry and Physics*, edited by D.R. Lide (CRC Press, London, 1993).

[223] H. Trinkaus, *Theory of the nucleation of multicomponent precipitates*, Phys. Rev. B **27**, 7372 (1983).

[224] V.V. Slezov, Y.J. Tkatch and J. Schmelzer, *The theory of decomposition of solid solutions*, J. Mater. Sci. **32**, 3739 (1997).

[225] J.-S. Li, K. Nishioka and I.L. Maksimov, *Generalized kinetic potential in binary nucleation*, Phys. Rev. E **58**, 7580 (1998).

[226] M.C. Schlamp, X. Peng and A.P. Alivisatos, *Improved efficiencies in light emitting diodes made with CdSe(CdS) core/shell type nanocrystals and a semiconducting polymer*, J. Appl. Phys. **82**, 5837 (1997).

[227] M. Bruchez Jr., M. Moronne, P. Gin, S. Weiss and A.P. Alivisatos, *Semiconductor nanocrystals as fluorescent biological labels*, Science **281**, 2013 (1998).

[228] W.C.W. Chan and S. Nie, *Quantum dot bioconjugates for ultrasensitive nonisotopic detection*, Science **281**, 2016 (1998).

[229] H. Hosono, *Importance of implantation sequence in the formation of nanometer size colloid particles embedded in amorphous SiO_2: Formation of composite colloids with Cu core and a CuO_2 shell by coimplantation of Cu and F*, Phys. Rev. Lett. **74**, 110 (1995).

[230] E. Cattaruzza, G. Battaglin, R. Polloni, T. Cesca, F. Gonella, G. Mattei, C. Maurizio, P. Mazzoldi, F. D'Acapito, F. Zontone and R. Bertoncello, *Nanocluster formation in silicate glasses by sequential ion implantation procedures*, Nucl. Instr. & Meth. B **148**, 1007 (1999).

[231] A. Meldrum, C.W. White, L.A. Boatner, I.M. Anderson, R.A. Zuhr, E. Sonder, J.D. Budai and D.O. Henderson, *Microstructure of sulfide nanocrystals formed by ion-implantation*, Nucl. Instr. & Meth. B **148**, 957 (1999).

[232] J.A. Wolk, K.M. Yu and E.D. Bourret-Courchesne, *Synthesis of GaN nanocrystals by sequential ion implantation*, Appl. Phys. Lett. **70**, 2268 (1997).

[233] C. Bonafos, B. Garrido, M. Lopez, A. Romano-Rodriguez, O. Gonzalez-Varona, A. Perez-Rodriguez and J.R. Morante, *Ion-beam synthesis and structural characterization of ZnS nanocrystals in SiO_2*, Appl. Phys. Lett. **72**, 3488 (1998).

[234] H. Reuther and M. Dobler, *Implantation and growth of large β-$FeSi_2$ precipitates and α-$FeSi_2$ network structures in silicon*, Appl. Phys. Lett. **69**, 3176 (1996).

[235] S. Hausmann, 1999, to be published.

[236] G. Rizza, F. Garrido, J.C. Pivin, J.C. Dran, L. Thomé, M. Gusso, L. Tapfer, A. Quaranta and P. Colombo, *Ion-beam mixing of metal-insulator multilayers: A promising technique for the formation of metallic nanophases*, Nucl. Instr. & Meth. B **127/128**, 574 (1997).

[237] R.H. Swendsen, J.-S. Wang and A.M. Ferrenberg, *New Monte Carlo methods for improved efficiency of computer simulations in statistical mechanics*, in *The Monte Carlo method in condensed matter physics*, Vol. 71 of *Topics in Applied Physics*, edited by K. Binder (Springer, Berlin, 1992), p. 75.

Danksagung / Acknowledgements

An dieser Stelle gilt mein besonderer Dank PROF. DR. WOLFHARD MÖLLER, der trotz der zeitaufwendigen Leitung des Instituts immer ein offenes Ohr für meine Anliegen hatte.

Ganz besonders möchte ich die hervorragende Betreuung durch DR. KARL-HEINZ HEINIG loben. In interessanten und oftmals sehr engagierten Diskussionen konnte ich immer seine hervorragende physikalische Intuition bewundern und von seinem fundiertem Verständnis (ionenstrahl-) physikalischer Sachverhalte profitieren. Dank seines regen Organisationstalents war es mir vergönnt, an diversen offiziellen und inoffiziellen physikalischen Veranstaltungen im In- und Ausland teilzunehmen.

Gerne werde ich die nette Gesellschaft in unserer theorielastigen Simulantengruppe (DR. HANS-ULLRICH JÄGER und DR. MATTHIAS POSSELT, ergänzt im Laufe der Jahre durch weitere Diplomanden, Doktoranden, Postdocs und Gäste) in Erinnerung behalten. Während der obligatorischen Frühstückspause oder am Mittagstisch rückten physikalische Probleme oftmals zugunsten aktueller Themen oder der allgemeinen Ost-West-Befindlichkeit in den Hintergrund.

Eine unschätzbare Hilfe war mir auch mein "privater" Systembetreuer DR. KARSTEN ALBE, der mir mit seinem profunden Computerwissen oftmals den Arbeitsalltag erleichtert hat.

Ohne den offiziellen Systembetreuer DR. MATTHIAS SCHLETT und die Kollegen aus dem Rechenzentrum wäre wohl so manches versehentlich gelöschtes file oder Daten von nicht gesicherten Festplatten verloren gewesen.

Mein besonderer Dank gilt DR. STEFAN REISS, dessen gut strukturiertes Simulationspaket zur OSTWALD Reifung mir einen guten Einstieg in die Thematik und einen Einblick in effektiver C Programmierung verschaffte.

Um die Qualität dieser Arbeit haben sich die Herren Dipl.-Phys. STEPHAN HAUSMANN und STEFANO PARASCANDOLA verdient gemacht durch das kritische Durchlesen vorläufiger Versisonen.

FRAU PFÖRTNER sei hier lobend erwähnt, die sich rührend und nicht ganz selbstlos (Fernleihbestellungen!) für den Fortgang meiner Arbeit interessierte.

Special thanks to WOODY WHITE for the very interesting and enjoyable stay in his group at OAK RIDGE NATIONAL LABORATORY. Without his generous support and the sponsorship of the DEUTSCHER AKADEMISCHER AUSTAUSCHDIENST I would have missed a lot, not to mention the numerous stimulating physical discussions.

On the same footing I place the hospitality at the CNRS-IN2P3-CSNSM in Orsay and

all the nice people I met there (among them MARYLENE PALARD, GIANCARLO RIZZA, ...). It was a great pleasure to discuss physical (and of course also non-physical) problems with PROF. DR. HARRY BERNAS as well as to get an introduction to TEM by DR. MARIE-ODILE RUAULT (although very interesting by itself, it convinced me to stick to computer physics).

My stay at the KURCHATOV INSTITUTE in Moscow in the lovely month of december belongs certainly to the most exciting events during my PhD period. Due to the hospitality of DR. ALEXANDER RYAZANOV I got an interesting insight into Russian physics.

Mein Dank gilt auch dem STIFTERVERBAND FÜR DIE DEUTSCHE WISSENSCHAFT, durch dessen generöse Unterstützung ich die Möglichkeit erhielt, eine internationale Konferenz in England zu besuchen.

Erklärung

Hiermit versichere ich, daß ich die vorliegende Arbeit ohne zulässige Hilfe Dritter und ohne Benutzung anderer als der angegebenen Hilfsmittel angefertigt habe. Die aus fremden Quellen direkt oder indirekt übernommenen Gedanken sind als solche kenntlich gemacht. Die Arbeit wurde bisher weder im Inland noch im Ausland in gleicher oder ähnlicher Form einer anderen Prüfungsbehörde vorgelegt.

Diese Dissertation wurde am Institut für Ionenstrahlphysik und Materialforschung im Forschungszentrum Rossendorf unter der wissenschaftlichen Betreuung von PROF. DR. WOLFHARD MÖLLER und DR. KARL-HEINZ HEINIG angefertigt.

Die Promotionsordnung der Fakultät für Mathematik und Naturwissenschaften der Technischen Universität Dresden vom 27. 9. 1994 erkenne ich an.

Dresden, den 28. Juni 1999

Thesen / Major statements of the work

1. An atomic and a mesoscopic computer simulation method have been employed to describe the governing physics of ion beam synthesis of nanostructures. Nucleation, growth, OSTWALD ripening, and coalescence of nanoclusters have been studied on different time and length scales and the effects of collisional mixing have been simulated in detail.

2. On an atomic level a kinetic 3D lattice Monte-Carlo method in the framework of the nearest-neighbor ISING model has been used, which allows to study the evolution of (implanted) impurity atoms in (quasi-) equilibrium as well as in athermal processes.

3. Atomic simulation parameters have been defined in terms of thermodynamical expressions in order to couple both computer techniques. The intrinsic solubility properties of the Monte-Carlo method have been shown to be of the ARRHENIUS-type. The GIBBS-THOMSON relation is demonstrated to be valid on a nanometer scale.

4. Based on the GIBBS-THOMSON relation an explicit expression for the surface tension has been derived in the temperature range well below the roughening transition.

5. For homogeneous systems the OSTWALD ripening behavior of nanoclusters in the size range of the capillary length has been studied by the Monte-Carlo method. It is shown that the standard LIFSHITZ-SLYOZOV-WAGNER theory of coarsening can not be applied in this size range.

6. An existing local mean-field model restricted to diffusion limited OSTWALD ripening has been extended to be applicable for an arbitrary degree of diffusion and reaction control. The simulation results for the intermediate coarsening regime have been compared to an alternative theoretical description, and the observed differences have been discussed.

7. The atomic and mesoscopic computer simulation methods have been combined to perform a multi-process and multi-scale modeling of the evolution of nanoclusters. Based on a detailed comparative study of the OSTWALD ripening behavior of precipitates, a well-defined interface between both models has been found.

8. The topic of self-organization of ion beam synthesized nanoclusters has been revisited. By combined atomic and mesoscopic simulations of as-implanted profiles it has been found that the recently predicted self-organization of nanoclusters is strongly suppressed by internal OSTWALD ripening, which was not taken into account before.

9. Combined atomic and mesoscopic simulations have been performed concerning the formation of periodic 2D arrays of quantum dots by a focused ion beam. The observed nanocluster patterns are shown to be governed by the competition between intra-spot and inter-spot OSTWALD ripening. It is predicted that for the formation of nanocluster arrays high-temperature rapid thermal annealing followed by a well-controlled cooling-down stage is superior to conventional annealing techniques.

10. The formation of nanoclusters during ion implantation has been studied systematically. It has been found, that the resulting nanocluster distributions are a function of the ratio of ion deposition to diffusion. A good correspondence has been observed with respect to temperature-dependent Au^+ implantation experiments into SiO_2.

11. Additional Monte-Carlo simulations predict that a controlled variation of the implantation conditions (decreasing the implantation temperature or increasing the ion current) can initiate a second nucleation regime, thus leading to a bimodal size distribution. Corresponding Au^+ implantations into SiO_2 are discussed with respect to these predictions.

12. Collisional mixing has been incorporated into the Monte-Carlo method. The resulting modifications of the GIBBS-THOMSON relation due to the competition between thermodynamically activated and ballistically induced processes have been studied. It is found, that collisional mixing increases the monomer solubility and decreases the capillary length as compared to the pure thermal case.

13. The effective capillary length has been shown to become negative for a large ratio of ballistic to thermal diffusion, as predicted recently. This regime is characterized by inverse OSTWALD ripening, that is the growth of small nanoclusters at the expense of large ones. As a consequence of this entirely new mode of nanocluster evolution, a delta-like size distribution is predicted, which is verified in corresponding Monte-Carlo simulations.

14. Collisional mixing induced nucleation of additional nanoclusters is shown to occur for very high mixing intensities or very low monomer diffusivities, which accompanied by inverse OSTWALD ripening causes the reduction of the mean nanocluster size.

15. The kinetic 3d lattice Monte-Carlo method has been properly extended in order to study various aspects of multi-impurity interactions:

    (a) Simulations have supported the understanding of ion beam synthesis of Ge nanoclusters in SiO_2 layers on Si in the presence of a weakly oxidizing annealing

atmosphere. In particular, the driving forces of the process causing the experimentally observed zone of Ge oxidation could be modeled.

(b) The topic of core/shell nanocluster formation by sequential ion implantation has been addressed. It has been shown that collisional mixing seems to be a major obstacle concerning ion beam synthesis of core/shell nanoclusters.

(c) Shifted-profile ion implantation of two species is proposed as an interesting option of compound nanocluster synthesis. For specific parameter relations Monte-Carlo simulation results predict the possibility of the formation of a very narrow layer of compound nanoclusters.

The stumbling way in which even the ablest of the scientists in every generation have had to fight through thickets of erroneous observations, misleading generalizations, inadequate formulations, and unconscious prejudice is rarely appreciated by those who obtain their scientific knowledge from textbooks.

James B. Conant, Science and Common Sense, 1951